Aeroacoustic Transfer of Leading Edge Serrations from Single Aerofoils to Low-Pressure Fan Applications

vorgelegt von
M.Sc.
Till Biedermann
ORCID: 0000-0002-9635-7949

von der Fakultät V – Verkehrs- und Maschinensysteme
der Technischen Universität Berlin
zur Erlangung des akademischen Grades

Doktor der Ingenieurwissenschaften
- Dr.-Ing. -

genehmigte Dissertation

Promotionsausschuss:

Vorsitzender: Prof. Dr. sc. Panagiotis Stathopoulos
Gutachter: Prof. Dr.-Ing. Christian Oliver Paschereit
Gutachter: Prof. Dr.-Ing. Kilian Oberleithner
Gutachter: Prof. Dr.-Ing. Matthias Neef

Tag der wissenschaftlichen Aussprache: 18. September 2019

Berlin 2019

Abstract

Leading edge serrations are well-known for their aeroacoustic potential in reducing aerofoil-turbulence interaction noise and are also associated with certain aerodynamic advantages. To prepare leading edge serrations for industrial application, two obstacles remain to be addressed. First is a combined analysis of the aeroacoustic and the aerodynamic performance of leading edge serrations to develop optimum designs. Second is the need to examine the transferability of the known effects of leading edge serrations from a single aerofoil to full rotors, which are considered to be the final area of application.

This thesis aims to assist in the transfer of a well-investigated aerofoil with serrated leading edges from the rigid to the rotating domain. With this purpose, a single aerofoil type is selected and thoroughly analysed, experimentally and numerically, to generate a reliable data basis for aerodynamic performance and noise reduction capability. Aside from gathering information on the overall performance, the spatial distribution of the noise sources is localised, and the spectral composition of the noise reduction is found to follow a clearly defined scaling law. Aerodynamically, generated vortices are found to be responsible for a complex three-dimensional separation mechanism of the leading edge serrations, causing a delay of stall.

The generated data basis is then used to design low-pressure axial fans of minimum complexity by keeping the initially chosen aerofoil type. The experimentally identified noise reduction mechanisms for the serrated axial fans are found to be more diverse than the single aerofoil and highly dependent on the inflow conditions and the operation point of the fan. A highly similar pattern for the spectral scaling of the noise reduction supports the finding that at optimum operation conditions, the previously identified noise reduction mechanisms for the single aerofoils are transferable to the rotating domain. On the other hand, additional aerodynamic mechanisms are found to dominate the noise reduction for the instability region of the fan, also contributing to reduced blade-to-blade interaction effects. Moreover, the blade-tip leakage flow is altered by delaying the development of coherent structures.

The next step towards a more general description of the aeroacoustic and aerodynamic dependencies is developing a comprehensive model based on artificial neural networks. This model allows a combined analysis of the aerodynamic and acoustic performance of rotors with serrated leading edges and shows an accurate prediction of the overall performance and the spectral composition of the radiated noise. It also enables the development of multi-objective optima for serration designs and motivates further studies into the generalisability of the observed trends. Furthermore, the developed model represents a feasible tool to create tailored serration designs for maximum efficiency in both aeroacoustics and aerodynamics, contributing to the development of future low-noise fans and rotating machinery.

Kurzfassung

Leading Edge Serrations sind hinlänglich für ihr Potential zur Reduktion von turbulenzinduziertem Schall bekannt. Ebenso können sie sich als aerodynamisch vorteilhaft erweisen. Mit dem Ziel, Leading Edge Serrations industriellen Anwendungen zugänglich zu machen, verbleiben primär noch zwei Hemmnisse. Zum einen die Notwendigkeit einer kombinierten Bewertung des aerodynamischen und des aeroakustischen Potentials mit dem Ziel der Identifikation optimaler Designansätze. Zum anderen sind Aussagen hinsichtlich der Übertragbarkeit der bekannten Schallreduktionsmechanismen von einem einzelnen Tragflügel hin zu rotierenden Strömungsmaschinen zu treffen, da letztere das finale Anwendungsgebiet von Leading Edge Serrations darstellen.

Diese Arbeit zielt darauf ab, bei dem Transfer eines umfassend analysierten Tragflügeldesigns mit Leading Edge Serrations hin zu einem rotierenden System zu assistieren. Hierzu wird ein für spätere rotierende Anwendungen sinnvolles Tragflügelprofil gewählt und sowohl experimentell als auch numerisch umfassend untersucht, um eine Datenbasis des aerodynamischen und aeroakustischen Potentials zu generieren. Neben Informationen über die globalen Eigenschaften, wurde ebenfalls die räumliche Lage der Schallquellen lokalisiert. Zudem konnte der Verlauf des spektralen Schallreduktionsvermögens einer klaren Gesetzmäßigkeit zugeordnet werden. In Bezug auf die Aerodynamik wurden Wirbelstrukturen, welche sich an den Leading Edge Serrations bilden, als ursächlich für einen komplexen dreidimensionalen Ablösemechanismus identifiziert, welcher eine verzögerte Strömungsablösung bewirkt.

Unter Beibehaltung des gewählten Tragflügelprofils wurde die generierte Datenbasis in einem zweiten Schritt zur Auslegung von axialen Niederdruckventilatoren niedriger Komplexität genutzt. Die hier experimentell identifizieren Schallreduktionsmechanismen sind, im Vergleich zu einem einzelnen Tragflügel, deutlich diverser und weisen eine klare Abhängigkeit vom Betriebspunkt des Ventilators sowie von den Einflussparametern auf. Unter optimalen Zuströmbedingungen kann eine klare Übertragbarkeit der Effekte vom ebenen in das rotierende System gezeigt werden. Im Gegensatz wird das Schallreduktionspotential im Instabilitätsbereich des Ventilators durch aerodynamische Strömungsphänomene dominiert, welche zudem zu einer vorteilhaften Beeinflussung von Schaufelinteraktionen beitragen. Des Weiteren wurde durch den Einsatz von Rotoren mit Leading Edge Serrations eine verzögerte Entstehung von kohärenten Strukturen im Blattspitzenbereich nachgewiesen.

Um einen weiteren Schritt in Richtung einer globalen Beschreibung der erhaltenen aeroakustischen und aerodynamischen Abhängigkeiten zu gehen, wurde ein umfassendes Modell generiert, welches auf dem Training künstlicher neuronaler Netze beruht. Das generierte Modell ermöglicht eine kombinierte Prognose der aerodynamischen und aeroakustischen Performance der getesteten Prototypen und weist sowohl im Zeitbereich als auch hinsichtlich der spektralen Zusammensetzung der Signale eine hohe Prognosegüte auf. Dies ermöglicht die Definition multikriterieller Optima bezüglich des Serration Designs und motiviert weiterführende Studien hinsichtlich einer Generalisierbarkeit der beobachteten Trends. Schlussendlich ermöglicht das generierte Modell maßgeschneiderte Designansätze für eine maximale aerodynamische und aeroakustische Effizienz, was einen sinnvollen Beitrag zur zukünftigen Entwicklungen schallarmer Ventilatoren und Strömungsmaschinen darstellt.

Content

IV. Appendices

Acknowledgements

In 2015, I moved to London to work on my master's thesis with the research group of Dr Tze Pei Chong at Brunel University London. This was the first time I encountered the bio-inspired leading-edge modifications, which now constitute my doctoral thesis. Since then you, Tze Pei, have been interested in my progress and continuously supported me both professionally and personally, for which I am deeply thankful.

Moving back from London to Düsseldorf, I spent the next years as a research assistant at the Institute of Sound and Vibration Engineering (ISAVE), affiliated with the University of Applied Sciences Düsseldorf. Here, I had the pleasure to work in a collaborative, supportive and motivating team with many competent colleagues at my side who are lots of fun to work with. Igor, Tobias and Gi-Don, I thank you all for the great time and the vivid memories. Special thanks are due to my office colleague and good friend Pasquale Czeckay. Since space is limited, I refrain from mentioning all the support I received from you. Moreover, I am particularly thankful to the head of our institute, Prof Jörg Becker-Schweitzer. You always volunteered as a firefighter whenever things went wrong. I am also grateful to Prof Frank Kameier, chair of fluid dynamics. From my undergraduate studies on, you showed interest in my professional (and sometimes in my personal) development, and we had plenty of memorable moments and intense discussions. Thanks for trusting in my capabilities.

During the research for my thesis, I had priceless assistance from all sides. I want to thank Dr Thomas Geyer of Brandenburg University of Technology for allowing me the chance to conduct the beamforming measurement campaign at their aeroacoustics facility. Also, thank you, Thomas, for the assistance in calculating the acoustic sound maps and for your interest to discuss the results again and again. It is always great meeting you in the conference season and I am looking forward to the next time.

Thanks also to Marius Reich of Centre for Innovative Energy Systems at HS Düsseldorf. Without your expert knowledge on artificial neural networks, Marius, my thesis would be less valuable. Also thank you as a friend for your interest in my studies and for your nerve-racking enquiries, which contributed to reflections on my research approaches. The experimental studies would not have been possible without the support of Stefan Jahr, FMDauto institute. Your efforts, Stefan, in prototyping this endless number of aerofoils were priceless. Thank you for sharing your expertise. Moreover, outstanding jobs were done by all the students I had the honour to supervise, in particular, Pasquale Czeckay, Nils Hintzen, Nina Balde, Oliver Koster, Denis Schreiber, David Delgado Hernandez, Daniel Delgado Hernandez, and Matthias Rother. You definitely proved that 'learning by teaching' works.

I am particularly thankful to Prof C.O. Paschereit of Technical University Berlin for being my supervisor during the last years of my thesis completion, for providing pragmatic solutions whenever problems occurred, and for paving my way. Thanks also to Prof Kilian Oberleithner of the Technical University Berlin for acting as my co-reviewer and to Prof Panagiotis Stathopoulos for creating such a productive athmosphere whilst acting as the chairman during the doctoral viva. Another big thank you is well deserved by Prof Matthias Neef of HS Düsseldorf, whose willingness to spontaneously act as my co-supervisor means a lot to me and whose comments on my first draft were priceless. Thank you.

I would also like to acknowledge the support of the German Academic Scholarship Foundation, which allowed me to freely develop my research interest and to sometimes dare viewing beyond the horizon.

The main burden, especially during the final phase of the study, was carried by my wife Katharina and my son Joona. There are no words to express my gratefulness. Thank you, Katha, for staying at my side, for your patience and also for coping with my darker moods ...and for grounding me whenever necessary.

'We are liable to mistake the predominant cause, unless we can measure the quantity of the effects produced.'

John Theophilus Desaguliers, 1745

To Katha.

List of Symbols and Abbreviations

Latin Symbols

A	serration amplitude	mm
A_E	enveloping surface of acoustic source	m^2
A_{el}	electric current	A
A_{Grid}	cross sectional area of the turbulence grid	m^2
A_{MP}	cross sectional area of the measurement plane	m^2
A_0	reference area	m^2
A_R	local area of a radial segment	m^2
A_{Serr}	area under a sinusoidal curve	m^2
A_{WS}	wetted-surface area (effective aerofoil area)	m^2
C	aerofoil chord length	mm
C_D	coefficient of drag	--
$C_{D,u}$	non-corrected coefficient of drag	--
C_F	skin friction coefficient	--
C_{FL}	theoretical coefficient of lift in potential flow	--
C_L	coefficient of lift	--
$C_{L,u}$	non-corrected coefficient of lift	--
C_p	static pressure coefficient	--
D	diameter	mm
D_{Hub}	hub diameter	mm
F_A, F_F	lift forces at aft and fore	N
$F_{D,}\, F_D{}^*$	drag forces (* indicates non-corrected quantities)	N
F_L	lift forces	N
$G_{11}(\omega), G_{22}(\omega)$	power spectral density	V^2s
$G_{12}(\omega), G_{12}^*(\omega)$	cross spectral density (* Fourier transform)	V^2s
H	nozzle height	mm
H_{Mesh}	mesh width	mm
K	downstream contraction factor of open jet	--
K_η	empirical constant	m^{-1}
K_X	longitudinal wave number	--
$\widehat{K}_x$	normalised longitudinal wavenumber	--
Ma	Mach number	--
N_{HP}	number of hyperparameters	--
$N_{Neurons}$	number of neurons	--
P_{aero}	aerodynamic demand	kgm^2s^{-3}
P_{el}	electric demand	W
Q	Q-criterion	s^{-2}
$\dot{Q}$	flow rate	m^3s^{-1}
R	radius (observer distance)	m
R_{Duct}	duct radius	m
R_{Hub}	hub radius	m
Re	Reynolds number	--
R_{spec}	specific gas constant of air	$J(kgK)^{-1}$
S	aerofoil span	mm
Sr, Sr_C	Strouhal number (chord-based)	--
Sr_A	Strouhal number (amplitude-based)	--
Sr_Λ	Strouhal number (based on integral length scale)	--

S_{rep}	area-equivalent blade span	m
S_{Strain}	strain rate	s^{-1}
T	spectral components of tonal character	Hz
Tu	turbulence intensity	--
U_{conv}	convective velocity of turbulent structures	ms^{-1}
U_{el}	electric voltage	V
U_0	free stream velocity	ms^{-1}
U_u, U_v, U_w	velocity vector in cartesian coordinate system	ms^{-1}
U_{Rot}	circumferential velocity	ms^{-1}
U_1,U_2	circumferential velocity at positions 1 and 2	ms^{-1}
Y_E	specific energy	m^2s^{-2}
a_S	prefactor for spectral scaling law according to [1]	--
a_0, b_0, c_0	zero readings of load cells (force measurements)	N
b	bias values (hyperparameter of an ANN)	--
b_{arc}	circular arc length	m
b_{LL}	constant according to Laws and Livesey [2]	--
b_S	offset factor for spectral scaling law	--
c	speed of sound	ms^{-1}
c_{u1}, c_{u2}	circumferential component of meridian velocity	ms^{-1}
c_{x1}, c_{x2}	axial velocity component of meridian velocity	ms^{-1}
d	aerofoil thickness	mm
d_{Bar}	mesh/grid bar diameter	mm
f	frequency	Hz
$f_{m,n}$	duct mode frequencies	Hz
f_{TEF}	turbulence eddy frequency	Hz
i	number of inputs	--
$j'_{m,n}$	Bessel coefficients	--
k	number of influencing parameters	--
k_C	ratio of A_{MP} and A_{Grid}	--
$l_y^L(\omega)$	turbulence correlation length	m
n	rotational speed	min^{-1}
n_{MAE}	normalised mean average error	--
n_{R^2}	number of samples	--
p_{baro}	barometric pressure	Pa
p_{RMS}	RMS value of acoustic pressure fluctuation	Pa
s_{SD}	standard deviation	div.
t	aerofoil thickness	m
t_p	blade pitch	--
u_τ	friction velocity	ms^{-1}
w	weighting values (hyperparameter of an ANN)	
w_{u1}, w_{u2}	circumferential component of relative velocity	ms^{-1}
w_1, w_2	relative velocity	ms^{-1}
x, y, z	streamwise, anti-streamwise, vertical coordinates	mm
$\hat{y}_i$	predicted response of i-th sample	div.
$\bar{y}_i$	mean value of observed response	div.
y^+	non-dimensional wall distance	--
z_B	number of fan blades	--
$z_{1,2}$	geodetic height	m

Greek Symbols

ΔA	streamwise amplitude distance	m
Δf	frequency resolution	Hz
Δp	static pressure rise	Pa
Δp_{Grid}	grid-dependent pressure loss	Pa
Δx	axial distance/ displacement	m
Δz_{Tip}	blade tip clearance of rotor	mm
$\Delta\Phi$	phase shift	rad
Θ	polar angle	deg
Λ_L	longitudinal integral length scale	mm
Λ_t	transversal integral length scale	mm
Λ_{TR}	empirical value for thickness ratio of NACA65	--
Ω	vorticity rate	s^{-1}
α_{DoE}	non-dimensional location of DoE star-points	--
β_0	flow angle	deg
γ	stagger angle	deg
γ-Re_θ	laminar/ turbulent transition model	--
γ^2	coherence function	--
δ_{TS}	non-dimensional throttling state	--
ε	window-specific shape factor	--
ε_{sb}	solid-blockage correction factor	--
ε_{wb}	wake-blockage correction factor	--
ζ	grid-dependent pressure-loss coefficient	--
ζ_{AoA}	correction factor for effective AoA	--
η	dynamic viscosity	Pas
η_{System}	system efficiency	--
θ_{Serr}	geometrical inclination angle	deg
λ	serration wavelength	mm
λ_{aero}	aerodynamic wavelength	m
λ_2	body shape factor	--
ν	kinematic fluid viscosity	m^2s^{-1}
ρ	fluid density	kgm^{-3}
σ	geometric wind tunnel shape factor	--
σ_s	rotor solidity	--
τ_w	wall shear stress	Pa
φ	flow coefficient	--
ψ	pressure coefficient	--
ω	angular frequency $\omega = 2\pi \cdot f$	s^{-1}
ω_0	angular design frequency	s^{-1}

Abbreviations

ABS	Acrylnitril-Butadien-Styrol-Copolymer	--
AoA	angle of attack	deg
ANN	artificial neural network	--
AR	aspect ratio	--
ATI	aerofoil-turbulence-interaction (noise)	--
BB	spectral components of broadband character	Hz
BBD	Box-Behnken design	--
BL	boundary layer	--
BPF	blade passing frequency	Hz
BS	block size	--
BSLN	baseline (configuration)	--
C-CCD	circumscribed central composite design	--
CLEAN	deconvolution beamforming algorithm	--
CLEAN˙SC	CLEAN based on source coherence	--
CPS	cross-power spectrum	dB
DES	detached eddy simulation	--
DoE	design of experiments (methodology)	--
FEM	finite element method	--
FW-H	Ffowcs-Williams and Hawkings (analogy)	--
ID	identifier	--
IP	influencing parameters	--
ISVR	Institute of Sound and Vibration Research	--
LE	leading edge	--
LES	large eddy simulation	--
LHS	Latin hypercube sampling	--
LLT	Prandtl's lifting line theory	--
MAE	mean average error	--
MAV	micro air vehicle	--
(MO)PSO	(multi-objective) particle swarm optimisation	--
MT	measurement trials	--
NACA	National Advisory Committee for Aeronautics	--
NASA	National Aeronautics and Space Administration	--
OASPL	overall sound pressure level	dB
OAPWL	overall sound power level	dB
OAWPL	overall wall power level	dB
OL	overlapping	--
PIV	particle image velocimetry	--
PSD	power spectral density	dB/Hz
PWL	sound power level	dB
PWM	puls-width modulated (electric motor)	--
RMS	root-mean-square (average)	div.
RTI	rotor-turbulence-interaction (noise)	--
SFC	skin friction coefficient	--
SPL	sound pressure level	dB
SST	shear stress transport (turbulence model)	--
TE	trailing edge	--
TV	target value	--
T-S wave	Tollmien-Schlichting wave	--
(U)RANS	(unsteady) Reynolds-averaged Navier Stokes	--

WPL	wall power level	dB
WS	wetted surface	--

I. Introduction

1 Preface

1.1 Motivation

Over the past decades, noise pollution has increasingly become the focus of attention as a key factor in physical and mental health. The high level of automation and industrialisation in developed countries, in particular, leads to an increased number of contact points between men and machines. This requires a well-thought-out strategy for reducing the noise in urban areas. Especially with regard to the aviation industry, this poses a main challenge since each low-noise design should come at the cost of aerodynamic penalties or losses in efficiency. On the other hand, promising technologies such as, for example, counter-rotating rotors are prevented from being widely used due to the significant level of radiated noise, even though they are aerodynamically efficient.

Peake and Parry [3] describe major changes in the composition of the acoustic signature of an aircraft. Initially, jet noise was the main noise source, which was reduced significantly by greatly increasing the bypass ratio of the turbines, leading to a reduction in the associated jet-mixing noise. The continuous decrease in jet noise led to an increase in relevance of fan noise, which by now constitutes the dominant noise source of modern turbomachines.
However, the ever-expanding air traffic, as well as the coalescence of airports and urban areas, calls for further reductions in noise load. This matches the 'Flightpath 2050' by the European Commission [4], which outlines Europe's vision on aviation. Compared to a typical aircraft, manufactured in 2000, a reduction in the noise load of 65% for flying aircraft is agreed. To fulfil these ambitious targets inevitably requires a comprehensive understanding of the underlying mechanisms of both aerodynamic and acoustic nature. Until now, two consecutive European projects, BROBAND and FLOCON, have been established to identify and to predict relevant turbofan noise sources, as well as to develop new methods for noise reduction. One of the main sources of noise was found to be aerofoil-turbulence-interaction (ATI) noise, leading to broadband noise radiation at the leading edges of the stator vanes. Various active and passive control applications were tested, and so-called leading edge serrations were found to be the most promising in terms of noise reduction. Inspired by the feather structure of owls or the tubercles of humpback whale flippers, these sinusoidal structures assist to significantly reduce the turbulence-ingested flow perturbation and the associated generation of noise.

However, this passive application is not only of interest to the aviation industry but may also benefit aviation-related industries, such as the automotive industry or the wind turbine industry. Especially for the latter, turbulent inflow noise is commonly reported for wind turbines [5], in which atmospheric turbulence interacts with the turbine blades. Moreover, even an aerodynamic benefit in terms of stall-reducing features for wind turbines was pointed out by Locke [6].

1.2 Origin

The technique of modifying aerofoil leading edges to influence the aerodynamic stall characteristics is mainly bio-inspired by humpback whales, which have pectoral flippers equipped with tubercles. In terms of acoustics, however, owls were found to possess similar comb-like structures at the leading edges of their wings, giving rise to a remarkable low acoustic signature. The combination of these features called the attention of many researchers around the world, promising benefits in both aerodynamic characteristics and noise radiation.

Fish and Battle [7] were the first to examine the morphological composition of Humpback whale pectoral flippers. The flippers were found to be symmetrical, and the mid-span cross-sections were shaped similarly to a $NACA63_4$-021 aerofoil. With an aspect ratio of $AR = 6.1$ and a slight backward-swept shape of 19 degrees, eleven tubercles were found on a

proband, with tubercles with a streamwise extension of 6.5 - 8.5% of the chord in spanwise locations of 33 % ≤ span ≤ 99.1 %. With regard to the working mechanisms, the authors suspected a function similar to that of large vortex generators, which postpone the stall by exchanging momentum with the boundary layer of the hydrofoils. This is considered extremely helpful for the complex feeding behaviour of humpback whales, whose bubble netting or inside-loop manoeuvres, among others, require very small turning radii, which are estimated by Fish and Battle to be approximately 7.4 m for a whale of 9 m in size.

On the other hand, in 1934, Graham [8] was the first to introduce the potential noise-reducing features of owls to the aerospace community. Generally, the low acoustic signature is attributed to three key features, namely the comb-like structures at the leading edges, a downy lower surface of the wings, and the trailing edge fringe. The leading edge comb was found to be a key contributor to the silent flight of the owl and, in particular, for reducing noise due to perturbations in the air flow.

'There is a remarkably stiff, comb-like fringe on the front margin of every feather that functions as a leading edge. The teeth of this comb are extensions of the barbs, or fibres, that form the front web of the feather. They vary in length and in distance apart according to the size of the bird and to their position in the wing. The largest of them are 4.0 mm. in length, and 0.75 mm apart.' [8]

Even more astonishingly, it is pointed out that the only owl species that does not possess leading-edge hooks is the Asian fishing owl (*Ketupa flovipes*). Because it is a fish-eating bird, evolution never needed to develop silent wings as the prey is not sensitive to the noise of the wings. In 1973, Anderson [9] published an experimental study on the constitution and the effect of the comb-like structures at the leading edges of owl wings. The combs analysed turned out to deflect the flow in a spanwise direction, leading to stationary spanwise vortices that, like the vortex lift on delta wings, delay separation only at high angles of attack and that show an extremely small drag profile at flight angles. The silent flight of owls was further investigated by Lilley [10], who extended the analysis of the aerodynamic mechanisms to the mentioned three key features of owl wings. Moreover, Ito [11] describes post-stall benefits at low Reynolds numbers, similar to the effects of humpback whale tubercles. More recently, the silent flight of owls was investigated experimentally by Sarradj et al. [12], performing flyover measurements and potentially inspiring further research into the testing of extracted features of owls by means of fences [13] or leading-edge hooks [14] for reducing leading-edge noise.

Up to now, numerous studies are available that focus on leading-edge structures with the purpose of reducing the radiated noise and/or improving certain aerodynamic parameters, such as the maximum stall angle or the post-stall lift performance. Both fields of research, however, are of high interest to the aviation industry as well as turbomachinery manufacturers. In an early form of this novel passive noise reduction or stall-delaying technique, serrated leading edges are already manufactured industrially [15], although no fundamental research has been carried out. Moreover, the potential benefit for rotors is evidenced by a first patent [16].

Even though leading-edge structures (leading edge serrations) are a promising technique for application in rotating machinery, the main research still focusses on rigidly mounted aerofoils, thereby disregarding the combined analysis of aeroacoustic and aerodynamic performance.

1.3 Scope of the Thesis

Up to now, research on serrated leading edges has basically focussed on rigidly mounted aerofoils, analysed either aerodynamically or acoustically since they provide desirable features for both these fields. Only few combined studies on serration effects are available, preventing the much-needed linking of aeroacoustics and aerodynamics. Furthermore, the eventual area of application is often mentioned to be rotating machinery, such as counter-rotating rotors, fans and blowers or aircraft engines. Nevertheless, only meagre attempts were made to transfer leading edge serrations from the rigid to the rotating frame by using the previously obtained knowledge on the serration effect.

The main research question is whether and under what circumstances the knowledge on the aerodynamic and acoustic performance of serrated leading edges in a rigidly mounted domain can be transferred to rotating applications. This includes the well-known noise reduction mechanisms of leading edge serrations as well as investigations into the effect of additional parameters for rotors, such as the blade-tip clearance gap, a varying circumferential velocity, different states of operation and blade-to-blade interaction effects. In addition, the role of modern rotor blade design parameters on the aerodynamic and acoustic feasibility of leading edge serrations remains to be defined.

The presented thesis aims at providing meaningful assistance for realising this transfer process by following a highly systematic strategy of transferring well-analysed aerofoils with serrated leading edges to an axial low-pressure fan application. The focus is on minimum complexity in order to draw direct conclusions about transferability. Monitoring of the aerodynamic and aeroacoustic properties throughout the whole process, as well as a repeated interlinking of the results, is expected to be the key to gaining deep insights into the mechanisms underlying the specific aerodynamic and aeroacoustic performance. Finally, the development of a combined model, taking into account aeroacoustic and aerodynamic properties, is considered meaningful for making a reliable approximation of the overall performance of serrated rotors. This does not only apply to the time domain but also to the spectral domain, particularly in terms of acoustics. The possibility of modelling the spectral composition provides vast opportunities for further optimising fans and blowers and is considered to be a first step towards industrial implementation of serrated leading edges.

1.4 Structure of the Thesis

In order to refine the scope of the thesis, a brief overview of the content of the individual sections of this work is provided below. In addition, the structure shown in Figure 1-1 hints at the strong interlinking of the different sections in order to realise the transfer process from the rigid to the rotating domain.

Section 2

- Aerodynamic investigation of aerofoils subjected to serrated leading edges:
  - Experimental study to determine the general performance of selected configurations by conducting measurements of lift and drag forces.
  - Supplementary numerical study to confirm experimental trends as well as to provide additional and more detailed insights into the aerodynamic working mechanisms.

Section 3

- Aeroacoustic study to monitor the acoustic performance of rigidly mounted aerofoils equipped with serrated leading edges:
  - Development of a statistical-empirical model by means of the design of experiments (DoE) approach to simultaneously describe the impact of five influencing parameters.
  - Localisation of the noise sources and identification of the effective noise reduction capability via an array-beamforming study, while excluding unwanted disturbing noise sources.

- Interrelation of aerodynamic and aeroacoustic findings by incorporating aerodynamic results into the statistical-empirical model and by generating multi-objective optima.

Section 4

- Transfer analysis from the single aerofoil to a low-pressure axial fan:
  - Definition of the test rig.
  - Rotor and blade design.
  - Analysis of inflow conditions to maintain comparability with the rigid domain.

Section 5

- Aeroacoustic study with a model rotor and successive blade variation to investigate the underlying mechanisms of serrated leading edges in the rotating frame:
  - Implementation of one serration design to be analysed both aerodynamically and aeroacoustically.
  - Identification of blade interaction effects.
  - Identification of possible noise reduction mechanisms using additional wall-pressure analysis.

Section 6

- Experimental parameter study for a rotating application by varying the serration design parameters as well as the inflow conditions:
  - Analysis of the same non-dimensional serration designs as in the rigid frame.
  - Detailed aerodynamic measurements of rotors with serrated leading edges.
  - Spectral analysis of filtered signals to identify commonalities of the broadband noise reduction effects for the rigidly mounted aerofoils and the investigated rotors.

Section 7

- Modelling of the analysed low-pressure fan application by means of artificial neural networks:
  - Modelling of the overall performance in terms of aerodynamics, aeroacoustics and wall-pressure fluctuations in the blade tip region.
  - Additional modelling of the spectral composition of the acoustic signals as well as the wall-pressure data, using a customised filtering approach.
  - Validation of the models obtained against independent data.
  - Extraction of overall and spectral trends for the serrations, as dependent on four influencing parameters, to provide further insights into the serration sensitivity of aerodynamic and aeroacoustic performance.
  - Definition of multi-objective optima to tailor optimum serrations for practical applications.

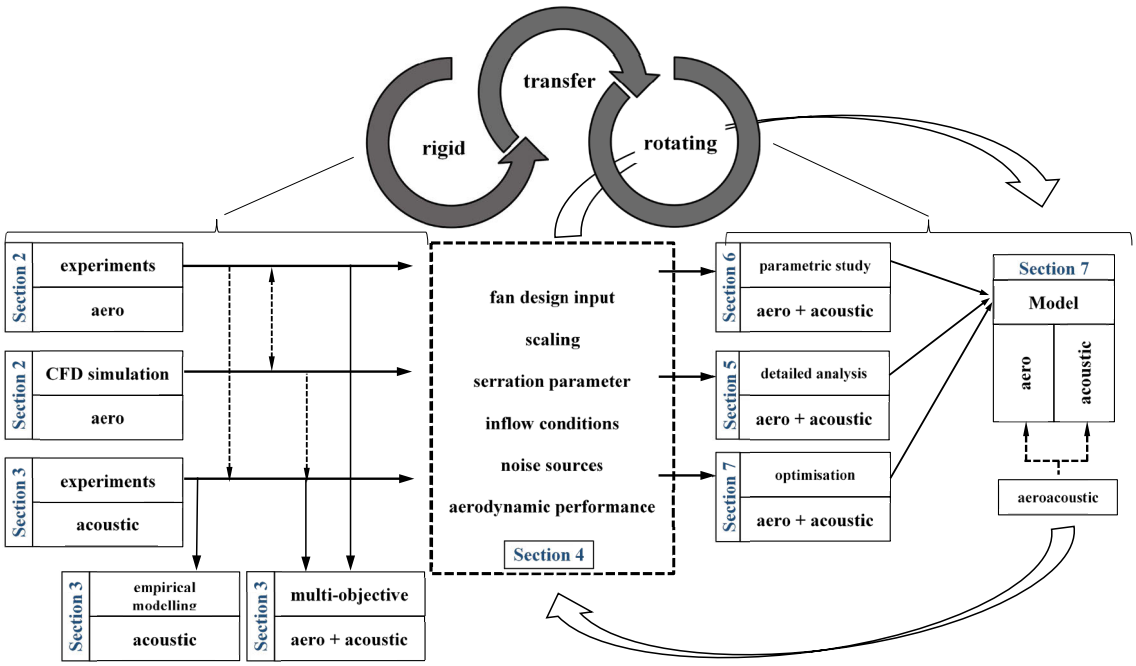

Figure 1-1 Schematic representation of the thesis structure as well as the interrelation of the individual sections.

1.5 Associated Publications of the Presented Work

Journal

Biedermann, T. M.; Kameier, F.; Paschereit, C. O. (2019): Successive Aeroacoustic Transfer of Leading Edge Serrations from Single Airfoil to Low-Pressure Fan Application. In: ***ASME. J. Eng. Gas Turbines Power,*** (). DOI:10.1115/1.4044362.

Biedermann, Till M.; Czeckay, P.; Geyer, T. F.; Kameier, F.; Paschereit, C. O. (2019): Effect of Inflow Conditions on the Noise Reduction Through Leading Edge Serrations. In: ***AIAA Journal***, Articles in Advance, pp 1–6. DOI: 10.2514/1.J057831.

Biedermann, Till M.; Reich, Marius; Kameier, F.; Adam, M.; Paschereit, C. O. (2019): Assessment of Statistical Sampling Methods and Approximation Models Applied to Aeroacoustic and Vibroacoustic Problems. Accepted for publication in: **Advances in Aircraft and Spacecraft Science AASS.**

Biedermann, Till M.; Chong, T. P.; Kameier, F.; Paschereit, C. O. (2017): Statistical-Empirical Modelling of Airfoil Noise Subjected to Leading Edge Serrations. In: ***AIAA Journal*** Volume 55 (issue 9), pp 3128–3142. DOI: 10.2514/1.J055633.

Proceedings until August 2019

Biedermann, Till M.; Kameier, F.; Paschereit, C. O. (2019): Successive Aeroacoustic Transfer of Leading Edge Serrations from Single Airfoil to Low-Pressure Fan Application. In: *Proceedings of* ***ASME Turbo Expo*** *2019.*

Biedermann, Till M.; Kameier, F.; Paschereit, C. O. (2018): Optimised Test Rig for Measurement of Aerodynamic and Aeroacoustic Performance of Leading Edge Serrations in Low-Speed Fan Application. In: *Proceedings of* ***ASME Turbo Expo*** *2018. DOI:* 10.1115/GT2018-75369.

Biedermann, Till M.; Chong, T.P.; Kameier, F.; Paschereit, C.O. (2018): On the Transfer of Leading Edge Serrations from Isolated Aerofoil to Ducted Low-Pressure Fan Application. In: *24th* ***AIAA/CEAS Aeroacoustics Conference****. DOI:* 10.2514/6.2018-2956.

Biedermann, Till M.; Czeckay, P.; Geyer, T.; Kameier, F.; Paschereit, C.O. (2018): Noise Source Identification of Aerofoils Subjected to Leading Edge Serrations using Phased Array Beamforming. In: *24th* ***AIAA/CEAS Aeroacoustics Conference****. DOI:* 10.2514/6.2018-3794.

Chong, Tze Pei; Biedermann, Till M.; Koster, O.; Hasheminejad, S. M. (2018): On the Effect of Leading Edge Serrations on Aerofoil Noise Production. In: *24th* ***AIAA/CEAS Aeroacoustics Conference****. DOI:* 10.2514/6.2018-3289.

Biedermann, Till M.; Kameier, F.; Koster, O.; Schreiber, D.; Chong, T. P.; Paschereit, C.O. (2017): Polyoptimisation of the Aerodynamic and Aeroacoustic Performance of Aerofoils with Serrated Leading Edges. In: *23rd* ***AIAA/CEAS Aeroacoustics Conference****. DOI:* 10.2514/6.2017-3493.

Biedermann, Till M.; Chong, T. P.; Kameier, F. (2016): Statistical-Empirical Modelling of Aerofoil Noise Subjected to Leading Edge Serrations and Aerodynamic Identification of Noise Reduction Mechanisms. In: *22nd* ***AIAA/CEAS Aeroacoustics Conference****. DOI:* 10.2514/6.2016-2757.

II. Single Aerofoils

2 Aerodynamics: Single Aerofoil

This section addresses the aerodynamic performance of aerofoils with serrated leading edges. As several aerodynamic advantages are known from recent research, but also some disadvantages in performance, a thorough review of the current state of research is carried out and the basic aerodynamic mechanisms extracted. The reported trends are contradictory, especially with regard to the design parameters of the leading edge serrations. Therefore, the following experimental and numerical study on a chosen single aerofoil type is intended to serve three purposes:

- Generation of a reliable data basis, concerning aerodynamic performance, by taking into account several design parameters and inflow parameters of leading edge serrations. This is intended to enable a transfer of leading edge serrations from a single aerofoil to rotating applications.
- Identification of promising and possibly restricting aspects in the application of serrations to the leading edges of the chosen aerofoil type. This serves to facilitate the assignment of the effects of leading edge serrations in the rotating domain, where more complex flow patterns are present.
- To gain knowledge about the underlying aerodynamic flow mechanisms to better understand the dependence of the overall performance on the serration parameters and to link the current research findings from the literature with the results obtained from this section.

2.1 State of the Art – Leading Edge Serrations

Sinusoidal, tubercled, undulated, scalloped, bumped, wavy or, more simply, serrated leading edges all refer, unless mentioned otherwise, to a comparable geometric pattern in which the leading edge of an aerofoil, a wing or a flipper is modified with a specific periodic pattern, of which an example is shown in Figure 2-1. For sake of simplicity, this variety is reduced to 'leading edge serration' since specific differences in geometry are acknowledged but not considered significant for analysing the fundamental aerodynamic mechanisms. Likewise, the smallest chordwise extension of a serrated aerofoil is referred to as 'root', knowingly disregarding alternative nomenclature such as trough or valley. The chordwise peak-to-root extension is defined as the serration amplitude A, whereas the spanwise extension of a single serration is referred to as the serration wavelength λ. The angle, resulting from a fixed ratio A/λ, is defined as the inclination angle θ_{Serr}, according to *Eq. 2-1* for sinusoidal serrations.

$$\theta_{Serr} = arctan\left(\frac{2 \cdot A}{\lambda}\right) \qquad \textit{Eq. 2-1}$$

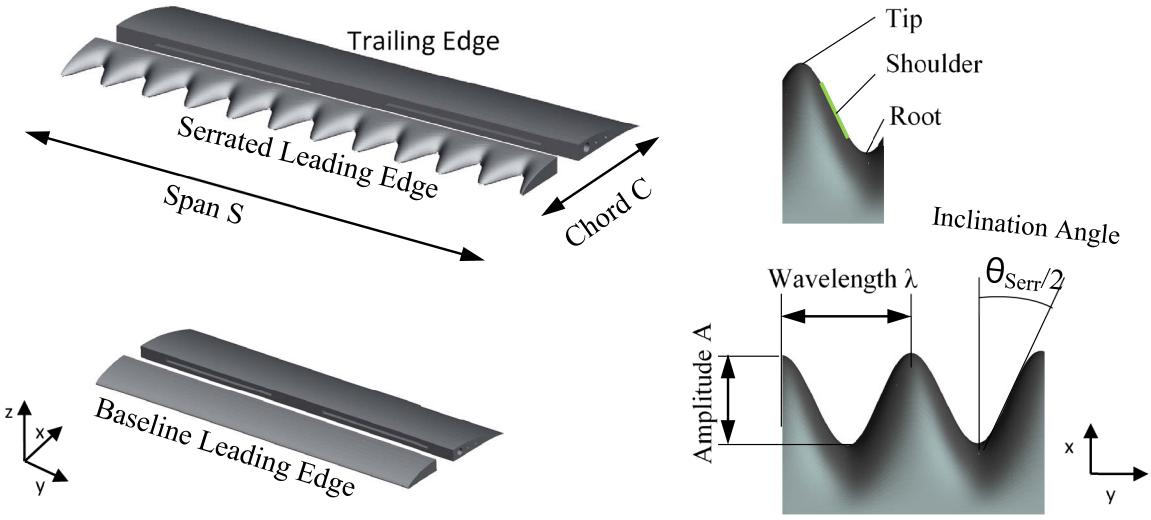

Figure 2-1 Sketch of a NACA65(12)-10 aerofoil subjected to leading edge serrations, including measures of importance.

2.1.1 Working Mechanisms

Vortex Generator

Most likely inspired by the silent flight of owls and the associated research into the noise reduction of gas turbine engines and rotors, Soderman [17] conducted an experimental study in 1972 to understand the underlying flow mechanisms, contributing to the previously observed noise reduction. In this context, leading edge serrations constructed by means of serrated flat (two-dimensional) brass strips of varying serration amplitudes A were tested, with the strips mounted at the lower surface of an aerofoil close to the leading edge. The serration amplitude, and the location of the serration on the aerofoil and the spacing between the serrations, were found to be the most important parameters. In contrast to the parameter definition of serrations in Figure 2-1, the spanwise distribution of the serrations cannot be called serration wavelength λ, since it appeared to be non-continuous, showing gaps of varying size between the single serrations. In short, serrations of small amplitudes ($A = 5.1$ mm) were observed to perturb the flow in the form of counter-rotating vortices, emanating from each serration and forming a circular pattern trailing downstream. This three-dimensional flow pattern helps to energise the boundary layer by high-momentum fluid transfer. As a consequence, an increase in the maximum lift, as well as an increase in the angle of attack at the maximum lift, was observed in combination with a drag decrease at high angles and no differences in drag at a zero angle of attack. For large amplitudes, however, different underlying flow mechanisms were suspected as they were found to obstruct the flow instead of perturbing it, hence resulting in a reduction of the aerodynamic performance. For narrow spanwise extensions of the serrations, a vortex generator effect is suggested. Vortex generators inject momentum into a boundary layer (e.g. making it turbulent) to delay flow separation. The background is that a turbulent boundary layer obtains a higher thickness than a laminar one and therefore shows higher drag, which is a non-desired feature. On the other hand, the higher velocity gradient of the turbulent boundary layer leads to higher kinetic energy, hence providing more resistance against the pressure gradient and so giving rise to separation. However, since the increase in maximum lift was also observed for serrations with a spanwise gap between the prongs, insensitive to the size of the prongs, Soderman [17] raises the question of whether a simple tripping effect of the boundary layer from laminar to turbulent instead of the vortex-generating effect might be the cause of the delayed stall as it would completely eliminate the laminar separation bubble.

Moving from the planar, two-dimensional brass strips investigated by Soderman [17] to fully three-dimensional leading edge serrations as depicted in Figure 2-1, a large variety of

studies were performed in recent years. Miklosovic et al. performed two successive studies, focussing on the aerodynamic properties of idealised humpback whale flippers with semi-span [18] and full-span [19] profiles. The results obtained show no decrease in the pre-stall performance for the semi-span model (unless in close vicinity to the baseline stall angle) but at the same time a significant increase at post-stall, including higher angles of attack for maximum lift. These results are quite unique compared to other studies [20–27]. Like Soderman [17], Miklosovic et al. [18] suggested a working principle similar to vortex generators, energising the flow by increased momentum exchange and keeping the flow attached despite the high adverse pressure gradient at higher angles of attack. Zhang et al. [28] also suggested low-profile vortex generators as a main effect of the serrations produced by control mechanisms for the boundary layer, which has been investigated in much more detail by Hansen et al. [25]. These authors observed counter-rotating structures, generated mainly at the roots of the serrations, forcing an interaction with the fluid of the boundary layer and leading to an exchange of momentum. In consequence, delayed stall angles, as well as improved post-stall performance, occurred. These counter-rotating vortices are suggested as a working mechanism, but its existence is also questioned by, for example, van Nierop et al. [29]. Hansen et al. [30] performed measurements of a NACA0021 profile, using particle image velocimetry (PIV), supplemented by a numerical study, and found a good fit between experimental and numerical results. The authors put forward a flow mechanism by which a separation zone is initiated behind serration roots and a 'canopy' is formed in the streamwise direction behind the root region and above the separation zone. This canopy is shielded or capsuled by continued inward flow of boundary layer vorticity, yielding increased circulation further downstream (continuous feeding), with a maximum at the trailing edge of the aerofoil. Counter-rotating vortices were identified in different streamwise planes, showing a decreasing intensity but an increasing size with increasing streamwise distance to the serrations. Furthermore, an increasing circulation was observed, reaching its maximum at the trailing edge. This is attributed to a continuous feeding with boundary layer vorticity through the sides of the canopy. The vorticity of the generated structures was found to increase with the angle of attack, and there is also some evidence that along the aerofoil chord, the vortical structures are continuously lifted from the surface of the aerofoil. At this point, the flow field becomes highly unsteady and starts to show strong time-dependent flow features.

Going one step further, Al-Okbi et al. [31] replaced the serrations at the leading edge by blowing holes in the leading edge to generate the well-known streamwise vortices, thus mimicking the serration effect both aerodynamically and aeroacoustically. Comparison of a classic serrated design and a blowing design with identical locations of vortex generators shows highly similar aerodynamic results, featuring a significant delay of the stall angle of $\Delta AoA = 5$ deg at A15λ10.

Spanwise Pressure Distribution

In contrast to the concept of counter-rotating vortices described by, for example, Hansen et al. [30], van Nierop et al. [29] proposed a different mechanism for the stall-delaying effect, by which the leading edge structures alter the spanwise pressure distribution. Mathematically, a close relationship between the thickness-to-chord ratio and the local stall angle for each cross-section of the aerofoil was described (maximum stall delay at small ratios). Assuming a similar thickness at the peak and the root of the serrations leads to the same pressure distribution for each cross-section but different chord lengths, resulting in higher adverse pressure gradients (high local thickness-to-chord ratio) for the root region (also confirmed by Hansen et al. [30] and Skillen et al. [32]). Thus, the point of separation is closer to the leading edges. In consequence, at these spanwise locations, the flow is already stalling at low angles of attack, whereas behind the serration peaks, a delay of the stall is expected. Via hydrogen bubble

visualisation at a NACA0021 aerofoil, Hansen et al. [25] showed a stronger downward turn of separated flow for serration peaks than for the root regions, which is consistent with calculations by van Nierop et al. [29] and indicates early flow attachment (or still non-separated flow) behind the peaks. This is also in agreement with results by Johari et al. [20]. Altogether, this leads to a more gradual overall stall (decreased abruptness) as well as higher maximum stall angles compared to the baseline reference case. Since the root regions are already stalling at low angles of attack, a reduced maximum lift of the serrations compared to the baseline case is expected. The model defined by van Nierop et al. [29] was compared to experimental data by Johari et al. [20] and was found to match qualitatively well. The delay of the stall angle is explained by the flattened-out lift curves with increasing serration amplitudes. For a complete stalling of the aerofoil, all the local cross-sections must be in stall as well. However, with increasing amplitudes, a reduction in the generated pre-stall lift and a flattening of the lift curve takes place, not even coming close to the initial lift values of the baseline, leading to stall [29].

However, following this path of argument, a stall delay is hard to determine as the aerofoil would increasingly stall until all cross-sections are stalling. Even more importantly, the developed aerodynamic model does not account for the improved post-stall performance described experimentally by several researchers [29, 26, 22, 33, 34, 20, 32, 35]. As pointed out by Borg [26], one possibility of reconciling the model by van Nierop et al. [29] with the improved post-stall performance of serrated aerofoils would be to combine the model with the vortex-generating mechanism of the serrations. Operating similarly to the vortex-lifting effect of a delta wing, these highly coherent structures lead to improved post-stall performance and an increase in strength with increasing angle of attack. However, the vortex-generated lift does not match the pressure-generated lift of a cambered aerofoil, and vortex lift is commonly associated with significant drag penalties.

Rostamzadeh et al. [22] performed an extensive numerical study associated with experimental surface pressure measurements of a NACA0021 with a single leading-edge serration, with the spanwise extension S being equal to the serration wavelength λ. The aim was to clearly identify the formation mechanism of the streamwise vortices and their impact on the reported beneficial generation of lift due to serrations. For the serrated aerofoil, maximum suction peaks at the tip and the root region were observed, matching the prediction by van Nierop et al. [29]. Numerically, spanwise vorticity was shown to ripple the spanwise vortex street, resulting in pairs of counter-rotating vortices in the streamwise direction, referred to as 'tip-vortices', in which each wavelength was suggested to be interpreted as small finite wing sections. As pointed out by Rostamzadeh et al. [22], a spanwise circulation of the flow as predicted by van Nierop [29] leads, according to Stoke's law, to a variation in spanwise vorticity and, in consequence, results in the development of spanwise counter-rotating vortices.

Pre-Stall Root Separation

As predicted by van Nierop et al. [29], Johari et al. [20] experimentally found indications of early separation of the flow in the root region of the serrations, even at smaller angles of attack than for the reference baseline case. Meanwhile, the flow at the serration peaks stays attached far beyond the usual stall angle. Other researchers obtained similar results, experimentally [19, 25, 36, 28, 34] and numerically [37, 30]. As pointed out by Zhang et al. [28], the early pre-stall separation at the roots but with attached flow at the peaks, also for post-stall angles, can account for the lower pre-stall performance of the serrations. In addition, this combination of separation at the roots and attached flow at the peaks is also responsible for the gentle stall (decreased abruptness), as well as the increase in the overall stall angle. More specifically, it is suggested that pre-stall mixing of the generated vortices in streamwise and spanwise direction is supporting a transition to a turbulent detached boundary layer at the

root location. The combination of these effects at the tip and the root of the serrations is expected to cause decreased pre-stall performance. The gentle stall process, improved post-stall performance and declined pre-stall performance were also confirmed by Cai et al. [38], showing numerical evidence of a high momentum region at the peaks and a low momentum region at the roots. Moreover, they also put forward an alternative cause of early separation in the root region due to the streamwise vortices at the shoulders of the serrations. The rotating nature of these vortices causes different local effective angle of attack for the roots (increased) and the peaks (decreased) of the serrations. This hypothesis is backed by Prandtl's lifting-line theory (LLT), stating that a downwash velocity leads to a decline in the effective angle of attack and the upwash velocity to an increase of the effective AoA. This downwash velocity on the peak suction section, and consequently an upwash at the root location, is induced by the aforementioned counter-rotating vortices, as outlined by Rostamzadeh et al. [22], with counter-rotating streamwise vortices observed to increase in size with the chord (stream tubes grow larger and vorticity disperses). This helps to prevent flow separation at peak locations as high-momentum fluid can be drawn from the surrounding fluid.

Pedro and Kobayashi [39] clearly visualised a delayed separation by investigating the shear stress at the surface of the aerofoil, showing regions of attached flow aligned with the serration peaks at a high angle of attack, whereas the straight counterpart shows large-scale separation. Rostamzadeh et al. [22] numerically showed separated flow regions via iso-surfaces of zero streamwise velocity and observed early separation in the root region but also attached flow at the peaks, even at high AoA. Increasing the amplitude extends the separated regime at high AoA and leads, compared to smaller amplitudes, to a reduced lift. For a NACA0021 aerofoil, Skillen et al. [32] experimentally showed increased surface pressure coefficients on the suction side of the root location compared to that of the peak location. This indicates strong spanwise pressure variations, possibly inducing secondary flows. The spanwise transportation of low-momentum fluid from the peak to the root of the serration replaces the high-momentum fluid from the free stream and leads to a delayed separation. The authors predicted the presence of additional hairpin vortices due to turbulent fluctuations, acting as a boost for the streamwise flow at the peak location, also delaying separation at these locations. These vortices arise from the separated shear layer and tend to flow towards the chordwise projected location of the peaks, contributing to attenuated flow behind the roots and improving the flow attachment behind the peaks. Moreover, Skillen et al. [32] proposed a spanwise pressure gradient that is induced by the serration geometry itself, leading to secondary flows of near-wall low-momentum fluid away from the serration tips towards the roots. High-momentum fluid from the free stream is re-energising the boundary layer downstream of the peak locations.

Bi-Periodicity, Post-Stall Unsteadiness, Compartmentalisation, Hysteresis Loop

Custodio [34] reported significant three-dimensional flow effects, so-called bi-periodic patterns, at high angles of attack . These patterns were visualised along the span, where only every other root shows similar flow structures instead of all neighbouring ones. Hence, if one root attracts fluid from the surrounding peaks, the neighbouring root repels it, and so on. This is especially the case for high wavelengths and high amplitudes, a situation in which the flow regimes of the single serrations interact with each other. This observation is backed by numerical work by Camara et al. [37] for a NASA LS(1)-0417 aerofoil. For low angles of attack, a clear periodicity in terms of vorticity and pressure coefficient contours was observed, whereas for high AoA, a bi-periodic flow pattern was seen, as reported by Custodio [34]. Experimentally, the occurrence of different patterns depending on the angle of attack was also confirmed by flow visualisation in a water tunnel at AoA = 14 deg [34]. Similar observations were made by Cai et al. [38], who found that the flow was highly symmetric at small angles of attack but that at higher angles, the flow pattern transformed into asymmetric and bi-periodic patterns, a process for which a compartmentalisation effect is suggested to be the physical mechanism.

Rostamzadeh et al. [22] observed bi-periodic post-stall behaviour at maximum amplitudes of a NACA0021 aerofoil, whereas a further study [40] with a higher aspect ratio of the same aerofoil and low serration amplitudes showed strong non-symmetric effects along the span at high angles of attack, which do not necessarily follow the flow pattern described by Custodio [34]. In addition, Cai et al. [38] found a remarkable reduction in the hysteresis effect of a $NACA63_3$-021 aerofoil. However, the suggested compartmentalisation effects are believed to influence the intensity of the hysteresis effect, as well as being the cause of the bi-periodic patterns. This was confirmed numerically by Pedro and Kabayashi [39], validating their model against experimental wind tunnel test data, which showed a good fit. In their study, the leading edge serrations (tubercles) of a semi-span model of a humpback whale flipper were observed to act like wing fences, resembling barriers and preventing the growth of separation from the tip to the root of the flipper. This is the case only for a semi-span model as the Reynolds number varies from the tip (low Re, primarily leading-edge separation) to the root of the wing (high Re, primarily trailing-edge separation). As for the semi-span study of Miklosovic et al. [18], the authors confirmed a higher maximum lift for the serrated aerofoil, accompanied by a higher post-stall drag, as well as a significant delay of separation. Moreover, large streamwise vortices, aligned with the tubercles for the mid-section, are identified, presumably re-energising the boundary layer with high-momentum fluid and delaying separation. The influence of three-dimensional flow effects is also vividly shown by the comparison of a full-span model to a semi-span model, as shown experimentally by Miklosovic et al. [19]. The full-span model shows lower maximum lift coefficients, especially for the pre-stall regime, and a reduced maximum stall angle compared to the semi-span model. Moreover, significant differences in the stall-characteristics of the underlying baselines become evident, pushing towards the conclusion that the serration efficiency benefits from the three-dimensional flow of the semi-span wing. The serration-induced vortices lead to compartmentalisation effects and prevent the growth of locally separated flow, affecting the semi-span aerofoil as a function of the planform shape and Reynolds number. Borg [26] investigated the effect of leading edge serrations on the dynamic stall and found clear evidence for the superior performance of the serrated leading edges in terms of higher lift and a significantly reduced hysteresis loop.

Spanwise Effects and Waviness Ratio

Many studies focussed on idealised flippers of the humpback whale by means of full-span models, applied to sinusoidal serrations with no spanwise change of the serration parameters. For some of these models, a significant delay of the maximum stall angle, as well as improved post-stall performance, was observed. However, against the background of understanding the global impact of a perturbation by a serrated wing on the aerodynamic performance, three-dimensional effects such as the waviness ratio need to be taken into account. The waviness ratio describes the spanwise length that is covered by serrations relative to the total span. Yoon et al. [21] numerically investigated the aerodynamic performance of a NACA0020 aerofoil by means of different waviness ratios, ranging from zero (baseline) to one (fully serrated), with a 'fixed' serration amplitude of 2.5%·C and a wavelength of 20%·C. Varying the angle of attack, they found no differences up to 12 deg for all cases tested. Entering the stall-sensitive regime (AoA > 12 deg), however, showed significant differences between the waviness ratios tested, for which a clear scaling with the waviness ratio was observed, resulting in an earlier stall (4 deg) for the fully serrated sample (high waviness ratio). The same applies to the reduction in pre-stall lift and the improved post-stall performance, with the latter being at its maximum for high waviness ratios. These findings are supplemented by additional work by Cai et al. [33], who numerically tested a single serration located at the spanwise centre of a full-span $NACA63_4$-021 aerofoil. The authors observed a marginal improvement of the total lift after stall due to local stall-delaying effects and possible indications of smoother stall entry.

In contrast, pre-stall asymmetric flow effects in the spanwise direction are expected to be responsible for the reduced lift and the increased drag. In conclusion, it becomes clear that a local perturbation by a limited number of leading edge serrations does not result in dominating three-dimensional effects that control the separation after an initial perturbation of the baseline. Hence, small waviness ratios do not suffice to obtain the desired aerodynamic properties provided by leading edge serrations. Even the worst case might occur, in which partially serrated aerofoils end up with a reduction of maximum lift but no significant delay of the stall or improved post-stall performance.

Aspect Ratio

Guerreiro and Sousa [35] focussed on finite serrated aerofoils with low aspect ratios (AR), AR = 1 and 1.5, at moderate Reynolds numbers for future application in micro air vehicles (MAVs) and showed a strong sensitivity of the performance to the aspect ratio. For a moderate Reynolds number (Re = 140,000), the maximum lift obtained as well as the stall angle decreased with increasing AR, albeit that the general influence of serration amplitude and wavelength turned out to be the same, with maximum lift for large amplitudes and large wavelengths. For a small AR, a maximum stall delay was obtained for small amplitudes and large wavelengths, even though no clear stall was observed for some of the cases tested. In general, the effect of serrations is less prominent for low aspect ratio aerofoils, presumably due to wingtip vortices that dominate the performance of the aerofoil. For a high AR, no delay but a more gradual stall is observed, with the serrations showing no sensitivity to the pre-stall performance but high post-stall lift for maximum amplitudes and maximum wavelengths. Moving to low Reynolds numbers (Re = 70,000), the general pattern of the aspect ratio dependency remains, but the serration performance shows a higher lift than in the reference case for almost all angles of attack. This is explained by a drastically reduced performance of the baseline case and a remarkable insensitivity to the Reynolds number. Still, the results are questionable, bearing in mind the underlying flow mechanics of leading edge serrations.

Chen et al. [41] investigated a symmetric NACA0012 aerofoil while varying serration amplitude and aspect ratio. Strong three-dimensional effects were observed with significant differences between the aspect ratios tested in a range of AR = 1…3. Since finite aerofoils were tested and no side plates, fences, etc., were applied, the results imply increasing effects of the tip flow, especially when reducing the AR. A maximum delay of stall of ΔAoA = 10 deg was observed for maximum amplitudes, independently of the aspect ratio. With a minimum aspect ratio (AR = 1), higher lift and less drag were obtained than for higher aspect ratios. The best lift-to-drag performance for AR = 1 was achieved for high amplitudes, and a maximum lift was observed for small amplitudes. For a high aspect ratio (AR = 3), the maximum pre-stall performance was measured for small amplitudes, changing towards higher amplitudes at post-stall. In contrast, Camara et al. [37], who performed numerical detached eddy simulations (DES) for a NASA LS(1)-0417 aerofoil, observed no significant differences in the lift and the drag coefficients from AR = 0.5 to 1 for a sinusoidal leading edge.

2.1.2 Parameter Influence

In addition to investigations into the aerodynamic effects of leading edge serrations, several studies on the effect of the serration parameters have emerged over the past years, showing a strong dependency of the performance on the test parameters chosen. The most common parameters studied are the serration amplitude A and the wavelength λ (already defining the inclination angle θ_{Serr} for sinusoidal serrations), the Reynolds number Re, and the range of angle of attack AoA. Nevertheless, the finiteness or infiniteness of an aerofoil including tip effects, the aerofoil geometry and the aspect ratio, as well as full- and semi-span aerofoils, also play an important role, not to mention the differences and restrictions in the numerical or experimental setups. In addition, the definition of the stall angle for the serrations turns out to be hard to determine, as stall occurs more gradual.

Therefore, Table 2-1 shows a summary of the influence of the serration parameters, as reported by different researchers over the past decade. For maximum lift, a highly arguable influence of wavelength can be seen, with a slight majority of the studies suggesting that high wavelengths are beneficial for maximum pre-stall lift. As for the amplitudes, however, the picture is somewhat clearer, and except for two studies, all the researchers agree on small amplitudes for maximum lift. This turns out to be consistent with the lift-to-drag ratio as well. For a maximum delay of the stall angle or an increase in the stall margin, a slight majority emphasis low amplitudes but, in general, agree on high wavelengths.

Aerofoil Differences

Interestingly, if the studies are divided according to the symmetry of the aerofoils investigated, the trends become more pronounced for the cambered aerofoils. Here, small amplitudes and large wavelength are required for maximum lift and high lift-to-drag ratios, as well as a maximum delay of stall. One exception is the NASA LS(1)-0417 aerofoil, showing, according to Table 2-2, the most aft position of maximum thickness as well as the maximum camber. The different performance of the symmetric and the cambered aerofoils is not surprising since the camber increases the overall lift, especially in the linear pre-stall regime [42]. Eventually, the serration geometry also appears to be slightly different for cambered aerofoils compared to symmetric ones. Serrations at aerofoils with strong camber show a rather semi-circular shape, with an almost two-dimensional shape on the pressure side and a fully three-dimensional shape on the suction side. In contrast, symmetric aerofoils show the same contours for the suction and the pressure side of the leading edge serrations, making the serration shape fully circular.

Table 2-1 Summary of studies on the parameter influence of leading edge serrations. Adverse trends of serration parameters compared to the majority of studies are depicted in bold. n/i = not investigated.

	Author	Ref	Year	Aerofoil	Re	Maximum				Focus			
						Lift (pre)	Lift (post)	Stall-Delay	Lift to Drag	Aero	Acoustic	Experim.	Num.
symmetric aerofoils	Johari et al.	[20]	2007	NACA63$_4$-021	$1.83{\cdot}10^5$	λ↓, A↓	λ↓, A↑	n/i, A↑	n/i	x		x	
	van Nierop et al.	[29]	2008	symmetric aerofoils	n/i	n/i	n/i	no λ, A↑	n/i	x		x	
	Hansen et al.	[23]	2009	NACA0021	$1.2{\cdot}10^5$	λ↓, A↓	n/i	λ↓, A↓	λ↓, A↓	x		x	
	Hansen et al.	[24, 25]	2010	NACA0021	$1.2{\cdot}10^5$	λ↓, A↓	λ↓, A↓	λ↓, A↓	n/i	x	x	x	
	Borg	[26]	2012	NACA0021	$1.3{\cdot}10^5$	λ↓, A↓	λ↓, n/i	none	λ↓, A↓	x		x	
	Chen et al.	[41]	2012	NACA0012	$1.233{\cdot}10^5$	n/i, **A↑**	n/i	n/i, A↑	n/i ,A↑	x		x	
	Kim et al.	[43]	2012	NACA0020	$10{\cdot}10^5$	λ±, n/i	λ±, n/i	none	n/i	x			x
	Zhang et al.	[44]	2013	NACA0014	$0.01{\cdot}10^5$	**λ↑,** A↓	n/i	n/i	λ↑, A↓	x			x
	Rostamzadeh et al.	[22]	2014	NACA0021	$1.2{\cdot}10^5$	**λ↑,** A↓	**λ↑,** A↓	(A/λ)↑	n/i	x		x	x
	Custodio (et al.)	[45, 34]	2015	NACA63$_4$-021	$4.5{\cdot}10^5$	λ↓, A↓	n/i, A↑	n/i, A↓	none	x		x	
cambered aerofoils	Guerreiro et al.	[35]	2012	NASA LS(1)-0417	$0.7{\cdot}10^5$, $1.4{\cdot}10^5$	λ↑, **A↑**	λ↑, A↑	λ↑, A↑	n/i	x		x	
	Gross and Fasel	[46]	2013	NACA64$_3$-618	$0.642{\cdot}10^5$	n/i, A↓	n/i	n/i, A↑	n/I, A↓	x			x
	Chaitanya et al.	[47]	2015	NACA65(12)-10	$6{\cdot}10^5$	n/i, A↓	n/i	n/i	n/i	x	x	x	x
	Chong et al.	[27]	2015	NACA65(12)-10	$1.5{\cdot}10^5$	λ↑, A↓	n/i	λ↑, A↓	n/i	x	x	x	
	Biedermann et al.	[48]	2017	NACA65(12)-10	$1.5{\cdot}10^5$-$2.5{\cdot}10^5$	λ↑, A↓	n/i	λ↑, A↓	λ↑, A↓	x	x	x	x
	Al-Okbi et al.	[31]	2018	NACA65(12)-10	$2.4{\cdot}10^5$	λ↑, A↓	n/i	λ↑, A↓	λ↑, A↓	x	x	x	

Comparing the suggested optimum parameters for the symmetric aerofoils by taking into account differences in thickness and the location of the maximum thickness reveals no clear trends for either the maximum pre-stall or post-stall lift, stall delay or lift-to-drag ratio. One indicator for the geometry dependency is presented by Hansen et al. [23, 25], who tested two symmetric aerofoils (NACA0021 and NACA65021) with and without leading edge serrations, with the main difference between the aerofoils being the thickness distribution. The maximum thickness of 21 %·C is the same for both models. In particular, the NACA0021 (maximum thickness at x = 30 %·C) shows a distinct stall, taking place with a sharp reduction in the lift, which is smoothened by the tested serrations (best general performance at small A and small wavelength, and a more gradual stall for high A). For the NACA65021 (maximum thickness at x = 50 %·C), however, the stalling characteristic is quite the opposite, showing a less pronounced decrease in lift. The tested serration still shows an improved post-stall performance and a strong pre-stall performance, suffering fewer losses than the NACA0021. This effect is attributed to the maximum thickness of the aerofoil being further aft compared to the NACA0021. This leads to an extension of the laminar flow, where the tubercles are working quite efficiently as the laminar boundary layer offers a momentum exchange. However, an alternative interpretation could be that for the NACA0021 baseline profile, the drop in lift due to stall is much more pronounced compared to the NACA65021.

In consequence, if all the studies of a numerical and experimental character were analysed by means of the boundary layer thickness distribution for the specific aerofoil types tested and put in relation to the A/λ ratios tested, more consistent trends might be observed. However, for the current thesis, these differences are disregarded by focussing on a single aerofoil, for

which great efforts have been made to generate a reliable data pool of aerodynamic and acoustic performance before moving to the rotating frame.

Table 2-2 Types of investigated aerofoils, including measures of importance, as normalised by cord length C.

	Reference	Type	max. thickness	pos. of max. thickness	max. camber	pos. of max. camber
symmetric	[20][45, 34]	NACA63$_4$-021	21%·C	35%·C	--	--
	[49, 50][41]	NACA0012	12%·C	22%·C	--	--
	[44]	NACA0014	14%·C	30%·C	--	--
	[18][19] [21] [43]	NACA0020	20%·C	30%·C	--	--
	[23],[24, 25][26],[22]	NACA0021	21%·C	30%·C	--	--
	[23, 25]	NACA65021	21%·C	50%·C	--	--
cambered	[35]	NASA LS(1)–0417	17%·C	40%·C	2.4%·C	65%·C
	[46]	NACA64$_3$-618	18%·C	35%·C	3.3%·C	50%·C
	[47][27][48][31]	NACA65(12)-10	10%·C	30%·C	6%·C	50%·C

2.1.3 Summary of Effects

For serrated leading edges, several studies of numerical and experimental nature exist, aimed at either describing the underlying flow mechanisms and/or the influence of the serration parameters on specific performance features. Several mechanisms were identified and agreed upon by a majority of the researchers, even though some details are still arguable. Moreover, a strong dependency on the aerofoil cross-section becomes evident in terms of the aerofoil performance and the strength of the identified mechanisms. This is, in particular, true for the effect of the serration parameters, namely the serration wavelength, the serration amplitude and the serration inclination angle. Depending on the aerofoil shape and the setup, even opposing trends of these parameters are reported. The main effects can be summarised as follows:

1. Vortex generators: Leading edge serrations induce streamwise vortices of counter-rotating nature, leading to momentum exchange and delayed flow separation [38, 39, 23, 25, 18, 28].
2. Vortex lift: As for delta wings at high angles of attack, vortices are generated at the leading edge, where the downwash causes additional lift, leading to delayed stall and increased post-stall performance for the leading edge serrations [9, 26, 19, 34].
3. Altering of the spanwise pressure distribution, for which at a similar thickness of the peaks and the roots the same pressure difference (pressure distribution) is to be overcome. This results in higher gradients at the roots and leads to early root separation but, therefore, also to a more gradual stall [29]. The early separation at the serration root, leading to reduced pre-stall performance and gradual stall, is confirmed by several other studies [29, 30, 20, 22, 34, 38, 27, 43, 25].
4. Compartmentalisation effects of the leading edge serrations, restricting the spanwise extension of the separation effects and preventing the growth of separation along the span of semi-span aerofoils, resulting in gradual stall [33, 38, 7, 39, 18]. This is further supported by the observation of non-uniform separation patterns over the span [7, 20, 29].

5. Unstable, bi-periodic post-stall effects [38, 34, 37, 22, 20].
6. Strong influences on the hysteresis loop [38, 26, 39].
7. Induced by the streamwise vortices at the shoulders of the serrations, the local effective angle of attack for the serration roots is increased and decreased for the locations of the serration peaks, also promoting delayed flow separation at peak locations [29, 38].
8. Decreased pre-stall lift performance, scaling mainly with the serration amplitude [20–27].
9. Increased post-stall lift compared to the reference case, either due to gradual stalling or vortex-lifting effects [29, 26, 22, 33, 34, 20, 32, 35].
10. Flattening of lift curves at high angles of attack with increasing amplitude [25, 20, 34].
11. More pronounced serration effects at high aspect ratios, also showing influences on serration parameters [41, 37, 35].

Especially since the aim of this thesis is a transfer of leading edge serrations from the rigid to the rotating frame, reliable information on the general performance of the aerofoil and the applied serrations is of fundamental importance. Hitherto, studies have failed to provide this required consistency, which emphasises the need to carefully analyse the aerofoils chosen for this study in both the rigid and the rotating system. The aerodynamic results for the defined model rotors in Sections 4.2, 5.3 and 6.1 allows for conclusions on the transferability of the aerodynamic findings for the single aerofoils, presented in the current section.

2.2 Force Measurements

2.2.1 Chosen Aerofoil Type

For all the analyses carried out, a cambered NACA65(12)-10 aerofoil was chosen, for two reasons. First, this aerofoil type is a well-known representative of axial-flow machines, such as fans and compressors. It has a high lift and a relatively smooth stall characteristic. Second, this aerofoil type was chosen for the previously mentioned EU-funded FLOCON [51] study, aimed at investigating aerofoil noise for future applications in rotating machinery, which is also the aim of the current thesis. In consequence, relatively much information on the aerofoil performance and the effect of leading-edge and trailing-edge serrations is available for this specific aerofoil type. For the NACA65-series, the basic parameters can be derived from the nomenclature of the individual [52], as shown for the cross-sectional view in Figure 2-2. For the NACA65(12)-10, the number *6* defines that the location of the maximum thickness is at $x/C = 40\ \%$, and the number *5* defines the chordwise location of the pressure minimum ($x/C = 50\ \%$). The number *12* indicates the theoretical lift coefficient in a potential flow of $C_{FL} = 1.2$ and can directly be related to the aerofoil camber. Finally, the number *10* denotes that the maximum thickness ratio is $d/C = 10\ \%$.

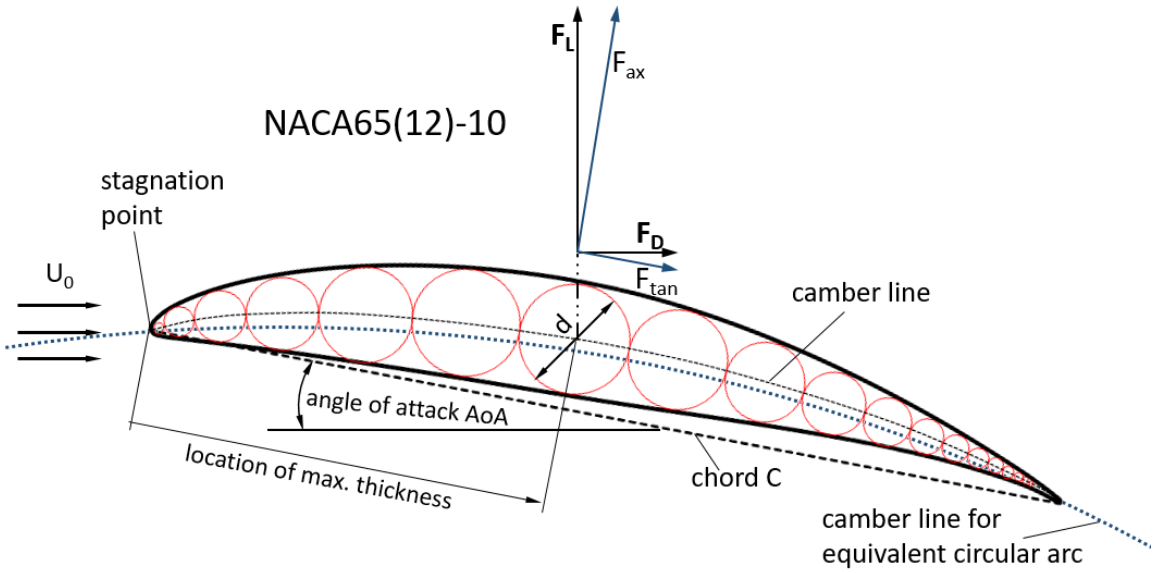

Figure 2-2 NACA65(12)-10 aerofoil profile, including nomenclature and indication of acting forces.

Exposed to a free stream, the aerofoil shape shows a characteristic pressure distribution, resulting in lift and drag forces, which describe the aerodynamic performance. Principally, the pressure distribution can be described according to Bernoulli's principle (*Eq. 2-2*), giving the one-dimensional relationship between static pressure and velocity:

$$\frac{p_1}{\rho} + \frac{{U_1}^2}{2} + g \cdot z_1 = \frac{p_2}{\rho} + \frac{{U_2}^2}{2} + g \cdot z_2 \qquad \textit{Eq. 2-2}$$

The distribution of the static pressure along the aerofoil chord was tested at Brunel University London by using a prototype aerofoil with ten pressure holes distributed along the aerofoil chord for both the suction and the pressure side [53]. For comparison, the pressure contours of a numerically modelled aerofoil (Section 2.3) for the same boundary conditions are extracted as well (Figure 2-3). Relative to the free-stream velocity, the static pressure shows a sharp increase when approaching the stagnation point since the velocity is reduced to zero. On the suction side of the aerofoil, the fluid is constantly accelerated until it reaches the point of maximum thickness at x/C = 40 % for the NACA65(12)-10. Consequently, the static pressure shows significantly smaller values for the suction side than for the pressure side and maximum negative pressure coefficients at maximum thickness. Further downstream the fluid is decelerated, leading to an increase in pressure and therefore also increased pressure coefficients. Due to the asymmetric aerofoil shape, apart from the leading-edge section, the pressure side shows a relatively constant pressure distribution. Hence, even at zero angles of attack, the NACA65(12)-10 already shows positive lift, which is further increased by increasing the angle of attack (AoA).

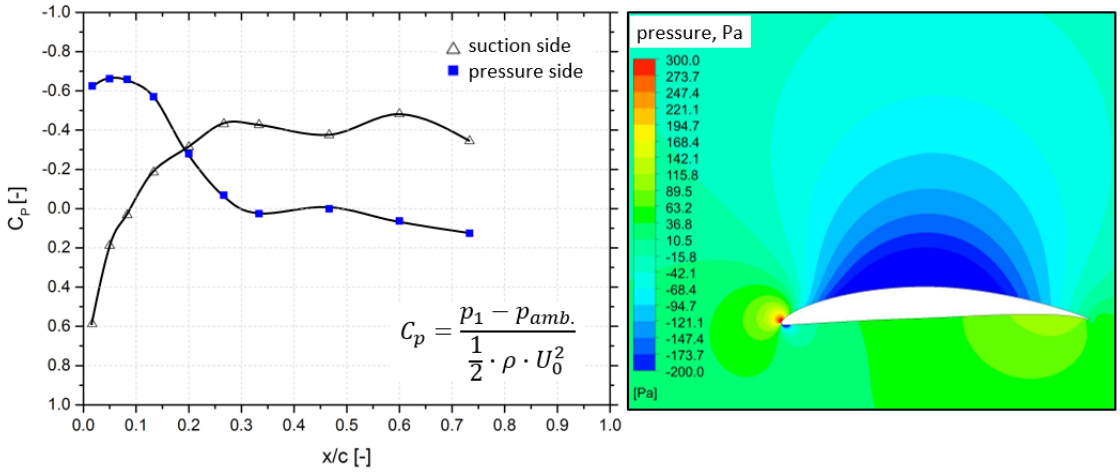

Figure 2-3 Experimentally obtained distribution of pressure coefficients (left [54]) and numerically obtained static pressure distribution of the NACA65(12)-10 aerofoil [55] at AoA = 0 deg and Re = 250,000.

For the upcoming aerodynamic and aeroacoustic analysis, this NACA65(12)-10 aerofoil type is equipped with sinusoidal leading edge serrations according to Figure 2-1 and tested in the rigid and the rotating domain.

2.2.2 Wind Tunnel Setup

Aerodynamic testing took place at the open circuit wind tunnel at Brunel University London [27], providing a closed test section of 500 mm x 500 mm. The wind tunnel is not acoustically treated and is not suitable for noise measurements. Instead, it is only used for measurements of the lift and drag produced by the aerofoil with serrated leading edges. Driven by an axial fan, air enters a nozzle and passes several screens and honeycomb meshes in order to generate a homogeneous velocity profile of little turbulence. In the mid-section, where the testing took place, the turbulence intensity was found to be $0.2\,\% \leq Tu \leq 0.3\,\%$, with maximum wind speeds of $U_0 = 35$ ms^{-1}. For the current study, the wind speed was limited to a maximum velocity of $U_0 = 25$ ms^{-1} since higher velocities bear the risk of inducing significant vibrations on the aerofoils at high angles of attack, obscuring the measurement results. The test section is comprised of interchangeable acryl glass walls, where the test samples can be inserted and mounted onto an intake rod, connected to the three-component balance. The force balance allowed the tested aerofoils to rotate about the horizontal axis, which enabled the gathering of the resulting lift forces F_L and drag forces F_D, which were measured via strain gauge load cells. For monitoring the boundary conditions of the study, the free-stream velocity U_0 was measured via a standard pitot-static tube, where, according to Bernoulli's law, the resulting velocity is a function of the air density ρ and the measured dynamic pressure component Δp_{dyn}. For generalisation purposes, the non-dimensional chord-based Reynolds number was determined.

$$U_0 = \sqrt{\frac{2 \cdot \Delta p_{dyn}}{\rho}} \; with \; \rho = \frac{p_{baro}}{R_{spec.} \cdot T} \qquad \textit{Eq. 2-3}$$

$$Re = \frac{U_0 \cdot \rho \cdot C}{\eta} \qquad \textit{Eq. 2-4}$$

As for the Reynolds number, the coefficients of lift and drag are used to normalise the obtained forces on the aerofoil by taking into account the wetted surface area of the aerofoil A_{ws}, the free-stream velocity U_0 and the fluid density ρ. These non-dimensional coefficients describe the performance independently of the actual aerofoil surface, as well as variations in span, chord or free-stream velocity. Note that the wetted surface A_{WS} of the serrated aerofoils is smaller than the surface of the straight baseline aerofoil since the serrations were cut into the main body of the aerofoil while keeping the maximum chord constant.

$$C_L = \frac{2 \cdot F_L}{\rho \cdot {U_0}^2 \cdot A_{ws}} \qquad \textit{Eq. 2-5}$$

$$C_D = \frac{2 \cdot F_D}{\rho \cdot {U_0}^2 \cdot A_{ws}} \qquad \textit{Eq. 2-6}$$

Due to the experimental environment, the coefficients of lift and drag were corrected for the restrictions of the wind tunnel (Appendix A.1). This included a blocking through the tunnel walls according to Barlow et al. [56], as well as wake blockage effects of the aerofoil, which occur particularly when the aerofoil experiences stall effects, hence showing large-scale separated flow.

Testing Procedure

Ten different geometries were tested, including nine aerofoil samples with leading edge serrations and one baseline aerofoil, as shown in Table 2-3, in which the peak-to-root value of the amplitudes is denoted by A and the corresponding serration wavelength by λ. The serration designs were chosen according to a circumscribed central composite design, explained in more detail in Section 3.3.1. Each sample was tested at two different free-stream velocities, $U_0 = 15$ ms^{-1} and $U_0 = 25$ ms^{-1}, resulting in Reynolds numbers of $Re = 1.5 \cdot 10^5$ and $Re = 2.5 \cdot 10^5$, respectively. The angle of attack was varied between AoA = ± 20 deg for the lower and AoA = ± 15 deg for the higher velocity, since the one-sided mounted aerofoil shows strong vibration effects for the higher velocity at AoA > +15 deg.

Table 2-3 Nomenclature and absolute as well as normalised measures of the leading edge serrations analysed. Baseline chord C = 0.15 m. Additional differentiation between experimentally and numerically analysed configurations.

ID	A [mm]	A/C [--]	λ [mm]	λ/C [--]	experimental [--]	numerical [--]
A12λ26	12	0.08	26	0.17	x	x
A22λ18	22	0.15	18	0.12	x	--
A22λ34	22	0.15	34	0.23	x	--
A29λ26	29	0.19	26	0.17	x	x
A29λ45	29	0.19	45	0.30	x	x
A29λ7.5	29	0.19	7.5	0.05	x	x
A35λ18	35	0.23	18	0.12	x	--
A35λ34	35	0.23	34	0.23	x	--
A45λ26	45	0.30	26	0.17	x	x
BSLN	--	--	--	--	x	x

The increment was ΔAoA = 1 deg, for which an accuracy of ± 0.2 deg was maintained using a rotating dial mechanism of the mounting plate. All measurements were conducted three times to generate a reliable data pool, as well as to perform an uncertainty analysis with a mean standard deviation of $s_{SD} = 0.07$ for the lift and $s_{SD} = 0.002$ for the drag coefficients, as shown in more detail in Appendix A.2.

2.2.3 Results and Discussion

For brevity, detailed results are presented only for $U_0 = 15$ ms^{-1}, although Appendix A.3 shows all results at $U_0 = 25$ ms^{-1}. However, the main dependencies remain highly similar for the two velocities tested. The baseline shows the maximum lift at AoA = 9 deg, with a further increase of the AoA showing moderate stalling effects, resulting in decreased lift. The thickness and the camber of the chosen NACA65(12)-10 design (Section 2.2.1) prevent the aerofoil from abrupt stalling at a certain angle and, therefore, allow high lift values to be obtained even at AoA far beyond the initial stall angle. The baseline results are in reasonable agreement with the external data for the pre-stall region provided by Bogdonoff [57] (Appendix A.2).

With serrated aerofoils (Figure 2-4 - Figure 2-5), generally quite similar aerodynamic performance compared to the baseline case with a straight leading edge is observed at zero AoA. The performance of the serrations at AoA ≠ 0 deg strongly depends on the serration design, showing clear dependencies on serration wavelength and amplitude.

Influence of Amplitude A

For a constant serration wavelength (Figure 2-4, left), all the serrations of varying amplitudes and the baseline show a comparable trend of linear increase in lift until reaching the incidental stall angle.

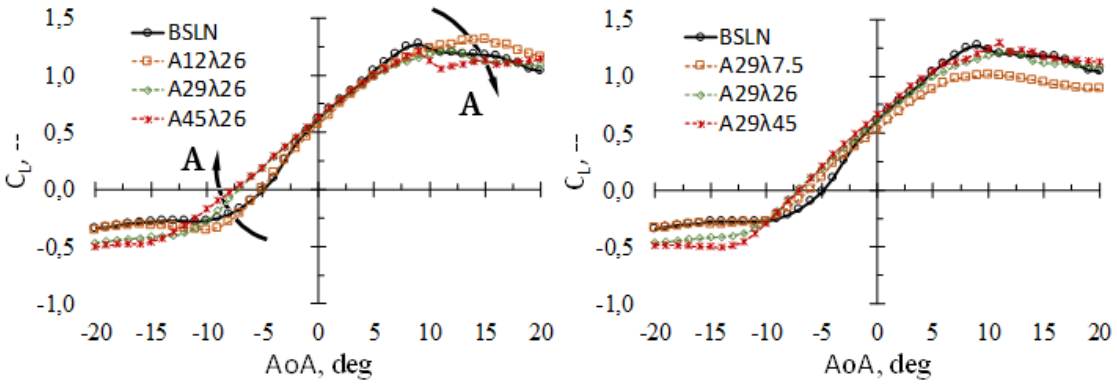

Figure 2-4 Coefficients of lift at varying serration amplitude A (left) and serration wavelength λ (right) for $U_0 = 15$ ms^{-1}.

Immediately before reaching the stall angle of the baseline at AoA = 9 deg, the serrations show a somewhat reduced lift, which might be attributed to local separation effects of the serration roots, as described by, for example, van Nierop et al. [29]. A further increase of the AoA shows gradual stall for the baseline and serrations of high amplitudes. In contrast, case A12λ26 shows superior performance compared to the baseline, resulting in higher post-stall lift coefficients and a clearly delayed stall entry of ΔAoA = 6 deg. Generally, a clear scaling with the serration amplitude is visible post-stall, leading to the highest lift and strongest stall delay for the smallest amplitudes, which can be attributed to reduced separation effects at the leading edges.

These effects become even more apparent when the coefficients of drag (Figure 2-5) are analysed, showing a clear increase for high amplitudes in the region in which stall is initiated (AoA ≥ 5deg). At negative AoA (-12 deg ≤ AoA ≤ 0 deg), however, the trends for the lift and

the drag appear to be reversed, with the highest amplitude showing the maximum lift (Figure 2-3). This can be attributed to a delayed separation on the pressure side of the aerofoil since the high amplitudes allow for a positive deflection effect of the incoming flow, also resulting in lower drag than for the baseline case in the associated region of AoA. In summary, increasing the serration amplitude leads to a clockwise rotation of the lift curve around the zero angle of attack axis. The reverse pattern is observed for the drag curves.

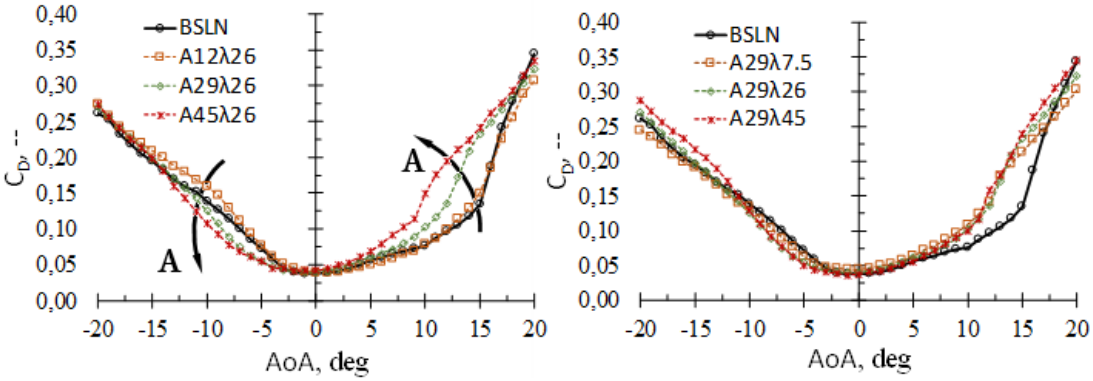

Figure 2-5 Coefficients of drag at varying serration amplitude A (left) and serration wavelength λ (right) for $U_0 = 15\ ms^{-1}$.

Influence of Wavelength λ

Keeping the serration design at a constant intermediate serration amplitude while varying the serration wavelength (Figure 2-4 right) results in a lift and drag performance comparable to that of the baseline case for the linear regime at -3 deg ≤ AoA ≤ 9 deg. In general, the best performance is observed for maximum wavelengths. Even post-stall, the serrated aerofoils maintain a high coefficient of lift, even showing slight amendments at AoA ≥ 15 deg. This holds true except for the smallest wavelength, A29λ7.5, for which significant penalties, particularly post-stall but also for smaller angles ≥ 0 deg, are observed. The narrow spanwise spacing (small λ) of this design in combination with large amplitudes results in serrations with relatively steep shoulders and blunt serration roots. These circumstances are expected to lead to strong three-dimensional effects along the aerofoil span, preventing the generation of significant lift for the leading-edge section x/C ≤ 0.3 of the suction side of the aerofoil. Separation effects are not expected to be the driving parameter for reduced lift performance since the drag shows a comparable trend for all the other cases.

Differences between the tested leading edge serrations become even more pronounced by analysing the lift-to-drag ratio (Figure 2-6), clearly showing the accumulative effect of lift and drag for the different serration parameters. Main differences are observed for angles of attack 0 deg ≤ AoA ≤ 17 deg, the most relevant region for practical applications. The increased drag due to partial separation at the serration roots in combination with the reduced lift for maximum amplitudes at high AoA results in a diagonally shifted lift-to-drag pattern towards low angles and low ratios for the highest serration amplitude (Figure 2-6 left). The amplitude controls a shift of the maximum point of lift from lower to higher values, while the curves are collapsing at zero degrees angle of attack.

For a varying serration wavelength, the minor differences in drag performance and, except for the A29λ7.5, rather small differences in lift show an almost vertical shift of the lift-to-drag curve (Figure 2-6, right). This stresses the differences between the individual serrations, which appear to scale clearly with the wavelength and show the maximum performance at large λ.

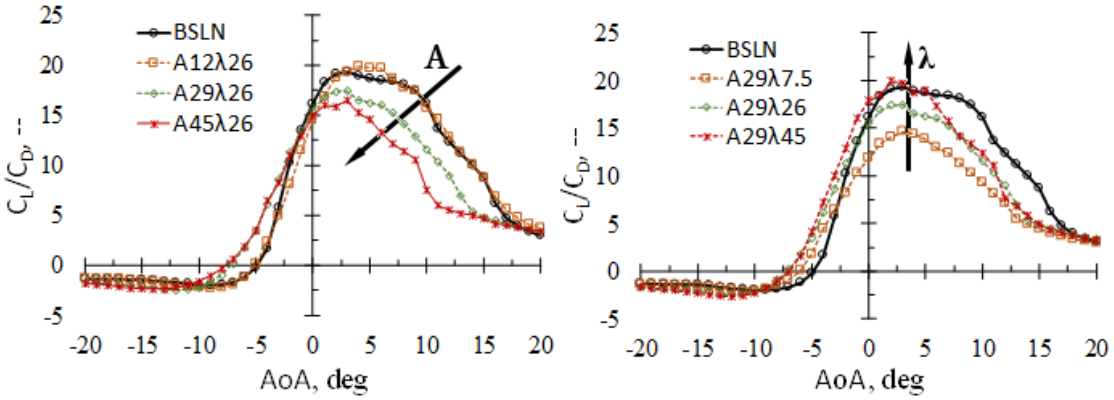

Figure 2-6 Lift-to-drag ratio at varying serration amplitude A (left) and serration wavelength λ (right) for $U_0 = 15$ ms^{-1}.

In terms of the previously mentioned feature of serrations to delay the onset of stall, the extracted shift in performance for serration amplitude and wavelength clearly shows the dominating nature of the serration amplitude. In summary, serrations with low amplitude (ΔAoA = 6 deg) and high wavelength (ΔAoA = 5 deg) show a maximum stall delay as well as a lift performance superior to the reference baseline case. The influence of all the tested serration parameters on specific aerodynamic parameters can be found in Table 2-4 and Appendix A.3.

Table 2-4 Summary of lift and drag performance for the 10 tested aerofoil cases at $U_0 = 15$ms^{-1} and for 20 deg ≤ AoA ≤ +20 deg.

ID	$C_{L\,zero\,AoA}$ [-]	$AoA_{zero\,CL}$ [deg]	$C_{L\,max}$ [-]	AoA_{crit} [deg]	$(C_L/C_D)_{max}$ [-]	A_{WS} [m^2]
A12λ26	0.56	-5.1	1.32	15.0	19.87	0.0702
A22λ18	0.58	-6.2	1.17	11.0	18.78	0.0668
A22λ34	0.58	-5.6	1.28	14.0	19.82	0.0668
A29λ26	0.62	-7.2	1.22	12.0	17.42	0.0645
A29λ45	0.66	-7.0	1.30	11.0	19.96	0.0645
A29λ7.5	0.53	-6.0	1.01	10.0	14.62	0.0645
A35λ18	0.66	-8.2	1.23	11.0	15.94	0.0624
A35λ34	0.64	-7.6	1.22	11.0	17.67	0.0624
A45λ26	0.63	-7.6	1.21	9.0	16.48	0.0591
BSLN	**0.61**	**-4.8**	**1.27**	**9.0**	**19.35**	0.0743

Figure 2-7 shows a juxtaposition of the lift and lift-to-drag performance for the two tested free-stream velocities $U_0 = 15$ ms^{-1} and $U_0 = 25$ ms^{-1}. Collapsing curves are found over almost the entire range of AoA for both the baseline and the A22λ18 case. Main differences are the slightly higher maximum lift-to-drag values for the baseline case due to a slightly decreased drag at $U_0 = 25$ ms^{-1}. Consequently, the influence of the free-stream velocity can be considered negligible, also showing highly similar trends for the different serrations tested (Appendix A.3).

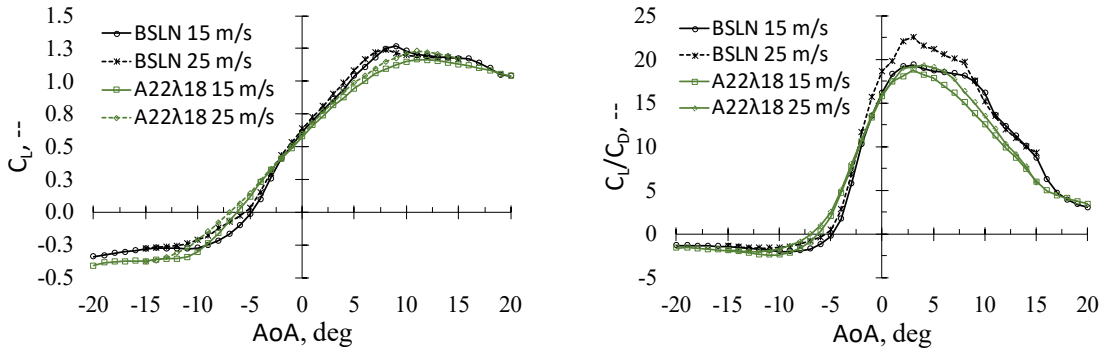

Figure 2-7 Coefficients of lift (left) and lift-to-drag ratio (right) of BSLN and A22λ18 for the two tested free-stream velocities $U_0 = 15\ ms^{-1}$ and $U_0 = 25\ ms^{-1}$.

2.3 Numerical Study

Deeper and more detailed insights into the aerodynamic effects are expected by conducting a numerical study. The pressure distribution helps to unravel the generation of the characteristic trends of lift and drag for the serrations, whereas analysis of the skin friction coefficients provides additional information with regard to the flow separation and the stall-delaying effects of serrated aerofoils. The numerical study focusses on five of the aerofoil configurations, tested experimentally in Section 2.2, namely the four serrations of extreme serration parameters (Figure 2-8) and the intermediate serration A29λ26. Parts of the following discussion are also published in Biedermann et al. [48].

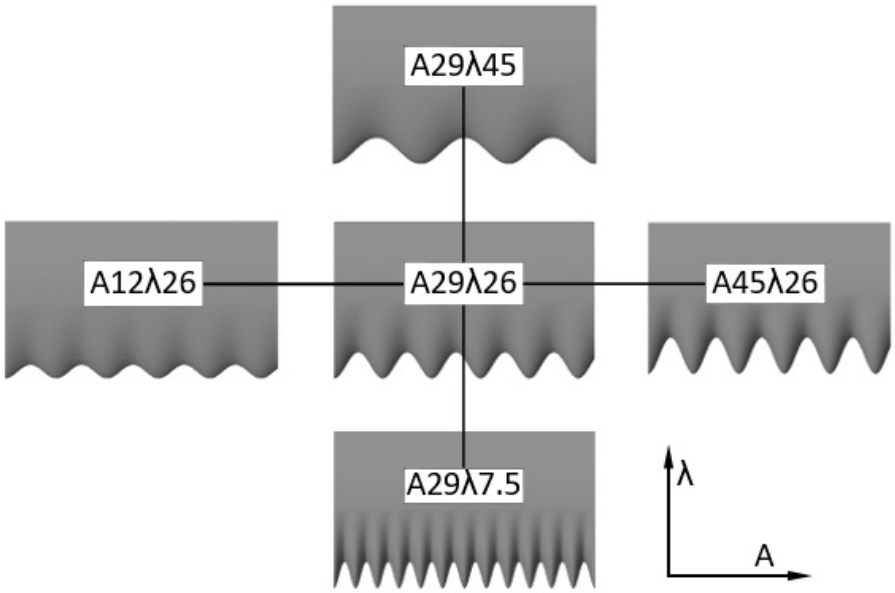

Figure 2-8 Location of the numerically tested leading-edge serration parameters within the 2-D experimental space.

2.3.1 Setup

The numerical setup consists of solving compressible (U)RANS equations, while modelling of the turbulent boundary layer took place by means of the shear-stress-transport (SST) turbulence model. In addition, the γ-Re_θ-transition model was applied in order to take into account the transition of the boundary layer from laminar to turbulent. For the pre-stall region, the numerical analysis was performed at steady state, since preliminary simulations showed no significant impact of transient effects on the lift and the drag performance. For determining the lift coefficients post-stall, however, more detailed transient simulations are necessary and

were carried out for example cases [48]. In terms of meshing, a structured mesh with hexahedrons was used (Figure 2-10). The dimensions of the meshed domain were set, based on the aerofoil chord, to a multiple of 18 in the streamwise (x-wise) direction and a multiple of 16 in the anti-streamwise (y-wise) direction. Regarding the aerofoil surface, the chord (x-wise) was meshed with 1170 nodes/m and the span (z-wise) with 1560 nodes/m. Special care was taken for the resolution of the leading and trailing edge of the aerofoil (Figure 2-10, right). Starting at the aerofoil surface, an inflation layer was defined by an expansion with a constant ratio of 1.1, while the location of the first layer was set to the non-dimensional value of $0.001 \leq y^+ \leq 1$ [48] in order to guarantee the precise resolving of the turbulent boundary layer via the chosen SST turbulence model (*Eq. 2-7*), where u_τ is the friction velocity, ν the kinematic viscosity, τ_w the wall shear stress and ρ the fluid density.

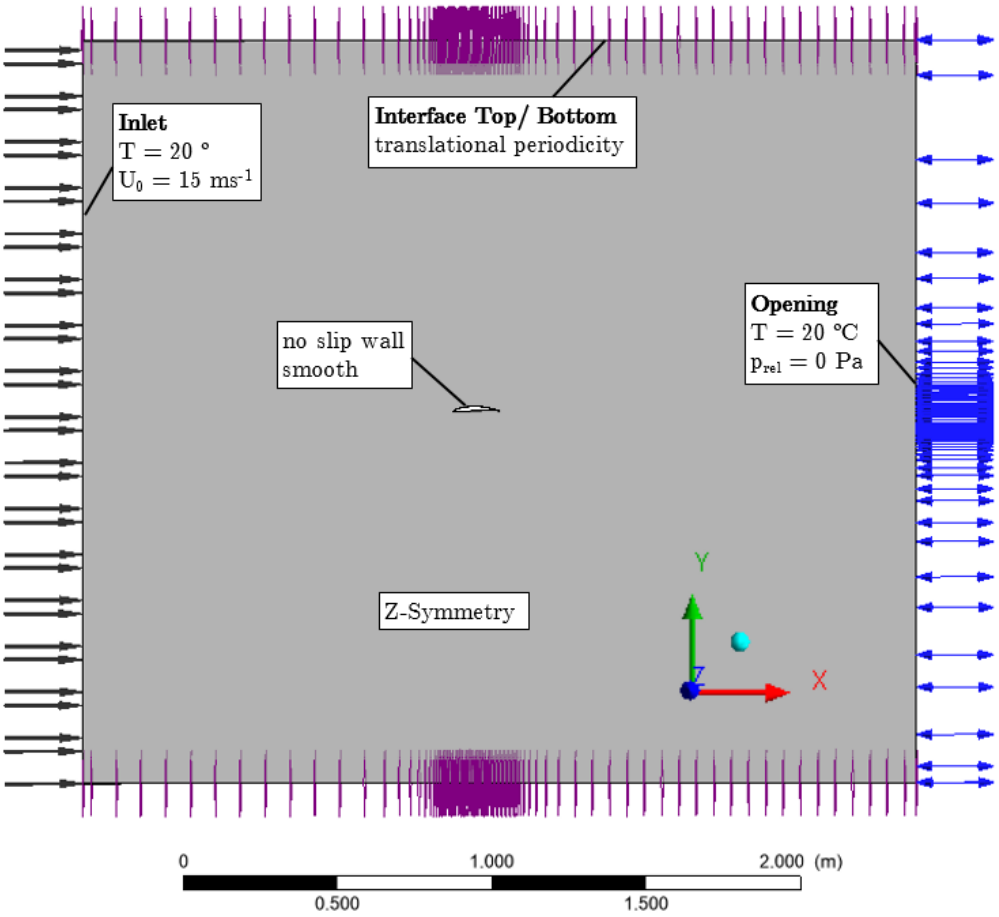

Figure 2-9 Side view of the computational domain, including relevant boundary conditions.

The chosen mesh parameters resulted in a total amount of $8{\cdot}10^6$ to $16{\cdot}10^6$ nodes in the final meshes. As for mesh quality criteria, the overall maximum dihedral angle was kept below 160 degrees, the aspect ratio (AR) below $AR < 200$ and the volume change below *6* [48]. Considerations on the grid quality were supplemented by a grid and domain study in order to prove the independency of the chosen scales. With regard to the spanwise extension of the domain, two cases were tested. First, the domain was limited to only one wavelength, neglecting possible spanwise interaction effects, and second, an extension of two wavelengths was investigated.

$$y^+ = {u_\tau \cdot y}/{\nu} \quad \begin{cases} u_\tau = \left({\tau_w}/{\rho}\right)^{1/2} \\ \tau_W = 0.0289 \rho \nu^{1/5} {U_0}^{9/5} x^{-1/5} \end{cases} \qquad \textit{Eq. 2-7}$$

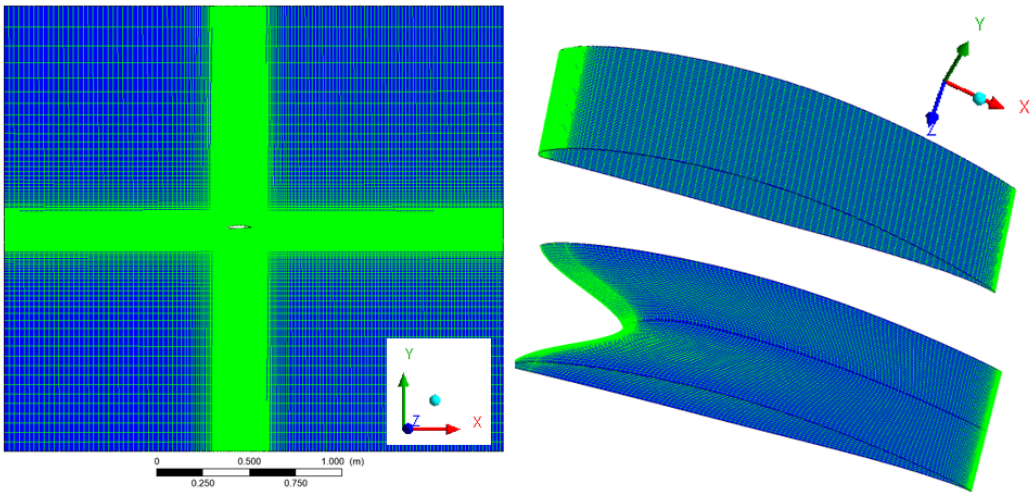

Figure 2-10 Extraction of the defined mesh for the numerical study. Full domain with visible inflation layer and position of the analysed aerofoil (left). Surface mesh of serrated (A29λ45) aerofoil with a refinement of leading edge and trailing edge (right).

2.3.2 Coefficients of Lift and Drag

The coefficients of lift and drag are already defined in *Eq. 2-5* and *Eq. 2-6*. However, for the determination of the required lift and drag forces in the numerical approach, the angle of the flow relative to the aerofoil chord as stated in *Eq. 2-8* and *Eq. 2-9* needs to be taken into account. Figure 2-11 shows the coefficients of lift and drag for all the five tested serrations at a spanwise extension of the computational domain to two wavelengths. Moreover, the lift-to-drag ratio hints at the total efficiency of the tested configurations. The single-wavelength study shows highly comparable results, which are presented in Appendix B.1.

$$F_L = F_{ax} \cdot cos(\alpha) - F_{tan} \cdot sin(\alpha) \qquad \textit{Eq. 2-8}$$

$$F_D = F_{ax} \cdot sin(\alpha) - F_{tan} \cdot cos(\alpha) \qquad \textit{Eq. 2-9}$$

Comparing the numerical results in Figure 2-11 with the observed experimental trends in Figure 2-4 – Figure 2-6 shows a remarkable fit of the lift coefficients for the linear pre-stall regime, which is also presented in Appendix B.2. However, some deviations are observed for the post-stall performance, being a function also of the spanwise extension of the computational domain since flow phenomena become highly unstable. The difficulty of modelling the stall effect of an aerofoil numerically is a commonly reported problem since the point of separation is highly unstable and depends on various influencing factors [58].

Moving to the influence of the serration parameters and therefore the angle-dependent patterns, Figure 2-11 shows definite similarities to the experimental results discussed in Section 2.2.3. The pre-stall lift coefficients of the baseline case match well with the two-dimensional X-Foil panel code [59] at identical boundary conditions. For both experimental and numerical results, the same scaling of lift and drag and lift-to-drag with the serration

wavelength and the amplitude is observed. Even more importantly, the previously observed shift of the lift-to-drag ratios in Figure 2-6 can be confirmed numerically, with a diagonal shift (stall-controlling effect) being present for the serration amplitude and a vertical shift (performance-controlling effect) for the serration wavelength. At zero angle of attack, the serrations are found to outperform the baseline reference case in terms of lift, which can be attributed to the local distribution of the surface pressure, as further outlined in Section 2.3.3. In consequence, the good qualitative agreement with the experimental findings also allows to analyse the numerical solution more deeply, for example by evaluating the boundary layer development, the surface pressure distribution and the skin friction.

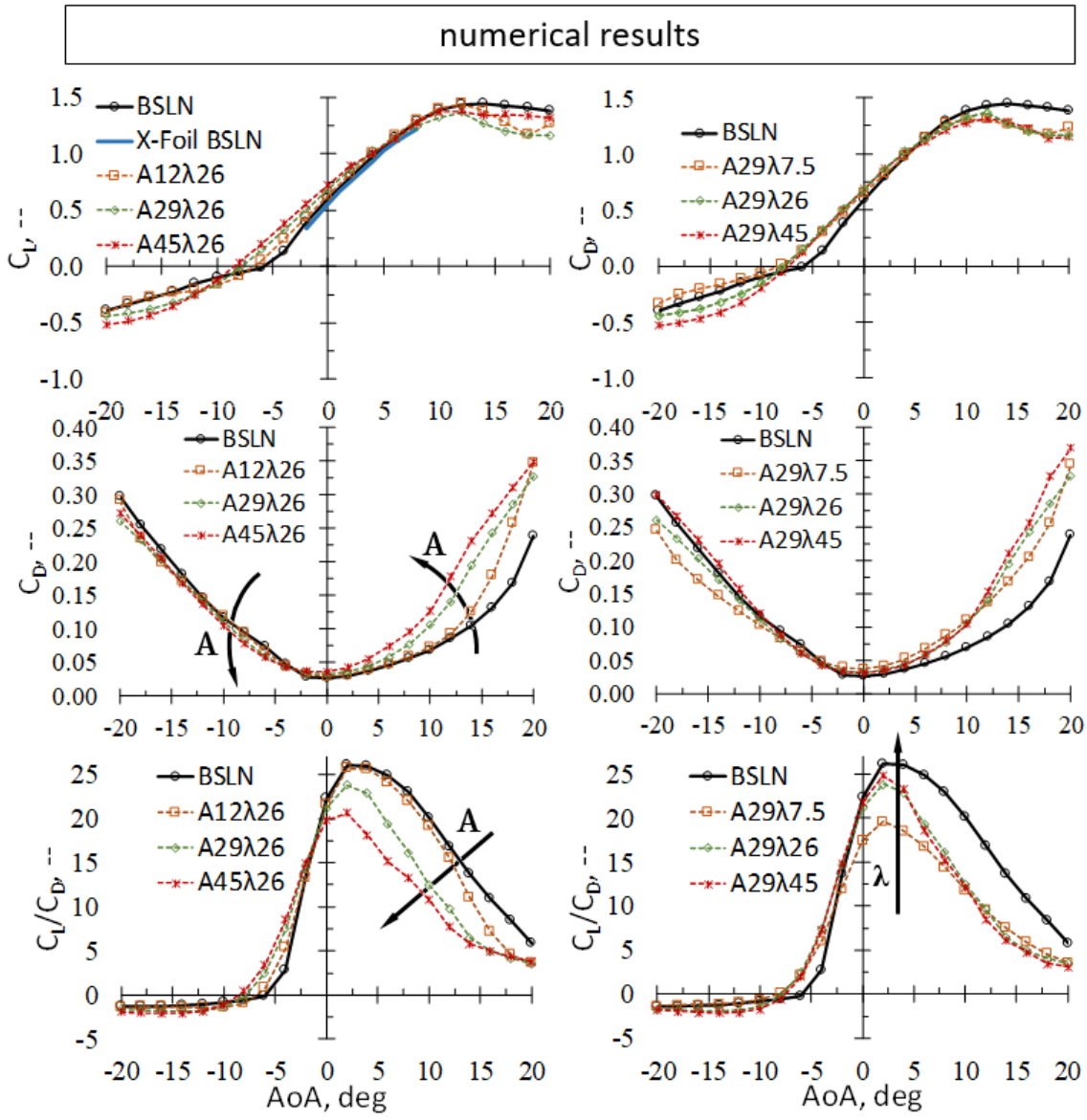

Figure 2-11 Overall aerodynamic performance in terms of the coefficients of lift (top), coefficients of drag (centre) and the lift-to-drag ratio (bottom). Variation of serration amplitude (left) and wavelength (right). Spanwise extension of the underlying computational space = 2 λ. Numerical results.

2.3.3 Local Lift Coefficients

Performing a numerical analysis allows extracting the pressure distribution on the suction and pressure side of the aerofoils for different spanwise locations. As a consequence, local lift coefficients can be determined according to *Eq. 2-10*, assuming an infinitesimal small extension in the spanwise direction.

$$C_L = -\int_0^1 \left(c_{P,suc.} - c_{P,press.}\right) d(X/C) \qquad \textit{Eq. 2-10}$$

Figure 2-12 shows the pressure coefficients according to *Eq. 2-11,* as well as the local coefficients of lift (*Eq. 2-10*), for three distinct spanwise locations by integration along the non-dimensional aerofoil chord x/C.

$$C_P = \frac{p - p_\infty}{\frac{\rho}{2} \cdot U_0^2} \qquad \textit{Eq. 2-11}$$

The trend of the pressure coefficients shows clearly that the associated local lift is dominated by the leading-edge section at x/C ≤ 0.3. For AoA = 0 deg, the root section of the serration experiences the strongest lift, which is meaningful because as a result of the design process of the serrations, this region is compressed, showing a blunter leading edge than the peak regions. Consequently, the local angle of attack for the root region is $\mathrm{AoA_{Root}} > \mathrm{AoA}$, leading to a higher lift at low global AoA but also to early separation effects. This is also described by van Nierop et al. [29], who state that the same pressure difference must be overcome for both the peak and the root region of the leading edge serrations, although for the latter at reduced chord. Hence, higher pressure gradients are observed for the roots, leading to early separation effects. This root-region of high lift apparently affects the full aerofoil and is considered the main cause for outperforming the baseline lift at zero angle of attack, as shown in Figure 2-11. Increasing the angle of attack to AoA = 12 deg (Figure 2-12, centre) shows a strong increase in the overall baseline (BSLN) lift, whereas the serration lift shows a lower performance. This is expected to be caused by the already high effective angles of attack of the root region due to the upwash effects, as described by Cai et al. [38]. Hence, the root already suffers from the first local separation effects while the peak location remains pre-stall. At maximum angle of attack, the lift coefficients for both baseline and serration tend to decrease due to stall phenomena, even though the baseline misses the expected distinct drop in lift since for the numerical solution, part of the separated structures seem to reattach close to the aerofoil trailing edge, as will become apparent from the contour plots presented in Section 2.3.4.

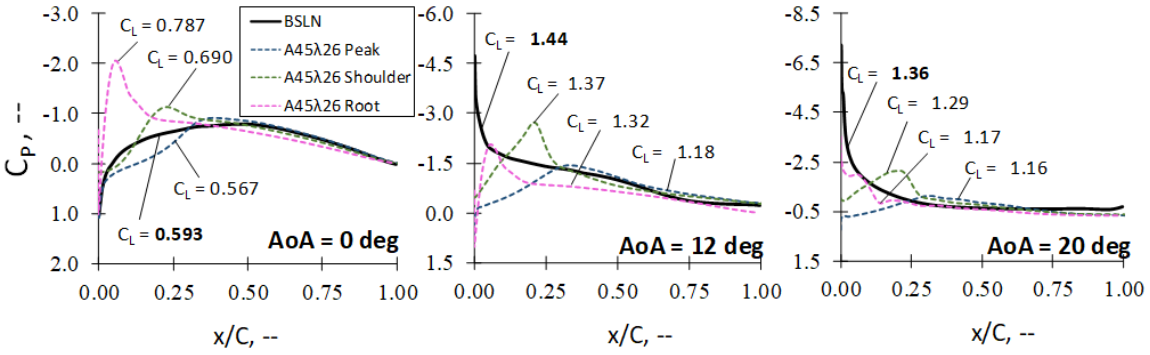

Figure 2-12 Local chordwise pressure coefficients for the aerofoil suction side as well as local coefficients of lift for the A45λ26 serration at AoA = 0 deg (left), AoA = 12 deg (centre) and AoA = 20 deg (right).

2.3.4 Skin Friction Coefficients

The skin friction coefficient C_F in *Eq. 2-12* describes the non-dimensional relation of the friction forces relative to the forces acting normal to a surface. A skin friction coefficient of $C_F = 0$, therefore, indicates a separated flow since no wall shear stress τ_w is present.

$$C_F = \frac{\tau_w}{\frac{1}{2}\rho v_\infty^2} \qquad \textit{Eq. 2-12}$$

For practical applications in rotating machines, the range 0 deg ≤ AoA ≤ 20 deg represents the most relevant region from overload to part-load conditions. This is why the analysis of the skin friction in this section is limited only to selected angles of attack within this range for all the aerofoil configurations analysed. Additional cases can be found in Appendix B.3.

At zero angle of attack (Figure 2-13), the skin friction coefficients indicate a smooth, attached flow over the aerofoil contour for all cases shown. Separation mainly occurs close to the trailing edges, where already a dependency on the serration parameters becomes visible. For the straight leading edge (BSLN), separation occurs at x/C ≈ 0.96, showing a constant pattern along the span. For the serrations, a similar pattern is visible for the spanwise peak locations, whereas at spanwise root locations a separation further upstream is visible. This pattern hints at the ability of the leading edge serrations to penetrate deep into the boundary layer on the suction side of the aerofoil, showing the strongest effect for high serration amplitudes and small serration wavelengths. At sufficiently high serration amplitudes, an early separation occurs close to the serrations for the spanwise location of the serration roots (A29λ26), a result that confirms findings by [30, 20, 22, 34, 38, 27, 43, 25] and the theoretical prediction by van Nierop et al. [29]. Since the aerofoil chord is significantly lower for the root locations and the same pressure distribution needs to be overcome as for, for example, the peak locations, the strong pressure gradient leads to this separation effect. This effect is held responsible for the lower pre-stall lift performance of serrated aerofoils compared to the straight leading edge. However, increasing the angle of attack (Figure 2-14 – Figure 2-16) shows a complex three-dimensional separation pattern for the serrated leading edges, with the local separation behind the roots. This separated regime expands from the leading edge region towards the trailing edge but also shifts towards the spanwise peak locations, generating a triangle-shaped locally separated flow. At sufficiently high amplitudes, the flow remains attached at the spanwise root locations at the trailing edge even at the maximum angle of attack AoA = 20 deg (Figure 2-16). This leads to the previously described smooth stall behaviour of the serrations. The three-dimensional separation pattern appears to be stabilised by large serration wavelengths. Meanwhile, for the baseline case, a continuous shift of the separated regime towards the leading edge takes place, leading to a decrease in lift. In consequence, the baseline is expected to stall more abruptly, which should lead to a break-even point at a certain angle of attack, at which the lift coefficients of the locally separated flow of the serrations outperform the strong separation effects of the baseline case. However, for the numeric simulations, the baseline shows some reattachment effects close to the trailing edge at higher angles, leading to additional vortex lift effects, preventing a significant drop in lift. This is also the case for serrations for which small wavelengths or small amplitudes prevent penetration of the boundary layer at the trailing edge (A29λ7.5 at AoA = 20 deg, and A12λ26 at AoA ≥ 14 deg), resulting in increased lift coefficients. Therefore, for the range of AoA investigated, no clear aerodynamic benefit of the serrations can be confirmed, although the superior stall-delaying potential becomes clearer. However, the direct relation between the observed skin friction coefficients and the resulting coefficients of lift can be seen, for example,

for the A45λ26 case, in which large scale vortices are generated that prevent extensive stall, as in the case for the baseline. This results in high post-stall lift but also, due to the vortices, in a significant increase in drag and hence a drop in the lift-to-drag performance. These vortices, however, are inducing high-momentum flow into the boundary layer, energising it and preventing separation.

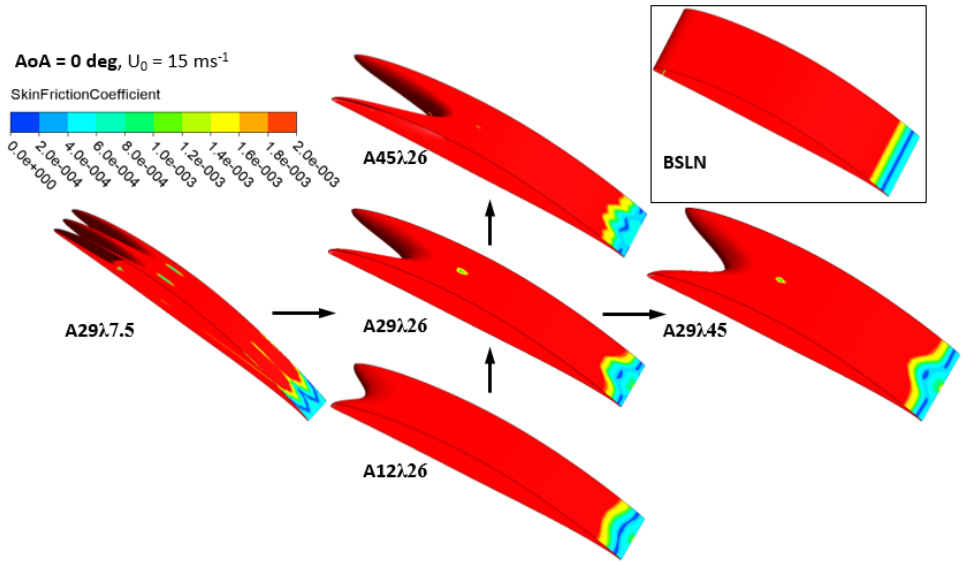

Figure 2-13 Skin friction coefficient for monitoring separation over the aerofoil contour. U_0 = 15 ms^{-1}, AoA = 0 deg.

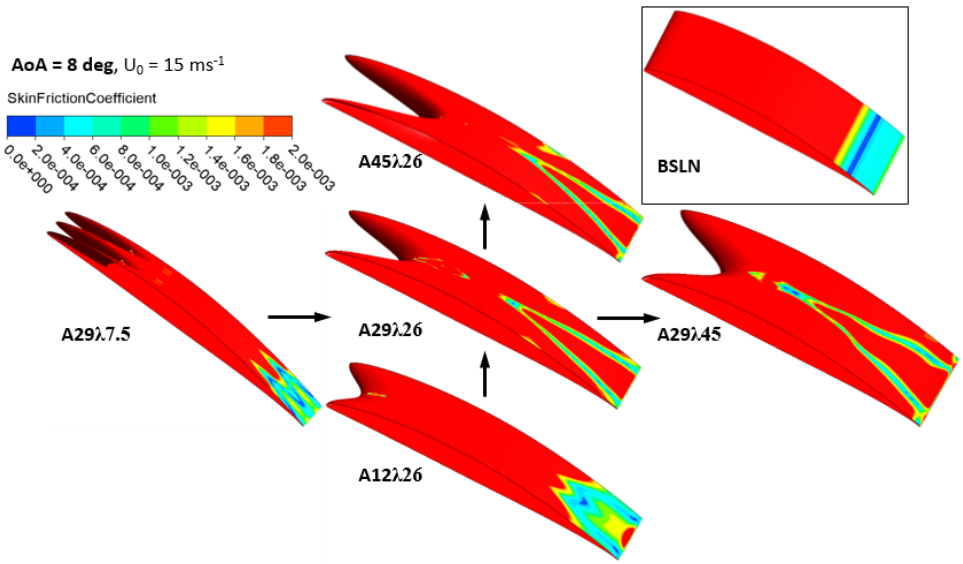

Figure 2-14 Skin friction coefficient for monitoring separation over the aerofoil contour. U_0 = 15 ms^{-1}, AoA = 8 deg.

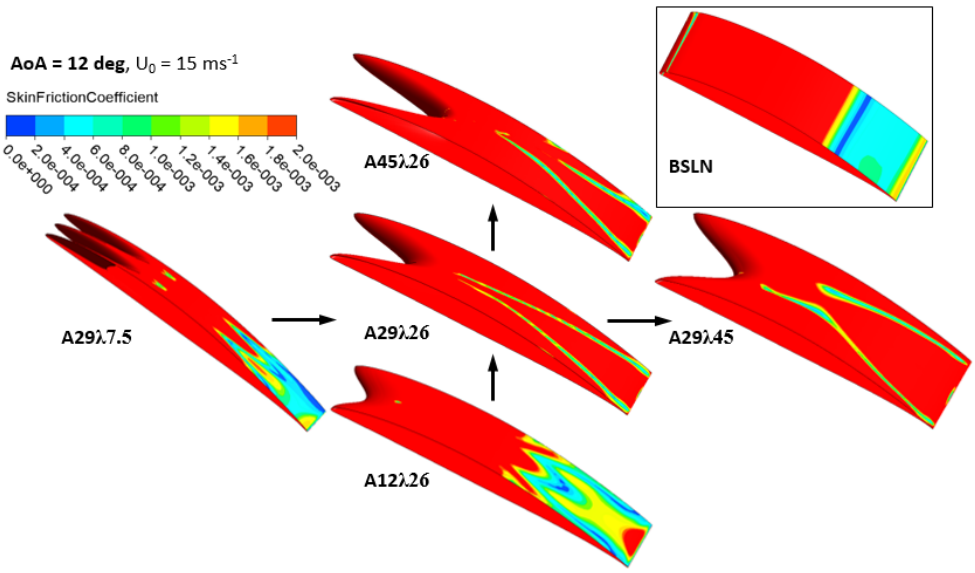

Figure 2-15 Skin friction coefficient for monitoring separation over the aerofoil contour. U_0 = 15 ms^{-1}, AoA = 12 deg.

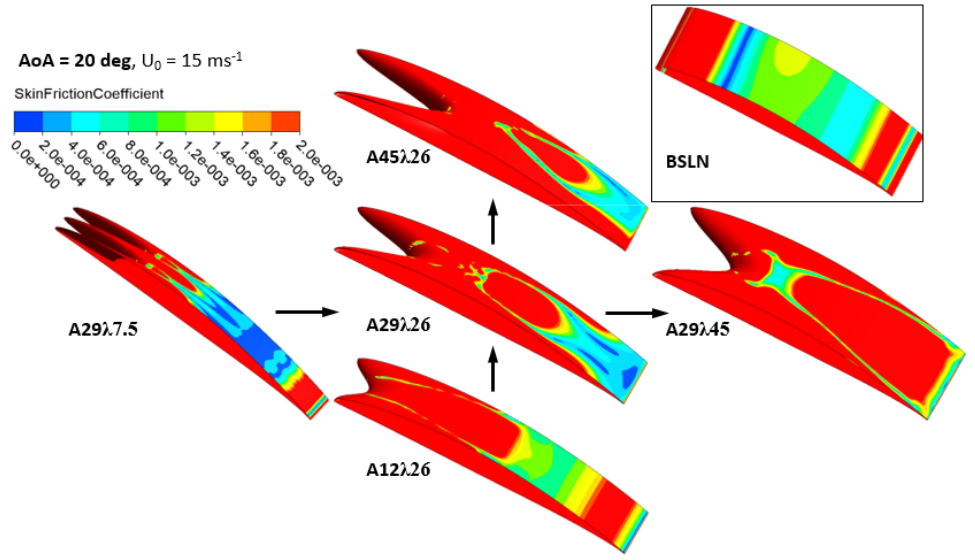

Figure 2-16 Skin friction coefficient for monitoring separation over the aerofoil contour. U_0 = 15 ms^{-1}, AoA = 20 deg.

In order to analyse whether and where local separation occurs at the spanwise root location of the serrated aerofoils, the skin friction coefficients SFC for the suction side were extracted in Figure 2-17, covering the angles near stall at AoA = 8 deg and AoA = 12 deg. For the baseline case, flow separation takes place at x/C = 0.88 at AoA = 8 deg, mitigating upstream to x/C = 0.72 at AoA = 12 deg. The tested serrations, on the other hand, show early separation at the root but improved chordwise performance after this initial stall, clearly scaling with the serration amplitude and wavelength. Here, maximum wavelengths and maximum amplitudes turn out to generate lift most efficiently, which is considered meaningful since the A/λ ratio determines the strength of the generated vortices at the leading edge that migrate downstream [22]. On the other hand, increasing the serration amplitudes results in blunter root profiles, hence promoting early separation effects.

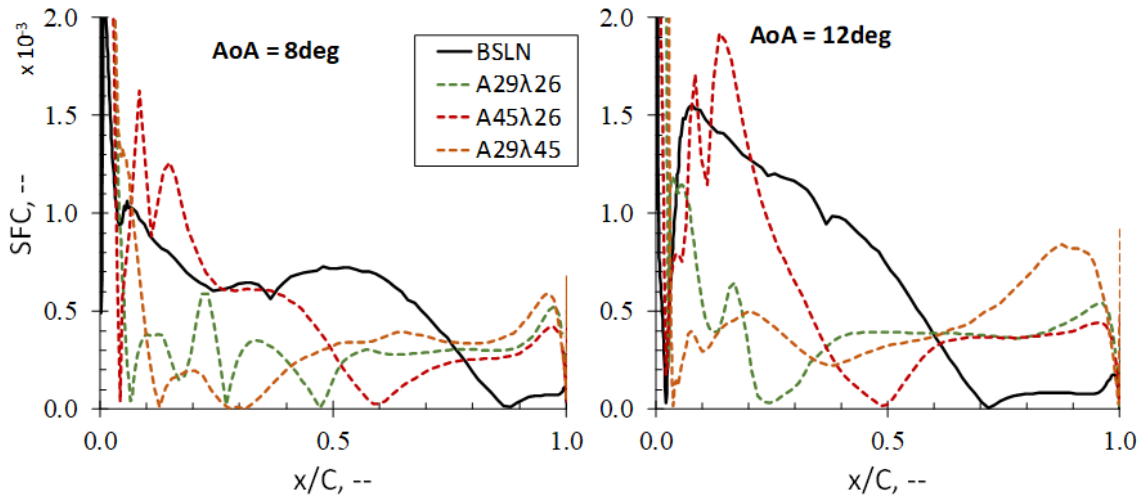

Figure 2-17 Skin friction coefficients at the root location of the leading edge serrations as well as for the BSLN case vs. the normalised local chord x/C. Pre-stall at AoA = 8 deg (left) and post-stall at AoA = 12 deg (right).

Extending the area of interest from the aerofoil surface towards the nearby flow regime by illustrating the Q-Criterion, Figure 2-18 (left) shows the generation of a large-scale vortical structures. Considering the deformation of fluid particles, the Q-criterion indicates the relative dominance of the rotational vs. the stretching component and is defined according to *Eq. 2-13* with Ω being the vorticity rate and S_{Strain} the strain rate [60].

$$Q = \frac{1}{2}\left(\Omega^2 - S_{Strain}^2\right) \qquad \textit{Eq. 2-13}$$

The observed structures are developed by the serrated profile and resemble canopies. These canopies are especially distinct for serrations of high amplitudes and moderate to high wavelengths. It is considered responsible for the observed three-dimensional separation pattern described previously (Figure 2-13 - Figure 2-16). In chordwise direction, the core of this canopy tends to develop upwards (U_v-direction), away from the aerofoil surface. For the U_u-component, an anti-streamwise recirculation pattern is observed, reaching zero velocity close to the aerofoil surface. The transverse velocity component (U_w), on the other hand, shows an inward rotation towards the serration roots. For the aerofoil surface covered by this canopy, the resulting velocity vector appears to be $\overline{U}_{uvw} > 0$ and shows no separation effects. A similar canopy, generated by leading edge serrations and dominating the separation process, including the delay of separation, is described by Hansen et al. [30], as shown in Figure 2-18 (right). The authors describe the canopy to be shielded by continued inward flow of the boundary layer vorticity, yielding increased circulation further downstream (continuous feeding), with a maximum at the trailing edge of the aerofoil. This continuous feeding process might prove beneficial in preventing the flow separation.

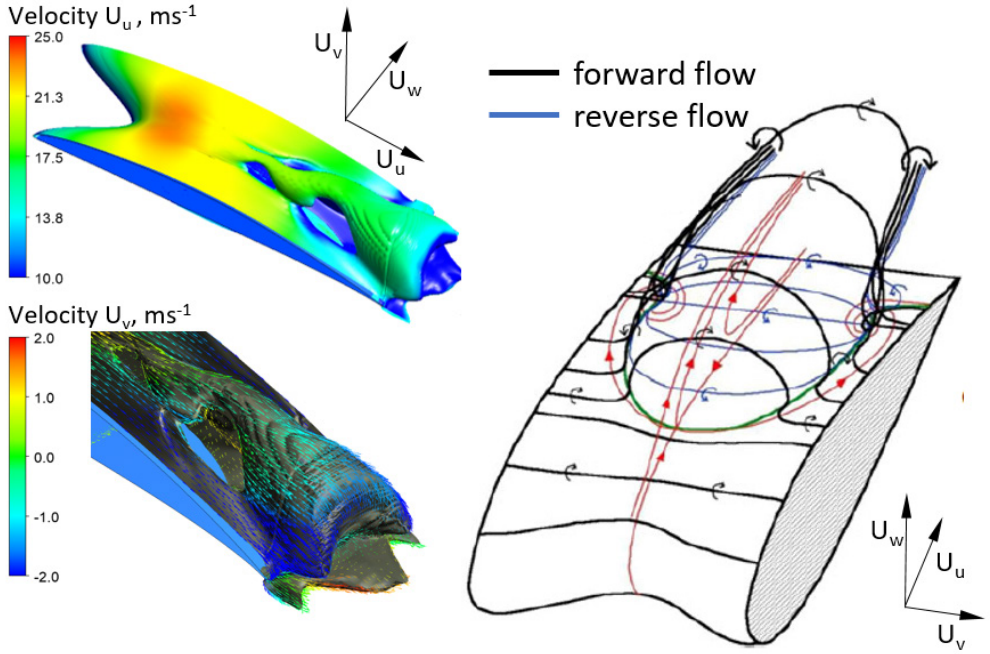

Figure 2-18 A29λ45, Q-criterion at threshold 4662 s^{-2} at AoA = 8 deg, coloured by axial velocity U_u (top left) and spanwise velocity component U_v (bottom left). Interpretation of the three-dimensional vortex line according to Hansen et al. [30] (right, reproduced with permission).

The location of the canopy appears to be congruent with the observed pattern of the skin friction coefficients in Figure 2-13 — Figure 2-16 and is considered to cause the related partial separation for the root region, while maintaining an attached flow at spanwise locations, corresponding to the serration peaks.

Moreover, pairs of streamwise counter-rotating vortices are described by several researchers to emerge between the serration peaks, leading to a momentum exchange and a resulting flow separation [38, 39, 23, 25, 18, 28]. In addition, Hansen et al. [30] describe these vortices to be the key effect in initiating the formation of the described canopy. Oil flow visualisation at the aeroacoustic wind tunnel facility of Brunel University London for an A45λ26 serration at $U_0 = 15$ ms^{-1} (Figure 2-19 and Figure 2-20) allows to experimentally compare the separation process to the simulated aerofoils for both the suction and the pressure side. For the oil flow experiments, counter-rotating structures are identified between the serration peaks. Numerical validation of the same aerofoil and at the same boundary conditions shows a highly similar pattern along the serrated surface (Figure 2-19, left): early separation at the serration roots, which initiates the generation of vortical structures that flow downstream and penetrate deep into the boundary layer at the trailing edge. For the pressure side (Figure 2-20), a counter-rotating pattern is also observed, presumably leading to an increase in drag.

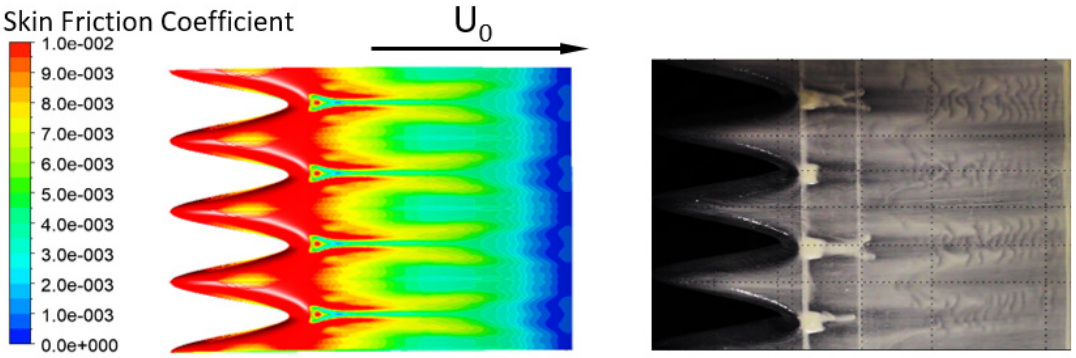

Figure 2-19 Numerically obtained skin friction distribution (left) vs. oil flow visualisation (right). Suction side of A45λ26 at $U_0 = 15$ ms^{-1} and AoA = 0 deg.

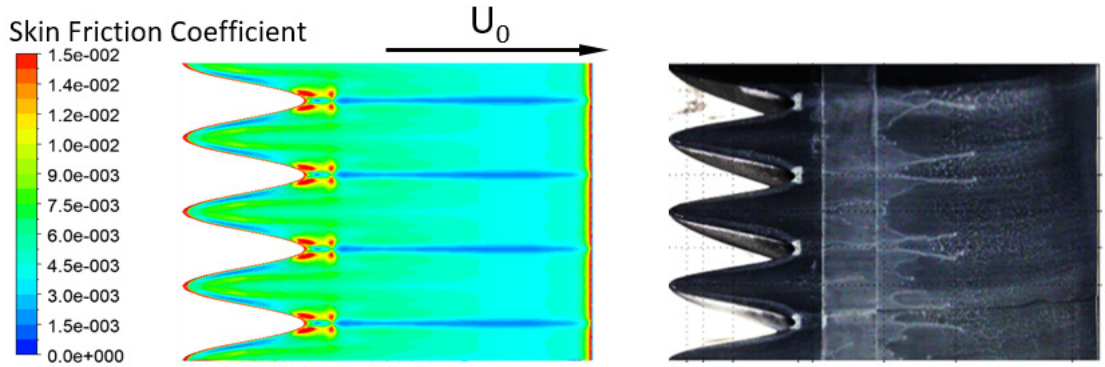

Figure 2-20 Numerically obtained skin friction distribution (left) vs. oil flow visualisation (right). Pressure side of A45λ26 at $U_0 = 15\ ms^{-1}$ and AoA = 0 deg.

2.4 Summary and Discussion

Up to now, extensive research efforts were aimed at understanding the effect of serrated leading edges in both a more global manner and with respect to the detailed vortex formation mechanisms. However, when it comes to the influence of the different serration parameters, the conclusions drawn by many researchers are not fully consistent and seem to depend on the aerofoil type chosen and the associated camber, as well as the boundary conditions and the specific setup. Since the aim of this thesis is to transfer the aerodynamic dependencies of serrated leading edges from the rigid to a rotating application, the lack of congruent information requires creating one's own aerodynamic database for the aerofoil type chosen. This ascertains that the resulting aerodynamic dependencies are reliable and valid and enables conclusions to be drawn on the rigid and the rotating domain in the following sections.

Consequently, extensive analysis of the chosen NACA65(12)-10 aerofoil was carried out. The experimental study provided meaningful results in terms of lift and drag coefficients, with small serration amplitudes, as well as high wavelengths, proving to be most beneficial. Small amplitudes also appear to lead to a small reduction in drag. Analysing the more relevant lift-to-drag ratio reveals a clear pattern, in which a diagonal shift of the maximum towards low angles of attack occurs with increased amplitudes. Moreover, compared to the baseline aerofoil, the maximum C_L/C_D ratio itself is attenuated as well. The underlying effect is attributed to early local separation effects (increased drag) at the serration roots with increasing serration amplitude. For the serration wavelength, however, seemingly minor dependencies in lift and drag were found to accumulate in terms of C_L/C_D, also showing a clear vertical scaling of the lift-to-drag performance for high wavelengths. In line with the dependencies of the shifted lift-to-drag ratio for maximum amplitudes, the most significant delay of the stall angle is obtained for the lowest serration amplitude.

The successively conducted numerical study aimed at providing more detailed insights into the main causes of the aerodynamic performance for five of the previously analysed serration configurations. The experimentally observed trends of lift and drag coefficients, as well as the shifting pattern for the lift-to-drag ratio, could be confirmed both qualitatively and quantitatively. Moreover, a complex three-dimensional separation pattern was extracted especially for high A and high λ, leading to only partial separation along the aerofoil surface, which is held responsible for generating the well-known smooth stall characteristics. This three-dimensional flow pattern appears to be a result of the existence of a large-scale vortical structure, resembling a canopy and being similar to the structure described by Hansen et al. [30]. This structure and the underlying complex flow pattern are believed to enable a feeding mechanism of the covered aerofoil surface with boundary layer momentum, and this mechanism helps to prevent local separation.

3 Aeroacoustics: Aerofoil-Turbulence-Interaction Noise

The current section deals with the aeroacoustic signature of aerofoils subjected to leading edge serrations. A review of the actual state of research shows much more comprehensible results than for the aerodynamic performance in Section 2.1. However, no study describes the systematic influence of serrations design parameters and inflow conditions on the aeroacoustic noise reduction capability of leading edge serrations; not to mention a combined aerodynamic and aeroacoustic analysis. Therefore, the experimental investigations in this section focus on three main aspects:

- Identification of the overall noise reduction capability of the leading edge serration configurations already analysed aerodynamically. This is intended to lead to the definition of multi-objective optima of aerodynamic and aeroacoustic performance, which are of high value when transferred to the rotating system.
- Identification of the noise reduction mechanisms, including spatial distribution of the noise sources. This includes localisation of the most sensitive regions, where noise reduction takes place. As for the aerodynamic results, this serves to facilitate the assignment of the effects of leading edge serrations in the rotating domain, where the acoustic sources and interdependencies are more complex and more diverse.
- Extraction of the spectral composition of the noise reduction due to serrated leading edges. This serves to enable a direct comparison between the single aerofoil and the full-rotor results based on the underlying scaling laws.

3.1 Aerofoil Theory

3.1.1 Noise Sources in General

As summarised in Figure 3-1, the acoustic signature of an aerofoil can be subdivided according to a handful of distinct noise source mechanisms. At smooth inflow conditions, noise is mainly generated close to the aerofoil trailing edge. This noise is of broadband character for the mid-to-high frequency range, with the spectral range being a function of the boundary layer thickness [61] since it is produced by the generation of small-scale turbulent eddies within the aerofoil boundary layer, migrating downstream. Additional discrete tones of high frequencies are generated if the boundary layer shows significant laminar characteristics, allowing the formation of an aeroacoustic laminar feedback loop. Under inflow conditions of increased turbulence, however, the acoustic signature is dominated by low-to-mid frequency broadband leading-edge noise, being a function of the free-stream velocity and the aerofoil chord [61]. The underlying effect is a strong interaction of the approaching turbulent structures and the rigid aerofoil, scattering into sound.

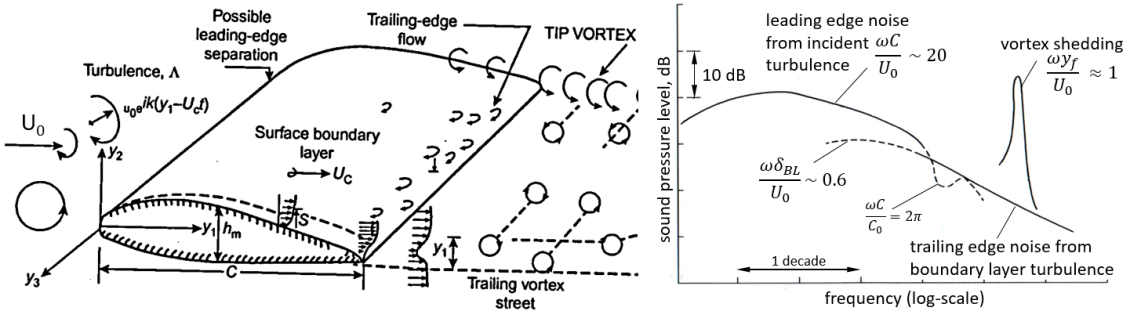

Figure 3-1 Schematic illustration of flow-induced noise, radiated by a rigidly supported aerofoil, as well as the associated spectrum of the acoustic signature (right) [61]. Reproduced with permission from Elsevier.

Increasing the angle of attack leads to flow separation and eventually to stall of the aerofoil, with large portions of the boundary layer being separated from the surface. In this case, low-frequency stall noise is generated, with the frequency being a function of the size of the separated structures. Finally, if the aerofoil tip is exposed to the free stream, tip vortices are generated, once again shedding into noise.

3.1.2 Leading-Edge Noise

Considering an incoming flow that is defined by high turbulence intensity, the incident turbulence impinges on the leading edge of the aerofoil and thus induces pressure fluctuations on the surface. These pressure differences are propagating at the speed of sound and are causing broadband noise emissions. Several previous studies are available concerning fluctuating lift forces of turbulent incoming flow and subsequent radiation of sound into the far field. These studies include those of Paterson and Amiet [62] and Oerlemans and Migliore [63], who describe the acting forces at the aerofoil leading edges as a result of an unsteady pressure field produced by the aerofoil in response to the impinging turbulence. Given a free stream, the convection of the turbulent structures within the turbulent flow leads to an interaction with the leading edge of the aerofoil. The turbulent eddies are bending and curving around the leading edge, inducing pressure fluctuations on both sides of the aerofoil, which eventually result in noise radiation [64].

Generally, leading-edge noise occurs in the low-frequency region, in which the turbulent structures are large. The largest dimension of an approaching coherent vortex can be expressed as the integral length scale Λ (Figure 3-2), which is an essential part of several models that describe the generation of leading-edge noise, including Amiet's model for flat plates [65]. Incorporating the Von Kármán model for isotropic longitudinal turbulence, Amiet proposed a simple expression for estimating the spectral radiation of the far-field noise of a flat plate subjected to incoming turbulence [65], as is shown in *Section 3.4.1*.

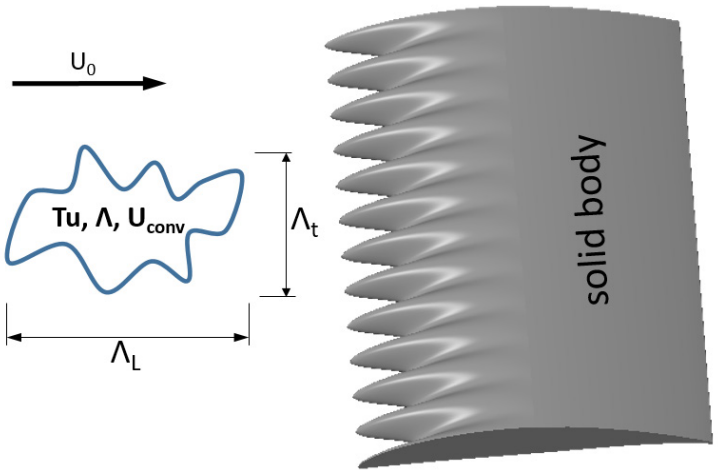

Figure 3-2 Qualitative representation of a coherent turbulent structure, approaching a solid surface. Indication of longitudinal Λ_L and transversal integral length scale Λ_t as well as the turbulence intensity Tu and the vortex convective velocity U_{conv}.

According to Carolus [66], one key issue in terms of noise generation at curved surfaces is the transient velocity relative to the aerofoil surface. The velocity profile strongly depends on the chordwise position of the aerofoil (accelerated vs. delayed flow). Consequently, the sound-generating mechanisms are also a function of the position. Moreover, the location of the sound sources depends on the aerodynamic and aeroacoustic compactness of the treated aerofoil. Aerodynamic compactness is given when the aerofoil chord length is smaller than the integral turbulence length scale Λ. In case of aerodynamic compactness, the flow induces an oscillating

angle of attack with respect to the aerofoil surface, which itself responds with oscillating lift and drag forces. In this case, the aerofoil as a whole radiates noise for frequencies satisfying the condition of acoustic compactness, requiring the chord length to be significantly smaller than the acoustic wavelength. In case of no aerodynamic compactness, the deformations of the eddies due to the interaction with the aerofoil cause an unsteady loading only for the leading edge. A maximum is obtained in the direct vicinity of the leading-edge tip before the turbulent structures stretch around the body and both the lift and the radiated noise decrease proportionally [64]. In consequence, a discrete area at the leading edge is formed that radiates noise.

Oerlemans and Migliore [63] observed that in case of high inflow turbulence, the leading-edge noise is dominant for all aerofoils investigated. Furthermore, they measured a rising broadband noise level with increasing sharpness of the leading edge. At low Mach numbers, the moderate flow velocities lead to moderate frequencies and thus high wavelengths, which result in acoustic compactness. In this case, the fluctuating pressure forces act as a dipole source.

Narayanan et al. [67] state that increasing the aerofoil thickness results in less aerofoil-turbulence-interaction (ATI) radiation since the turbulence gusts are locally slowed down when approaching the leading edge. Ayton and Chaitanya [68] performed an analytical investigation, supplemented with experimental results, into the effect of the nose radius of the leading edge on the radiated noise of aerofoils. High-frequency far-field noise is significantly reduced for high nose radii and low Mach (Ma) numbers. For higher Mach numbers, however, an increase upstream but a decrease downstream is predicted for blunt leading edges (LE). Even though the aerofoil thickness is still the main parameter for controlling ATI noise, the bluntness of the leading edge is an important parameter, also holding possibilities of reducing ATI noise by designing the leading edges in an intelligent way. The underlying effect is outlined by Gill et al. [69], who state that a flow distortion near the leading edge is the main effect for ATI noise reduction, which can be achieved by large aerofoil thickness or large nose radii or both. Apart from the presented overview, several on-going studies on the effect of different aerofoil parameters with regard to ATI noise generation are available [70–72, 69, 73–75].

3.1.3 Trailing-Edge Noise

Many different parameters influence the dynamics of the interaction of a free flow and a lifting surface, such as the development and the transition of the boundary layer. Due to boundary layer transition, small eddies are being generated within the boundary layer, which migrate downstream and cause pressure fluctuations on the aerofoil surface. Desquesnes et al. [76] investigated the flow around a two-dimensional NACA0012 aerofoil. In accordance with previous studies, they observed two different phenomena of acoustic response, depending on the Reynolds number and the angle of attack:

- A spectrum of broadband character but with a dominant frequency, as well as some other significant peaks at equidistant locations
- A spectrum of mainly broadband character

Hence, the frequency spectrum of the radiated noise of an aerofoil differs in dependence on the source. In contrast to the turbulent inflow, which causes mainly broadband noise at the leading edge, boundary layer turbulence, including an acoustic feedback loop, causes broadband noise as well as tonal noise due to interactions with the trailing edge [77].

Broadband Noise

The broadband contribution of the acoustic signature, generated at the trailing edge, is located mainly in the regions of average to high frequencies. The developing mechanisms for this noise generation principle often seem of minor importance and are less investigated in recent research. However, measurements by Arbey and Bataille [78] confirm Fink's [79] assumption that the broadband contribution is caused by boundary layer instabilities whose aerodynamic fluctuations are diffracted at the trailing edge. Moreover, Arbey and Bataille [78] observed a congruency of the peak in the acoustic spectrum of the far field and the wall-pressure spectrum (near field) at the trailing edge of the aerofoil.

Discrete Noise

The periodic shedding of vortices at the aerofoil trailing edge leads to the generation of noise at distinct frequencies, which may be referred to as tonal effects. Similar to the exposure of a rigidly mounted circular cylinder in a free stream, in which vortex shedding and the development of a Kármán vortex street occurs in dependence on the Reynolds and the Strouhal number, the development of a vortex street at an aerofoil trailing edge also depends on the Reynolds number. Principally, vortex shedding at the trailing edge of an aerofoil occurs if the boundary layer on at least one side of the aerofoil remains laminar until close to the trailing edge. Hersh and Hayden [80] observed loud, distinct tones due to fluctuating surface forces in case of a smooth laminar flow with chord-based Reynolds numbers $8.33 \cdot 10^4 < \mathrm{Re} < 3.33 \cdot 10^5$. Furthermore, they placed a tripping wire at the pressure side in the laminar boundary layer of the aerofoil and observed vanishing tonal effects. In consequence, as soon as the boundary layer turns turbulent, a suppression of the vortex shedding takes place because the character of the vortex shedding in the wake changes from periodic to random. Different studies on aerofoil trailing-edge noise revealed that the tonal noise source is close to the trailing edge. An alternative concept for the generation of the tonal noise, however, is the generation of a self-excited feedback loop, by which Tollmien-Schlichting waves (T-S waves) from the laminar boundary layer on the pressure side are amplified and are rolling up into the vortices, which then propagate downstream towards to aerofoil trailing edge. Finally, these vortices interact with the trailing edge, resulting in significant noise radiation of the scattered oscillating field [81, 76].

3.2 State of the Art – Leading Edge Serrations

3.2.1 Noise Reduction Mechanisms

Several experimental, numerical and analytical studies were conducted in recent years, aimed at identifying the underlying mechanisms of the role of serrated leading edges in reducing aerofoil-turbulence-interaction (ATI) noise. By now, the main mechanisms are identified, even though there are still some gaps when it comes to a more detailed analysis of the aerodynamically coupled generation and reduction of noise. Up to date, five main effects have crystallised, as summarised below. Subsequently, a more detailed description of the underlying mechanisms is provided. The five main effects of serrations with respect to noise reduction capability are as follows:

1. The cut-off effect, by which the noise source at the serration shoulders is attenuated since swept shapes are less prone to generate ATI noise. This takes place in the mid-to-high frequency range since the serration roots are still radiating significant low-frequency noise.
    a. Kim et al. [74] 2016
    b. Turner and Kim [82, 83] 2016/17

2. Reduction of spanwise correlation coefficients, manifesting itself in decorrelation of the unsteady edge response along the shoulders of the leading edge serrations.
    a. Haeri et al. [84] 2014
    b. Chaitanya et al. [47] 2015
    c. Chen et al. [85] 2015
    d. Kim et al. [74] 2016

    Decorrelation effects are also proved by observing spanwise incoherent response times or a reduction in spanwise coherence for the mid-to-high frequency range.
    a. Lau, Haeri and Kim [86] 2013
    b. Chaitanya et al. [47] 2015
    c. Kim et al. [74] 2016

3. Destructive interference effects of the scattered surface pressure along the span, taking place between peak and root or between root and root. These effects dominate the very high-frequency range before the self-noise of the aerofoil starts to limit a further noise reduction.
    a. Chaitanya et al. [47, 1] 2015/17
    b. Kim et al. [74] 2016
    c. Lyu et al. [87] 2017

    Effects on decorrelation for the mid-frequency range and destructive interference for the high-frequency range are supplemented by observations of significant spanwise phase shifts of the surface pressure response.
    a. Lau, Haeri and Kim [86] 2013
    b. Haeri et al. [84] 2014
    c. Kim et al. [74] 2016
    d. Turner and Kim [82, 83] 2016/17

4. Modification of the acoustic sources by altering the incoming turbulence, leading to an attenuated interaction with the rigid surface and a broadband noise reduction.
    a. Chaitanya et al. [47] 2015
    b. Chen et al. [85] 2015

5. Shift from cut-on to cut-off modes, preventing far-field noise radiation.
    a. Clair et al. [88] 2013
    b. Ayton and Kim [89] 2018

Source Cut-Off

As already mentioned, several numerical studies hint at spanwise differences in terms of the associated correlation coefficient and, in consequence, also the underlying aeroacoustic effects, leading to the observed noise reduction. A more detailed numerical study into these phenomena was carried out by Kim et al. [74], using serrated aerofoils of zero thickness (flat plates). Synthetic turbulence of isotropic character was used, with the turbulent eddies impinging on the solid body at zero AoA. The study aimed at supplementing an experimental study by Narayanan et al. [67], showing a comparable setup. Overall, a good fit between

numerical and experimental results was obtained. Since the root region of the serrations was found to radiate noise most significantly for low frequencies, the noise reduction takes place mainly for the mid- to high-frequency region. Source cut-off is considered to be the most powerful parameter for significant noise reduction in this frequency band. The cut-off defines a strong attenuation of the acoustic sources in the region of the serration shoulder due to the local sweep. As pointed out by Roger and Carazo [90], a swept geometry is less likely to generate ATI noise than straight leading edges. In consequence, the sound sources become less efficient for the shoulders of the leading edge serrations since the main lobes of radiation are altered significantly due to the local sweep.

Decorrelation Effects

Another supplementing effect for noise reduction is enhanced decorrelation of the surface pressure fluctuations along the span, resulting in out-of-phase radiation of the acoustic energy. Lau et al. [86] performed numerical work on a NACA0015 with serrated leading edges. The test samples were subjected to a single-mode turbulent gust of specified longitudinal aerodynamic wavelength, while the surface pressure distribution was analysed by evaluating six transducer points, distributed along the aerofoil span. The noise reduction effect is attributed to spanwise incoherent response times due to stronger phase variations (desynchronised gust response) of the surface pressure fluctuations, a mechanism that is also confirmed by Kim et al. [74], who carried out numerical research for serrated flat plates. The locally dispersing spanwise pressure fluctuations lead to a global reduction of the unsteady forces, as manifested by a reduction in the spanwise coherence (the magnitude increases from tip to root). By means of this underlying mechanism, the generation of horseshoe vortices are expected to produce a highly non-uniform velocity distribution, leading to a strong altering pattern of acoustic sources along the shoulder of the serration, efficiently reducing ATI noise. Another numerical study of a serrated flat plate was carried out by Haeri et al. [84], who applied a more realistic synthetic turbulence for the inflow conditions. This allowed designing the spectral composition of the velocity fluctuations with respect to the longitudinal spectrum of isotropic turbulence according to Von Kármán, covering a broad frequency range instead of identifying a single gust frequency. Because of the observed phase differences of the surface pressure fluctuations for higher frequencies, a vortex deformation mechanism is proposed. This is further supported by a significant reduction in the spanwise coefficients of the two-point correlation for the pressure signal when serrations are implemented as it is also shown by Kim et al. [74] in Figure 3-3 (left). The continuous decrease is observed from the peak in the spanwise direction until a maximum decorrelation is reached at the serration root (spanwise distance $1/2 \cdot \lambda$). Subsequently, a steady increase in correlation coefficients follows, approaching the coefficients of the baseline when two adjacent serration peaks are correlated (spanwise distance 1λ). The mechanism proposed by Haeri et al. [84] is consistent with the experimental findings by Narayanan et al. [67, 91], who suggested comparable mechanisms of noise reduction for flat plates and real aerofoils. The reduction in spanwise correlation coefficients was also confirmed by Chen et al. [85], who performed LES simulations in conjunction with the FW-H aeroacoustic analogy, using a rod located upstream of a serrated NACA0012. Numerically, a 2.4 dB noise reduction was obtained at the vortex shedding frequency of the rod, which was further improved to a 10 dB difference for higher frequencies. A reduction in the RMS surface pressure fluctuations was observed, leading to a reduction in ATI noise according to Amiet's theory. More specifically, the reduction took place mainly at the shoulders and the peak of the serration, whereas a slight increase in strength was observed for the root region.

Destructive Interference Effects

Two periodic signals can show interference effects, depending on their phase relation. If the signals are in phase ($\Delta\phi = 0, 2\pi, 4\pi, \ldots$), constructive interference occurs, amplifying the resulting signal. Conversely, if the signals are inversely phased, destructive interference occurs, which might even lead to an extinction of the signal if the signal amplitudes are of the same value. The required condition can be stated as $\Delta\phi = \pi$ and its odd multiples.

The hypothesised phase variations along the shoulders of the serrations, leading to desynchronised response times of the surface pressure fluctuations, are further supported by substantial experimental work by Chaitanya et al. [47]. These resulting reductions in correlation coefficients are considered to be the main noise reduction mechanisms for low to mid frequencies. For high frequencies, on the other hand, destructive interference effects between the tip and the root of the serration are the more prominent mechanisms. These destructive interference effects match the findings of Kim et al. [74], who observed that the main remaining noise sources of serrated leading edges are located at the roots of the serrations for low frequencies and at the root and the peak for higher frequencies. More specifically, for efficient destructive interference effects, two conditions are required: a significant phase shift and comparable source strengths for the signals that interact with each other. For the peak and the root sources, the latter condition is fulfilled for the higher frequency range, whereas the first condition is solely a function of the serration amplitude. Thus, a higher noise reduction is achieved for phase differences approaching $\Delta\phi \rightarrow \pi$.

This matches the outcome of the study by Kim et al. [74], showing that the correlation of the near-field (surface pressure) signals with the far-field noise had a much stronger correlation for the root than for the peak region. This is proposed to be due to the different spectral compositions of the peak and the root surface pressure fluctuations, with more low-frequency fluctuations at the root and more high-frequency components at the peak. Additional analysis of spectral phase interference clearly showed phase interferences for the serrated leading edges over the entire frequency range, with a qualitatively good match between the near-field and the far-field. Interestingly, discrete regions, leading to a sharp increase in noise reduction, were observed at conditions for which the phase differences were at their maximum. The effect of destructive interference is also visible when the noise reduction spectra of serrated leading edges are analysed, with the noise reduction increasing continuously from low to high frequencies, at which the more efficient interference effects take place. The effects described above are supported by the experimental results of Chaitanya et al. [47]. Moreover, the prominent contribution of destructive interference effects on the noise reduction for higher frequencies can also be confirmed by the mathematical model defined by Lyu et al. [87], showing close agreement with experimental data. Here, at a given minimum serration amplitude, a well-correlated scattered surface pressure leads to significant destructive interference effects.

Ayton and Kim [89] derived an analytical approach to describe the ATI noise of serrated flat plates. Since only one acoustic mode is considered to propagate into the far field, the solution obtained is of relatively low complexity and thus allows conclusions to be drawn on the underlying noise reduction mechanism. In their model, a noise reduction of serrated flat plates is assessed both qualitatively and quantitatively, and a good fit to the experimental and numerical data was obtained. The analytical model also allows the extraction of leading-edge noise only, which is hard to obtain in any experimental study. The key parameters were found to be the maximum tip-to-root ratio (serration amplitude) and the streamwise wave number of the incident gust (most effective for high-frequency gust). The noise reduction is attributed to two mechanisms in the far field. First, acoustic interference effects of the scattered pressure field were observed. These effects were found to be of either destructive character for high amplitudes or of constructive character for low amplitudes. Consequently, the latter might lead to a partial increase in noise.

Second, if the serration amplitude was increased, a redistribution of acoustic energy from low cut-on modes to higher cut-off modes was observed, with no far-field radiation for the latter modes. This results in substantial noise reduction, and even if constructive interference takes place, reduced noise is radiated into the far field.

Acoustic Source Strength at the Serration Peak and Root

As pointed out by Haeri et al. [84], approaching vortical structures are deformed by any straight leading edge, where the interaction contributes to surface fluctuations and hence the generation of ATI noise along the full span. However, for the serrations, this deformation is observed only for the peak and the root locations, identifying these regions as the main contributors to the radiated noise. The underlying aerodynamic mechanism of the generation of these remaining noise sources for the root and the peak of the serrations was investigated by Turner and Kim [83]. In summary, they found that emanating horseshoe vortices alter the flow field, leading to an enhancement in the source strength for the root and a reduction for the serration peak. Turner and Kim [82, 83] performed a numerical study of the fully three-dimensional compressible Euler equations by using a flat plate that undergoes a vortical disturbance. The defined disturbance was chosen to be a single Gaussian vortex, covering the full span, but unlike for single-mode gusts or harmonic gusts, a broader frequency band is covered by this approach. This single vortex travels downstream along the serrated leading edge, where the authors tried to identify the correlation between the small-scale flow physics and the resulting wall-pressure fluctuations that are held responsible for the acoustic far-field radiation. Generally, the serration root and peak show no sweep, as is also true for the straight leading edge. Hence, these regions are not likely to reduce the acoustic sources due to their obliqueness. This also matches the findings of Kim et al. [74], showing that the strength at the root was similar to that at the straight leading edge and almost independent of the serration geometry (Figure 3-3). However, against all expectations, a significantly reduced source strength was observed for the peak region.

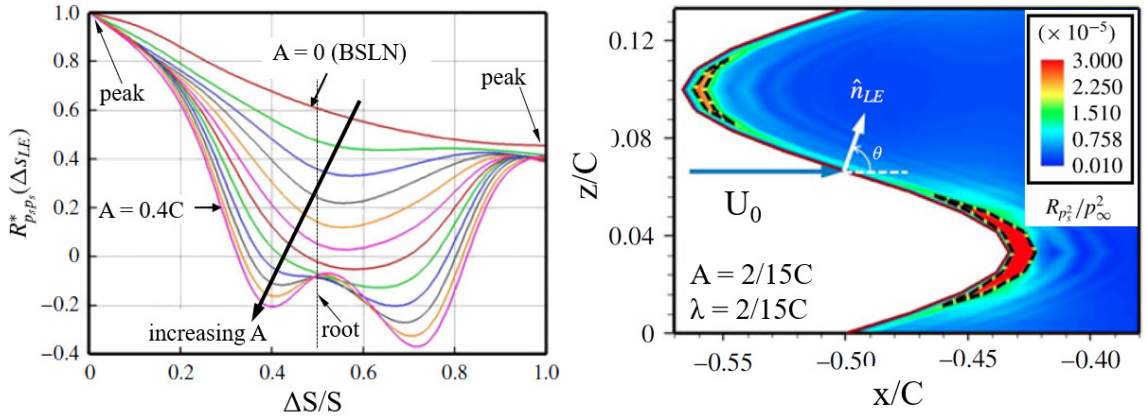

Figure 3-3 Normalised two-point correlation function of the surface pressure fluctuations along a single serration contour (left) for varying serration amplitude A and level of surface pressure fluctuations (right). Figure taken from Kim et al. [74]. Reproduced with permission.

Turner and Kim [83] identified a complex system of horseshoe vortices, which are generated at the serrations and give rise to the different acoustic patterns at the serration peak and root. A simplified illustration of the generation mechanism is reproduced in Figure 3-4. These vortices are generated by the induced downwash velocity ($U_v < 0$) of the approaching vortex, reducing to zero at wall condition ($U_v = 0$). The resulting strong spanwise velocity gradient ($\Delta U_v/\Delta U_x > 0$) induces strong spanwise vorticity (counter-clockwise) and generates a stationary vortex at the serration peak. However, since the spanwise vorticity possesses a non-uniform character for the sinusoidal shape of the leading edge, a streamwise vorticity component is also

produced, leading to the generation of counter-rotating vortices along the serration shoulders. These three vortices are creating the system of horseshoe vortices described earlier. In the time one single gust passes the leading edge, this vortex system is created twice, first due to the upwash motion in front of the approaching gust and then due to the downwash motion behind the gust. In consequence, the spanwise direction of rotation also changes between clockwise and anti-clockwise. Having a closer look at the spanwise distribution of the single vortices, it appears that for each peak there is a counteracting rotation of the vortices, leading to reduced strength of the vertical perturbation. On the other hand, a reverse flow is present for the roots, leading to a reinforced strength of the surface pressure fluctuations. This complex mechanism results in a reduced strength of the velocity perturbation for the serration peaks, whereas the root region experiences a reinforcement. This mechanism is proposed to be responsible for a reduced noise source at the serration peak as well [83].

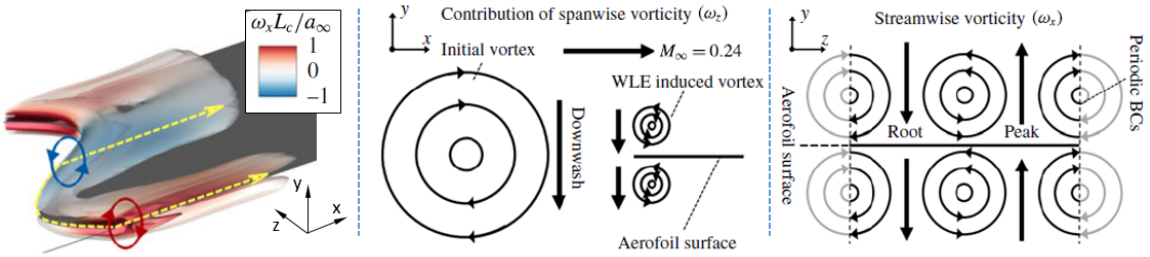

Figure 3-4 Illustration of the vortex pattern of the serrated leading edge investigated numerically by Turner and Kim [83]. Q-Criterion, coloured via the streamwise vorticity $\omega_x L_C/a_\infty$ (left), side-view on vortex mechanism via the spanwise vorticity (centre) and front-view on vortex mechanism via the streamwise vorticity (right). Reproduced with permission.

3.2.2 Spectral Noise Reduction Composition and Scaling Laws

Recent numerical and experimental studies basically agree that aerofoil-turbulence-noise reduction due to serrated leading edges takes place mainly in the mid-to-high frequency range. The upper limit is defined by the dominating nature of aerofoil self-noise. Hence, aerofoils of zero thickness (flat plates) usually show significant noise reduction up to 10 kHz, whereas realistic aerofoils have a lower maximum frequency of about $6 - 8$ kHz [67, 92]. Moreover, the conditions of the incoming turbulence are another limiting parameter. As shown by the experimental results of Clair et al. [88], a spectral noise increase over a wide frequency band of 100 Hz $\leq$ f $\leq$ 10 kHz (up to 20 dB between 300 Hz $\leq$ f $\leq$ 2 kHz) was obtained for a NACA65 due to ATI noise. This range, at the same time, represents the frequency band at which leading edge serrations might effectively reduce ATI noise. Especially for numerical studies in which harmonic or single-mode gusts were used as the inflow conditions, this possible effective frequency range appears to be highly affected. On the other hand, in the range of the lower-frequency limit (f = 100 Hz), many experimental studies are contaminated by external noise sources of the free jet or by the self-noise of the turbulent grids used, consequently showing a certain variety between 100 - 500 Hz. An experimental variation in the serration amplitude and wavelength for flat plates was carried out by Narayanan et al. [67] and, of a more preliminary character, in [91]. Moreover, selected cases were also tested for more realistic NACA65 aerofoils. Based on experimental results, the authors defined a minimum frequency above which significant noise reduction ($>$ 3 dB) takes place for the investigated aerofoil, also showing a good fit to external experimental data, such as those from Clair et al. [88]. This lower-frequency limit (*Eq. 3-1*) is based on the serration amplitude A, leading to lower initial frequencies for the highest amplitudes. In other words, the lower limit of noise reduction is reached as soon as at least half of the transversal turbulent length scale Λ_t of the incoming eddies fits into the serration amplitude.

$$f_{min} = \frac{0.5 \cdot U_0}{A} = \frac{U_0}{\Lambda_t} \qquad \textit{Eq. 3-1}$$

The spectral noise reduction continuously increases from low to high frequencies. The maximum is reached at the point of intersection, at which aerofoil self-noise due to the turbulent boundary layer starts to become increasingly dominant, forcing a decreasing performance for frequencies beyond this point. A more recent study by Chaitanya et al. [1] extends the work by Kim et al. [74]. This new study confirms the general mechanisms, but more detailed work is done as well. Here, a simple single-gust model is derived, resulting in a scaling of the spectral noise reduction, with the source strengths assumed to be uniform. The spectral noise reduction is stated to scale according to *Eq. 3-2*, with the prefactor generally being $a_S = 10$. The upper limit of the possible noise reduction can be achieved at $b_S = 10$ at an optimum wavelength and takes place in the low-to-intermediate frequency range, in which leading-edge noise is dominant. It is based on an amplitude-based Strouhal number Sr_A (*Eq. 3-3),* suggesting that the ratio of amplitude to aerodynamic wavelength of the gust A/λ_A, rather than the inclination angle θ_{Serr}, plays the more important role in terms of maximum noise reduction. Schematic spectra of a straight and a serrated leading edge under highly turbulent inflow conditions are presented in Figure 3-5 (left), whereas the resulting spectral noise reduction in terms of the sound power level (PWL) according to *Eq. 3-2* is shown in Figure 3-5 (right).

$$\Delta PWL = PWL_{BSLN} - PWL_{Serr} = a_S \cdot lg(Sr_A) + b_S \qquad \textit{Eq. 3-2}$$

$$Sr_A = \frac{f \cdot A}{U_0} \qquad \textit{Eq. 3-3}$$

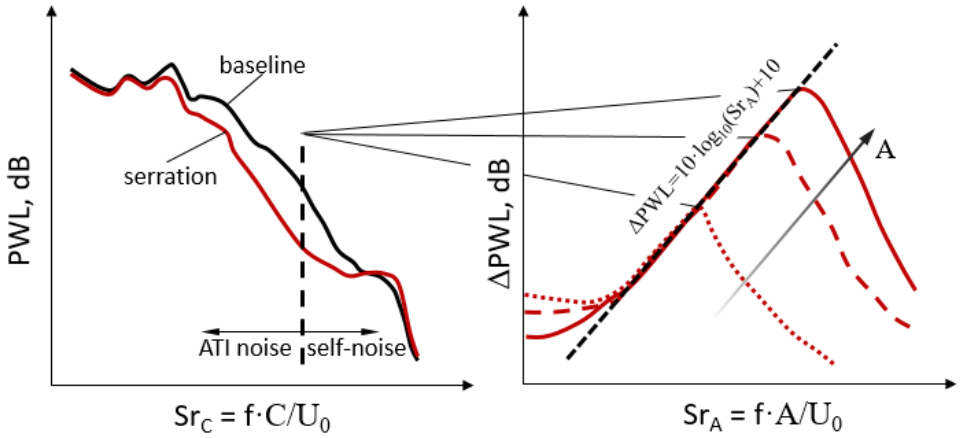

Figure 3-5 Schematic spectra of baseline and serrated aerofoil (left), scaled by aerofoil chord C, and spectral noise reduction of serrations (right) with varying serration amplitudes A.

Note that the distance-independent sound power level (*Eq. 3-4*) is composed of the sound pressure level (SPL) and the enveloping surface A_E, describing the covered hemispherical or spherical surface around the acoustic source at a given distance. Moreover, by incorporating the air density ρ and the speed of sound c, the ambient conditions in terms of the atmospheric pressure and the temperature are compensated as well.

$$PWL = SPL + \left[10lg\left(\frac{A_E}{A_0}\right) - 10lg\left(\frac{\rho c}{\rho_0 c_0}\right)\right] \begin{cases} \rho_0 c_0 = 400\ Nsm^{-3} \\ A_0 = 1m^2 \end{cases} \qquad \textit{Eq. 3-4}$$

$$\mathrm{SPL} = 10 \cdot log_{10}\left(\frac{p_{RMS}^2}{p_0^2}\right), p_0 = 2 \cdot 10^{-5}\ Pa \qquad \textit{Eq. 3-5}$$

The sound pressure level SPL itself (*Eq. 3-5*) represents the logarithmic relationship between the RMS-pressure fluctuation and the human hearing threshold $p_0 = 2{\cdot}10^{-5}$ Pa at f = 1 kHz. The overall sound pressure level (OASPL), as well as the overall sound power level (OAPWL), describes the resulting level after summing (discrete value integration) the local SPL (PWL) for the considered frequency band (*Eq. 3-6* - *Eq. 3-7*).

$$OASPL = 10 \cdot log_{10}\left(\sum_{i=f_{min}}^{i=f_{max}} p_i^2 \Big/ p_0^2\right) \qquad \textit{Eq. 3-6}$$

$$OAPWL = OASPL + 10 \cdot log_{10}\left(\frac{A_E}{A_0}\right), A_0 = 1m^2 \qquad \textit{Eq. 3-7}$$

Influence of Free-Stream Velocity, Reynolds Number and Mach Number

With regard to different free-stream velocities, the overall noise reductions were observed to collapse, but for small differences, for serrations of identical geometry [1]. Hence, a close relation to a spectral scaling with the Strouhal number according to *Eq. 3-3* can be expected, with the serration amplitude turning out to be a useful normalisation parameter. This observation matches results by Clair et al. [88], who identified significant lower frequencies (f_{min} = 300 Hz at 20 ms^{-1}) for noise reduction at low free-stream velocities compared to higher velocities (f_{min} = 1.5 kHz at 60 ms^{-1}). Moreover, the overall level was also found to be inversely proportional to the jet speed, showing a slightly higher noise reduction for minimum speed, as is also confirmed by [67, 93, 92]. Following a more detailed approach, Narayanan et al. [67] performed blow-down experiments by continuously varying the wind tunnel speed. An identical spectral composition of the noise reduction for different flow speeds was found when the noise reduction is scaled via the Strouhal number. This could be confirmed for flat plate and realistic aerofoils alike. The experimental study by Chong et al. [27] revealed a velocity-dependent spectral scaling (500 Hz ≤ f ≤ 4 kHz) of the ATI noise reduction, with a power of $U_0^{1.1}$ in a range of 20 $ms^{-1} \leq U_0 \leq$ 40 ms^{-1} and a power of $U_0^{0.4}$ for 40 $ms^{-1} \leq U_0 \leq$ 60 ms^{-1}.

Roger et al. [94] developed an analytical model for the noise reduction of serrated leading edges that is based on Amiet's [65] flat-plate theory. Although of preliminary character since no thickness and no three-dimensional effects were considered, the supercritical or subcritical character of impinging turbulence was identified as the main parameter for the acoustic radiation. The threshold of the critical inclination angle at which a gust turns subcritical is proposed to be influenced by the Mach number, hence playing a key role in the effectiveness of the serrations. However, experimental verifications took place only at low Ma numbers, preventing further evidence.

Flat Plates vs. Real Aerofoils

For simplicity, many of the presented studies on serrated leading edges focussed on flat-plate aerofoils (or zero thickness aerofoils for analytical approaches). However, serrated leading edges are eventually intended for applications at inlet guide vanes, stator vanes in turbomachinery or at the blades of rotating machines, where real, three-dimensional aerofoil profiles exist, differing significantly from the studied flat-plate designs. This leads to the question of whether the observed noise reduction mechanisms are transferable to these more complex shapes.

An experimental study carried out by Narayanan et al. [67] included a direct comparison between a flat-plate aerofoil and a NACA65 high-lift aerofoil for serrated leading edges. The essential physics of the spectral noise reduction was found to be maintained, even though the real aerofoils were found to be significantly less effective. Both cases showed a significant noise reduction in a frequency band of 500 Hz $\leq$ f $\leq$ 8 kHz, with a maximum overall reduction of 9 dB for the flat plates, whereas only 7 dB for the real aerofoil could be confirmed. The reduced noise reduction performance of three-dimensional aerofoils can be attributed to the more dominant nature of the generated self-noise in the form of high-frequency broadband noise. This is due to the higher adverse pressure gradients compared to the flat plates and hence a more energetic turbulent boundary layer, leading to a more intense scattering of acoustic pressure [1]. This self-noise represents the natural upper frequency below which noise reduction due to the leading edge serrations are taking place.

By means of a more practical application, Gruber et al. [95] tested NACA65(12)-10 aerofoils in a tandem configuration, in which the trailing edge of the front aerofoil and the leading edge of the rear aerofoil were equipped with serrations. Here, a broadband noise reduction of 5 - 8.5 dB was obtained, attributed mainly to the leading edge serrations of the rear aerofoil. The total noise radiation by the two aerofoils was found to be clearly dominated by interaction leading-edge noise of the rear aerofoil, with the trailing edge dominating the high-frequency part. This provides some confidence that the main acoustic effects of serrated leading edges are not masked by the self-noise of three-dimensional aerofoils. However, this is valid only for configurations dominated by leading-edge noise and with a turbulent boundary layer, in which the self-noise does not contain tonal components due to, for example, an aeroacoustic laminar feedback loop. Interestingly, PIV measurements by Chaitanya et al. [47] revealed that under given circumstances, the leading edge serrations are also able to influence the aerofoil self-noise by increasing the thickness of the boundary layer, resulting in less high-frequency noise radiation.

Another reason for the reduced noise reduction capability of realistic aerofoils compared to flat-plate aerofoils is directly linked to thickness effects of the leading edge. As pointed out by Narayanan et al. [67], the high leading-edge radius of thick aerofoils shows a stronger attenuating upstream effect on the approaching turbulent eddies, leading to less ATI noise radiation than for low-thickness aerofoils. Lau et al. [86] performed numerical work on a NACA0015 with serrated leading edges, with the test samples subjected to a single-mode turbulent gust of specified longitudinal wavelength. Amongst other parameters, they varied the aerofoil thickness from 5% C – 20% C according to the NACA0005, 0010, 0015 and NACA0020 profiles. Remarkable thickness-dependent changes in the noise directivity patterns were observed, with more upstream noise radiated for the thick aerofoils. The pattern of the noise reduction due to serrated leading edges, on the other hand, shows no significant differences in magnitude or directivity at a fixed ratio of serration amplitude to length of the incident gust. This continuity of directivity is confirmed experimentally by Polacsek et al. [92] for a NACA65(12)-10 aerofoil, showing no differences in directivity between serrated and straight leading edges.

3.2.3 Influence of the Design Parameters of Leading Edge Serrations

Apart from the underlying mechanisms of the noise reduction due to serrated leading edges, several researchers performed detailed investigations into the effect of the serration parameters on the specific aeroacoustic mechanisms. Table 3-1 briefly summarises these studies, in which, interestingly, the focus is either on the analysis of flat plates or on the NACA65(12)-10 aerofoil. Flat plates significantly reduce the complexity for analytical and numerical approaches, whereas the specific NACA profile, also chosen for the current thesis, is motivated by the beneficial aerodynamic features as well as the initial EU-funded FLOCON and BROBAND studies, acting as a trigger for subsequent studies.

Generally, most of the studies summarised in Table 3-1 agree on the need for large serration amplitudes A and small serration wavelengths λ for obtaining maximum decorrelation effects along the serration shoulder and on significant interference effects between the peak and the root regions of the serrations. The serration amplitude, though, usually represents the dominant parameter compared to the serration wavelength.

Table 3-1 Summary of studies on the aeroacoustic influence of the parameters of leading edge serrations. n/i = not investigated.

Author	Ref	Year	Aerofoil	Maximum			Focus		
				Decorrelation Effects	Destructive Interference	ΔPWL, ΔSPL	Analytical	Experimental	Numerical
Narayanan et al.	[67, 91]	2014 2015	flat plate	A↑	n/i	log(A↑)		x	
Chaitanya et al.	[1]	2017	NACA65(12)-10	θ_{Serr}↑	$\lambda/\Lambda_t = 4$	λ↓, A↑,		x	
Chong et al.	[27]	2015	NACA65(12)-10	n/i	n/i	λ↓, A↑,		x	
Haeri et al.	[84]	2014	flat plates	A↑	n/i	n/i			x
Ayton and Kim	[89]	2018	flat plate	n/i	n/i	A = C/3.5	x		
Turner and Kim	[82, 83]	2016 2017	flat plate	n/i	n/i	A < C/7.5			x
Lau et al.	[86]	2013	flat plate	A↑	n/i	A/Λ_t= 0.3-1 λ/Λ_t = 1-1.5			x
Kim et al.	[74]	2016	flat plate	A↑, θ_{Serr}↑	cos(ϕ)=-1	A↑			x
Chaitanya et al.	[37]	2015	NACA65(12)-10	A↑, λ/Λ_t = 2	n/i	A↑, λ/Λ_t = 2			
Chen et al.	[96]	2016	NACA0012	n/i	n/i	A↑, λ↓,		x	x
Lyu et al.	[87]	2017	flat plate	n/i	$\omega \cdot A/U_0 >> 2$	λ↓, A↑,	x		
Polacsek et al.	[92]	2011	NACA65(12)-10	A↑, λ/Λ_t = 2	n/i	A↑, λ/Λ_t = 2		x	x

On the other hand, according to Chaitanya et al. [1], the serration wavelength represents the key parameter for obtaining a coherent excitation of only one half of the serration contour (one tip, shoulder and root). This condition is fulfilled if the serration wavelength equals half of the size of the incoming turbulent structure ($\lambda/\Lambda_t = 2$). Considering maximum interference effects

between the serration peak and root, however, results in a ratio of $\lambda/\Lambda_t = 4$, opposing the previously mentioned ratio for maximum decorrelation [1]. In terms of the maximum noise reduction with regard to the serration amplitude, several researchers report a saturation beyond a certain threshold [67, 91, 89, 82], making it necessary to consider the cost-value ratio by means of aerodynamic penalties for high serration amplitudes.

3.2.4 Angle of Attack

The performance of serrated leading edges at higher angles, even at stall conditions, is considered to be an important issue. This is the case particularly when this technique is implemented in, for example, fans and blowers or even multi-stage compressors, in which the incidence angles can vary significantly. However, several of the available studies on the aeroacoustic effect of leading edge serrations took into account a variation in the angle of attack, but only to a limited extent [27, 47, 88]. This is especially true for experimental studies in the commonly used open free jet of limited dimensions. For these studies the investigated effective range of AoA is rather small, since the geometric angle of attack requires a correction to account for the deflection and curvature of the flow due to the aerofoil [97]. Moreover, there is limited knowledge on the influence of high angles of attack on the noise reduction capability of leading edge serrations. The numerical work by Lau et al. [86] considered angles of attack $0 \text{ deg} \leq \text{AoA} \leq 3 \text{ deg}$ for a symmetric NACA0015 with serrated leading edges. They observed no changes in the directivity of radiated noise or the reduction capability of serrations, although the total noise radiation increases for higher angles. Moreover, Polacsek [92] identified a slightly attenuated noise reduction capability with increasing AoA from 0 deg to 15 deg, confirmed by Clair et al. [88], who reported an influence of the AoA, with the maximum noise reduction ΔSPL for serrations obtained at zero degrees. However, it is questionable to evaluate and compare the absolute noise reduction capability for different angles of attack on the dB scale, since the reference value $\bar{p}_{Serr}$ is not constant (*Eq. 3-8*), giving rise to masking effects of the physical dependencies. The observed attenuation in noise reduction for high AoA matches the results of Myers and Kerschen [98], who analytically showed that the ATI noise of a flat plate increases quadratically for $0 \text{ deg} \leq \text{AoA} \leq 10 \text{ deg}$ at $\text{Ma} = 0.75$. In consequence, for a higher SPL level of the straight leading-edge reference cases at high AoA, the reduction in acoustic pressure must be significantly higher in order to obtain the same noise reduction on the dB-scale for lower absolute levels (low AoA).

$$\Delta SPL = SPL_{BSLN} - SPL_{Serr} = 20 \cdot log\left(\frac{\bar{p}_{BSLN}}{\bar{p}_{Serr}}\right) \qquad \textit{Eq. 3-8}$$

A first study focussing explicitly on the acoustic effects of leading edge serrations of aerofoils near stall conditions was published recently by Lacagnina et al. [99]. In this fundamental study, NACA65 aerofoils were tested experimentally with effective angles of attack of up to 23 deg. The study focussed on a detailed description of the stall effect and on a correlation analysis between near-field wall-pressure fluctuations and the radiated far-field noise. Implementing leading edge serrations revealed a significant low-frequency noise reduction of up to $\Delta\text{PWL} = 7 \text{ dB}$ for $200 \text{ Hz} \leq \text{f} \leq 700 \text{ Hz}$ at AoA at which relevant separation appeared. Maximum noise reduction effects were observed for high serration amplitudes and small serration wavelengths, which matches the general trend of reducing ATI noise at low angles of incidence. However, one downside is a remarkable noise increase for frequencies above the dominant aerodynamic frequency of the separated structures, hence leading to a reduced spectral upper threshold for higher AoA. The effect of noise reduction for the lower frequencies persists until $\text{AoA} = 17 \text{ deg}$ for selected configurations but, in general, tends to decrease with

the level of incidence since the separated flow becomes larger and of lower frequency. The effect of the leading edge serrations on the separated flow structures near stall is confirmed by the coherence spectra, showing a shift of the coherent noise sources towards lower frequencies when the serrations are implemented. Moreover, low-frequency noise (20 – 30 Hz) due to shear layer flapping of the straight leading edges is eliminated completely, showing the stabilising effect of serrations. Presumably, the reason for the frequency shift is that the separated eddies, which are usually located closely above the aerofoil surface, are migrating outwards for the serrated cases. Even though this was partly validated by hot-wire measurements, another explanation could be an efficient elimination of the coherent sources while simultaneously streamwise vortices of lower frequencies are induced, generated by the serration contour itself, as described by several researchers [38, 39, 23, 25, 18, 28].

3.2.5 Serrated Leading Edges for Trailing-Edge Noise Reduction

Apart from the serrations' ability to efficiently reduce aerofoil-turbulence-interaction noise at highly turbulent inflow conditions, the serrations can also be used to reduce tonal noise close to the trailing edge (TE), radiated due to an aeroacoustic laminar feedback loop. In general, the underlying reduction mechanisms are well understood and were investigated by, for example, Hansen et al. [24], Chong et al. [27] and Chen et al. [96], suggesting high amplitudes and low wavelengths for efficient reduction. In accordance with this, the generation of streamwise vortices was suggested to affect the generation of the downstream boundary layer, triggering a bypass transition and, in consequence, suppressing tonal noise generation, leading to a local noise reduction of up to 30 dB. The research by Hersh, Soderman and Hayden [100] builds a bridge between the tonal and the broadband noise reduction. Here, leading edge serrations were analysed for the reduction of vortex shedding noise (low Reynolds number) associated with stationary and rotating aerofoils, where a significant noise reduction of 4 – 8 dB was achieved. The noise generation took place by periodic fluctuating forces close to the trailing edges, which are generating tonal noise. This noise disappears at stall conditions since the vortex shedding becomes broadband. The serrations, however, are able to eliminate these tones by generating chordwise trailing vortices on the suction side, forcing a transition to turbulent and changing the wake from periodic to random. Most interestingly, for high angles of attack the broadband noise is also reduced.

The effect of leading edge serrations on the radiation of aerofoil self-noise was further analysed by Turner and Kim [101]. Their approach was to regard the leading edges (LE) and trailing edges (TE) individually by numerically contrasting semi-infinite and finite chord aerofoils without considering the effects of aerofoil thickness or camber. In summary, implementing the trailing edge into the numerical setup leads to an additional portion of high-frequency noise as a result of a scattering of unsteady surface pressure due to a recently bisected vortex at the TE. Moreover, an increased level of oscillation was observed as a result of phase interferences of LE and TE sources, altering the directivity. The main finding was that even though the trailing-edge components do not dominate the acoustic spectra at highly turbulent inflow conditions, the leading-edge noise reduction might be adversely affected by a disadvantageous combination of trailing-edge noise and a change in the oscillation of the spectra. In consequence, higher noise than for the baseline case might be observed for extreme upstream observer angles when leading edge serrations are implemented. On the other hand, using a cambered NACA65 aerofoil, Chaitanya et al. [47] showed that a marginal reduction in trailing-edge self-noise can be obtained by means of leading edge serrations. This investigation was further elaborated by Lacagnina et al. [102] using a tripped aerofoil to ensure a fully turbulent boundary layer. Especially for small negative angles of attack, a reduction of self-noise was observed in a frequency range of 200 Hz $\leq$ f $\leq$ 10 kHz, with the best performance at

high amplitudes and small wavelengths. Although not fully understood yet, the underlying mechanism is proposed to be closely related to an altering structure of the velocity and turbulence spectrum on the aerofoil's pressure side close to the trailing edge. The serrations supposedly help to break down large vortical structures into smaller ones and thus to reduce noise.

3.2.6 Advanced Serration Designs

Since investigations into the aeroacoustic working mechanisms of leading edge serrations were the focus of many recent studies, the basic effects are well understood by now, offering possibilities of optimising the serration shape based on the conclusions drawn. When it comes to optimisation, one can generally differentiate between modifications of the remaining source mechanisms (splitting roots, adding slits, dual frequencies, etc.), as shown in Figure 3-6, and modifications of the transfer path (destructive interference effects, incoherent spanwise excitation).

Alternative design concepts are proposed by, for example, Chaitanya et al. [103] and Turner et al. [104], who investigated so-called double-wavelength (or dual-frequency) serrations. Slitted and chopped-peak serrations are discussed by Chaitanya et al. [105]. The working principles of this new generation of serrations are similar as they aim at increasing the effect of destructive interference between the single roots of the serrations, where the main remaining noise sources are located (Section 3.2.1). The double-wavelength design was found to be the most effective one and is therefore presented as an example. The basic idea of this serration design is to further weaken the remaining noise source at the serration root by generating additional sources of similar strength (similar serration amplitudes) with a specified streamwise displacement to obtain destructive interference effects.

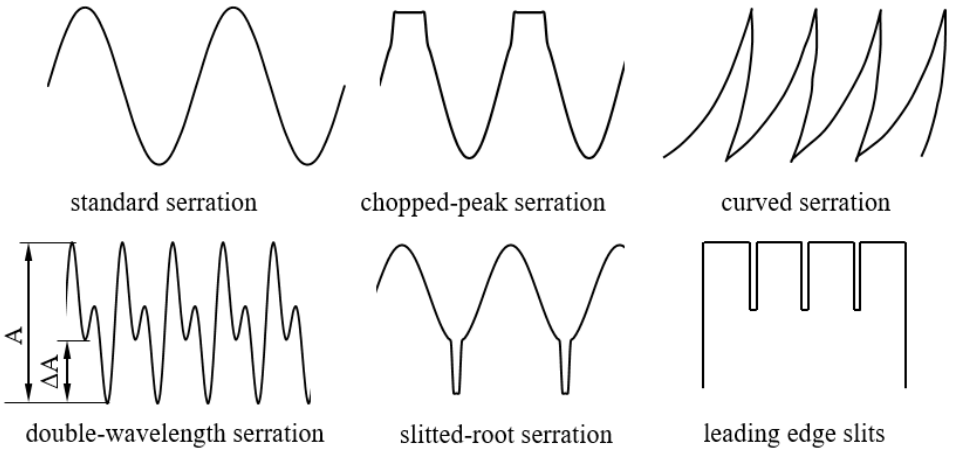

Figure 3-6 Different types of leading edge serrations.

For the previously discussed single-wavelength serrations, the dominant mechanisms are decorrelation effects at low frequencies and destructive interference effects at high frequencies. For the new design, the latter effects are shifted towards the lower frequencies, enhancing the noise reduction performance. The streamwise displacement of two adjacent roots causes an adjustable phase shift of the response time, being only a function of the amplitude. The time delay caused by the convective velocity of the eddies for travelling from one serration root to the other results in maximum destructive interference for the design frequency ω_0. In summary, given a double-wavelength serration with a streamwise distance between the roots of ΔA (Figure 3-6 bottom-left), the corresponding frequency for maximum destructive interference at

a phase shift of $\Delta\phi = \pi$ is described by *Eq. 3-9*, where the convective velocity U_{conv} of the travelling turbulent structures needs to be taken into account.

$$\omega_0 = \frac{\pi \cdot U_{conv}}{\Delta A} \qquad \textit{Eq. 3-9}$$

Here, maximum destructive interference effects take place with decreasing reduction for frequencies with phase shifts from $\Delta\phi = \pi$ to $\phi = 0$ or $\phi = 2\pi$. For practical applications, however, the effective frequency band is narrower, since aerofoil self-noise starts to become more dominant. The same holds true for odd harmonics of the design frequency if sufficient coherence of the noise sources can be maintained for higher frequencies. In consequence, the absolute frequency range increases with the convective vortex velocity U_{conv}.

One of the main benefits is that the double-wavelength approach adds the destructive interference effect for low-to-mid frequencies while maintaining effective cut-off effects along the serrated span, as described by Kim et al. [74]. Hence, the new approach can even outperform the initially defined scaling law of the noise reduction, as stated per *Eq. 3-2*. However, the previously described noise reduction effects suffer small penalties since for the advanced design, smaller wavelengths ($\lambda/\Lambda_t = 4$) than the initially defined wavelength for optimum decorrelation ($\lambda/\Lambda_t = 2$) are required.

The experimental study on double-wavelength serrations is complemented by Turner et al. [104], who performed high fidelity numerical analysis using an approaching single Gaussian vortex on a flat-plate aerofoil. Basically, the main finding by Chaitanya et al. [103] was confirmed, with the observed phase shift between adjacent roots found to be in the range $\Delta\phi = \pi \pm 3$ deg for maximum noise reduction. The authors found that the source strength characteristics of this novel serration design are similar to those of single serrations of high wavelength for low frequencies and to those of serrations of low wavelength for higher frequencies. However, extending this effect of destructive interference towards the maximum possible noise reduction leads, instead of serrations, to 'simple' slits (Figure 3-6 bottom-right). At a given optimum slit width, coherent sources of comparable strength are generated at both ends of these slits, leading to a noise reduction of up to 18 dB for the low-frequency region [106–108].

Another design approach is pursued by Juknevicius et al. [109], who tested straight and curved serrations (Figure 3-6 top-right; additional parameters of inclination angle and curvature radius) of the add-on type for thin aerofoils with the purpose of reducing leading edge noise. The idea is to increase the effective serration amplitude without increasing the chordwise extension of the serrations. This approach is in line with conclusions drawn by Ayton and Kim [89] or Haeri et al. [84], who found that large serration amplitudes are efficient in terms of noise reduction but also affect the aerodynamic performance by significant margins. Moreover, additional shielding effects of the curved serrations are expected, yielding an even more effective noise reduction. This is meaningful because according to Kim et al. [74], the remaining main noise sources are located at the roots of the serrations. The curved serrations were found to provide an additional 5 dB broadband noise reduction to the 9 dB reduction of the straight serrated flat-plate aerofoils tested. Since this is ongoing research, there is no evidence yet that the observed improved noise reduction is caused by the spanwise displacement of the serration roots, preventing interaction with the turbulent structures.

Apart from testing leading-edge blowing as an aerodynamic substitute for leading edge serrations (Section 2.1.1), additional aeroacoustic testing was carried out by Al-Okbi et al. [31]. The small blowing jets were found to outperform the corresponding serrations at low frequencies but also to induce significant high-frequency self-noise.

The efficient low-frequency noise reduction effect might be explained in terms of more stable and controllable flow conditions of the blowing. In principle, the synthetically generated streamwise vortices are expected to oppose and dissipate the incoming coherent structures and, in addition, to generate a buffer zone before these structures impinge on the leading edge.

3.2.7 Summary and Transfer Analysis

As is reported in the previous Sections 3.2.1 - 3.2.7, great efforts were made to understand the aeroacoustic noise reduction mechanisms of serrated leading edges. At a global scale, the underlying principles are well understood by now, although small aspects remain to be confirmed. This is especially the case for the reported vortex formation mechanisms, leading to different surface pressure fluctuations for the tip and the root region of the serrations. Another example is an experimental validation of the noise source distribution along the serration contour, hitherto identified only numerically. Moreover, more research with regard to the relationship between the near-field surface pressure fluctuations and the resulting far-field noise radiation, including the influence of various serration design parameters and varying flow conditions, is needed.

Focussing on the influence of the serration parameters serration amplitude and wavelength, the identified aeroacoustic trends are highly congruent, as opposed to the aerodynamic dependencies discussed in Section 2.1.2. Even though this might partly be due to the limited variety of investigated aerofoil types, the observed trends are considered to be valid for a wide area of applications. For maximum noise reduction, high amplitudes and small wavelengths in a range of $\lambda/\Lambda_t = 2$ (maximum decorrelation) to $\lambda/\Lambda_t = 4$ (maximum interference) are preferred, where Λ_t represents the transversal length scale of the incoming turbulent structure. However, the angle of attack, the Reynolds number and the conditions of the incoming turbulence also play a role in terms of the noise reduction capability.

All the available aeroacoustic studies focussed on a very limited number of parameters, lacking a comprehensive approach that describes the aeroacoustic performance of a serrated aerofoil with respect to all the extracted main influencing parameters. This highlights the need for a combined study on the parameter effects, ideally also taking into account the aerodynamic performance of the serrated leading edges, as done in the form of an aeroacoustic study described in Section 3.3. The scaling laws outlined in Section 3.2.2, however, can be referenced and validated against the array beamforming results described in Section 3.4, allowing an isolated analysis of the leading-edge noise only. Moreover, these beamforming results also allow conclusions to be drawn on the effect of leading edge serrations on the trailing-edge noise, hence challenging the findings in Section 3.2.5.

Eventually, the extracted noise reduction mechanisms will serve as a reference for applying leading edge serrations to the rotating applications introduced in Sections 1 - 7. This includes the overall dependencies on the parameters as well as the spectral composition of the noise reduction due to serrated leading edges. Nevertheless, additional influencing factors, not yet investigated, such as the blade-tip gap or the radius-dependent circumferential velocity of rotating, ducted machines, need to be taken into account for the rotating domain as well.

3.3 Aeroacoustic Study

The serrated aerofoils, analysed aerodynamically in Section 2.2, are further investigated with the aim of describing the aeroacoustic performance, taking into account the main influencing parameters, namely the serration amplitude and serration wavelength, the Reynolds number and the turbulence intensity, as well as the angle of attack. A statistical-empirical model, based on the design of experiments (DoE) approach, is developed, which allows the full experimental space to be described with high accuracy while keeping the experimental effort at

a reasonable level. In a second step, the experimentally obtained aerodynamic results are embedded into the aeroacoustic statistical-empirical model for the same range of angles of attack. This allows to define multi-objective optima for the system considered. Note that Section 3.3 shows re-evaluated and extended content of the published work by Biedermann et al. [110].

3.3.1 Methodology

For the analysis of a defined physical experimental space by varying several influencing parameters, the classical method would be to vary one of the parameters while keeping the others constant. This procedure will then be repeated for each parameter of interest (raster method). This might be an easy and effective method for describing the influence of these parameters on a certain target value with high accuracy. On the other hand, this only holds true as long as the number of parameters is small and the interdependencies between the parameters are disregarded.

Increasing the number of parameters inevitably leads to an exponential rise in the number of necessary measurement trials (MT). According to the n-permutation in *Eq. 3-10*, analysing a system with five parameters (k) and varying the parameters on five levels each (n) results in 3125 measurement trials $MT_{n\text{-}per}$. This represents a hardly manageable experimental volume. Instead, applying the statistical design of experiments (DoE) approach as per *Eq. 3-11* leads to a significant reduction in the experimental volume to 43 trials (circumscribed central composite experimental design, C-CCD) without a significant loss of information on the system's behaviour. A brief description of this methodology, as well as the different possible experimental designs, can be found in the engineering statistical handbook of NIST/SEMATECH [111], as well as in Siebertz et al. [112]. Generally, the DoE approach keeps the experimental volume manageable and facilitates the detailed analysis of multiple parameters with reasonably high accuracy [110].

$$MT_{n-per} = n^k = 3125 \qquad \textit{Eq. 3-10}$$

$$MT_{DoE-CCD} = 2^k + 2 \cdot k + 1 = 43 \qquad \textit{Eq. 3-11}$$

So-called experimental designs are commonly used for obtaining as much information on a system as possible while keeping the experimental effort at a minimum. A design consists of different combinations of factor settings, so-called factor-level combinations. However, the available approaches to sampling the (experimental) space of interest, which is defined by the maximum and minimum values of the parameters, show a large variety and must be defined prior to any experimental study.

For this study, a circumscribed central composite design (C-CCD) is used to sample the experimental space (Figure 3-7). The C-CCD consists of a two-level factorial design that samples information equidistantly on the inside of the design space as well as so-called star points that lie at the borders of the design space. The centre points are re-sampled to establish predefined statistical properties, which are orthogonality and rotatability in this case. The relative distance of the star points to the central point is a function of the statistical properties as well. Orthogonality allows a non-commingled estimation of the factor effects in successive modelling, while rotatability allows the assumption that the variance of the predicted response is only a function of distance to the centre point. Consequently, the C-CCD consists of five different settings for each factor, as can be seen in Figure 3-7 [113].

The experimental space is spanned by the influencing parameters (IP) in the range of IP ∈ ($-\alpha_{DoE}$, $+\alpha_{DoE}$), where $\pm\alpha_{DoE}$ represents the non-dimensional minimal and maximal settings of each individual influencing factor.

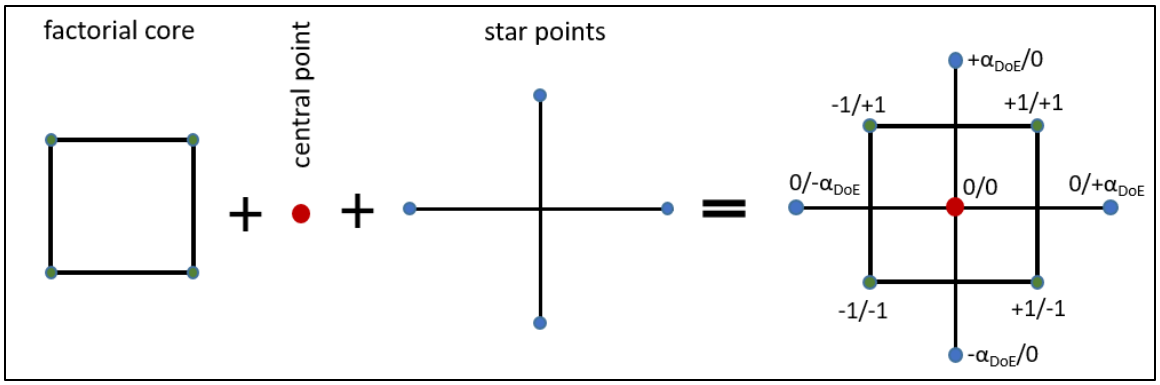

Figure 3-7 Composition of a 2D experimental space (two influencing parameters), based on a circumscribed central composite design (C-CCD). Schematic according to Siebertz et al. [112].

3.3.2 Influencing Parameters

As mentioned previously, a set of five parameters, namely the Reynolds number (Re), the turbulence intensity (Tu), the serration amplitude (A/C) and the serration wavelength (λ/C), normalised by the aerofoil chord, and the angle of attack (AoA) are analysed as influencing parameters. These parameters were chosen based on a literature study and on preliminary investigations, identifying them as the main influencing factors. The transversal integral length scale Λ_t is considered an important influencing factor as well, although this factor is extremely hard to control experimentally. Therefore, this parameter will be monitored as accompanying quantity, but no modelling with regard to Λ_t takes place. The limits of the chosen modelling parameters, as well as their five levels according to the chosen C-CCD design, are listed in Table 3-2.

Table 3-2 Influencing parameters [110] and individual parameter settings in a range of $\pm\alpha_{DoE}$ for the five levels of the experimental design (C-CCD).

	Unit	**$-\alpha_{DoE}$**	**-1_{DoE}**	**0_{DoE}**	**$+1_{DoE}$**	**$+\alpha_{DoE}$**
x_{Nondim}	--	*-2.378*	*-1.0*	*0.0*	*+1.0*	*+2.378*
Re	--	250,000	351,422	425,000	498,578	600,000
Tu	*%*	2.08	3.07	3.79	4.51	5.50
A_{Serr}/C	--	0.080	0.144	0.190	0.236	0.300
λ_{Serr}/C	--	0.050	0.122	0.175	0.228	0.300
AoA	*deg*	-4.0	-1.7	0.0	1.7	4.0

The acoustic experiments took place at the open-jet wind tunnel of the aeroacoustic facility at Brunel University London. The exit nozzle, which has a dimension of 100 × 300 mm, is situated inside a semi-anechoic chamber (4.0 × 5.0 × 3.4 m). It can produce a typical turbulence intensity varying between 0.1 and 0.2 % [27, 114]. The maximum jet velocity is about $U_0 = 80$ ms^{-1}. Especially since the open-jet wind tunnel possesses a nozzle of relatively small dimensions, a change in the geometrical angle of attack of the aerofoils strongly affects the properties of the shear layer, an effect that results in interdependencies with regard to the effective aerofoil angle. Brooks et al. [115] defined the wind tunnel correction (*Eq. 3-12*) as a function of nozzle height H and aerofoil chord C in order to obtain the same pressure distribution over an aerofoil as in unbounded flow for the purpose of a direct comparison. Although the initial study was performed without consideration of the aerofoil camber, the stated relation is valid for small angles of attack, as also shown by Lacagnina et al. [99].

$$\zeta_{AoA} = (1 + 2 \cdot \sigma)^2 + \sqrt{12\sigma} \qquad \textit{Eq. 3-12}$$

$$\sigma = \frac{\pi^2}{48}\left(\frac{C}{H}\right)^2$$

$$\zeta_{AoA} = \frac{AoA_{geom}}{AoA_{eff}} \approx 2.51 \qquad \textit{Eq. 3-13}$$

Based on the defined correction factor, the geometrical angle of attack needs to be varied in a range of -10 deg ≤ AoA ≤ 10 deg for obtaining effective changes of -4 deg ≤ AoA_{Eff} ≤ 4 deg.

Turbulence Intensity

To generate elevated turbulence intensities Tu of the free stream, several turbulence grids are inserted upstream of the aerofoil inside the nozzle of the aeroacoustic wind tunnel. As per the criteria suggested by Laws and Livesey [2], all the turbulence grids are biplane square meshes with a constant ratio between the mesh size and the bar diameter ($H_{Mesh}/d_{Bar} = 5$). Using the turbulence prediction model by Aufderheide et al. [116], which is based on the work of Laws and Livesey [2], five different turbulence grids that were predicted to generate turbulence in the range of Tu = 2.1% and 5.5% were manufactured according to *Eq. 3-14*. The turbulence intensity appears to be a function of the mesh size H_{Mesh}, the loss coefficient of the grid ζ and a factor K to compensate for the wind tunnel contraction downstream. The virtual position x_0 (Figure 3-8) is considered to be in the order of $x_0 = 10 \cdot H_{Mesh}$ to guarantee isotropic turbulence. According to Laws and Livesey, the factor b_{LL} is approximately $b_{LL} \approx 100$ in case of a biplane grid with $H_{Mesh}/d_{Bar} \approx 5$ [2]. The downstream contraction factor K is based on the ratio k_C of grid cross-sectional area A_{Grid} to the area of the wind tunnel measurement plane A_{MP} downstream, being approximately the size of the nozzle exit A_{MP} = 0.1 m x 0.3 m.

$$T_u^{ADH} = 100 \cdot \sqrt{\frac{H_{Mesh} \cdot \zeta}{b_{LL}(x - x_0)}} \cdot K \qquad \textit{Eq. 3-14}$$

$$K = \sqrt{\frac{1}{2k_C}\left(1 + \frac{ln\left(k_C^{3/2}\left(1 + \sqrt{1 - k_C^{-3}}\right)\right)}{k_C^3\sqrt{1 - k_C^{-3}}}\right)}, k_C = \frac{A_{Grid}}{A_{MP}} > 1 \qquad \textit{Eq. 3-15}$$

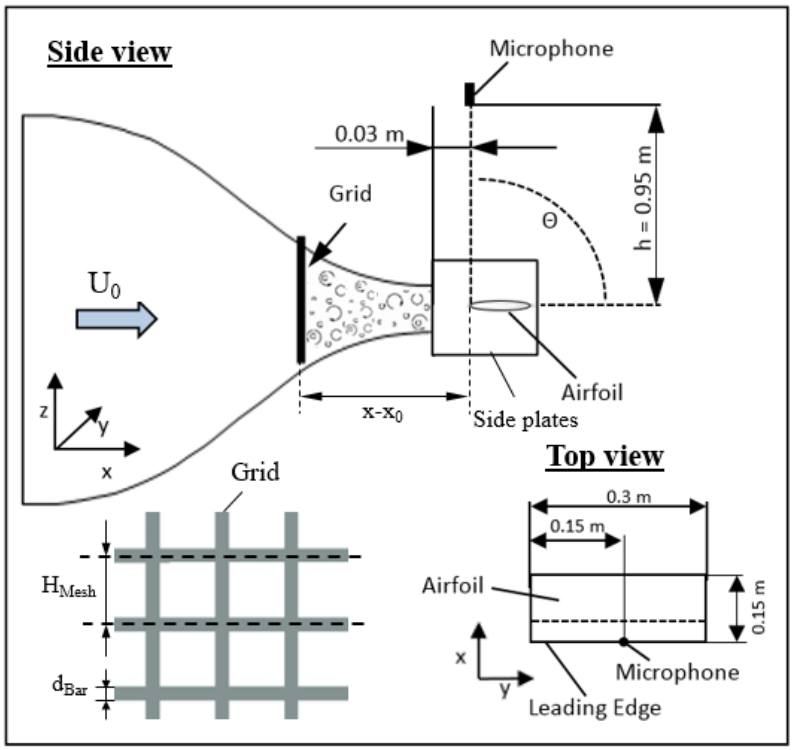

Figure 3-8 Schematic of the experimental setup according to Biedermann et al. [110] as well as turbulence grid nomenclature.

In order to determine the turbulence intensity, a right-angled Dantec Dynamics 55P14 miniature 1D hot-wire probe was placed 30 mm downstream of the nozzle exit, which coincides with the aerofoil leading-edge tip when installed. The turbulence intensity was measured without a mounted aerofoil but with the turbulence grids and side-plates installed. The mean velocity U_0 and the Tu profiles were recorded at 106 locations over the whole nozzle exit area.

For the generated turbulence, isotropic conditions are desired to allow more general conclusions to be drawn about the modelled system. Since only one-dimensional hot-wire measurements were conducted, the measurement results are compared against the longitudinal spectrum of isotropic turbulence, according to Liepmann and Von Kármán. According to Rozenberg [117], the bi-dimensional spectrum of the turbulence $G_{\omega\omega}(K_x,0)$ in *Eq. 3-16* can be written as a product of the power-density spectrum of the vertical velocity fluctuations $G_{\omega\omega}(\omega)$ and the correlation length of the fluctuating velocity $l_y(\omega)$.

$$G_{\omega\omega}(K_x,0) = \frac{U_0}{\pi} \cdot G_{\omega\omega}(\omega) \cdot l_y(\omega) \qquad \textit{Eq. 3-16}$$

The two theoretical models proposed by Von Kármán and Liepmann are the most common models for describing isotropic turbulence. For the current analysis, however, Liepmann's approach in *Eq. 3-17* is applied, with K_X being the streamwise wave number.

$$G^L_{\omega\omega}(\omega) = \frac{\bar{\omega}^2 \Lambda_{\omega\omega}}{2\pi U_0} \cdot \frac{1 + 3K_x^2 \Lambda_{\omega\omega}^2}{(1 + K_x^2 \Lambda_{\omega\omega}^2)^2} \qquad \textit{Eq. 3-17}$$

Limiting the evaluation to the square velocity fluctuation $\overline{\omega}^2$ and the longitudinal integral length scale Λ_L reduces *Eq. 3-17* to the one-dimensional power-density spectrum defined in *Eq. 3-18*, following Rozenberg [117].

$$G_{uu}^{L}(\omega) = \frac{\overline{u'^2}\Lambda_L}{\pi U_0} \cdot \frac{1}{1 + K_x^2 \Lambda_L^2} \cdot G_{Kolm.}, \qquad K_x = \frac{\omega}{U_0} \qquad \textit{Eq. 3-18}$$

The resulting spectra need to be multiplied by a factor of two to obtain a single-sided spectrum. Furthermore, a factor of $2 \cdot \pi$ is applied to convert the frequency to *Hz*. G_{Kolm} is used to compensate for the dilution in the high-frequency region, caused by the Kolmogorov scale, by applying the exponential function given in *Eq. 3-19*. The empirical constant K_η controls the gradient of the roll-off at high frequencies [117, 53] and is related to the Kolmogorov subspace.

$$G_{Kolm.} = exp\left(-\frac{9}{4} \cdot \left(\frac{K_x}{K_\eta}\right)^2\right), \qquad K_\eta \approx 4.3 \cdot 10^3 m^{-1} \qquad \textit{Eq. 3-19}$$

The characteristic region of the generated turbulence is defined as the region in which the power density starts to decrease and the power density scales according to the Kolmogorov spectrum with $f^{-5/3}$. The dependencies of the resulting power density spectrum become clear by non-dimensionalising the spectrum. A reduced frequency is obtained by multiplying the frequency with the integral turbulence length scale Λ_L divided by the mean velocity U_0 (*Eq. 3-20*).

$$Sr_\Lambda = \frac{f \cdot \Lambda_L}{U_0} \qquad \textit{Eq. 3-20}$$

The magnitudes of the power density subside by scaling the mean velocity with a power of 0.5. As is shown in Figure 3-9, the power density spectrum reduces to a single characteristic curve, which is independent of the mean velocity. The measurement results show an excellent fit to the theoretical approach, particularly for the relevant mid-frequency region. As a consequence, the generated turbulence can be assumed to be isotropic, and the complexity of the Tu reduces accordingly from *Eq. 3-21* to *Eq. 3-22* [118].

$$Tu = \sqrt{\frac{\overline{u'_u}^2 + \overline{u'_v}^2 + \overline{u'_w}^2}{3(\overline{u_u}^2 + \overline{u_v}^2 + \overline{u_w}^2)}} = \frac{1}{\sqrt{3}} \cdot \frac{\overline{|u'|}}{\overline{U}} \qquad \textit{Eq. 3-21}$$

$$Tu_{iso} = \frac{\sqrt{\overline{u'_u}^2}}{U_\infty} = \frac{\overline{|u_{u'}|}}{\overline{U}} \quad with\ \overline{u'_u}^2 = \overline{u'_v}^2 = \overline{u'_w}^2 \qquad \textit{Eq. 3-22}$$

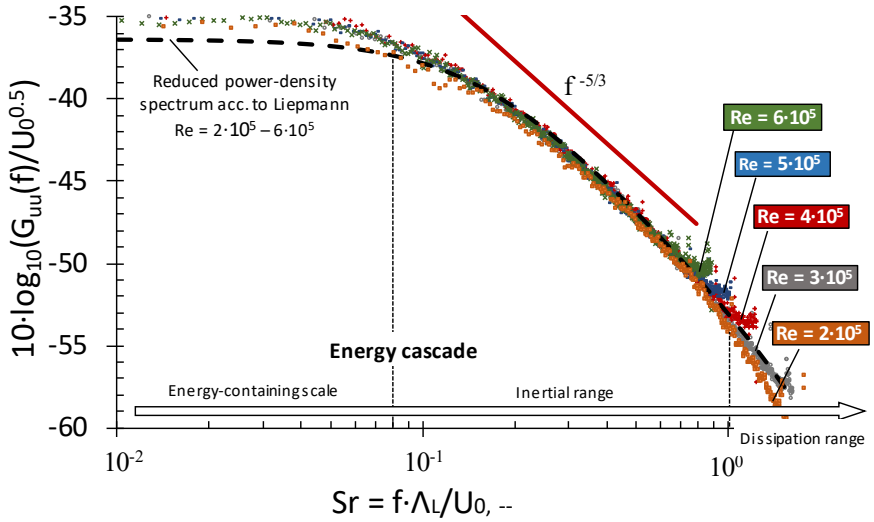

Figure 3-9 Normalised longitudinal turbulent energy spectra for isotropic turbulence according to Liepmann at 200,000 ≤ Re ≤ 600,000 and Tu = 3.9 %. The streamwise location of the measurement coincides with the aerofoil leading edge [110].

3.3.3 Target Values

Prior to the modelling, it is important to first identify meaningful target values for the present study. The target values (TV) can be described by means of all the influencing parameters in the first and second orders, as well as the interdependencies between the influencing parameters IP (*Eq. 3-23* [110]).

$$TV_i = f\left\{\sum_{j=1}^{n}\left(\left(IP_j + IP_j^2\right) + \sum_{k=1}^{n}\left(IP_j \cdot IP_{j+k}\right)\right)\right\} \quad \begin{cases} i = 1..3 \\ j = 1..5 \\ k = 1..4 \end{cases} \qquad \textit{Eq. 3-23}$$

Defining the target values is a crucial part of the evaluation of the experimental data. They are expected to describe the system with the necessary accuracy. This study focusses on the overall sound reduction of a serrated LE compared to a baseline LE and does not predict the sound pressure level (SPL) at a particular frequency. Consequently, the target values of interest are limited to the overall sound pressure levels OASPL (*Eq. 3-24*, *Eq. 3-25*), describing the dependencies of the sound generation for the baseline and the serrations and facilitating the analysis of the influence of each case on the possible noise reduction. It is important to note that single-microphone measurements were performed. Hence, the influences on the acoustic directivity are disregarded. As shown in *Eq. 3-24*, the noise produced by a baseline leading edge (LE) is a function of the Reynolds number, turbulence intensity, and angle of attack. In the case of serrated LE, additional influences of the serration wavelength and serration amplitude must be taken into account (*Eq. 3-25*). Subtracting the $OASPL_{Serr}$ from the $OASPL_{BL}$ results in an overall noise reduction ΔOASPL as stated per *Eq. 3-26*.

$$OASPL_{BSLN}[dB] = 20 \cdot log\left(\frac{\bar{p}_{BSLN}}{p_0}\right) \rightarrow f(Re, Tu, AoA)) \qquad \textit{Eq. 3-24}$$

$$OASPL_{Serr}[dB] = 20 \cdot log\left(\frac{\bar{p}_{Serr}}{p_0}\right) \rightarrow f\left(Re, Tu, \frac{A}{C}, \frac{\lambda}{C}, AoA\right) \qquad \textit{Eq. 3-25}$$

$$\Delta OASPL[dB] = OASPL_{BSLN} - OASPL_{Serr} = 20 \cdot log\left(\frac{\bar{p}_{BSLN}}{\bar{p}_{Serr}}\right) \qquad \textit{Eq. 3-26}$$

An overview of the chosen target values is given in Table 3-3, differentiating between acoustic and aerodynamic quantities. Incorporating the aerodynamic results into the statistical-empirical model is based on two considerations. First, a possible influence of the Reynolds number on the covered linear regime of -4 deg ≤ AoA ≤ 4 deg is neglected for the coefficients of lift and drag. This is considered appropriate since these coefficients are normalised by the free-stream velocity, as is also validated by a comparison at Re = 150,000 and Re = 250,000 (Section 2.2.3). Second, the aerodynamic influence of the turbulence intensity is disregarded since serrations are well-known for forcing an early transition of the boundary layer; hence, the turbulence intensity is not expected to cause differences in lift and drag. This was also validated numerically for example cases. In summary, the aerodynamic target values are solely a function of the angle of attack and the serration parameters A/C and λ/C. The stated differences in the coefficients of lift and drag are defined according to *Eq. 3-27* and *Eq. 3-28*.

$$\Delta C_L = C_{L,BSLN} - C_{L,Serr} \qquad \textit{Eq. 3-27}$$

$$\Delta C_D = C_{D,BSLN} - C_{D,Serr} \qquad \textit{Eq. 3-28}$$

Table 3-3 Acoustic and aerodynamic target values (TV), independent of each other, but a function of the influencing parameters TV = f(Re, Tu, A/C, λ/C, AoA).

Acoustic	Unit	Aerodynamic	Unit
$OASPL_{BSLN}$	*dB*	$C_{L,\,Serr}$	--
$OASPL_{Serr}$	*dB*	$C_{L,\,BSLN}$	--
$\Delta OASPL$	*dB*	$C_{D,\,Serr}$	--
		$C_{D,\,BSLN}$	--
		ΔC_L	--
		ΔC_D	--

3.3.4 Setup and Preliminaries

Because of the chosen experimental C-CCD design as well as the number of influencing parameters for the design of experiments (DoE) approach, a total of ten different leading edge serrations were investigated (Table 2-3). These include one configuration with a straight leading edge, serving as the baseline case (BSLN). To conduct free-field measurements of the ATI noise (aerofoil-turbulence-interaction noise), the aerofoil was held by side-plates to keep the aerofoil

in place and to maintain a two-dimensional flow profile [27]. Noise measurements in the aeroacoustic wind tunnel were made by a single PCB™ 1/2-inch pre-polarised ICP® condenser microphone at polar angles of $\Theta = 90$ degrees at a vertical distance of h = 0.95 m from the leading edge of the aerofoil at mid-span (Figure 3-8). The acoustic data were recorded at a sampling rate of 40 kHz, with the measurement time set to 20 s. In the spectral analysis, Hamming windows were used for windowing at 50 % overlap by using a block size of 1,024, yielding a frequency resolution of $\Delta f = 43$ Hz and resulting in 1,718 averaged blocks for the generated spectra [110]. To define spectra where the spectral amplitudes are independent of the chosen frequency resolution and as well as of the windowing process, the power spectral density is defined according to *Eq. 3-29* and *Eq. 3-30*. Here Δf represents the chosen frequency resolution and ε a window-specific shape factor. As a consequence, all the power spectral density (PSD) spectra presented in this study have a 1 Hz frequency bandwidth.

$$PSD = 10log_{10}\left(\frac{G_{11}(\omega)}{p_0^2}\right) \qquad \textit{Eq. 3-29}$$

$$G_{11}(\omega) = \frac{p'^2(\omega)}{\varepsilon \cdot \Delta f} \qquad \textit{Eq. 3-30}$$

The frequency range ($f_1 \leq f \leq f_2$) for the analysis of the overall sound pressure level (OASPL) is set to $f_1 = 300$ Hz and $f_2 = 10$ kHz. This value of f_1 was chosen based on the cut-off frequency of the anechoic chamber. The selected value of f_2 excludes possible influences by the aerofoil self-noise from the trailing edge, which is not related to ATI noise.

Since it is known that the OASPL could be very sensitive to the choice of f_1, a careful sensitivity study was performed to examine the change in OASPL and ΔOASPL with regard to the different values of f_1. The sensitivity study demonstrates that both the OASPL and the ΔOASPL are reasonably unaffected for $f_1 \geq 200$ Hz. Therefore, the current choice of $f_1 = 300$ Hz should be able to characterize the ATI noise accurately in the OASPL analysis [110].

The test matrix, defined according to the chosen C-CCD sampling model, consists of 43 samples with individual levels of the five investigated parameters plus 16 repetitions of the central point to be able to determine the statistical spread of the measurement results as well as to maintain statistical properties such as orthogonality and rotatability. The final test matrix is shown in Appendix C.1. It is essential to conduct the measurements in a fully randomized order to exclude systematic measurement errors. Moreover, each sample point is measured twice to improve the reliability of the signals gathered.

The sound pressure level on the logarithmic *dB* scale was explicitly chosen so that the data could be fed into the statistical-empirical model. Although the underlying physical quantity is the sound pressure in *Pa*, the logarithmic scaling of the sound pressure level in *dB* represents a more natural scaling of the acoustic phenomenon. Approximations of the linear or squared sound pressure, instead, would result in strong deviations and only poor approximation for all the lower sound pressure levels since very small differences in sound pressure yield significant changes in the SPL. Hence, the resulting model would involve a weighting in accuracy with a trend towards high OASPL.

3.3.5 Development of the Statistical-Empirical Model

After conducting the experiments, the aeroacoustic statistical-empirical model was developed by using the measurement data gathered to define a linear combination (regression function) of the influencing parameters in linear and quadratic order according to *Eq. 3-23*. Moreover, the linear interdependencies between the single influencing parameters are also incorporated. More specifically, deriving from *Eq. 3-23* the target value of the overall sound pressure level for the serrations $OASPL_{Serr}$ results in *Eq. 3-31*, where f_i^* represents the 21 unknown prefactors, which are defined using the data analysis software Statistica®. The same procedure is applied to the remaining target values, with the detailed functions presented in Appendix C.2.

$$\begin{aligned} OASPL_{Serr} = {} & f_1^* + f_2^* Re + f_3^* Re^2 + f_4^* Tu + f_5^* Tu^2 + f_6^* \frac{A}{C} + \\ & f_7^* \left(\frac{A}{C}\right)^2 + f_8^* \frac{\lambda}{C} + f_9^* \left(\frac{\lambda}{C}\right)^2 + f_{10}^* AoA + f_{11}^* AoA^2 + f_{12}^* Re \cdot Tu + \\ & f_{13}^* Re \cdot \frac{A}{C} + f_{14}^* Re \cdot \frac{\lambda}{C} + f_{15}^* Re \cdot AoA + f_{16}^* Tu \cdot \frac{A}{C} + f_{17}^* Tu \cdot \frac{\lambda}{C} + \\ & f_{18}^* Tu \cdot AoA + f_{19}^* \frac{A}{C} \cdot \frac{\lambda}{C} + f_{20}^* \frac{A}{C} \cdot AoA + f_{21}^* \frac{\lambda}{C} \cdot AoA \end{aligned} \qquad \textit{Eq. 3-31}$$

After validating the quality and the reliability of the regression functions obtained, target values at arbitrary factor combinations within the limits of the analysed experimental space can be predicted.

The fit of the statistical-empirical model with regard to the input data is shown in Figure 3-10. The diagonal line represents a perfect match of observed (measured) vs. predicted data, with the blue dots indicating the samples within the experimental space. As can be seen, these samples are well distributed, covering a wide range of values. For the absolute noise radiation $OASPL_{Serr}$, the data fit is excellent; for the ΔOASPL, the fit is of lower but still reasonable quality. The increased spread of the latter is attributed to accumulative measurement uncertainties for the baseline and the serration measurements, which are interconnected by *Eq. 3-26*.

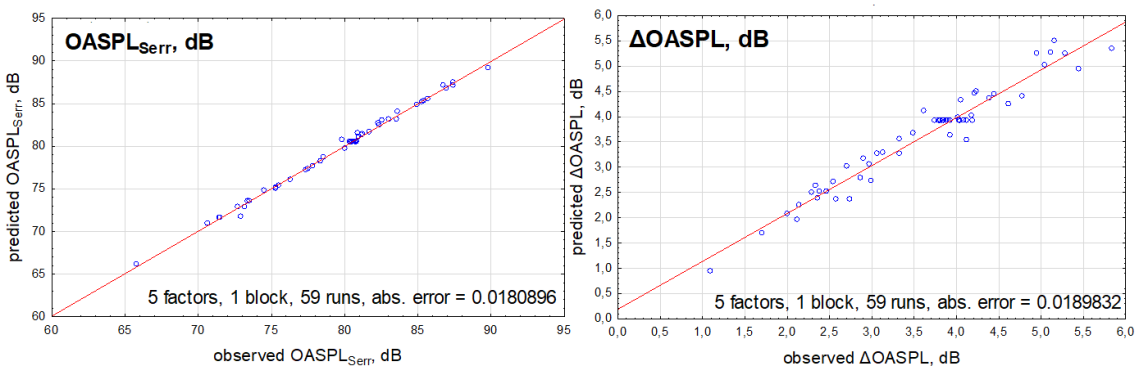

Figure 3-10 Prediction and observation plots for the target values of the serrated overall sound pressure level $OASPL_{Serr}$ (left) as well as the overall noise reduction ΔOASPL (right).

3.3.6 Validation of the Statistical-Empirical Model

The validation process of the model is tripartite. First, validation against independent test data with extreme settings of the parameters within the experimental space is performed. These points are traditionally hard to approximate with high accuracy. Second, validation against an extensive data pool of 192 reference measurements, which stem from a preliminary study by Chong et al. [27], is carried out.

Finally, the third approach aims at extending the statistical-empirical model to include external test data from the aeroacoustics facility of the University of Southampton. Here, apart from different testing parameters, the aerofoil surface, the observer distance and the measurement environment were slightly different. As will be shown, the aeroacoustic statistical-empirical model is highly accurate and, therefore, provides a good tool for optimisation purposes.

The deviations between model and test data, or the lack of fit, can be expressed via the normalised mean absolute error n_{MAE}. This error is defined by the averaged deviations between predicted values $\hat{y}$ and observed values y, based on the predicted mean value as stated per *Eq. 3-32*.

$$n_{MAE} = \frac{MAE}{\frac{1}{n}\sum_{i=1}^{n}\hat{y}_i} \quad with \quad MAE = \frac{1}{n}\sum_{i=1}^{n}|(\hat{y}_i - y_i)| \qquad \textit{Eq. 3-32}$$

1. Statistical-Empirical Model Validation with Extreme values

The statistical-empirical model was tested against 12 independent test samples within the experimental space, with at least one out of the five influencing parameters showing a maximum or minimum level. As can be seen from Figure 3-11, a good overall fit is obtained, although the serrated model shows some significant deviations in terms of the n_{MAE}, particularly resulting from the approximations at minimum wavelength in conjunction with high Tu or high AoA at low Re.

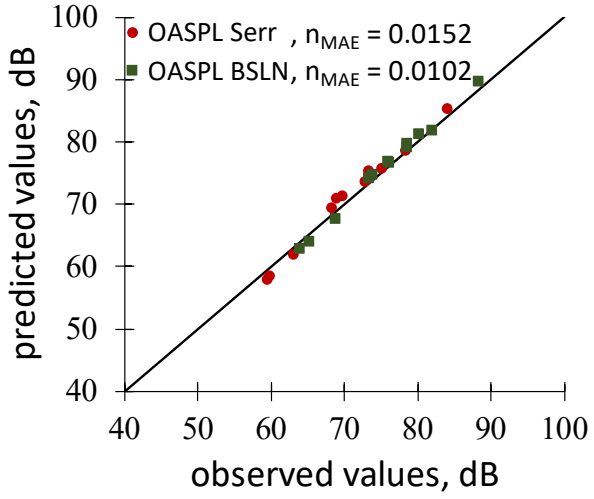

No. --	Re --	Tu %	A/C --	λ/C --	AoA deg
1	500,000	5.5	0.19	0.18	0.0
2	280,000	5.5	0.19	0.18	0.0
3	550,000	2.1	0.19	0.18	0.0
4	260,000	2.1	0.19	0.18	0.0
5	350,000	3.8	0.24	0.23	-3.2
6	320,000	3.8	0.14	0.12	-3.2
7	280,000	4.5	0.14	0.12	3.2
8	310,000	4.5	0.24	0.23	3.2
9	360,000	5.5	0.30	0.18	0.8
10	340,000	5.5	0.19	0.05	0.8
11	270,000	2.1	0.30	0.18	-0.8
12	310,000	2.1	0.19	0.05	-0.8

Figure 3-11 Validation measurements in the outer region of the experimental space. Extreme settings are indicated by the grey background colour.

2. Statistical-Empirical Model Validation with Raster Data by Chong et al. [27]

As mentioned previously, Chong et al. [27] provided a data pool of 192 test samples by continuously varying the Reynolds number, the serration amplitude A/C and the serration wavelength λ/C. The Tu, however, was varied as a categorical quantity by testing three different turbulence grids. The developed statistical-empirical model was used to predict the expected target values at the same parameter settings as communicated by Chong et al. [27]. Then, these predicted values can be compared to the provided measurement data. Figure 3-12 (left) shows the fit of the model, incorporating all the independent test samples provided. As can be seen both visually and by means of the n_{MAE} error, the fit of the model for the $OASPL_{Serr}$ is remarkable. In Figure 3-12 (right), the absolute values for the serrated noise radiation $OASPL_{Serr}$, as well as the noise reduction ΔOASPL, are shown for varying Reynolds number and serration amplitude.

The predicted trends (straight lines) accurately match the measurement data (symbols). However, as observed for the fit of the initial statistical-empirical model (Figure 3-10), slightly higher deviations are observed for the ΔOASPL, since uncertainties of the underlying influencing parameters tend to accumulate.

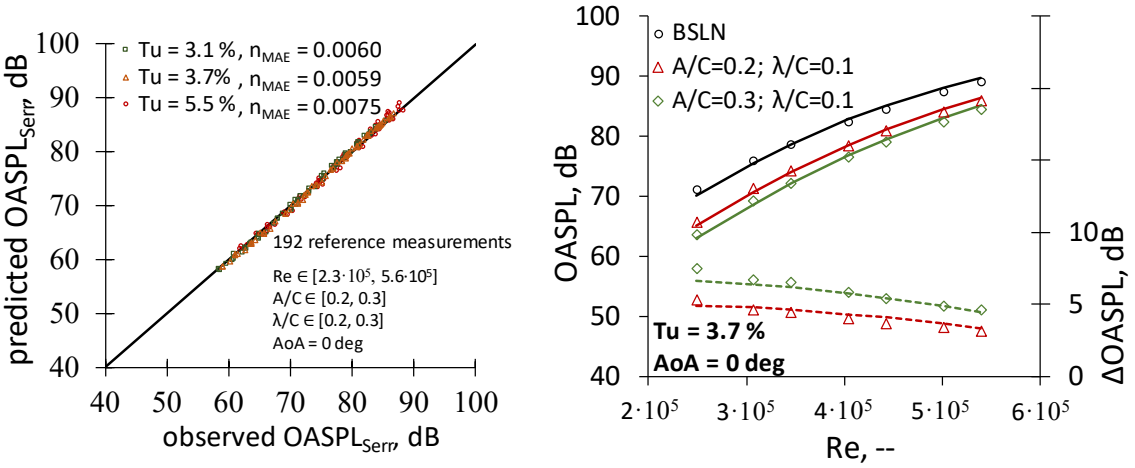

Figure 3-12 Validation measurements comparing the raster measurements from Chong et al. [27] with the developed statistical-empirical model. Left: OASPL$_{Serr}$ of observed vs. predicted values; right: absolute comparison of the OASPL with independent validation data (points = measurements, curves = model prediction).

3. Statistical-Empirical Model Validation with External Data

Final validation of the developed statistical-empirical model (see also [110]) takes place by comparing the predicted OASPL and ΔOASPL with external data [47] obtained independently in the aeroacoustic wind tunnel at the Institute of Sound and Vibration Research (ISVR), University of Southampton. The aerofoil used in the ISVR is of the same NACA65(12)-10 type, with a chord length C = 150 mm and a span S = 450 mm. The authors forced a bypass transition of the boundary layer from laminar to turbulent by tripping tapes in order to prevent the production of laminar instability tonal noise [47]. At an elevated level of free-stream turbulence, the leading edge noise is considered to be the dominant noise source. Therefore, in this case, the boundary layer tripping can be assumed to have no influence on the radiated noise [63, 77]. The turbulence intensities at the ISVR were generated at Tu = 2.5 % and 3.2 %, and the incoming flow velocities were U_0 = 20 ms^{-1}, 40 ms^{-1}, and 60 ms^{-1}. The difference in distance of the far-field microphone location is corrected for by the monopole 1/R-scaling law according to *Eq. 3-33*,

$$OASPL(R_2) = OASPL(R_1) - \left|20 \cdot log\left(\frac{R_1}{R_2}\right)\right| \qquad \textit{Eq. 3-33}$$

$$\Delta OASPL = \left|20 \cdot log\left(\frac{R_1}{R_2}\right)\right|$$

where R_1 and R_2 are the absolute distances between the source and the observer (measurement location) at a polar angle of Θ = 90 deg. Note that there is a slight difference in the definition of the serration parameters, with the ISVR adopting the 'same wetted-area' principle. This means that the serration peak extends the initial aerofoil chord length by A/2. Therefore, the resulting differences in aerofoil surface between the statistical-empirical model and the validation data were also compensated for by a linear scaling.

Twelve measurement points were analysed at AoA = 0 deg and Tu = 2.5 % at Reynolds numbers of Re = 394,188 and 624,348. The serration amplitudes are varied by $0.1 \leq A/C \leq 0.35$, and the serration wavelengths are varied by $0.05 \leq \lambda/C \leq 0.25$. Applying the specific boundary conditions of the ISVR test rig to the current statistical-empirical model yields the predictions of the OASPL for both the baseline and the serrated aerofoils, which are shown in Figure 3-13.

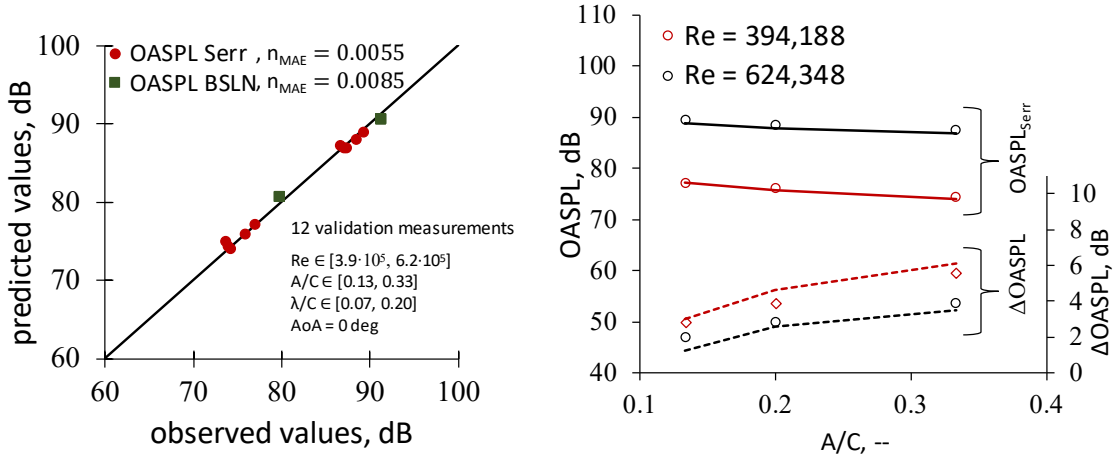

Figure 3-13 Comparison of the statistical-empirical model against external data, provided by the ISVR, University of Southampton. Prediction vs. observation (left) and absolute values (right, the curves indicate predictions, the symbols indicate the measurement results).

It becomes clear that an excellent agreement was achieved between the predicted and the measured data. The OASPL reduces when the serration amplitude increases, as predicted by the statistical-empirical model. The overall noise reduction ΔOASPL also demonstrates a good agreement with the predictions, although with a slightly larger discrepancy due to the accumulated errors in the OASPL, resulting from both the baseline and the serrated aerofoils. Altogether, the current statistical-empirical model can be regarded as a robust tool for predicting the ATI broadband noise subjected to serrated leading edges.

3.3.7 Aeroacoustic Dependencies

Main Effects

Figure 3-14 shows the Pareto diagrams of the two most important target values, with the ΔOASPL representing the linear difference between the OASPL of the serrated and that of the straight aerofoil under the same inflow conditions. In total, the presented results of each target value are based on 59 measurement points, each repeated twice for obtaining a stable mean value with a low statistical spread. All measurements were carried out in a randomised order, resulting in a time-consuming measurement campaign but also providing a statistically highly reliable data pool.

As can be seen from Figure 3-14 (left), the noise radiation, foremost, scales linearly with the Reynolds number, the turbulence intensity and the serration amplitude. Quadratic influences (indicator Q) of the turbulence intensity and the Reynolds number, followed by a linear effect (indicator L) of the AoA, are significant as well, although of secondary importance. Quantitatively, the strength of each effect is indicated as well, with negative values resulting in attenuated effects and positive values resulting in stronger effects. Comparing the two presented target values shows, for example, that increasing the serration amplitude leads to a linear attenuation of the radiated noise (Figure 3-14 left) but also causes a strong reinforcement of the noise reduction capability (Figure 3-14 right).

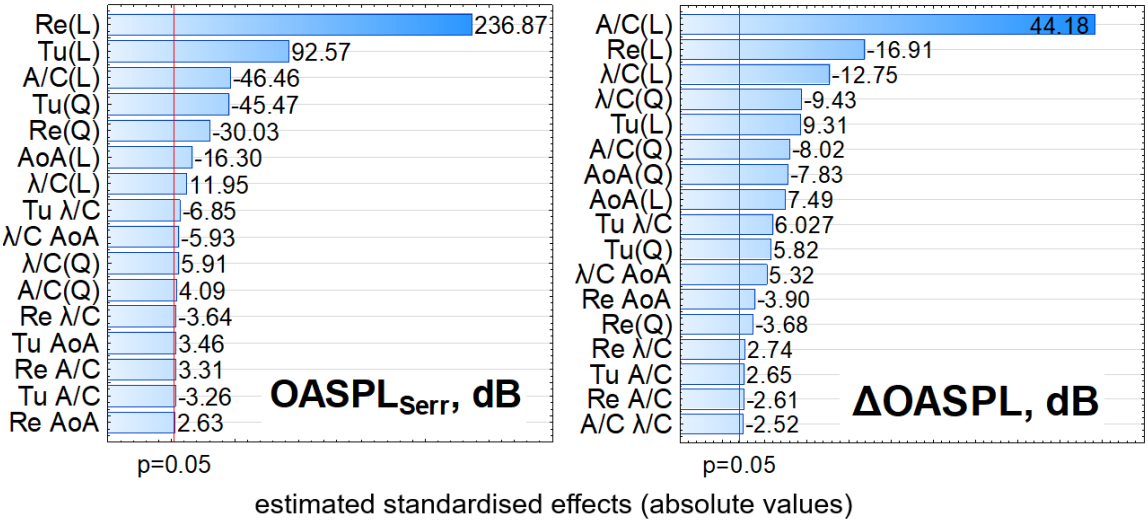

Figure 3-14 Pareto diagrams, including the strength of the effects and the threshold of statistical significance ($p = 5$ %). The overall sound pressure level of the serrations $OASPL_{Serr}$ (left) and the overall noise reduction ΔOASPL (right). Q indicates quadratic effects, and L indicates linear influences of the factors. Positive values indicate reinforcing effects; negative values indicate attenuating effects.

The mean effect of all the five parameters analysed is plotted in Figure 3-15, showing the effect of all the individual influencing parameters on the overall noise reduction ΔOASPL, while all the other parameters remain in intermediate positions. The serration amplitude has the highest intermediate effect, with an almost linear relationship between the A/C and the ΔOASPL, before reaching an asymptotic level when the A/C is increased further. The serration wavelength λ/C shows a non-linear behaviour, with the optimum achieved at intermediate wavelength, beyond which the noise reduction capability is weakened considerably [110]. The predicted profile of the influence of the turbulence intensity Tu exhibits a large level of noise reduction at high Tu levels. In contrast, at low Tu, a low level of noise reduction is predicted. This is in agreement with theory, since a high Tu is known to cause a high level of broadband noise radiation from a lifting surface. This, in turn, facilitates an increase in the noise reduction capability when a serrated leading edge is used. However, it is important to note that the effects of the individual parameters on the overall noise reduction in Figure 3-15 cannot be attributed to the serrated leading edges only, because different levels of Re, Tu and angle of attack AoA can also affect the baseline straight leading edge [110].

Despite their quite general character, the trends already provide an overview of the significance and effect of the single parameters. In order to provide statements of more conclusive character for the transfer of the obtained dependencies to practical applications, multi-objective optima will be defined in Section 3.3.8.

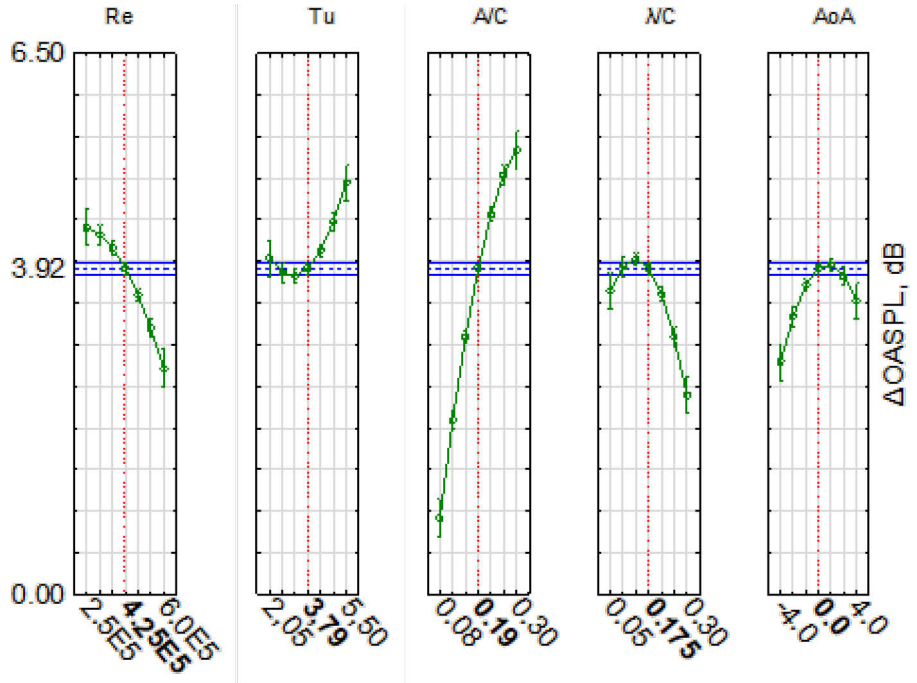

Figure 3-15 Mean effect of the influencing factors on the target value ΔOASPL with ΔOASPL = 3.92 dB when all parameters are on intermediate levels as indicated in bold.

Bringing the dependencies shown in Figure 3-15 towards a maximum noise reduction, or in other words, maximising the underlying functional relationship of ΔOASPL as shown in Figure 3-16, results in a minimum Reynolds number and a maximum Tu and A/C, as well as $\lambda/C \in [0.13, 0.2]$ and AoA ∈ [0, 3.3]. This identified setting of maximum performance is tested experimentally, clearly confirming the proposed parameter settings. At optimum conditions, a reduction of up to ΔOASPL = 7.7 dB is predicted, with experimentally a ΔOASPL = 7.6 dB obtained for [Re = 250,000, Tu = 5.5%, A/C = 0.3, $\lambda/C = 0.2$, AoA = 0 deg], which is well within the relatively large 95% confidence interval of 7.7 dB ± 0.68 dB.

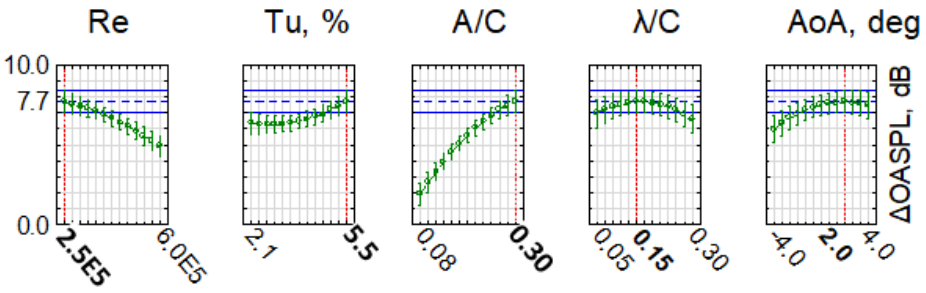

Figure 3-16 Predicted maximum of target value ΔOASPL within the limits of the experimental space. Optimum factor levels indicated in bold.

Interdependencies

Apart from the main effects of either linear or quadratic nature, the statistical evaluation also provides information on statistically significant interdependencies between single parameters. As can be seen from Figure 3-14 (left), the most significant interdependencies for the ΔOASPL occur in the form of Tu·λ/C and AoA·λ/C, which require a more detailed discussion.

For the interdependency of the serration wavelength and the turbulence intensity (λ/C·Tu), at low Tu, small serration wavelengths are needed in order to achieve a high level of noise reduction, as exhibited by the red region in Figure 3-17 (left). As the Tu is related to the integral length scale Λ *of* the incoming gust, large serration wavelengths are expected to be less effective in the decorrelation effects, especially if the incoming structure is characterized by small turbulent eddies. As was also observed for low to intermediate Tu, previous investigations suggested that serration wavelengths should be small to achieve a good level of noise reduction, although in general the impact of the serration wavelength is not as dominant as that of the serration amplitude [47, 86, 27]. However, at high Tu, serration wavelengths of intermediate values are far more effective in reducing the OASPL, as shown in Figure 3-17 (left). This agrees with the finding from a recent study by Chaitanya et al. [47], stating that the optimum serration wavelength is twice the size of the incoming turbulent structure in the form of the transversal integral length scale Λ_t. This is additionally supported by a detailed spectral analysis by Biedermann et al. [110], in which the serrated leading edge serrations were found to respond with higher sensitivity at high Tu, regardless of the level of the serration wavelength. For the low Tu case, however, a wider spread is observed for the noise reduction efficiency among the different serration wavelengths, with a low serration wavelength tending to achieve higher noise reduction. At low or intermediate Tu, large serration wavelengths become ineffective in noise reduction.

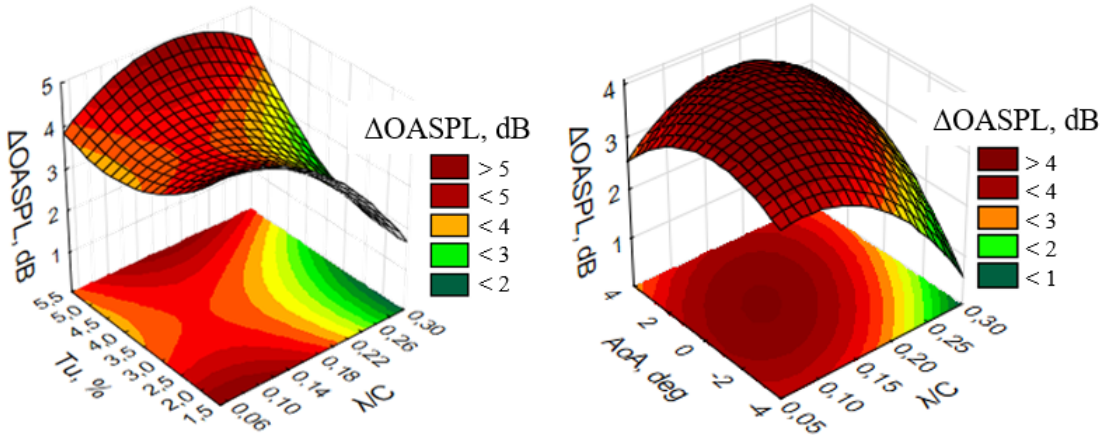

Figure 3-17 Contour plot of overall noise reduction with regard to interdependence effects between the turbulence intensity and the serration wavelength Tu·λ/C (left) and angle of attack and serration wavelength AoA·λ/C (right). Adopted graphs according to [110].

In addition to the interdependency between the turbulence intensity and serration wavelength described previously, another interdependency between the angle of attack and the serration wavelength (AoA ·λ/C) was found to be significant (Figure 3-17 right). In general, the level of noise reduction by the serrated leading edge serrations is at its maximum at zero angle of attack, an observation that is in agreement with other studies [27, 47]. However, at a large negative AoA, small serration wavelengths are needed to achieve a reasonably large noise reduction (red region), whereas serration wavelengths of intermediate dimensions are preferable at large positive AoA [110]. The underlying principle of this interdependency could be related to the specific semi-cyclic shape of the leading edge serrations relative to the stagnation point of the incoming flow. In the case of a zero angle of attack, the serration wavelength that can achieve the largest noise reduction is defined by how well it can decorrelate the spanwise coherence of the turbulence eddies, and how efficiently it can facilitate a 'nozzle effect' to accelerate the flow from the serration tip to the serration root and so reduce the Tu level. At a negative AoA, the incoming gusts will significantly impinge upon the projected area of the upper surface of the leading edge.

In this case, the use of small-wavelength serrations is a logical choice. Because a small serration wavelength will cause many three-dimensional undulations on the upper surface of the leading edge, the serration effect will persist to achieve interaction noise reduction. In the case of a positive AoA, the incoming flow will naturally impinge on the lower surface of the leading edge. However, the planar geometry at the lower surface of the serrated leading edge means that the three-dimensional undulation can no longer be obtained by using a small serration wavelength. Instead, a larger serration wavelength is preferable to avoid the direct impingement between the incoming gusts and the leading edge geometry [110].

3.3.8 Pareto Optimal Solution

As shown in Section 3.3.7, the statistical-empirical model can be used for maximising individual target values, such as the ΔOASPL. However, this often does not suffice to describe a system to the desired level of granularity since multi-objective optima are needed, especially when two or more objectives are conflicting. This is particularly true for aeroacoustics, in which the dilemma of opposing trends of aerodynamics and aeroacoustics is a common challenge. This means that the optimum solution for one objective can lead to an undesired solution for another objective. Computational expensive unbiased multi-objective optimisation is able to compute Pareto optimal solutions, visualised by so-called Pareto fronts, which separate non-efficient from non-realisable solutions. The Pareto fronts also help to select the best solutions [113]. These Pareto fronts are computed via the multi-objective particle swarm optimisation (MOPSO) algorithm as proposed by Coello et al. [119], representing an extension of the meta-heuristic particle swarm optimisation (PSO) approach. The intent is to optimise multiple continuous cost functions in order to obtain a combined optimum. This is achieved in an iterative process by defining a population (swarm) of particles, which explores the search space (here: experimental space) for the best potential solution in order to determine the 'flight direction' towards an unbiased optimum front. This makes a premature weighting of the individual target values superfluous. After identification of the currently dominating solution, this information is handed down to the next generation of particles in the subsequent iterative loop, creating a new swarm, which once again explores the search space. Eventually, this converges to globally dominating particles, characterising the final Pareto front.

For brevity and to maintain a certain degree of interpretability, the optimisation process was limited to two target values only. In order to allow a combined analysis of aerodynamic and aeroacoustic data, the experimentally obtained data (Section 2.2.3) for the coefficients of lift and drag were also developed into DoE regression functions, as is outlined in Section 3.3.3 (compare Appendix C.3). This is possible only because the same set of leading edge serrations was investigated for both studies. The Pareto optimum solutions were computed by implementing the MOPSO algorithm in *MATLAB*.

Combining the generated statistical-empirical models of the aeroacoustic and the aerodynamic performance of serrated aerofoils, Figure 3-18 and Figure 3-19 show the Pareto optima obtained for the four most meaningful sets of target values, as listed in Table 3-4.

Table 3-4 Defined pairs of target values for the localisation of the Pareto front as well as the desired optimisation towards a minimum or a maximum of the target values (TV).

No.	TV I	TV II	Desired
1	ΔC_L	ΔOASPL	Min/Max
2	ΔOASPL	$OASPL_{Serr}$	Max/Min
3	$C_{D,Serr}$	$C_{L,Serr}$	Min/Max
4	$C_{L,Serr}$	$OASPL_{Serr}$	Max/Min

Figure 3-18 (left) shows, for example, the difference in lift ΔC_L when the baseline and the serrated aerofoils are compared. Note that negative ΔC_L means a higher lift coefficient for the serrated case than for the baseline. Consequently, an optimum solution of best lift performance of the serration while maintaining a maximum overall noise reduction is achieved at minimum angle of attack AoA = -4 deg, maximum serration amplitudes A/C = 0.3 and intermediate wavelengths λ/C = 0.12. As seen for the aerodynamic study in Section 2.2.3, intermediate to high wavelengths are beneficial for generating lift, whereas the amplitude represents the dominating parameter for the reduction of broadband LE noise. For the serrated aerofoils, not only a maximum noise reduction compared to the baseline case is desirable but also a low acoustic signature in general. As Figure 3-18 (right) shows, this is obtained for maximum amplitudes and minimum wavelengths, characterising the noise reduction optimum. Moreover, at low Tu, less ATI noise is generated, hence significantly reducing the overall level of radiated noise. However, at maximum AoA and minimum Re, a meaningful noise reduction of ΔOASPL = 6.3 dB is still achieved.

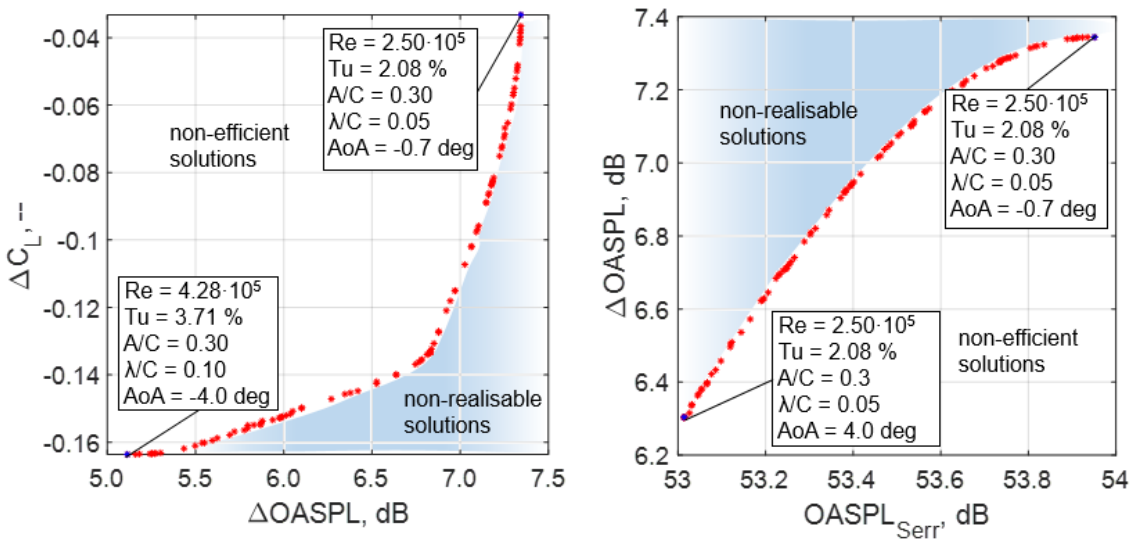

Figure 3-18 Multi-objective Pareto optimal solutions for sets of target values as stated per Table 3-4. Left: differences in lift coefficients ΔC_L vs. the overall sound pressure level reduction ΔOASPL (left). Right: ΔOASPL vs. the absolute noise radiation of aerofoils with serrated leading edges $OASPL_{Serr}$.

Focussing on aerodynamic target values only (Figure 3-19, left), minimum drag at maximum lift or, equivalently, maximum lift-to-drag ratios are obtained for minimum amplitudes, coinciding with previous observations in Section 2.2.3. Finally and according to aerofoil theory, maximum lift is generated for high angles of attack (AoA = 4 deg), while at high serration amplitudes, the turbulence intensity, as well as the serration wavelength, needs to be kept low for a minimum noise radiation (Figure 3-19, right).

The results indicate the ability of the statistical-empirical model to resolve conflicting trends of aeroacoustic and aerodynamic character when the parameter settings are chosen in an intelligent way. This provides the opportunity to tailor an optimised design for clearly specified boundary conditions of the aerofoils. This property is expected to be of high value for a transition of the serrated leading edges from the rigid to the rotating frame. For the moment, the multi-objective solutions are valid only for the investigated experimental space, defined by the limits of the five influencing parameters as well as the chosen boundary conditions and the specific aerofoil profile. However, the observed accuracy of the statistical-empirical model to predict data points at slightly different testing conditions in Section 3.3.6 also indicates a certain generalisability of the model. In this respect, the defined Pareto optimal solutions, too, are expected to keep their validity to a certain extent.

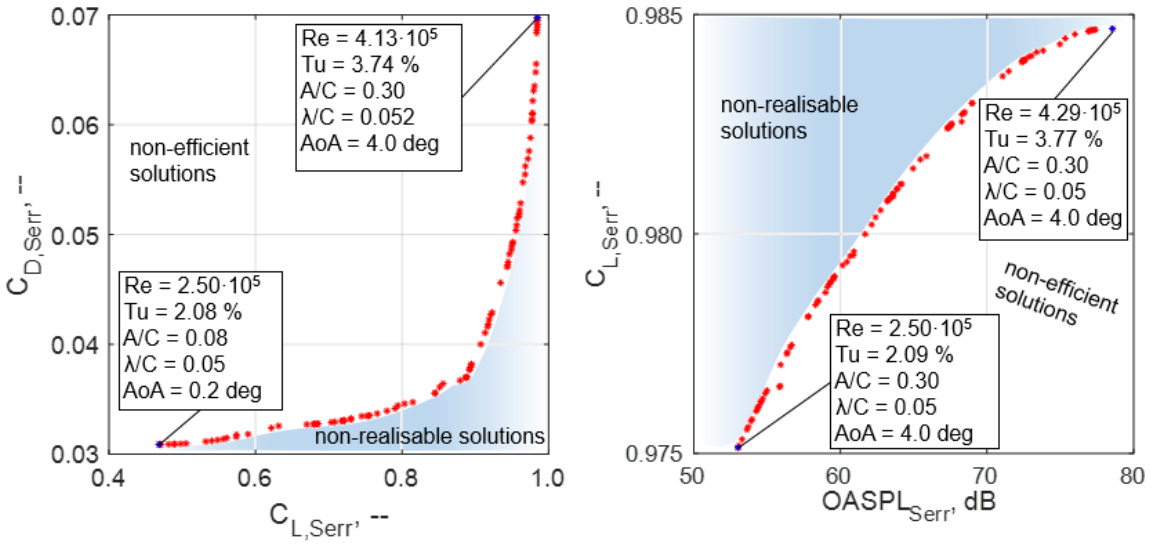

Figure 3-19 Multi-objective Pareto optimal solutions for sets of target values as stated per Table 3-4. Left: coefficients of drag $C_{D,Serr}$ vs. coefficients of lift $C_{L,Serr}$ of aerofoils with serrated leading edges. Right: $C_{L,Serr}$ vs. the absolute noise radiation of aerofoils with serrated leading edges $OASPL_{Serr}$.

3.4 Spectral Insights into the Serration Effects

This section aims at giving insights into the spectral composition of the acoustic signatures with and without serrated leading edges. The spectral scaling of the noise reduction is analysed with respect to various influencing parameters. Moreover, the effective noise reduction capability was extracted by means of an aeroacoustic measurement campaign using array beamforming. Subsequently, the results were further processed in order to identify the spatial location where the main noise reduction of leading edge serrations takes place. Finally, the differentiation between leading-edge and trailing-edge noise reduction by using serrations provides motivation for the use of serrations in rotating machinery.

3.4.1 Spectral Scaling with Tu, U_0, A, λ

The hitherto defined statistical-empirical model is limited to the overall effect of the serrated leading edges and does not take into account the spectral composition of the underlying signals. However, partial spectral analysis is possible by extracting the spectra of the individual test samples from the investigated experimental space. Chaitanya et al. [103] stated that the spectral noise reduction scales according to *Eq. 3-2*, in which the noise reduction due to the serrated LE increases logarithmically with the amplitude-based Strouhal number (at mid-to-high frequencies) until the noise is masked by the self-noise at high frequencies. Conversely, only little reduction is expected for the very low frequencies. These characteristics can also be reproduced for the current experimental results. Figure 3-20 shows the ΔSPL spectra for a number of cases involving different serration wavelengths and amplitudes, as well as a varying turbulence intensity and Reynolds number. When the serration amplitude is fixed but with different serration wavelengths (Figure 3-20a), the spectra demonstrate a linear increase in ΔSPL from mid-to-high frequencies until ΔSPL reaches about 12 dB for the one with the smallest serration wavelength (see also [110]). After reaching this peak, the ΔSPL begins to drop for higher frequencies due to the prominence of the self-noise radiation. As shown in Figure 3-20b, when the serrated leading edge is subjected to different flow velocities, it produces a ΔSPL spectral shape that is very similar to the shapes presented by Narayanan et al. [67] and Chaitanya et al. [47]; that is, the effective frequency range underpinning the ΔSPL will increase with increasing flow velocity. Figure 3-20c shows the influence of the serration

amplitude on the ΔSPL spectra, which demonstrates that a larger level of noise reduction can be achieved with a larger serration amplitude. This observation is consistent with the results reported by Narayanan et al. [67]. Finally, Figure 3-20d shows the influence of the free-stream turbulence intensity on the noise reduction, which is consistent with earlier results [110].

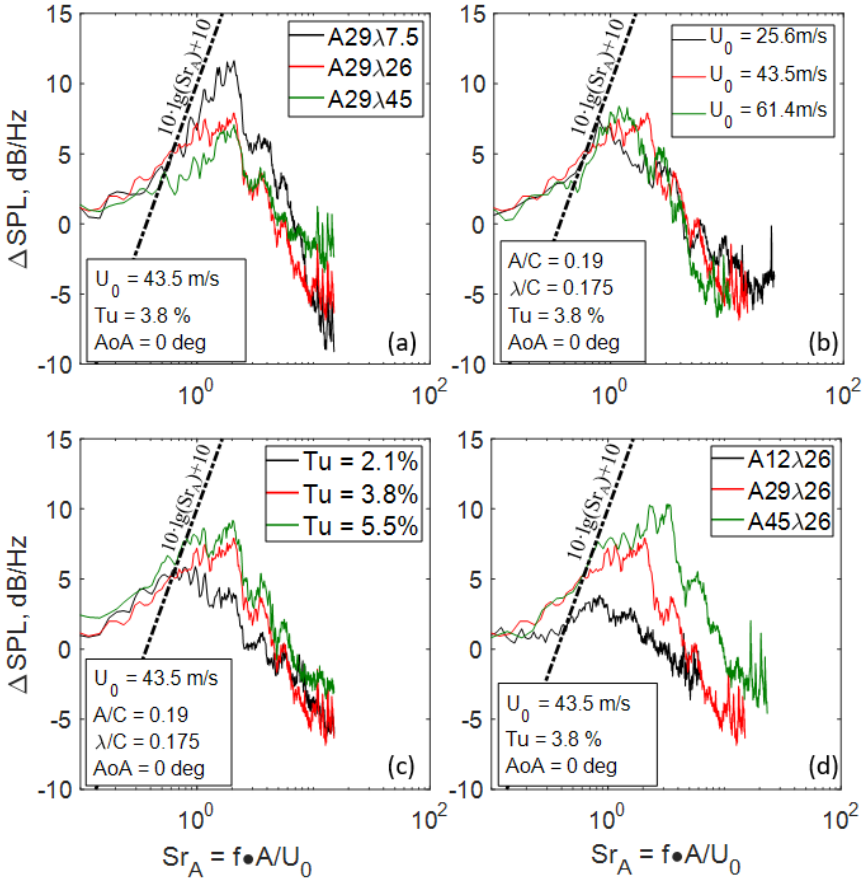

Figure 3-20 Spectral scaling of the noise reduction ΔSPL with the Strouhal number, normalised by the serration amplitude. Variation of serration wavelength (a), free-stream velocity (b), turbulence intensity (c) and serration amplitude (d) [110].

Even though the general trends of the spectral noise reduction can be confirmed, the absolute differences with the stated scaling law (*Eq. 3-2*) lead to the question of whether and how the gathered acoustic signals are contaminated by external noise sources that cannot be attributed to the leading edge of the aerofoil. Especially when it comes to a more detailed analysis of the spectral noise reduction effects of serrated leading edges, noise from, for example, the wind tunnel itself, the turbulence grids used or the trailing edge of the aerofoil might blur the clarity of the results obtained.

As mentioned in Section 3.1.2, Amiet et al. [65] proposed a model for describing the acoustic signature in terms of the power spectral density (PSD, *Eq. 3-29*) of a flat plate that interacts with incoming turbulence, hence disregarding all other noise sources. Amiet's model was slightly modified by taking into account the aerofoil thickness according to Gershfeld [71], resulting in the power spectral density as stated per *Eq. 3-34*.

$$PSD(\omega) = \frac{S}{\pi C}\left(\frac{2\Lambda_L}{3\pi R}\right) Tu^2 \rho^2 U_0^4 \left[\frac{\Gamma\left(\frac{1}{3}\right)}{\Gamma\left(\frac{5}{6}\right)}\right]^2 \frac{\widehat{K}_x^2}{\left(1+\widehat{K}_x^2\right)^{\frac{7}{3}}} exp\left(\frac{-\omega \cdot d}{2U_0}\right) \qquad \textit{Eq. 3-34}$$

$$\widehat{K}_x = -\frac{\omega}{U_0 k_e}, \qquad k_e = \frac{\sqrt{\pi}}{\Lambda_L}\frac{\Gamma\left(\frac{5}{6}\right)}{\Gamma\left(\frac{1}{3}\right)}$$

where Λ_L is the longitudinal integral length scale of the turbulence, Tu is the turbulence intensity, R is the observer distance, S the aerofoil span, d is the aerofoil thickness, $\widehat{K}_x$ is the normalised longitudinal wavenumber and Γ is the gamma function. This model is used to validate the ATI noise produced by a baseline, straight leading edge aerofoil, already measured in the context of generating the data for developing the statistical-empirical model (Section 3.3.4). The Λ_L and Tu were measured independently via hot-wire anemometry. The model takes into account the cross-power spectral density of the surface pressure on the aerofoil caused by the turbulence.

It can be seen from *Eq. 3-34* that the SPL scales with the fourth power of the free-stream velocity U_o, while the frequency scales with the aerofoil span and U_o. Figure 3-21 shows the comparison of the power spectral density of the far-field noise between Amiet's flat-plate theory and the experimental results of the aerofoil for the baseline, straight leading edge at three different flow velocities [110].

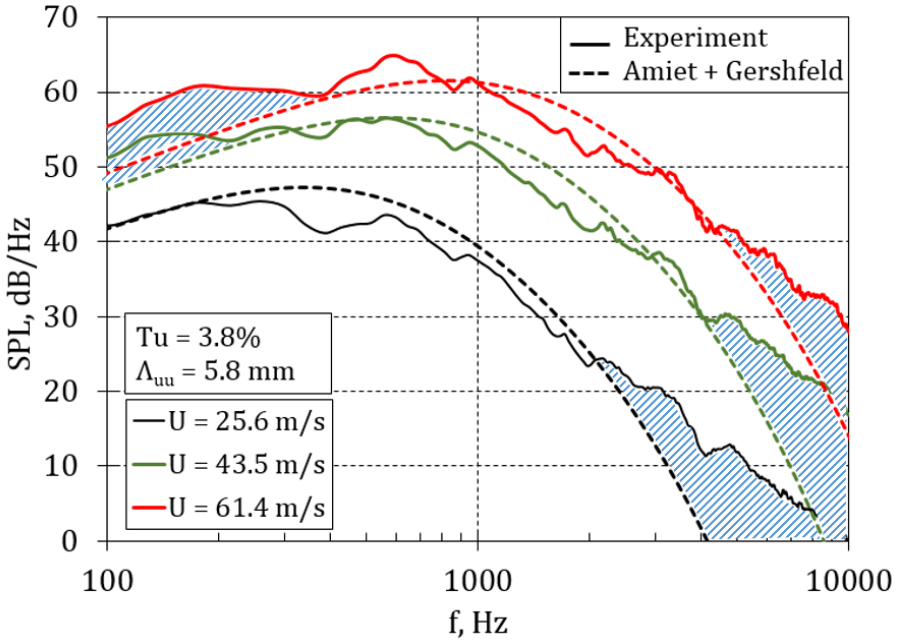

Figure 3-21 Comparison of the NACA65(12)-10 aerofoil with the leading-edge noise model by Amiet for different free-stream velocities [110].

There is reasonably good agreement with Amiet's flat-plate model for the mid-frequency range. The under-prediction at the high frequencies is mainly due to the dominance of the trailing-edge self-noise, which is not considered in Amiet's leading-edge noise model. Also for the low frequencies, a discrepancy between the measurement and the prediction is clearly observed in case of increasing free-stream velocities. This discrepancy can be attributed to the larger influence of the open-jet noise in the experiment, showing an increased interaction of the shear layer with the surrounding fluid.

A meaningful way to exclude this external noise from the trailing edge and the environment is to analyse the radiated noise of the tested aerofoils via a beamforming approach, as is pursued in Section 3.4.2. This approach enables a spatial differentiation of the individual noise sources and consequently can assist in identifying the effective noise reduction capability of serrated leading edges.

3.4.2 Noise Source Localisation via Array Beamforming

Many of the available experimental studies on serrated leading edges bear the risk of being influenced by unwanted external noise sources, such as noise from the open jet, grid-generated vortex shedding noise or aerofoil self-noise [87, 67, 88]. By using an array beamforming approach [77], this section aims to identify the location of the main noise reduction as a function of the serration parameters and the inflow conditions. This is achieved by restricting the analysis to a limited integration area in close proximity to the aerofoil leading edges. The results obtained are expected to supplement the current knowledge on the serration effects while also providing motivation for an extended application area of serrated leading edges. The beamforming study was conducted at the aeroacoustics facility at the Brandenburg University of Technology (BTU Cottbus). Significant parts of this section are also published in Biedermann et al. [120, 121].

Setup

Five different serrations as well as a baseline case, serving as a reference, were tested while varying the turbulence intensity (Table 3-5). Testing took place in the aeroacoustic wind tunnel at BTU Cottbus University [122] by implementing the microphone array beamforming technique and the CLEAN-SC algorithm [123], as well as a shear layer correction method [77]. CLEAN-SC is known to be a reliable and fast deconvolution algorithm, especially for aeroacoustic noise sources [124–126]. Furthermore, mounting of the samples on a six-component balance enabled a simultaneous determination of the aerodynamic forces. The maximum chord and thickness of the aerofoils were held constant by cutting the serrations into the aerofoil front part. As specified by Figure 3-22, the serration geometries are predominantly defined by their amplitude and wavelength. The chosen test setup is highly similar to that described by Geyer et al. [77]. In order to generate elevated turbulence levels for the analysis of aerofoil-turbulence-interaction noise, two coarse grids are mounted upstream of the aerofoils' leading edge [120].

Table 3-5 Summary of boundary conditions for the experimental beamforming setup [120].

nozzle diameter D	0.2	m	chord, span	0.15, 0.495	m
jet diameter at leading edge [18]	0.16	m	serration amplitudes A	12, 29, 45	mm
distance nozzle to aerofoil	0.2	m	serration wavelengths λ	7.5, 26, 45	mm
no. of microphones (Panasonic WM-61A)	56	--	angle of attack AoA	$-4 \leq AoA \leq +4$	deg
beamforming focus grid resolution	5	mm	Reynolds number	350,000 (250,000)	--
streamwise expansion of integration area	90	mm	turbulence intensity Tu	0.5, 3.7, 5.1	%
spanwise expansion of integration area	120	mm	longitud. turbulence length scale Λ_L	--, 5.1, 5.8	mm
NACA65(12)-10 aerofoil	--	--	transversal turbulence length scale Λ_t	--, 2.5, 2.9	mm

For the determination of the turbulent properties, hot-wire measurements were conducted, showing a good spatial homogeneity. The integral length scale was obtained by fitting the one-sided power spectrum G_{uu} of the velocity fluctuations $\bar{u}^{'2}$ to the formulation of isotropic and homogeneous turbulence as described by Hinze [127] in *Eq. 3-35*

For the aerofoil, no forced tripping has been applied as preliminary measurements revealed an early transition of the boundary layer due to the high level of incoming turbulence, resulting in highly comparable sound pressure levels with and without tripping devices.

$$G_{uu}(f) = \frac{4\bar{u}^{'2}\Lambda_L}{U_0\left(1+\left(\frac{2\pi \cdot f \cdot \Lambda_L}{U_0}\right)^2\right)} \qquad \textit{Eq. 3-35}$$

The transversal length scale Λ_t, associated with the noise generation at the aerofoil leading edges, can be derived from the longitudinal length scale Λ_L. Assuming isotropic conditions, the normal components of the longitudinal length scale are known to differ by a factor of two, as outlined by Roach et al. [128] and Hinze [127]. It is known from the literature that the length of an open jet is approximately five times its initial diameter [129]. According to the theorem of intersecting lines, the diameter of the free open jet at the aerofoils' leading edge is determined to be 0.16 m according to *Eq. 3-36*, with D being the nozzle diameter, Δx the streamwise distance and Δy the expansion of the free jet normal to the flow direction.

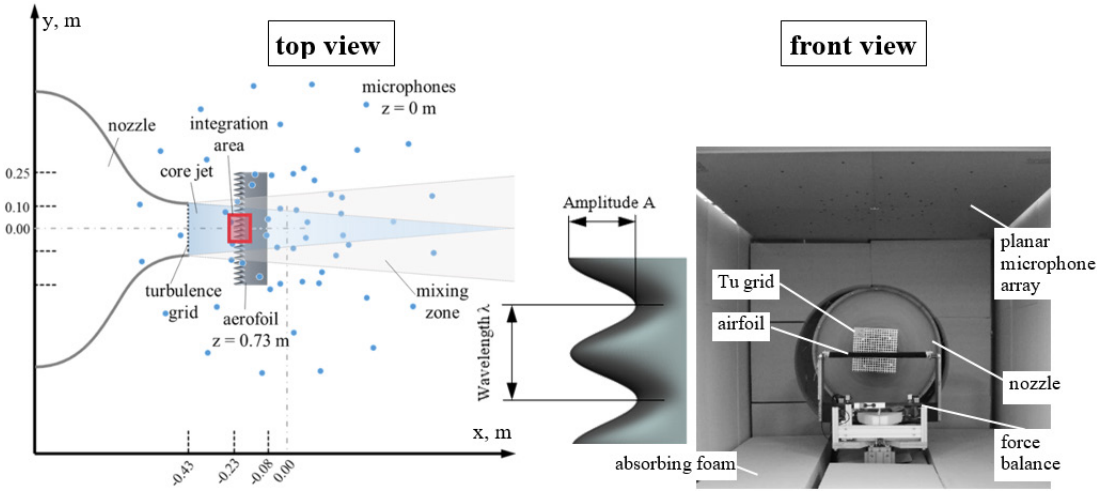

Figure 3-22 Left: Schematic of the microphone array used. The red box indicates the integration area for spectral analysis. Right: Picture of aerofoil mounted in the semi-anechoic enclosure [120].

$$\Delta y = \frac{5D - \Delta x}{5D} \cdot D \qquad \textit{Eq. 3-36}$$

The resulting circular area of the open jet in the measurement plane is converted into an equivalent rectangular form in order to obtain a representative height for determining the effective angle of attack according to *Eq. 3-12*. In consequence, the range of the geometrical angle of attack was chosen to be in accordance with an effective AoA ∈ [-4, 4], being congruent with the statistical-empirical model in Section 3.3.2.

Aerodynamic Validation

The aerodynamic results for both the initial experimental study at Brunel University London (Section 2.2.3) and the current beamforming study are compared in Figure 3-23. Qualitatively, the trends for varying the angle of attack agree well, although significant differences in the absolute values of the determined coefficients of lift occur as the tested aerofoils are not fully enclosed by the core jet (Figure 3-22, left), thus leading to interactions between the aerofoil outer region and the shear layer.

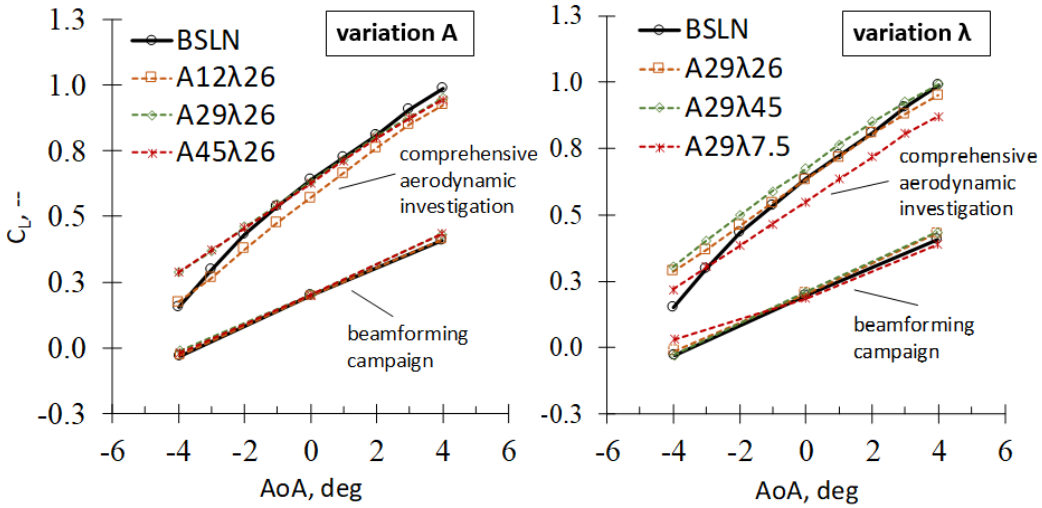

Figure 3-23 Comparison of previously gathered external data of aerodynamic performance [48] vs. obtained aerodynamic forces, accompanying the array beamforming study. Variation of serration amplitude (left) and serration wavelength (right).

Acoustic Data Processing

The recorded acoustic signals were processed by using the CLEAN-SC beamforming algorithm, resulting in two-dimensional sound maps, which allow for a qualitative localization of the noise sources. The plane of analysis was chosen to be aligned horizontally with the leading-edge tip of the tested aerofoils. For brevity, only sound maps for the (1kHz), 2 kHz and 4 kHz octave bands are presented [120]. Octave bands of higher order are not significantly affected by the serrations and do not contribute to a level-relevant noise reduction. Octaves of mid-frequencies $f_{Oct} < 1$ kHz, however, do play a role in terms of noise reduction, but an evaluation is restricted by the resolution of the chosen experimental setup.

Aeroacoustic Validation

Summing the frequency lines of the serrated cases and comparing them to the baseline case result in an overall sound pressure level reduction ΔOASPL (*Eq. 3-26*), as shown in Figure 3-24 (right). The highest overall noise reductions are achieved for maximum amplitudes (ΔOASPL = 7.1 dB) and minimum wavelengths (ΔOASPL = 5.3 dB), a result that matches previous findings. Thus, this represents the classic aeroacoustic dilemma of opposing trends because the aerodynamically most beneficial serration is the one with minimum amplitude and maximum wavelength (A12λ45) [120]. With the aim of getting to know the dimension of the external influencing noise sources and to see whether these disturbances affect the total noise reduction, the results obtained are compared to the statistical-empirical model discussed in Section 3.3. The labels in Figure 3-24 (right) indicate the extracted values for the beamforming study vs. the predicted values at the respective parameter settings for the serration amplitude, the serration wavelength, the turbulence intensity, the Reynolds number and the effective angle of attack. For the present study, this statistical-empirical model has been adapted to the varying boundary conditions at the current setup, and the expected noise reduction (ΔOASPL) has been predicted with respect to the chosen test parameters.

The fit between model and measurement results within the presented study is of high quality, with the maximum deviation ($\Delta_{Predict}$ =1 dB) occurring when minimum wavelengths are considered. The performance suggests only a small potential contamination of the statistical-empirical model by external noise sources in the frequency band of 300 Hz ≤ f ≤ 10 kHz, at least when it comes to relative differences between baseline and serrations in terms of the ΔOASPL [120].

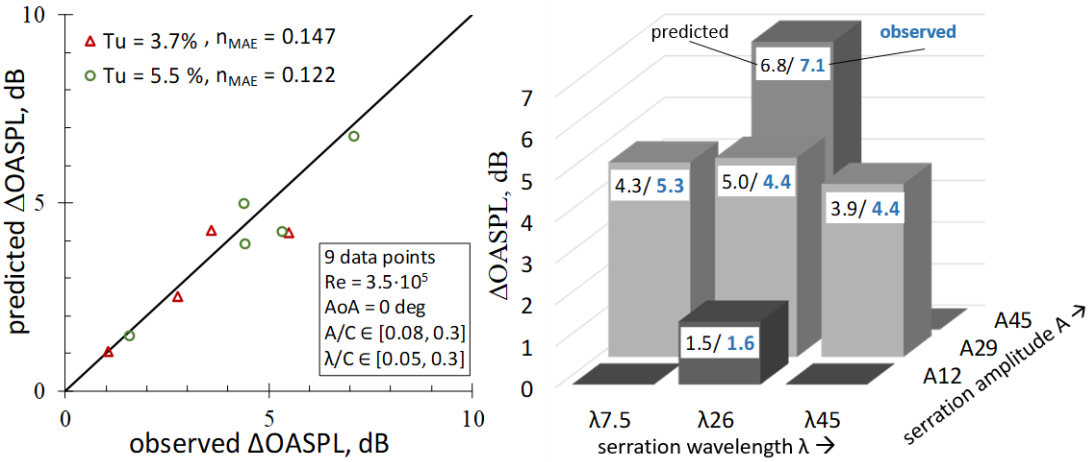

Figure 3-24 Comparison between the observed ΔOASPL from array beamforming with the predicted values of the statistical-empirical model in a frequency range 300 Hz ≤ f ≤ 10 kHz at Tu = 5.1 %. Fit of the model (left) and juxtaposition of absolute level (right).

Aeroacoustic Effect of Serration Parameters and Turbulence Intensity

Focusing on the baseline case for the 2 kHz octave band in Figure 3-25 (left) shows a clear attribution of the noise sources to the aerofoil leading edge, indicating inflow conditions of high turbulence (see also [120]). Yet at higher frequencies (Figure 3-25, right), additional noise sources at the trailing edge are visible, which are presumably due to high-frequency aerofoil self-noise, caused by the turbulent boundary layer. Nonetheless, the leading-edge noise still represents the dominant noise source. After introducing leading edge serrations, an efficient elimination of leading-edge noise for both octave bands is observed, with a clear scaling of amplitude and wavelength, although the effect of the wavelength is of secondary importance. The sound pressure levels for the integration area show a continuous decrease in leading-edge noise with increasing serration amplitude and decreasing serration wavelength, indicating the aeroacoustic efficiency of the serrations ($\Delta SPL_{2kHz} = 11.7$ dB, $\Delta SPL_{4kHz} = 8.9$ dB at Tu = 5.1 % for A45λ26).

Independently of the serration analysed, the noise sources at the trailing edge remain at a constant position, showing highly similar levels of noise radiation. However, the sound maps (Figure 3-25) suggest that the localized noise sources at the leading edge slightly shift downstream with increasing serration amplitude. This coincides with the numerical findings of Kim et al. [74] and Chaitanya et al. [47], also presented in Figure 3-3, who state that the remaining noise sources of serrations are located at the serration root for low frequencies and at the serration peak and root for higher frequencies. Nevertheless, until now, this finding lacked experimental evidence. Due to the restrictions in spatial resolutions, the results presented in Figure 3-25, too, do not provide a clear confirmation but qualitatively suggest that the pattern described by Kim et al. [74] is true [120].

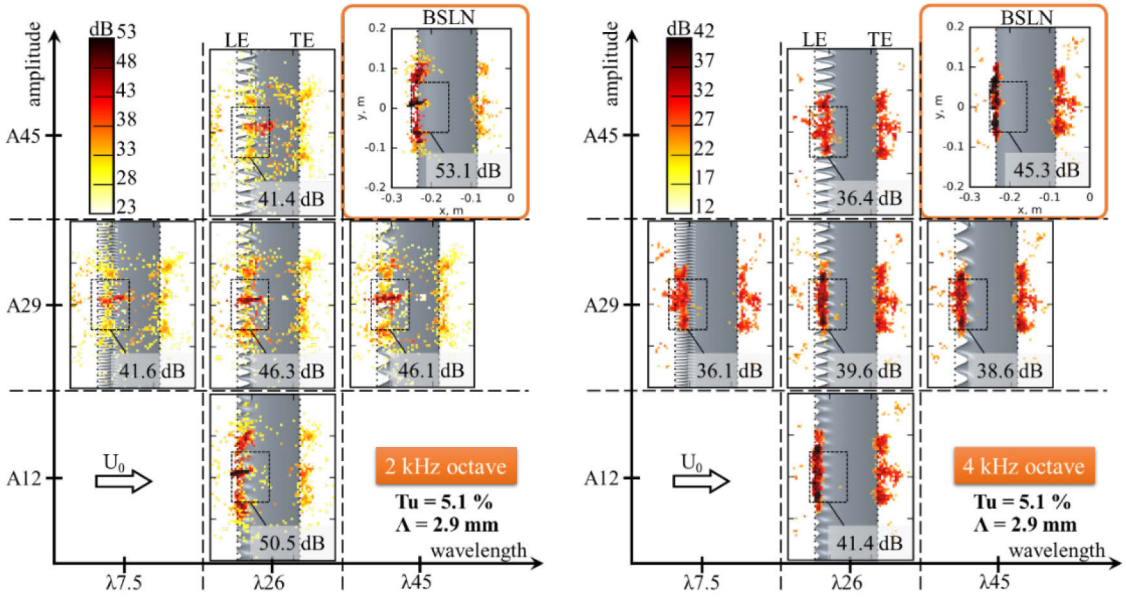

Figure 3-25 Sound maps with variation of serration amplitude A and wavelength λ. Tu = 5.1 % and at Re = 350,000, AoA = 0 deg. Results obtained for the 2 kHz octave band (left) and the 4 kHz octave band (right). Dashed box indicates the chosen integration area [120].

Influence of Incoming Tu

Reducing the level of the incoming turbulence intensity from Tu = 5.1 % (Figure 3-25) to Tu = 3.7 % (Figure 3-26) leads to a reduction in the total sound pressure level while maintaining the general scaling of the noise reduction with amplitude and wavelength of the serrations. For the 4 kHz octave band at Tu = 3.7%, less noise reduction is observed for all cases tested but in particular for the A29λ26 and A29λ45. These cases also show a decreased noise reduction capability for the 2 kHz octave band, whereas all other cases show improved noise reduction. This holds true in particular for the A29λ7.5 and A45λ26, yielding the highest A/λ ratio or the smallest inclination angle, respectively [120]. In addition, a higher sensitivity to the serration wavelength (A29λ7.5) for the low Tu case is observed, which may be linked to an improved ratio of the transversal turbulent length scale Λ_t to the serration wavelength λ, required for incoherent excitation. On the other hand, the observed pattern extends the previously reported maximum noise reduction capabilities for a single serration [1], as is discussed further below.

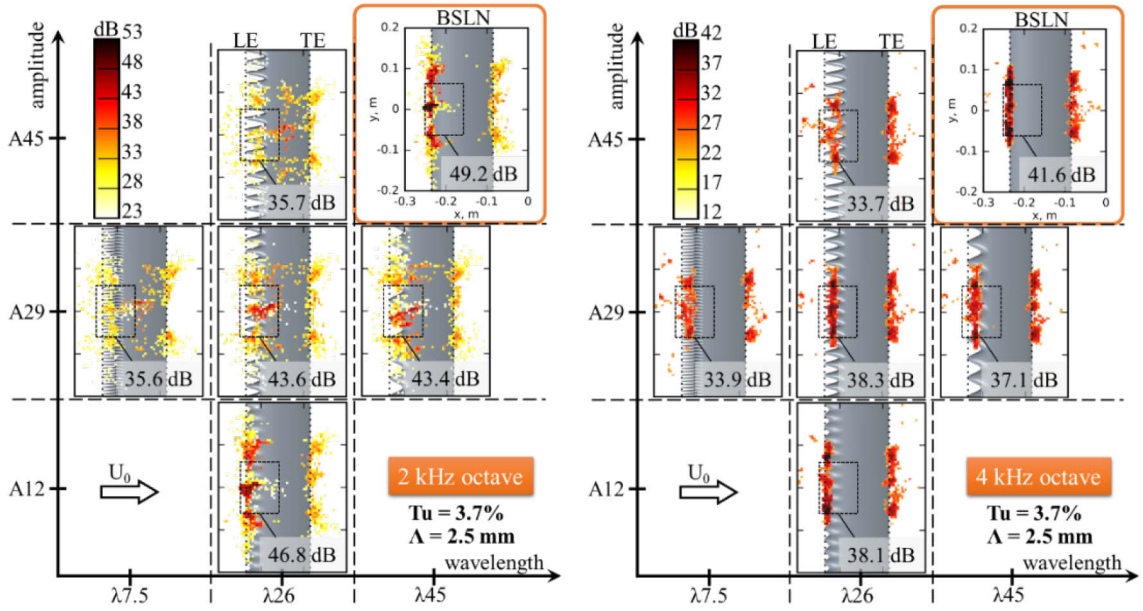

Figure 3-26 Sound maps with variation of serration amplitude A and wavelength λ. Tu = 3.7% at Re = 350,000, AoA = 0 deg. Results obtained for the 2 kHz octave band (left) and the 4 kHz octave band (right). Dashed box indicates the chosen integration area [120].

Narrow-band spectra for the individually tested cases are obtained by integrating the noise sources within the defined area in close vicinity to the aerofoils' leading edges, minimising the influences of unwanted background noise of low frequencies (wind tunnel + turbulence grids) and high frequencies (aerofoil trailing edge). Figure 3-27 shows the spectral noise reduction compared to the reduction in the baseline case, scaled by the Strouhal number, with the serration amplitude acting as characteristic length. To avoid the occurrence of non-physical peaks due to small gaps in the narrow-band spectra of either the baseline or the serrated case, a 6th order one-dimensional median filter is applied to smoothen the signal of the spectral noise reduction [120]. As mentioned in Section 3.4.1, Chaitanya et al. [1] stated that the noise reduction scales according to *Eq. 3-2*. Maximum noise reduction is reported to occur for an offset factor $b_S = 10$ and at a constant prefactor $a_S = 10$ at low to intermediate frequencies, at which leading-edge noise is dominant. Contrary to these findings, the current results shown in Figure 3-27 indicate a different scaling when the scaling constants a_S and b_S are fitted to the experimentally observed noise reduction trends. Here, the prefactor turns out to be $a_S = 15$ (rather than $a_S = 10$) and the maximum offset $b_{S,max} = 10$, outperforming the initially proposed scaling law in the mid-frequency region. As can be seen in Figure 3-27, this most efficient serration design (A29λ7.5) shows a ratio of the serration wavelength to the transversal turbulent length scale of $\lambda/\Lambda_t = 2.6$. Most interestingly, the optimum λ/Λ_t ratio defined by Chaitanya et al. is $\lambda/\Lambda_t = 2$ for maximum decorrelation effects at the serrations shoulders and $\lambda/\Lambda_t = 4$ for the optimum out-of-phase condition (destructive interference), enclosing the observed optimum in the beamforming analysis.

Usually, the maximum turning point of the spectral noise reduction is influenced by the magnitude of aerofoil self-noise, holding the potential to mask the maximum noise reduction effects. The improved noise reduction capability in the mid-frequency region, and hence the modified scaling law, is expected to be due to the absence of this aerofoil self-noise (trailing-edge noise, boundary-layer noise, shedding noise of the turbulence grids) for the chosen beamforming integration area. For higher frequencies, the spectral noise reduction tends to decrease, since the dominant nature of the generated ATI noise decreases [120]. The maximum offset $b_S = 10$ is approached only for maximum amplitudes ($b_S = 8.5$) and minimum wavelengths ($b_S = 10$).

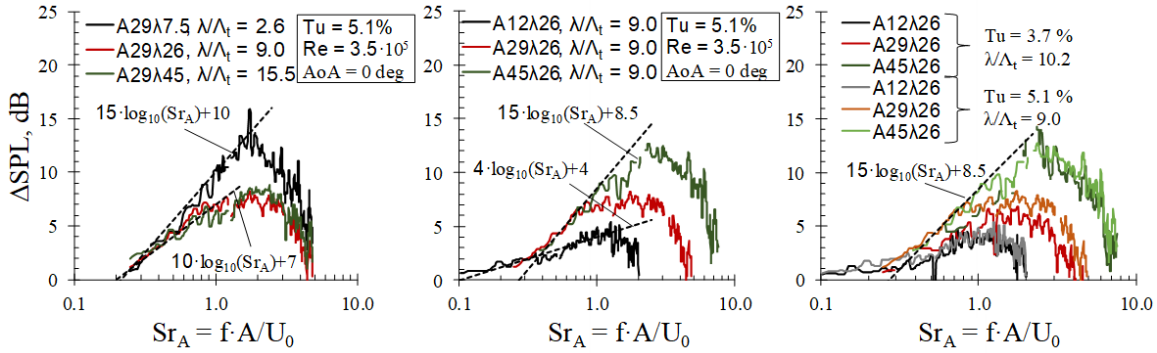

Figure 3-27 Spectral noise reduction (500 Hz ≤ f ≤ 5.8 kHz, 6th order median filtered) obtained from the 2D integration area with varying serration wavelength λ (left), serration amplitude (centre) and Tu (right), Re = 350,000, AoA = 0 deg [120].

Influence of the Angle of Attack

Extending the spectral analysis to different angles of attack reveals some noticeable patterns (see also [121]). In Figure 3-28, the obtained noise radiation (for the defined sector of integration) of the baseline case and the A29λ26 case is plotted for minimum (left), zero (centre) and maximum (right) angles of attack. This data are compared to the single-microphone measurements of the initial aeroacoustic study (Section 3.3). Although slightly different boundary conditions are applied in terms of free-stream velocity, turbulence intensity and angle of attack, the results are qualitatively comparable. Note that the plotted power spectral density (PSD) signals for the single-microphone measurements in Figure 3-28 include all the present noise sources and not only spectra related to a specific sector close to the aerofoil leading edge, as is the case for the beamforming results. Both data sets exhibit a clear dependency of the noise radiation on the angle of attack, leading to a significant broadband noise reduction at $0 \leq \text{AoA} \leq +4$ deg. For high negative angles, however, additional high-frequency noise is radiated by the serrated aerofoils, leading to a significant spectral decrease in noise reduction. Comparing the data sets in Figure 3-28 reveals a remarkable spectral similarity, with an increase in high-frequency noise taking place at the same frequencies ($f \geq 1.5$ kHz) at negative angles of attack [121].

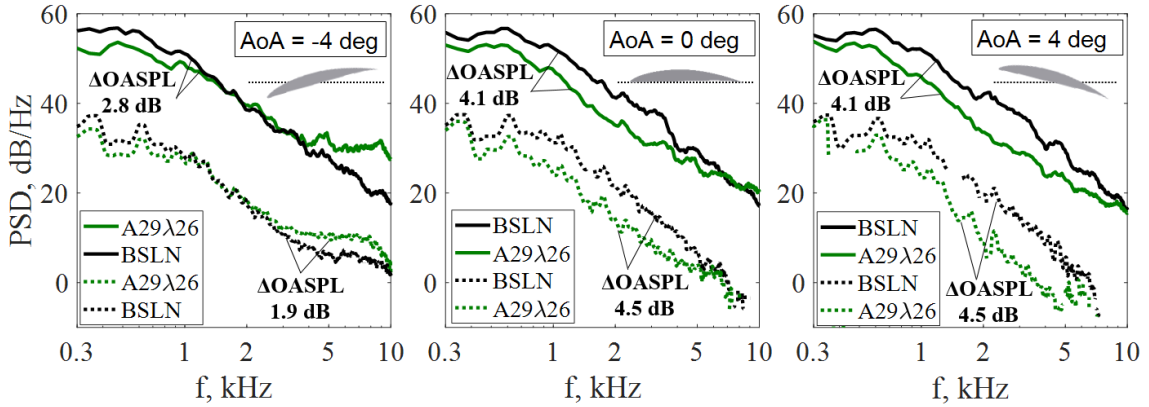

Figure 3-28 Comparison of spectra for the baseline and an A29λ26 serration at different angles of attack. Single-microphone measurements from Brunel University (straight lines at Re = 425,000, Tu = 3.8%) and beamforming spectra (dotted lines, Re = 350,000, Tu = 5.1%), both evaluated at 300 Hz ≤ f ≤ 10 kHz [121].

This effect is closely related to the interdependency of the angle of attack and the serration wavelength (AoA·λ/C) mentioned in Section 3.3.7, in which it is seen that the smallest serration wavelength does not necessarily lead to a maximum noise reduction across the whole frequency range [27]. It is proposed that cross-flow effects through the serrations are responsible for the

attenuation of the noise reduction capability with minimum serration wavelengths λ and maximum AoA. This observed dependency on the AoA is considered to be of high importance as serrated leading edges are eventually intended to be implemented in rotating systems, in which non-congruent inflow conditions for the blades are common and might strongly affect the aeroacoustic effectiveness of leading edge serrations.

Going one step further, the sound maps in Figure 3-29 illustrate the noise source distribution at three octave bands for the A29λ26 and the baseline case at different angles of attack. Varying the angle of attack for the baseline case shows a similar noise radiation for zero angles of attack and positive angles of up to AoA = +4 deg, albeit that a small reduction of trailing-edge noise can be observed for the 4 kHz octave band. This small reduction can be attributed either to the known fact that the spectral peak of trailing-edge noise shifts towards lower frequencies when the angle is increased [130] or to differences of the turbulent boundary layer thickness. Moving to negative angles, however, shows a clear relative reduction in leading-edge noise for all analysed octave bands of the baseline case. This specific behaviour can be attributed to the cambered design of the NACA65(12)-10, where, at negative angles, an upwash of the incoming turbulent structures towards the aerofoil's suction side occurs and, due to the acceleration of the fluid, stretching effects of the vortices lead to less radiation of broadband leading-edge noise [121].

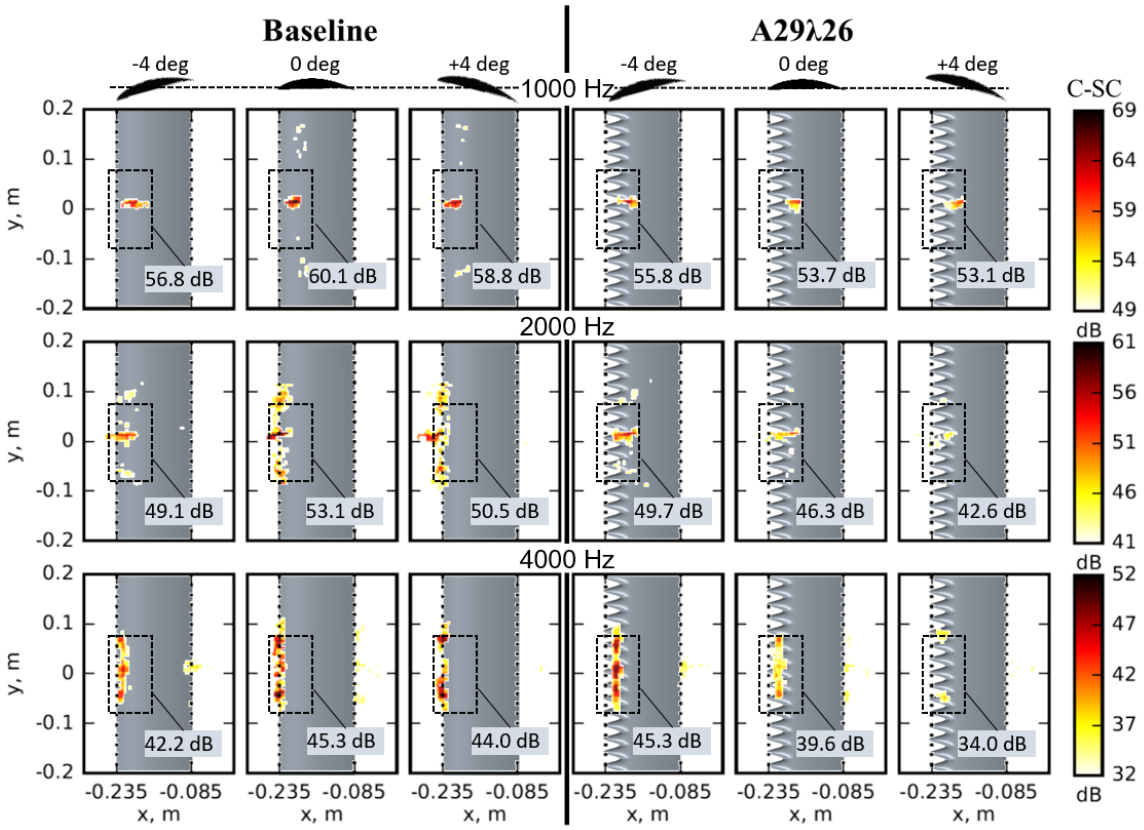

Figure 3-29 CLEAN-SC sound maps for the 1 kHz (top), 2 kHz (centre) and 4 kHz (bottom) octave bands with varying angle of attack AoA at Tu = 5.1 % and Re = 350,000. Baseline (left) vs. A29λ26 (right) [121].

Yet, in the case of the analysed serrations, a quite contrary pattern was observed, in which negative angles lead to an increase in leading-edge noise and positive angles show the lowest noise radiation for the leading edge. The prominent location of the acoustic sources right at the leading edge for the 4 kHz octave band supports the previously mentioned suspected cause in the form of a cross-flow from the suction side through the serration gaps to the pressure side. Still, a fraction of additional noise is also added by increased vortex shedding effects at the trailing edge at high negative angles (AoA = -4 deg). These opposing trends of baseline

and serration result in a negative accumulative effect when it comes to the noise reduction capability at negative angles of attack, which is remarkably attenuated by an increase in the A29λ26 leading-edge noise and a decrease in the baseline noise radiation compared to the situation with zero angle of attack. This pattern can be seen in more detail in Figure 3-30, in which the spectral noise radiation for the baseline case and for one of the most efficient serrations (A29λ7.5) is plotted at varying angle of attack -4 deg ≤ AoA ≤ +4 deg. Especially with increasing angles of attack, the serrated case shows a strong sensitivity to the noise radiation, particularly at frequencies f ≥ 1 kHz. In general, good noise reduction is achieved for the 1 kHz octave band, whereas for higher octave bands (2 kHz, 4 kHz), no reduction but even a noise increase at high negative angles is observed [121].

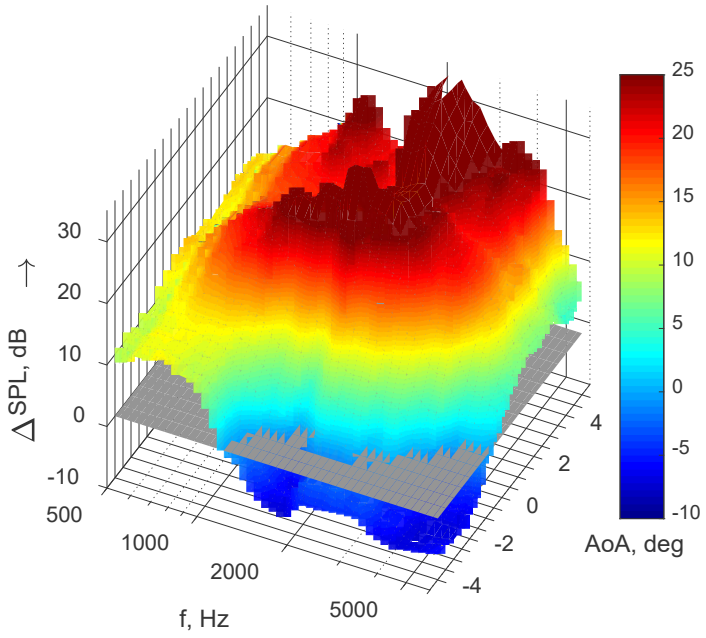

Figure 3-30 ΔSPL in 1/12th-octave bands for BSLN vs. A29λ7.5 at varying angle of attack with Re = 250,000 and Tu = 5.1 %. ΔSPL ≤ 0 (dark blue) indicates a noise increase due to the serrations.

3.4.3 Leading-Edge Noise vs. Trailing-Edge Noise

Figure 3-31 displays a contrasting juxtaposition of an aerofoil subjected to low- (no grid, Tu = 0.5 %) and high-turbulent (Tu = 5.1%) inflow conditions, testing the baseline case and the acoustically most efficient A29λ7.5. Analysing the aeroacoustic performance of the baseline at low Tu (Figure 3-31, top) clearly shows the presence of significant noise sources close to the aerofoils' trailing edge, which stem from boundary layer turbulence [120]. For Figure 3-31 (bottom), however, a turbulence grid is installed, leading to inflow conditions of high turbulence. The comparison shows a clear change of the dominating noise sources from trailing-edge to leading-edge noise when the inflow conditions are altered towards high turbulence, just as has been described in the recent literature [63, 66, 61]. As shown previously, introducing serrations at high Tu (Figure 3-31, bottom) reveals a significant decrease in the noise sources close to the leading edge.

Interestingly, at low Tu, the serrations also hint at possibilities of reducing the dominant trailing-edge noise by ΔSPL = 13.7 dB for the 2 kHz and ΔSPL = 11.5 dB for the 4 kHz octave band (Figure 3-31, top). Moreover, even at high Tu, a marginal noise reduction for the trailing edge of ΔSPL = 3 dB for the 2 kHz octave band is observed. The noise reduction also manifests

itself in the extracted trailing-edge noise spectra in Figure 3-31 (right). The underlying principles for a reduction in noise sources at the leading or trailing edge, however, are expected to be of a different nature. For the trailing-edge noise reduction, one possible hypothesis is that the serrations act as vortex generators, generating stretched, worm-like vortices that are, at low Tu, able to force an early transition of the boundary layer to a fully turbulent state and to reduce the vortex shedding effects at the trailing edge [120]. This would agree with recent findings by Chong et al. [131] and Hansen et al. [24]. On the contrary, for the leading-edge noise, the serration contour directly acts as a noise reduction mechanism.

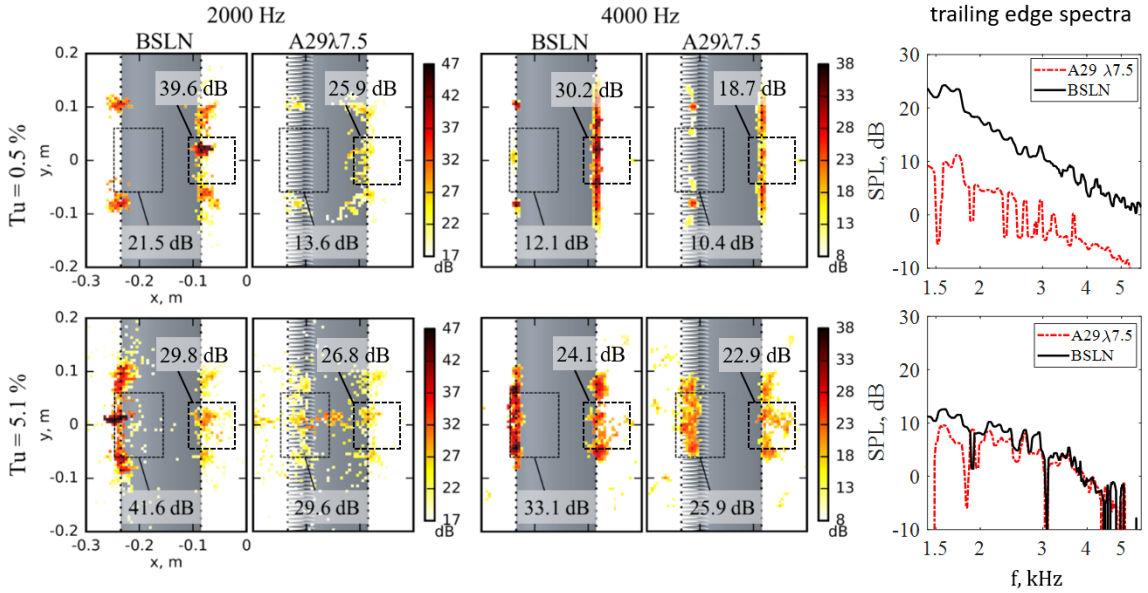

Figure 3-31 Sound maps via CLEAN-SC of the 2 kHz octave band (left) and the 4 kHz octave band (right). Comparison of the baseline and the A29λ7.5 case without using a turbulence grid; Tu = 0.5% (top) and Tu = 5.1 % (bottom), Re = 250,000, AoA = 0 deg. Additional plot of the broadband trailing edge spectra (right) [120].

The observed trailing edge noise reduction can be supplemented by hot-wire measurements, conducted at Brunel University London by Chong and Biedermann et al. [131]. Measuring the streamwise turbulence distribution of a serrated aerofoil of A = 45 mm and λ = 26 mm, as well as the distribution of the baseline case at U_0 = 24 ms^{-1} and AoA = 0 deg, shows vortical structures, emanating from the serration roots (Figure 3-32). On the suction side, a split-and-merge effect takes place, which results in a spanwise shift of the vortical structures by almost 180 deg [131]. Interpolating the chordwise planes shown in Figure 3-32 indicates the presence of streamwise worm-like vortical structures, which appear to be aligned with the roots of the serrations in the spanwise direction. The turbulent structures on the pressure side are lifting up from the surface, leading to laminarised regions of low Tu, presumably due to secondary flow effects (counter-rotating structure of vortices). The shift of the vortical structures from the suction side relative to the structures on the pressure side results in strong interactions in the wake region and might give rise to destructive interference effects (out-of-phase effects) in the wake region.

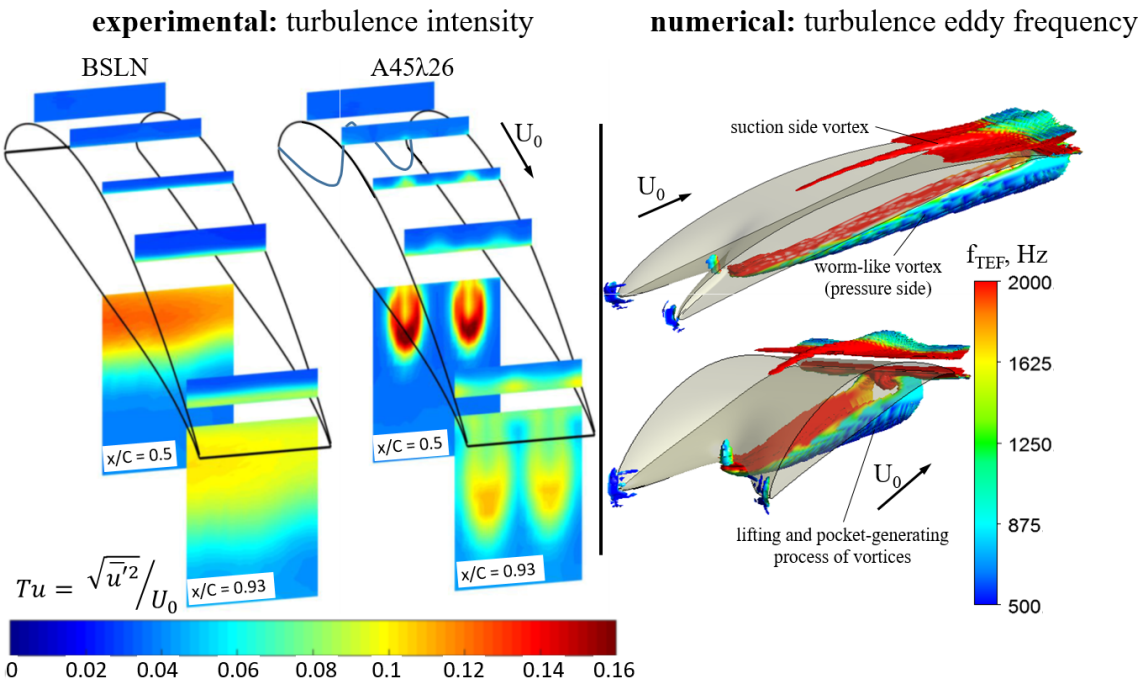

Figure 3-32 Left: Distribution of the intensity of the boundary layer turbulence via hot-wire measurements for the BSLN and the double-wavelength A45λ26 aerofoil at U_0 = 24 ms^{-1} and AoA = 0 deg [131]. Right: numerically obtained turbulence eddy frequency f_{TEF} of a single-wavelength A26λ45 at U_0 = 25 ms^{-1}, AoA = 0 deg, Tu = 5 %.

In Figure 3-33, further measurements of the turbulent structures were carried out by taking into account all spatial velocity components. This is expected to provide additional knowledge on the effective frequency range and the intensity of the generated vortices. The impact of these structures on the near wake at x/C = 1.05 can be seen in the turbulent spectrum, covering the wake in close vicinity to the aerofoil trailing edge (Figure 3-33). Once again, low-energy pockets are visible between the vortices on the pressure side, where the turbulent coiling structures are transporting turbulent energy away from the surface, making it even more difficult to classify the boundary layer close to the trailing edge as being turbulent (since calmed considerably). The BSLN, on the contrary, shows a grown-together wake, radiating as a single source. Overall, the frequency range of relevance is found to be f < 3 kHz, with the pressure side of the baseline clearly showing a lower frequency range of $f(\sqrt{u'^2 + v'^2}) < 1\ kHz$ than the pressure side of the serration, whose frequency range is $f(\sqrt{u'^2 + v'^2}) < 3\ kHz$.

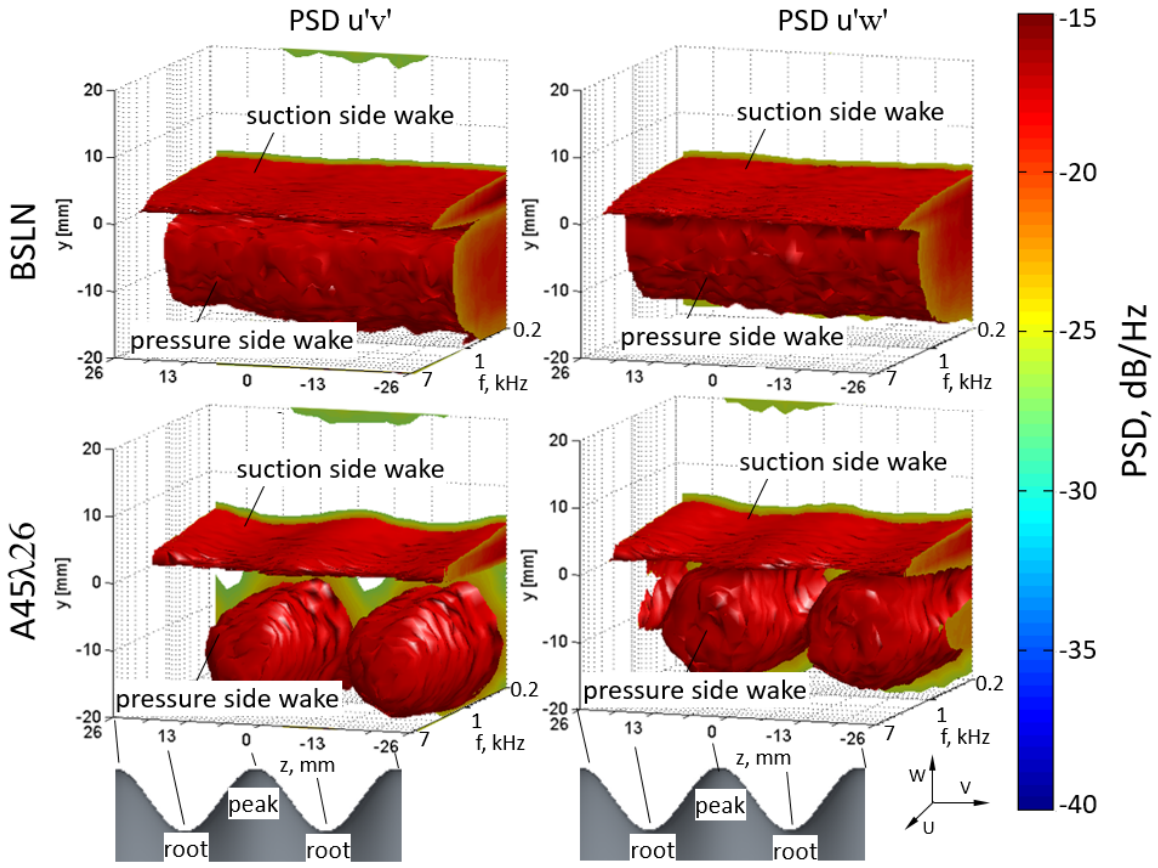

Figure 3-33 Spectral content (PSD) of velocity fluctuation $\sqrt{u'^2 + v'^2}$ (left) and $\sqrt{u'^2 + w'^2}$ (right) for the baseline (top) and the A45λ26 serration (bottom), obtained via hot wire measurements with a 2D-probe. Measurement plane in near-wake at $x/C = 1.05$ at $Re = 250{,}000$, $AoA = 0$ deg and $Tu = 2.5\%$.

These observations match the acoustic findings. As can be seen from Figure 3-31 (right), narrow-band spectra were generated for the trailing-edge section only, providing further insights into the noise reduction. For the high Tu case, the trailing-edge noise is already at a relatively low level, hence providing a limited noise reduction capability for the serrations. Nevertheless, due to the generated vortices from the leading edge, more scattered noise sources are expected to be present at the trailing edge, which can be reduced by the out-of-phase conditions of the vortical structures from the suction vs. the pressure side. For low Tu, the trailing edge noise represents the main noise source, but the sound map in Figure 3-31 (top centre) also indicates some leading edge noise reduction. This might be due to a successful suppression of a leading edge separation bubble, as was also described by Chong and Biedermann et al. [131] and Lacagnina et al. [102]. As for the high-turbulent case, the significant trailing-edge noise at low Tu can be attributed to the destructive interference effects of the vortical structures from the pressure and suction sides of the aerofoil, interacting in the wake but, in this case, with a vastly increased effect.

3.5 Summary and Discussion

For the aeroacoustic study, the NACA65(12)-10 aerofoils equipped with the same serrated leading edges as for the aerodynamic study in Section 2.2 were tested in order to link aerodynamic and aeroacoustic results. A statistical-empirical model was developed that allows estimating the resulting overall sound pressure, as well as the reduction in sound pressure level, within the defined experimental space. This experimental space is spanned by five independent influencing parameters, namely the Reynolds number, the turbulence intensity, the serration amplitude, the serration wavelength and the angle of attack. The model was validated against different independent data pools and was found to be highly accurate and stable. Two significant interdependencies of $AoA \cdot \lambda/C$ and $Tu \cdot \lambda/C$ were observed. Incorporating the aerodynamic target value from the analysis in Section 2.2.3 permitted the generation of unbiased multi-objective optima, which allow to find the optimum parameter settings for the dilemma of opposing aerodynamic and aeroacoustic trends. This is considered vital for a rotating application of serrated leading edges.

Spectral insights into the noise reduction were obtained by the analysis of single-microphone measurements, which matched fairly well with the previously reported results by others. However, considering the influences of possible external noise sources indicated the need to analyse the cleared spectral noise radiation and reduction for the leading-edge section only. Consequently, a study on the noise radiation characteristics of serrated leading edges and the resulting noise reduction by the use of array beamforming is presented. The chosen approach enables the exclusion of unwanted noise sources that are not attributed to the leading edge. This resulted in a more accurate characterisation of the noise reduction capability of the leading edge serrations. In general, the results compare well with the previous studies, and serrations with high amplitudes and small wavelengths are identified as acoustically most beneficial [120].

The maximum obtained noise reduction for the 2 kHz octave band was found to be $\Delta OASPL = 13.6$ dB, with the observed spectral scaling slightly outperforming the previously reported [1] maximum noise reduction capability in the mid-frequency region, in which the aerofoil self-noise usually begins to attenuate the effectiveness of noise reduction via leading edge serrations [120].

The corresponding ratio of transversal turbulent length scale to serration wavelength ($\lambda/\Lambda_t = 2.6$) appears to be enclosed by the optima for maximum destructive interference effects and for maximum decorrelation effects according to [1]. In addition, a trend of shifting noise sources relative to an increasing serration amplitude is observed, providing the first qualitative experimental evidence in support of the numerically inferred distribution of noise sources along the aerofoil chord according to [74].

With regard to the angle of attack, a clear sensitivity to the high-frequency noise radiation was observed and could be linked to the previously discussed interdependency of $AoA \cdot \lambda/C$. Moreover, spatial identification of the noise sources indicates that this high-frequency noise radiates from the leading edge, underpinning the conclusions drawn on the underlying aerodynamic mechanism in Section 3.3.7.

Finally, the comparison of high and low-turbulent inflow conditions highlights the need for more extensive investigations into the ability of the serrations to reduce trailing-edge noise at low Tu conditions, although supplementary hot-wire measurements show large vortical worm-like structures, which are held responsible for this reduction [120].

In summary, the observed and analysed influences of the individual parameters, as well as the localisation and identification of the noise sources, are considered crucial for a successful transfer of the serrations to low-pressure axial fans. Due to the increased complexity of rotating systems, identification of the various noise source mechanisms appears to be highly restricted. The same applies, although to a slightly less extent, to the aerodynamic effects as well.

III. Rotating Applications

4 Transfer Analysis – From Aerofoil to Rotor

The following chapter deals with linking the findings obtained from rigidly mounted aerofoils, including both aerodynamic and aeroacoustic properties. These findings are interpreted for the eventual implementation of leading edge serrations in rotating applications, such as low-pressure axial fans. Here, a more complex noise generation pattern exists, and the aerodynamic behaviour also needs to be taken into account.

4.1 Acoustic Properties of Low-Pressure Axial Fans

The approach to ascribing all noise generation mechanisms to either idealised monopole, dipole or quadrupole radiators was first put forward by Goldstein and was refined and adopted by many other researchers over recent years. However, based on this analogy, Neise [132] derived a well-known overview of the potential sources of axial-fan noise, as shown in Figure 4-1. The associated qualitative spectrum of the acoustic signature is provided by Wright [133] in Figure 4-2, giving detailed insights into the impact of the different noise sources.

The stated monopole and quadrupole sources are of no technical relevance for the operation range considered for low-pressure axial fans. Monopole noise is noise radiation due to the blade thickness. In this mechanism of noise radiation, a pulsating pressure field is generated due to the motion of fluid when a blade cuts through it, resulting in an unsteady change in the flow rate. Lowson [134] states that this monopole radiation has a negligible impact on blade-tip speeds smaller than the speed of sound or on blade tips with a Mach number $Ma < 1$. The quadrupole radiation, on the other hand, involves the effect of fluid particles in the free stream, undergoing shear stresses based on the motion of the fluid. However, this is considered relevant only for $Ma \geq 0.8$ [135, 136].

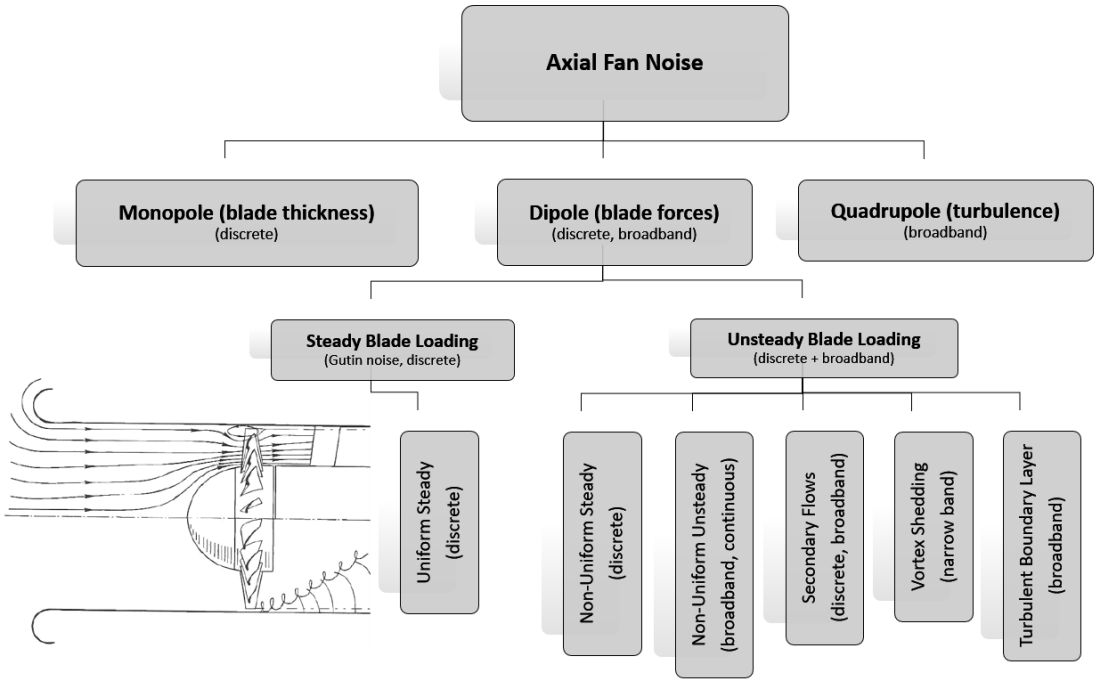

Figure 4-1 Overview of noise sources for fans and blowers according to Neise [132]. Schematic of flow through an axial fan by Kameier [137].

4.1.1 Dipole Noise of Axial Fans

The dipole noise involves flow-induced loading noise, which includes all types of interaction noise between the flow and a rigid surface, such as the blades, the hub, the stator and the casing [138].

Steady Blade Loading: Uniform Steady Flow

For a rotating blade, lift and drag forces are acting on the suction and the pressure side, respectively. Although this loading is constant at a uniform stationary flow, the standing observer perceives pulsing pressure disturbances of a periodic character. As was first described by Gutin [139], these pressure disturbances are radiating in the form of tonal noise, which is also known as 'Gutin noise'. The corresponding frequency at which Gutin noise radiates is the so-called blade-passing frequency (BPF), which is a function of the rotational speed n and the number of fan blades z_B (*Eq. 4-1*). The influence of Gutin noise on the acoustic signature, however, is found to be rather negligible for low Mach numbers [140, 141, 66].

$$BPF = n \cdot z_B \qquad \textit{Eq. 4-1}$$

Unsteady Blade Loading: Non-Uniform Steady Flow

The same conditions as for the Gutin noise, with the exception of a flow field experiencing a spatially non-uniform distribution, causes an unsteady response of the resulting periodic pressure pulses due to the acting lift and drag forces on the fan blades. Once again, the radiation frequency corresponds to the blade-passing frequency BPF, but compared to the Gutin noise, the noise due to an unsteady flow field is radiated with a significantly increased efficiency [142, 137].

Unsteady Blade Loading: Non-Uniform Unsteady Flow

If the non-uniform flow field shows additional unsteady phenomena or, in other words, if the incoming velocity is a function of space and time, broadband components are added to the acoustic signature. Common temporal disturbances of unsteady character are the free-stream turbulence (stochastic) and more coherent turbulent structures such as vortices travelling downstream and interacting with the fan blades. As stated by Sharland [142], rather high levels of the free-stream Tu are required for significant noise radiation, whereas large-scale structures in the form of vortices or eddies are highly efficient in generating broadband noise [66]. This phenomenon is not restricted to rotating machines but represents a general noise generation mechanism for lifting surfaces, as also described in Section 3.1.2. A brief overview of recent research with regard to rotor-turbulence-interaction (RTI) noise for axial fans is also given in Section 4.1.2.

Unsteady Blade Loading: Secondary Flows

Secondary flows are a wide and still important area of research. In particular, the backflow effect for the blade-tip region is mentioned, in which fluid travels from the pressure to the suction side of the blades. Vortices are generated and interact with the rigid blade surface in the tip region, leading to highly unsteady pressure fluctuations, as investigated by Kameier and Neise [143] and Na et al. [144]. Another phenomenon is large-scale structures separating from a surface, be it under stall conditions from the suction side of the blades or due to a non-optimal design from the hub region of a rotating machine. Depending on the origin of the above-mentioned flow phenomena, they can be non-synchronised (rotating instabilities) or synchronised (rotating stall) with the rotor speed. Moreover, the counter-rotating structures, generated by leading edge serrations, are also classified as secondary flows, which have the potential of interacting with neighbouring structures.

Unsteady Blade Loading: Vortex Shedding

No differences exist in the mechanism of vortex shedding for rigid aerofoils and axial fans, but the resulting acoustic signature changes its characteristics. Vortex shedding can be of either stochastic or periodic nature. For example, stochastic shedding takes place at a sharp aerofoil trailing edge, showing a turbulent boundary layer. Another example is small-scale separation effects, such as those that occur in the instability region of a fan characteristic curve. These pressure fluctuations are radiated broadband and are able to dominate the acoustic signature [145]. At congruent inflow, though, the first mentioned trailing-edge broadband noise due to the sharp trailing edge is the more pronounced source [142].

At conditions of deep stall, however, the shedding process becomes more periodic, as is also the case for blunt aerofoil trailing edges since a Kármán vortex street is generated. In this case, discrete noise of narrow-band character is radiated. Clear tonal effects are prevented by the radius dependence of the circumferential velocity, hence resulting in a spanwise shift of the radiating frequency. Tonal effects, though, are observed when periodic shedding for rigid bodies occurs, as can be the case for stators, struts, inlet guide vanes or the casing.

Unsteady Blade Loading: Turbulent Boundary Layer

As already described for the single aerofoil in Section 3.1.3, pressure fluctuations within the turbulent boundary layer result in broadband noise radiation, but the global impact is of quite limited extent.

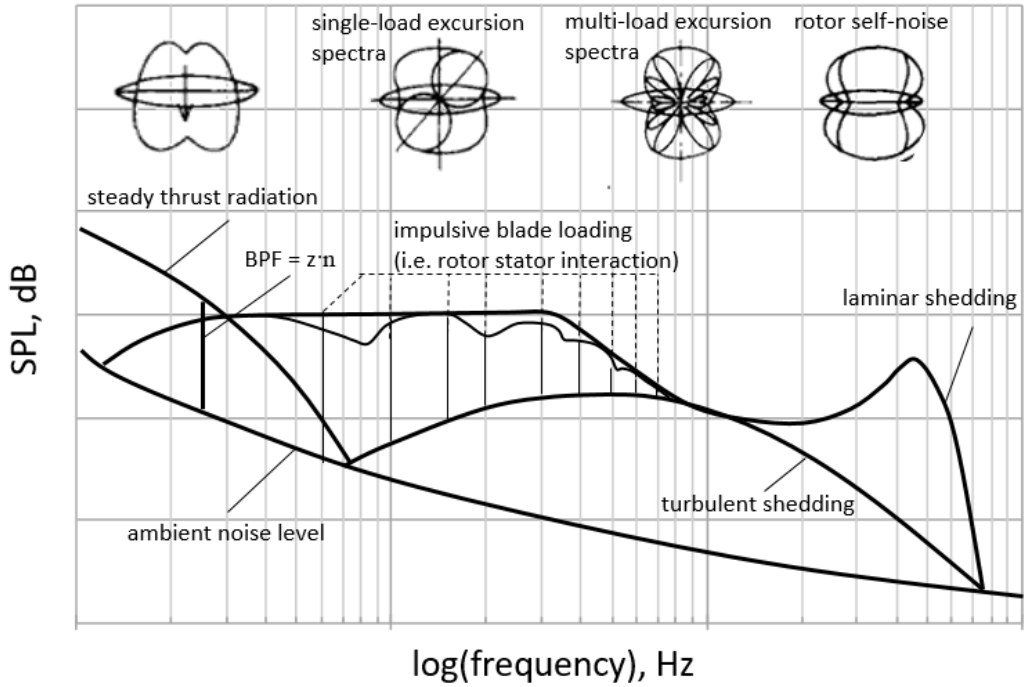

Figure 4-2 Schematic of acoustic spectrum of axial flow machines, adopted from Wright [133]. Reproduced with permission from Elsevier.

4.1.2 Rotor-Turbulence-Interaction Noise

Under turbulent conditions, a rotor blade can radiate noise of broadband character. If, on the other hand, large-scale turbulent structures are cut by more than one blade, the noise can also become narrow-band, with peaks around the BPFs or their harmonics [146]. The underlying effect is a blade-to-blade correlation.

Schneider [147] experimentally investigated ducted low-pressure axial fans while varying inflow turbulence. Apart from developing a semi-empirical noise prediction model, Schneider observed that the level of inflow turbulence clearly affects the radiated noise in the low-to-intermediate frequency region. Also partly due to the passive generation of turbulence via turbulence grids, the maximum effects can be seen for the pre-stall region at high flow rates. These findings were also confirmed by Reese et al. [145], who numerically modelled the previously described setup, aiming at predicting the rotor-turbulence-interaction (RTI) noise by comparing different modelling approaches, and a good fit to experimental results was obtained. Furthermore, a significant broadband noise contribution under turbulent inflow conditions was also confirmed experimentally by Carolus and Stremel [148], who measured the pressure fluctuations of a ducted low-pressure axial fan. Combined analysis of surface pressure fluctuations and the radiated far-field noise led to increasing high-frequency components with increasing chordwise distance from the leading edge of the fan blades. This observation indicates that the turbulent boundary layer is the driving parameter for the high-frequency blade surface pressure, unaffected by the induced free-stream turbulence. The high sensitivity of the surface pressure towards the boundary layer conditions is particularly distinct for the suction side of the blades. However, the distribution of the low-frequency components, which correspond to acoustically compact blades, appears to be clearly dominated by the region close to the leading edges, radiating RTI noise, and hence also by the level of incoming turbulence.

The effect of inlet distortion on the tonal noise generation was investigated by Daroukh et al. [149]. Based on RANS simulations, the results indicated a strong effect in the blade-tip region, leading to an overall noise increase of up to 3 dB. A considerable modification of the wake in the blade-tip region is suggested to be responsible, hence leading to significant variations in the noise level at the BPF.

Zenger et al. [150] investigated two axial fans with forward-skewed and backward-skewed blades at varying levels of grid-generated turbulence ($7\ \% \leq \mathrm{Tu} \leq 28\ \%$), including noise source localisation methods using a microphone array method. They observed a noticeable increase in broadband noise at frequencies below 4 kHz. In line with previously reported results of Carolus and Stremel [148], the main turbulence-sensitive sources were found to be close to the blade's leading edges. Moreover, the sensitivity of the tested rotors to the incoming turbulence turned out to depend on the chosen fan design, resulting in maximum amplifications for forward-skewed blades. At clean inflow, forward-skewed fans clearly showed superior performance with regard to the radiated noise. However, increasing the level of turbulence shows a local increase in the SPL of up to $\Delta\mathrm{SPL} = 15$ dB, whereas only a maximum increase of $\Delta\mathrm{SPL} = 3$ dB is observed for the backward-skewed fan, already showing high SPL at low Tu for the low-frequency range. The explanation provided is that at forward-skewed blades, the approaching turbulent structures have no possibility of migrating outwards along the span as is the case for the backward-skewed blades. Hence, no dissipation of turbulent energy can take place before the interaction with the fan blades takes place, resulting in strong pressure fluctuations and, consequently, in a more distinct increase in noise.

4.1.3 Spectral Composition of Acoustic Signature

As briefly discussed for the qualitative spectrum of Wright [133] in Section 4.1.1, Figure 4-3 shows measurement results by Biedermann et al. [151], in which the spectral acoustic signature of a single NACA65(12)-10 aerofoil in a free-stream open jet and the signature of a ducted 6-blade fan at design conditions are compared. The test rig and the testing conditions are discussed more extensively in Section 4.3. Both fan and single aerofoil feature the same aerofoil profile when the level of the incoming turbulence is varied.

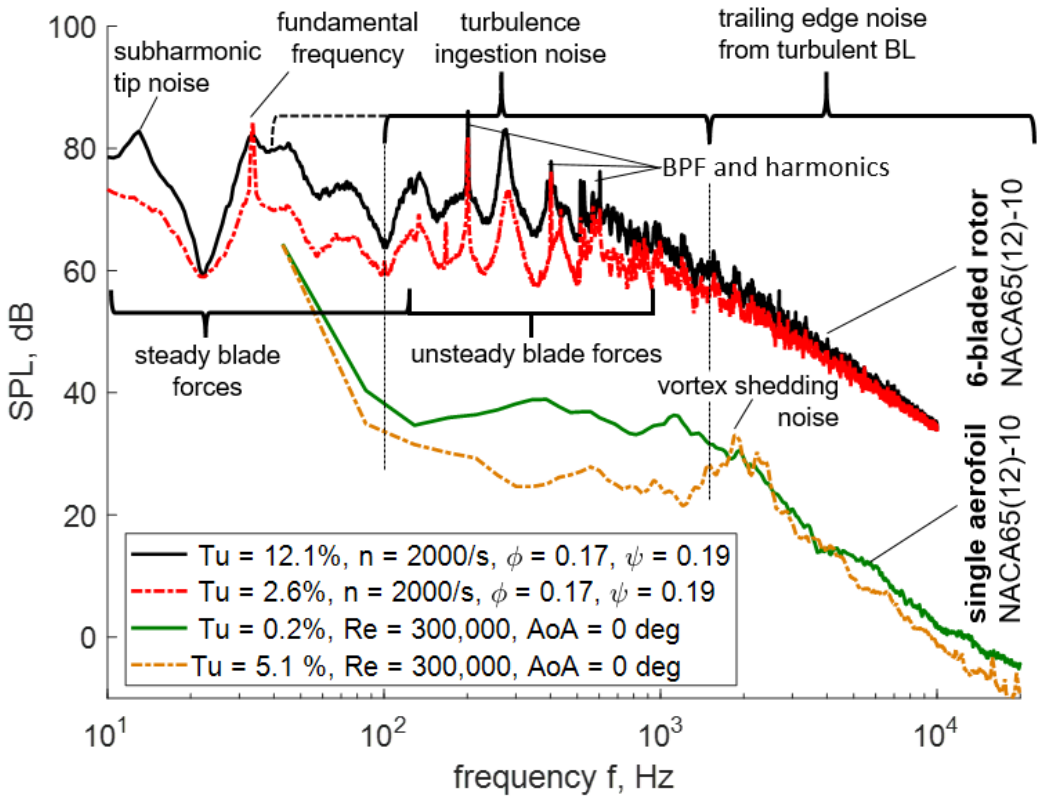

Figure 4-3 An example of juxtaposition of the radiated sound pressure level of a single NACA65(12)-10 aerofoil vs. the acoustic signature of a 6-bladed axial fan, featuring the NACA65(12)-10 as fan blades [151]. Comparable operation conditions in rigid and rotating frame.

It becomes apparent that, even though both signatures show a sensitivity to higher levels of incoming turbulence, the complexity of the rotor's aeroacoustic signature is significantly increased. For the single aerofoil under high-turbulent inflow conditions, level-dominating noise of broadband character is radiating from the leading edge. For the rotor, on the other hand, additional noise sources might play a level-relevant part in the acoustic signature [151]:

- blade-tip effects
- noise due to secondary flows
- rotor-strut-interaction noise
- trailing-edge vortex shedding noise
- large-scale separation noise

The relevance of these noise sources varies as a function of the particular operating point on the fan's characteristic curve, described by the flow coefficient φ. When it comes to the implementation of leading edge serrations, only little is known about the aeroacoustic and aerodynamic efficiency of this passive noise reduction application under non-optimal operation conditions [151]. Moreover, for rating the noise reduction capability of leading edge serrations, additional boundary conditions, not yet investigated, are to be taken into account.

4.2 State of the Art — Rotating Leading Edge Serrations

Every now and again the scientific community shows interest in applying serrated leading edges to rotating machinery to benefit from the well-known effects of stall delay and acoustic noise reduction as described for rigidly mounted aerofoils. However, fundamental studies on rotating serrations, be it numerical or experimental, with an aerodynamical or an aeroacoustical focus, are a rare sight. Consequently, only little is known about the efficiency of serrated leading edges when rotating, about possible blade interaction effects, about effects of a radius-dependent velocity profile on noise reduction, or about possible three-dimensional effects along the span or interaction between serrations and the blade-tip region of rotating machines.

Aerodynamic Application

Asghar et al. [152] applied leading edge serrations to small-scale aircraft propellers. The focus of this experimental study was to investigate the aerodynamic performance based on three regions. First, in the tip region, the effects of streamwise vortices on the usual boundary layer separation were investigated. Second, in a mid-radius region, the serration effects were described while neglecting tip or hub effects. Third, the serration effects were examined also in a region close to the hub, where separation at low Reynolds numbers might occur. For the study, one rotor with serrations of constant wavelength and one with a constant inclination angle $\theta_{Serr} = f(A/\lambda)$ were compared against a baseline rotor. Unfortunately, only the overall performance was tested; hence no information on the underlying principles that are contributing to the changes in efficiency was provided. One of the main findings was that serrations of constant inclination angle θ_{Serr} are outperforming the constant-wavelength rotor. Applying serrations only to the mid-radius region showed an increase in efficiency of up to +6 %, whereas an increase of +5 % was obtained for the tip region. On the other hand, a serrated hub region contributed only insignificantly, showing only a slight delay of separation due to the increased vorticity. One interesting outcome of the study was that the spanwise combination of serrated regions not necessarily led to an accumulation of effects. The increase in efficiency for a serrated tip and mid-radius region decreased to +5 %, the root and tip regions showed +4 %, and a combination of root region plus mid-radius serration yielded +2 %. The fully serrated rotor showed an overall performance increase of only +1 % at a constant incidence angle and of +2.5 % at a constant wavelength.

Another numerical study on the hydrodynamic effect of leading edge serrations for marine propellers was conducted by Ibrahim and New [153]. Here, only little improvement in thrust (up to + 1.5 %), associated with decreases in efficiency, was observed at low advance ratios, whereas for higher ratios a negligible increase in efficiency and marginally lower thrust (< 1 %) was reported. However, the poor effect of the leading edge serrations might be attributed to the low serration amplitude and the large serration wavelength of the three-blade propeller tested. As reported for rigidly mounted aerofoils (Section 2.1.2), this again indicates the controversial nature of leading edge serrations, being highly dependent on the chosen application range, including rotor shape and operation conditions.

A large-scale low-pressure rotor of D = 2.24 m, equipped with 16 blades and a significant tip clearance of 6.5 % of the blade radius, was modelled numerically by Corsini et al. [154]. Leading edge serrations were applied only to the outer region close to the tip of the fan blades. In summary, the serrated leading-edge geometry showed a reduced performance curve of the pressure rise pre-stall but also higher pressure coefficients beyond stall. These findings appear to be qualitatively similar to those obtained for rigidly tested aerofoils (Section 2.1.3) featuring serrated leading edges. Moreover, counter-rotating structures, too, were identified for the serrated blade-tip region, providing evidence for a strong attachment of the flow in this region, thus resulting in a stall delay due to the serrations.

In order to choose an appropriate number of serrations, associated with adequate serration dimensions, the authors presented a design methodology to determine three parameters for a desired vorticity distribution at the trailing edge of the blade tip, namely the number of serrations (starting at blade tip), the size of the serration wavelength and the size of the amplitude. This design approach is based on numerical LES studies of two rotors. Defining a diffusion factor according to Lieblein [155] and using it to define the blade-tip leakage vortex, the authors demonstrated that the outer 20 % of the fan blades is responsible for the separation and hence the strong stalling effects. In reverse conclusion, the outer 20 % of the blade span is the only region where serrations are applied. The size of the serration amplitudes is defined by the relative velocity distribution at the rear third of the blade chord. The studied vortex intensity of serrations was used to define an optimum between drag increase pre-stall and lift recovery post-stall. Finally, the serration wavelength was chosen based on an optimum defined in a previous numerical study of a rigidly mounted aerofoil by Corsini et al. [156].

Aeroacoustic Application

One of the first studies reporting on the use of leading edge serrations for noise reduction of rotors was an experimental study by Arndt and Nagel [157]. A two-blade model rotor with NACA0012 blades was investigated, revealing a reduction in rotational noise, but unfavourable changes in the blade loading also led to losses in aerodynamic efficiency.

Taking a lead from the previously presented aerodynamic study of serrations for large-scale low-pressure axial fans, Corsini et al. [158] extended the focus of their research to include the aeroacoustic performance. Once again, a numerical study for a baseline rotor and a rotor equipped with serrations for the outer 20 % of the blade span was conducted and validated against experimental data. Numerically, a reduction in the overall sound power level of $\Delta OAPWL = 2.3$ dB was obtained. The radial distribution of the noise sources, however, shows a different pattern, with even a noise increase for the near-hub region, whereas especially close to the blade tip significant noise reduction effects for the serrated region were observed, resulting in an overall noise reduction. The authors suggested that the blade-tip vortex is the cause of this reduction. This is supplemented by observations of changes in the axial and the tangential velocity pattern near the blade tip from periodic (f = BPF) to bimodal (f = BPF and $2 \cdot$BPF). Moreover, visualisation of the acoustic sources indicated a complete redistribution when serrations are implemented, affecting the full blade, even though only the upper 20 % of the blades were serrated.

Reducing the rotor dimensions to those of classic automotive cooling fans, an experimental study on the aeroacoustic effect of leading edge serrations was carried out by Zenger et al. [159] for a fan diameter D = 0.495 m, applying serrations to state-of-the-art fan blades. Generating high-turbulent inflow conditions via a turbulence grid in close vicinity to the rotor, serrations of 5 % chord in serration amplitude and decreasing serration wavelength from hub to tip were added to forward-skewed blades, thereby exceeding the original chord length of the blades. Measurements took place in a test chamber according to ISO 5801 [160] at low- and high-turbulent conditions. Even though the effective blade surface increases, the static pressure rise

shows a marginal decrease for moderate to high flow rates when compared to the non-serrated baseline. The same is true for the aerodynamic efficiency, showing a loss of up to $\Delta\eta$ = -10 %. However, post-stall, no significant differences between the baseline and the serrated rotor were observed. Regarding the aeroacoustic performance, slightly lower levels of maximum ΔOASPL = 1 dB for the high-turbulent and ΔOASPL = 1.8 dB for the low-turbulent case were obtained at maximum flow rates. The main reduction effects were attributed to the tonal components of the radiated noise, indicating that the serrations play a role in reducing unsteady blade forces. These effects turn out to be quite similar to the effects of blade skew and sweep.

Discouraged by the previously obtained results, the researchers chose flat-plate blades for a subsequent study of more rudimentary character [161]. Moreover, also fan blade skew and sweep were disregarded. Four configurations of varying serration amplitude (13 – 17 %·C) and serration wavelength (7 – 10 %·C) were cut into the fan plates. Due to the flat plates chosen, these serrations were only of a two-dimensional shape. As is known from a previous analysis of flat plates under highly distorted inflow conditions, flat plates are more prone to ATI noise than realistically profiled aerofoils [162], especially when possessing a blunt leading edge. As a consequence, leading edge serrations are more efficient for the reduction of flat-plate noise [67, 91]. Compared to the previously analysed state-of-the-art rotor, the sound pressure level of the baseline rotor increases by almost 10 dB at low turbulence and high flow rates. Moreover, the aerodynamic efficiency, too, decreases considerably. Varying the turbulent conditions had only little effect on the noise radiation of the baseline rotor. However, given the increased noise reduction potential, the introduced leading edge serrations contribute to a broadband noise reduction at low turbulence of up to ΔOASPL = 10 dB for maximum serration amplitude and minimum serration wavelength, with the wavelength as the driving parameter. At high Tu, the noise reduction is more constant, at a level of around ΔOASPL = 5 dB, without any clear dependency on the serration parameters. Aerodynamically, the leading edge serrations lead to an increase in efficiency and in static pressure rise when compared to the reference rotor. This increase is attributed to aerodynamically beneficial effects in the blade-tip region, where the serration-generated vortical structures in the streamwise direction are expected to interact with radial flow components of the blade, hence reducing the tip leakage effects, as also outlined by Corsini et al. [154].

4.3 Test Rig for a Rotating Application

For transferring the investigated aerofoils to the rotating frame by means of low-pressure axial fans, a test rig needs to be defined. The key requirements, leading to the definition of the test rig, are fourfold:

- simultaneous measurement of aerodynamic and acoustic properties
- high levels of grid-generated turbulence under the same (near) isotropic conditions as for the rigidly mounted aerofoils
- reasonable homogeneity of inflow velocity profiles
- comparable to the industrial standards to pave the way for practical applications

The need to provide high levels of turbulence at a sufficient distance from the tested rotors, and the possibility of measuring the acoustic signature of the fan on both the suction and the discharge side while monitoring the aerodynamic performance, were key factors in the choice of a test rig according to *ISO 5136 – Determination of sound power radiated into a duct by fans and other air-moving devices – In-duct-method* [163]. Moreover, the ISO 5136 also represents the commonly used standard in the industry for rating the acoustic performance of fans. This excludes the use of a test chamber as described in the ISO 5801 [160], which would be an alternative to the chosen in-duct-method but focusses mainly on the aerodynamic performance. Moreover, it provides only limited possibilities of generating a significant level of turbulence at a sufficient distance upstream of the rotor. Figure 4-4 shows the schematic of the chosen test rig, which is further outlined in Sections 4.3.1 – 4.3.2. Significant parts of the presented setup are also published by Biedermann et al. [164, 151].

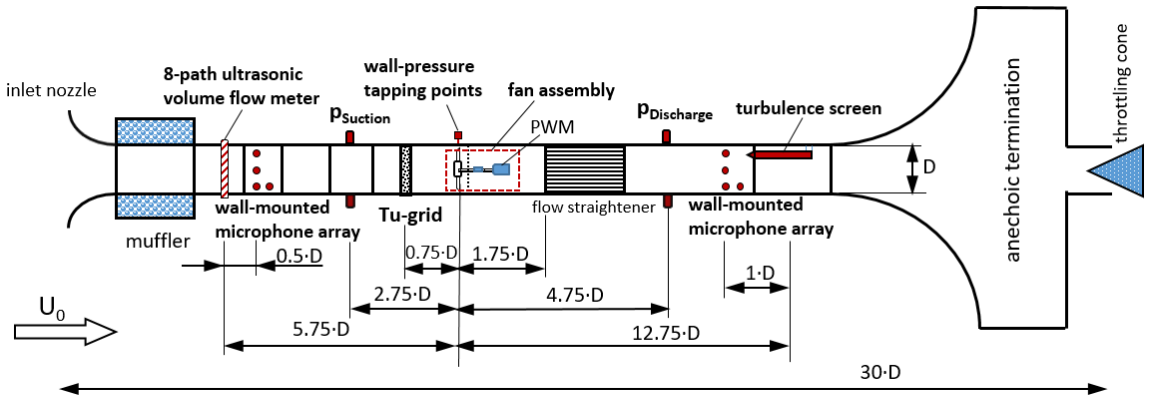

Figure 4-4 Schematic of the test rig according to DIN ISO 5136 [151, 163] for the in-duct-method to simultaneously test the aerodynamic and aeroacoustic performance of rotating machines.

4.3.1 Aerodynamic Properties

The inlet nozzle in Figure 4-4 ensures smooth inflow conditions. The free-stream velocity U_0 and, consequently, the flow rate is obtained by using an eight-path ultrasonic volume flow analyser or a pitot-static tube at x/D = 5.75 upstream of the axial fan. Characterisation of the static pressure rise is achieved by differential pressure measurements between the suction and the discharge side of the fan assembly, where for each location six pressure tapping points are used for obtaining the circumferentially averaged static pressure. On the suction side, the pressure measurement takes place x/D = 2.75 upstream of the rotor, whereas for the discharge side, the measurement plane is located x/D = 1 behind a star-type flow straightener according to ISO 5801 [160]. The flow straightener is used to convert the swirl back to pressure energy and to enable aeroacoustic measurements of increased accuracy. At x/D = 0.75 upstream of the rotor blade's leading edges, different turbulence grids are inserted in order to generate high-turbulent and near-isotropic inflow conditions. Grid design took place according to the method

proposed by Laws and Livesey [2], being congruent with the design method for the rigidly mounted single aerofoils analysed previously in Section 3.3.4 [164]. The resulting grid-generated turbulent properties are further analysed in Section 4.4. However, due to the specified dimensions of the test rig according to the ISO 5136 standard and the need to implement turbulence grids, the previously described determination of the static pressure rise (suction vs. discharge side) not only results in a static pressure rise of the rotor itself but also includes effects of the turbulence grids and the flow straightener. The pressure loss that occurs due to the turbulence grids used is compensated for by specifying the non-dimensional pressure loss coefficient ζ according to *Eq. 4-2*.

$$\frac{\Delta p_{Grid}}{\rho} = \zeta \cdot \frac{U_0^2}{2} \qquad \textit{Eq. 4-2}$$

Finally, an automatically driven throttling cone on the discharge side of the test rig allows the point of operation to be controlled. For monitoring the aerodynamic performance of the tested fan, the system efficiency η_{system} is defined according to *Eq. 4-3*, with Δp being the static pressure rise (suction vs. discharge pressure), $\dot{Q}$ the flow rate, U_{el} the electric voltage and A_{el} the electric current. However, for the analysis, only the electrical power of the fan-driving unit is utilised via monitoring the voltage supply and measuring the amperage, using a measuring calliper. Accordingly, the definition used for the efficiency includes the electric efficiency of the puls-width modulated (PWM) electric motor and represents the efficiency of the fan assembly instead of the pure efficiency of the rotor [164].

$$\eta_{system} = \frac{P_{aero}}{P_{el}} = \frac{\Delta p \cdot \dot{Q}}{U_{el} \cdot A_{el}} \qquad \textit{Eq. 4-3}$$

4.3.2 Aeroacoustic Properties

Aeroacoustically, the test rig is treated with a muffler to dampen the suction-side noise and with an anechoic termination for the discharge side in order to prevent back-reflections of the radiated noise due to impedance differences at the duct end. The walls of the duct are made of steel plates with a thickness of 4 mm and can, particularly for the low- and intermediate-frequency range, be considered reverberative. Hence, with the boundary condition of the sound particle velocity at the walls being equal to zero, the Bessel coefficients $j'_{m,n}$ can be determined, and the cut-on frequency or, equivalently, first duct mode can be determined according to *Eq. 4-4*, in which for the free-stream velocities considered, only minor influences on the resulting frequencies are present. For a duct of diameter D = 0.4 m and a maximum free-stream velocity of $U_0 = 10$ ms^{-1}, the cut-on frequency turns out to be $f_{0,1} = 501$ Hz ($j'_{1,0}$=1.84118).

$$f_{m,n} = \frac{j'_{m,n}}{2\pi R} \cdot c \cdot \sqrt{1 - Ma^2} \qquad \textit{Eq. 4-4}$$

Below the frequency of the first duct mode, the sound field consists solely of propagating plane waves, whereas for higher frequencies the sound field acquires an increasingly diffuse character, leading to increased interaction for higher duct modes. For obtaining high-quality acoustic information, measurements at varying circumferential positions in combination with sufficiently high averaging are required. Moreover, the proper choice of microphone treatment plays a crucial role in reducing the effects of aerodynamic disturbances of the aeroacoustic signals

gathered. The ISO 5136 standard proposes the application of nose cones for free-stream velocities $U_{0,max} \leq 20$ ms^{-1} and turbulence screens (sampling tubes) for $U_{0,max} \leq 40$ ms^{-1}. For an expected free-stream velocity of $U_{0,max} \approx 10$ ms^{-1}, even foam balls are considered feasible. All these treatments aim at reducing the possible influence of aerodynamic pressure disturbances to a minimum. However, for the current setup, a slightly different approach was chosen. Aiming at reducing blockage effects in the flow, which occur particularly for foam balls, 1/4" B&K condenser microphones were chosen and flush-mounted to the inner duct wall. These microphones exhibit a side-vented pressure field design in order to ensure a proper equalisation of the atmospheric pressure. Even though low lateral magnitudes of aerodynamic pressure fluctuations due to smooth inflow conditions at the suction side and de-swirled flow on the discharge side can be assumed, the existence of significant pressure fluctuations within the duct boundary layer cannot be neglected. The presence of protection grids, however, leads to a spatial separation of the microphone membrane from the aerodynamic pressure fluctuations within the boundary layer. On the other hand, these microphone grilles are prone to induce additional noise due to vortex shedding and resonance effects. Investigations by other researchers indicate that especially for low Mach numbers, the increase in noise with a protection grid, as compared to the membrane only case, is marginal in a frequency range of $2 \leq f \leq 12$ kHz [165]. Further investigations [166] came up with the suggestion to mount the microphones as flush as possible in order to reduce noise from alternative mounting possibilities, such as recessing (vortex shedding noise) or protruding the microphones (higher turbulence). In order to increase the accuracy and reliability of the aeroacoustic measurements, three microphones were used for the suction and discharge side each, distributed equidistantly in the circumferential direction of the duct (Figure 4-5). For validation purposes, another two microphones were included with axial displacement. Finally, as can be seen in Figure 4-4, a 1/2" B&K 4133 condenser microphone was used in a B&K UA0463 turbulence screen, featuring high-degree turbulence noise suppression and especially constructed for the measurement of airborne noise in air ducts. The turbulence screen is mounted in-line with the duct at a distance of 0.04 m from the wall, allowing direct comparison to the measurement procedure according to the ISO 5136 standard.

For validation, measurements with the 1/2" microphone and the B&K 4133 turbulence screen were performed inside the duct, where aerodynamic disturbances are reduced to a minimum (Figure 4-5). Comparing the acoustic signal at operation conditions to the averaged signal of the three wall-mounted microphones shows a remarkable fit in a frequency range of up to $f \leq 2$ kHz. The increasing gap between the signals at higher frequencies is due to a construction-conditioned damping effect of the slitted tube. Even at frequencies above $f > 2$ kHz, the wall-mounted microphones show no masking effects and prove their ability to capture the acoustic signature.

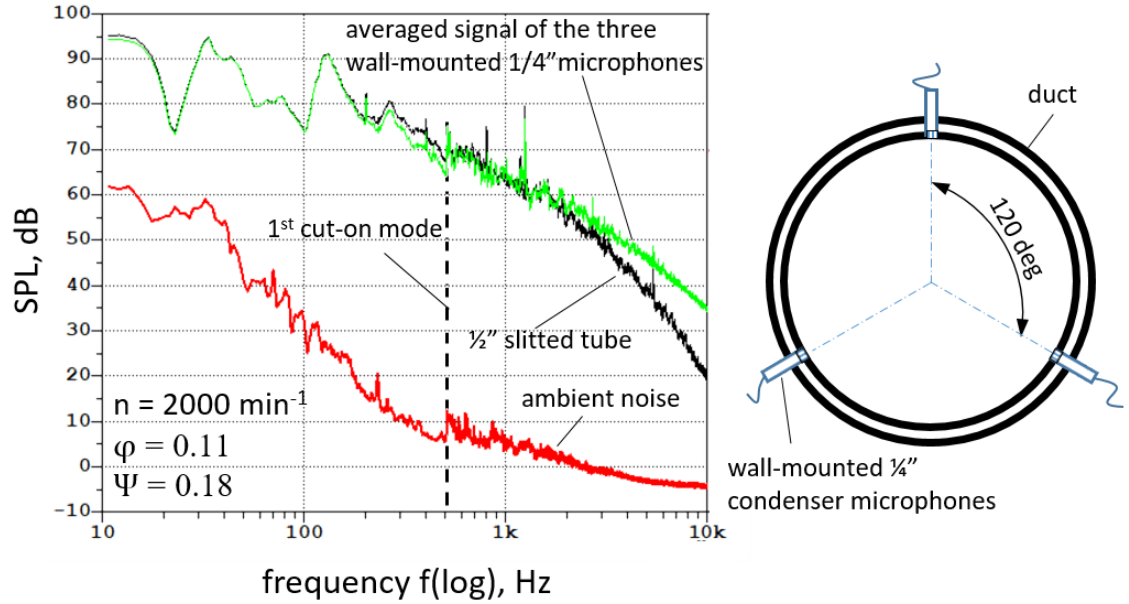

Figure 4-5 Left: Comparison of the acoustic spectra of the signals obtained via the three averaged 1/4" wall-mounted microphones and the 1/2" microphone with slitted tube, relative to the ambient noise level. Right: Sketch of the circumferential distribution of the wall-mounted microphones inside the duct.

The fan assembly is shown in Figure 4-6, in which the rotor and the electric motor are mounted on a spindle. Special care was directed to the number and location of the struts. Four M8 threaded rods run through the hollow fan spindle, each forming two struts, which were, for stability reasons, additionally supported by small steel tubes and fixed via locknuts on the outside of the duct. In order to prevent the transfer of solid-borne noise, shock absorbers were mounted between duct and fastening. The first set of struts was mounted 0.2 m (x/D = 0.5) downstream of the fan, and the second set 0.4 m (x/D = 1). The distance between rotor and struts was maximised in order to reduce the effects of rotor-strut interaction to a minimum. All struts were, in addition, equipped with Scruton wires to suppress eventual periodic vortex shedding. The rotational speed of the rotor was obtained by using a triaxial acceleration sensor on the fan spindle, representing a minimal-invasive high-resolution method while, in addition, providing information on the vibrations of the system [164]. The signal was analysed in the frequency domain at a frequency resolution of $\Delta f = 0.25$ Hz, giving a measurement accuracy for the rotational speed of $\Delta n = \pm 7.5$ min^{-1} [164].

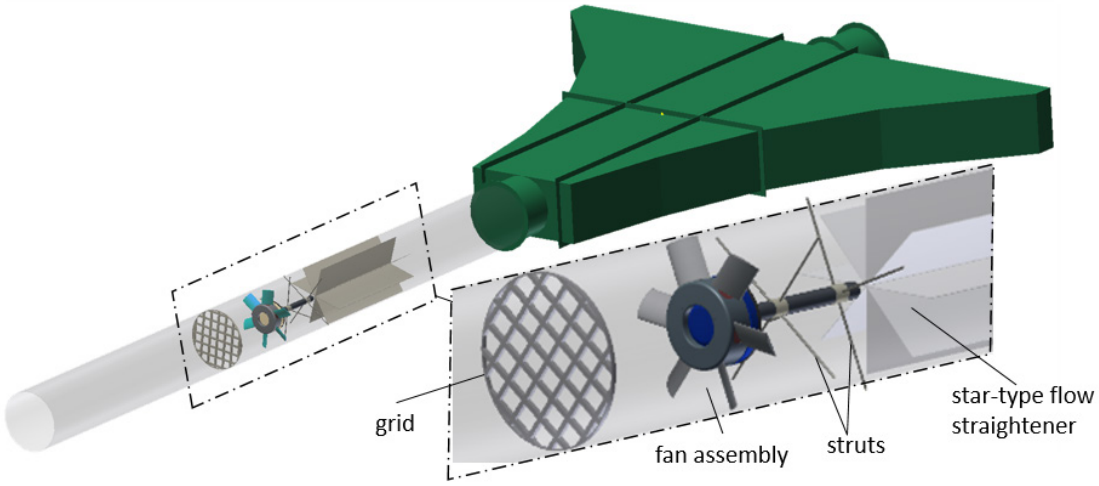

Figure 4-6 Mounted fan assembly and anechoic termination. The zoom shows the chosen strut configuration of the setup [167].

Information on the unsteady wall-pressure field in close vicinity to the blade tips is expected to provide additional insights into the effect of leading edge serrations [151]. Therefore, two pressure tapping points (Figure 4-7) are defined at a circumferential distance of one blade passage, that is, at 60 deg. As in the procedure described by Möser and Neise [168], for each tapping sensor, a cannula tube with an inner diameter of 1.2 mm ($f_{Cut\text{-}On} \approx 8.3$ kHz) is flush-mounted to the duct surface with the purpose of communicating with the pressure field inside the duct. On the opposite side of the cannulas, a rapid prototyped coupler is used, incorporating a 1/4" B&K condenser microphone in order to gather information on near-field unsteady wall-pressure phenomena. Apart from calibrating the level of the sensors, knowledge on the phase between the latter is of essential importance to justify an interpretation of the results obtained [151]. Accordingly, two capsules of a sound intensity probe are employed, showing no significant change in phase up to frequencies of 4.5 kHz [151] (Appendix D.1).

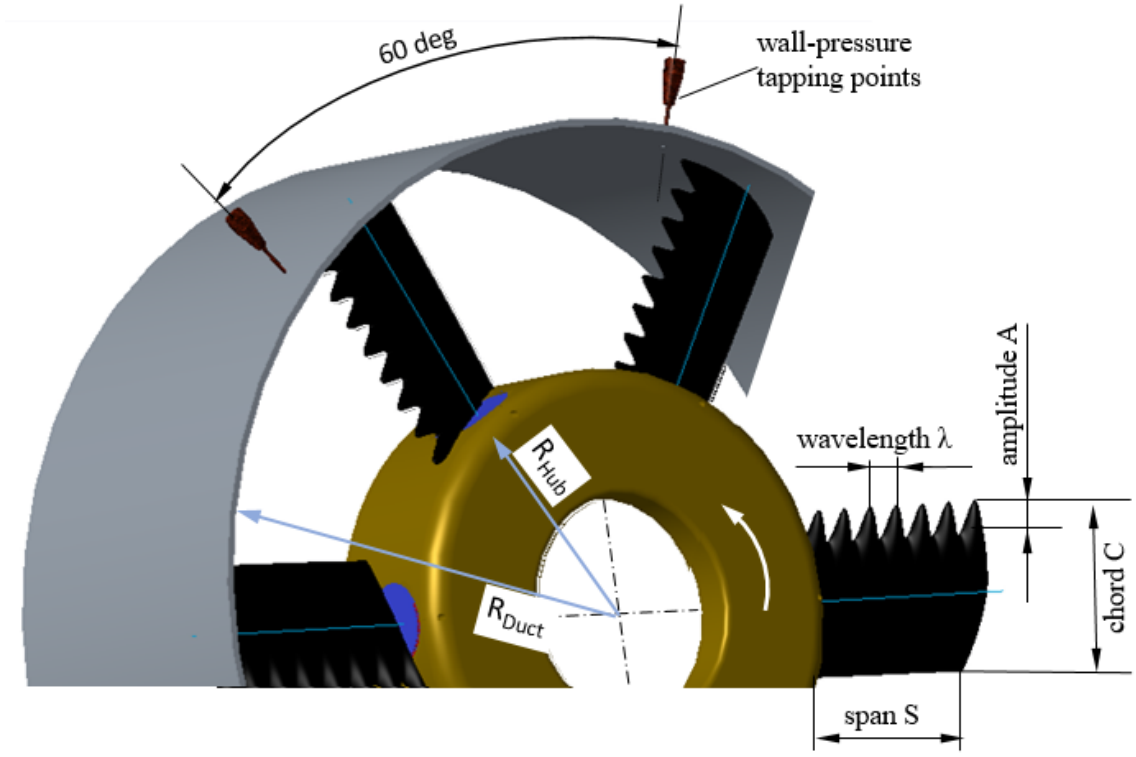

Figure 4-7 Rotor and duct, including wall-pressure tapping points to obtain near-field information [151].

4.4 Turbulent Inflow Conditions

In this section, an extensive analysis of the inflow conditions of the defined test rig, presented in Section 4.3, is given. Parts of this study have also been published by Biedermann et al. [164, 167].

The general purpose of this study focusses on turbulence-generated rotor interaction noise, in which the leading-edge noise of the rotor blades is expected to represent the dominant noise source [169, 145, 146]. Hence, a high level of turbulence is required. Recent studies and noise prediction models usually refer to turbulence of isotropic or near-isotropic character, including the analysis of the rigidly mounted aerofoils in Section 3. To enable a comparison, the same requirement is also applied to the rotating domain. According to Laws and Livesey [2], biplane square meshes with a constant ratio of mesh size and bar diameter of $H/d = 5$ are again defined to generate an elevated level of turbulence of high isotropic character at a sufficient distance from the grid. Table 4-1 and Figure 4-8 (left) show the grids used for the presented study, including relevant design parameters [167].

Table 4-1 Grid nomenclature and parameters of tested grids for the ducted test rig according to DIN ISO 5136.

Type	Unit	G_{00}	G_{01}	G_{02}	G_{03}	G_{04}	G_{05}
$\mathbf{d_{Bar}}$	[m]	--	20	16	12	8	4
$\mathbf{H_{Mesh}}$	[mm]	--	100	80	60	40	20
$\mathbf{H/d}$	[--]	--	5	5	5	55	5

For obtaining data on the local distribution of the free-stream velocity and the grid-generated turbulence in the duct, 1D hot-wire measurements were conducted. A rotating duct (Figure 4-8 right) was implemented in the test rig, where the hot-wire probe was mounted and traversed in radial direction from duct wall to the centre of the duct. Over the measurement duration of 60 seconds for each radial position, the channel rotated by 360 deg at constant velocity normal to the measurement direction of the hot-wire probe, covering the full angular path. The hot-wire data with a spectral resolution of up to 10 kHz were averaged in angular steps of 10 deg, producing over 53,690 samples per step. The turbulence grids were located $\Delta x = 0.3$ m upstream of the probe location, enabling the generated vortices to break down and mix towards isotropy. The probe location was chosen according to the imaginary position of the fan during the aeroacoustic experiments [164].

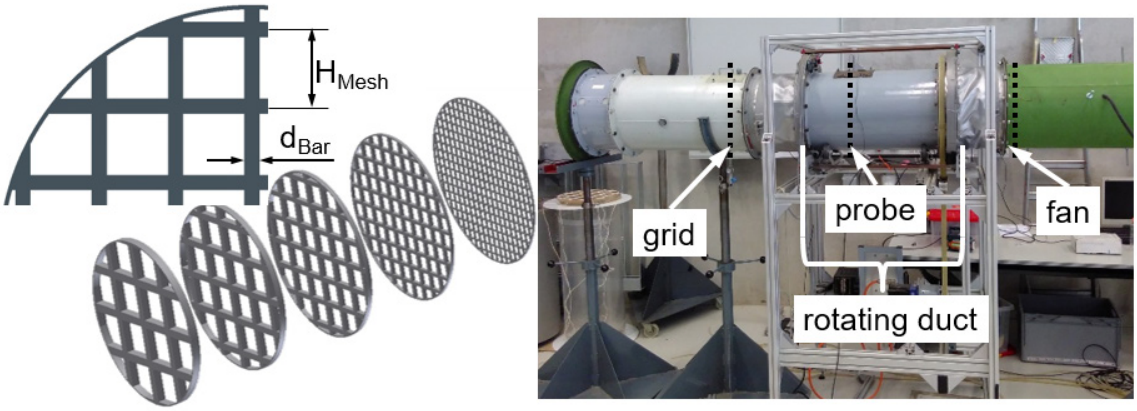

Figure 4-8 Rotating duct, implemented in the test rig for the analysis of the turbulent inflow properties [164].

Figure 4-9 shows results of the obtained distribution of the velocity, the turbulence intensity and the longitudinal length scale in the duct with the coarsest turbulence grid applied. The contours of all other tested grids are presented in Appendix D.2 and D.3. The velocity contour in Figure 4-9 (left) shows the features of the classical turbulent velocity distribution in the form of high gradients close to the wall. The pattern appears to be quite uniform, where the grid is expected to possibly act, apart from generating turbulence, as flow straightener, especially stabilising the outer regions, where the boundary layer is located [167]. Nevertheless, the non-uniform character of the G_{01} velocity pattern hints at the influence of the grid bars, located 0.3 m upstream. Overall, the results obtained show a reasonably good homogeneity and are considered to be sufficient for the intended purpose [164].

Moving the focus to the turbulence intensity, a similar pattern to that of the velocity distribution can be observed. For the grid G_{01}, turbulence intensities of up to $Tu \leq 20$ % are achieved (Figure 4-9, centre), showing a uniform distribution in the centre of the duct. Towards the outer regions, a significant increase in the turbulence intensity is visible, which can clearly be ascribed to the decreasing denominator in the mean velocity due to the no-slip condition at the wall [167]. The integral length scale was obtained by fitting the one-sided power spectrum

of the velocity fluctuations to the formulation of isotropic and homogeneous turbulence as described by Hinze [13] in *Eq. 3-35*.

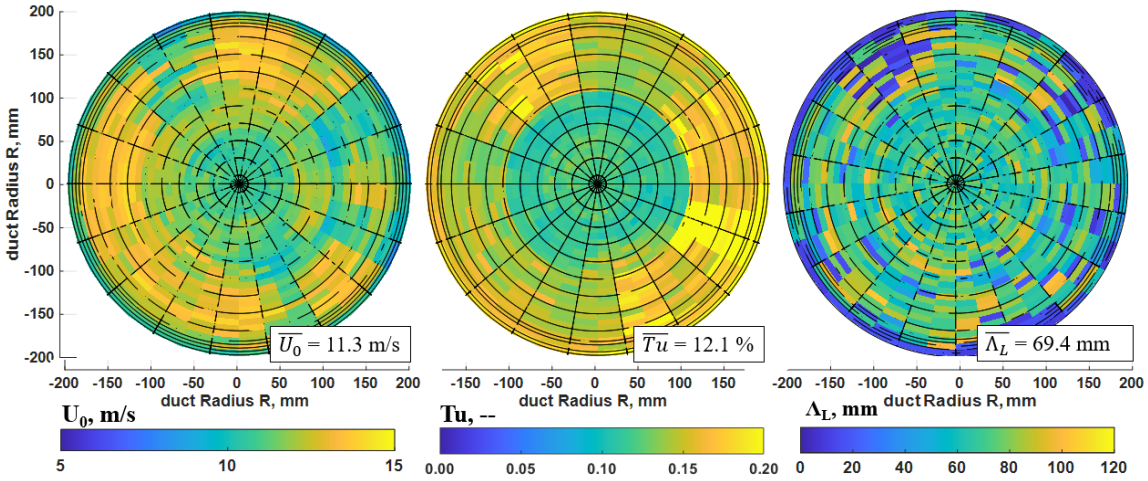

Figure 4-9 Grid G_{01}: local distribution of longitudinal velocity, turbulence intensity and integral length scale [151]. $n = 2000\ min^{-1}$, distance grid-to-probe $\Delta x = 0.3$ m.

Circumferential averaging of the data obtained leads to more general profiles of the three investigated quantities, as shown, for example, in Figure 4-10 (right). Here, the strong influence of the duct boundary layer on the velocity profile, and hence on the turbulence intensity and the integral length scale, becomes apparent. In order to obtain representative values for each grid, the data were once again averaged over a radius of $R_{Duct} = 0.15$ m to avoid these influences of the wall boundary layer. As mentioned earlier, the hot-wire probe is located $\Delta x = 0.3$ m downstream of the turbulence grids. As the table in Figure 4-10 (left) clearly indicates, the turbulence intensity follows the model by Laws and Livesey [2], predicting the most elevated turbulence at maximum mesh size and bar diameter (grid G_{01}). Moreover, the trend of the standard deviation S_{SD} indicates that the higher intensities are mainly due to an increase in the fluctuating quantity and not in the mean velocity [164].

Type	$\overline{U_0}$	$\overline{Tu}$	$\overline{S_{SD}}$	$\overline{\Lambda_L}$	$\overline{\Lambda_t}$
--	m/s	%	m/s	mm	mm
G_{01}	11.3	12.1	1.36	69.4	34.7
G_{02}	12.0	9.6	1.15	66.8	33.4
G_{03}	11.8	7.5	0.88	64.7	32.4
G_{04}	11.8	5.3	0.62	54.9	27.5
G_{05}	12.2	3.6	0.43	43.3	21.7
G_{00}	13.3	2.6	0.34	37.9	19.0

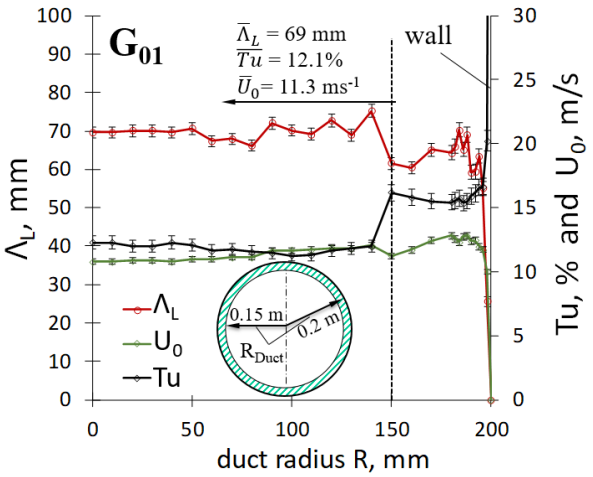

Figure 4-10 Left: Summary of averaged properties of the inflow conditions for the turbulence grids tested [151]. Right: An example plot of the circumferentially averaged properties of the flow for the coarsest grid G_{01} at $n = 2000/min$, $\varphi = 0.2$ [151].

To sum up, the generated incoming turbulence of the rotor blades to be analysed is in a range of 3.7 % ≤ Tu ≤ 12.1 % and is, therefore, higher than the turbulence of the rigidly mounted aerofoils analysed in Section 3. The transversal length scale, associated with the noise generation at the aerofoil leading edges, is derived from the longitudinal length scale by assuming isotropic conditions [128, 127], as discussed in Section 3.4.2.

The turbulent fluctuations of the velocity are assumed to be constant in all spatial directions (constant longitudinal to transversal velocity ratio), leading to an isotropic turbulence intensity. This property is of high importance because the turbulent structures are impinging in a circumferential direction on the fan blades rather than in the direction of the main flow. At a given isotropy, the magnitude of the measured turbulent fluctuations in the mean flow direction can be equated with the magnitudes in the circumferential direction, providing a scale of the turbulent inflow conditions at the blade leading edges. However, Laws and Livesey [2] state that a minimum distance of roughly ten times the mesh diameter between grid and measurement location approaches isotropic conditions. In the conducted experiments, the coarsest grids G_{01} and G_{02} would require distances of 1.0 m and 0.8 m, respectively, to fulfil this condition. Lower distances might lead to unacceptable downstream inhomogeneities [164]. Therefore, a spectral analysis of the 1D hot-wire signals was conducted and compared to the theoretical energy spectrum of Liepmann for longitudinal isotropic turbulence as stated per *Eq. 3-18* and *Eq. 3-20*. Figure 4-11 shows the power spectral density of the turbulent energy, scaled with the mean flow velocity and plotted over the non-dimensional Strouhal number. The data sets of grid G_{00} (without grid), G_{01} and G_{02} are analysed at radial positions of 0.15 m ≤ R_{Duct} ≤ 0.198 m, starting at mid-span of the fan blades (R = 0.15 m) towards the wall region of the duct (R = 0.198 m). The results demonstrate that the turbulence model agrees well with the measurements, although larger deviations for the model occur close to the wall, especially at high frequencies [167]. A similar trend is observed when the grid dimensions are increased (G_{00} → G_{02} → G_{01}), with high-frequency deviations becoming more prominent. The turbulent cascade theory describes that the turbulent energy scales with $f^{-5/3}$ in the inertial range and with f^{-7} in the dissipation range, which can be confirmed for the former range, whereas a diffuse transition to the latter region is observed [167]. Generally, the turbulence intensity can be shown to be of near-isotropic nature even for the coarse grids with large mesh widths (G_{01}).

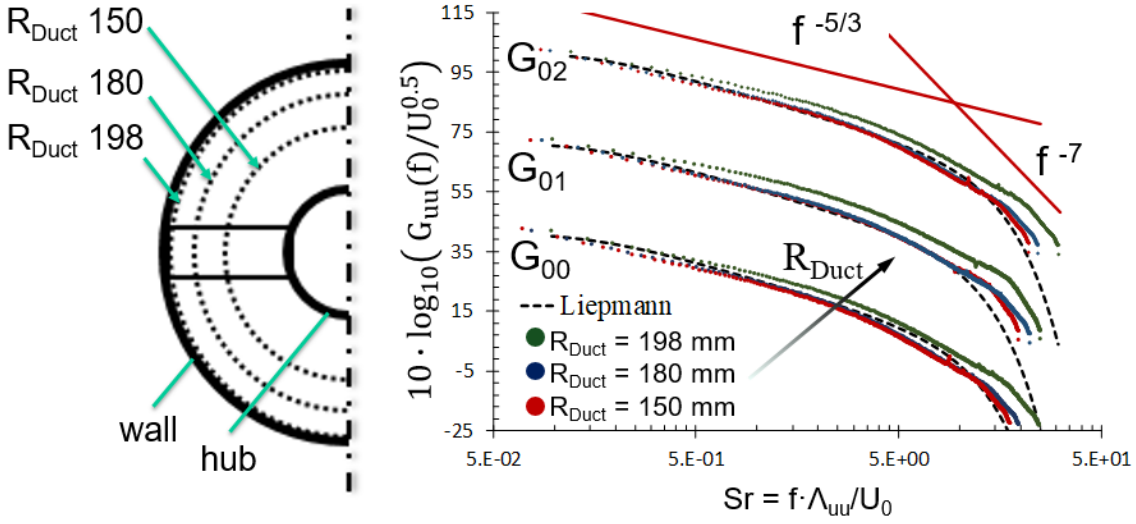

Figure 4-11 Turbulent energy of three chosen grids for three radial positions, and comparison to the theoretical spectrum for longitudinal isotropic turbulence according to Liepmann (dashed curves) [167].

4.5 Rotor Design

The common approach to designing an axial fan is to first define the point of operation at which the required pressure rise overcomes a certain resistance of the system while maintaining a required flow rate. At this specific point, the efficiency of the fan should be at its maximum, due to blade-congruent inflow conditions. As a consequence, the desired operating point usually determines the profile of the fan blades. However, for the current study, no such point is defined nor required. This leads to various degrees of freedom in the design process. The main requirement for the transfer from the rigid to the rotating system, on the other hand, is to maintain the originally investigated NACA65(12)-10 profile so that a link between both systems can be established.

4.5.1 Blade and Rotor Design

Chord, Number of Blades

The solidity σ_S, defined as the reciprocal value of the space-to-chord ratio in *Eq. 4-5*, describes the spacing of the blades with respect to the blade chord (Figure 4-12). For low solidities, the rotor can be assumed transparent, which means that no significant interference effects between consecutive blades and their associated boundary layers and wakes are present. According to Carolus [66], this condition is fulfilled for $\sigma_S \leq 0.7$. As a consequence, the rotor blades can be regarded individually, which gives the possibility of designing the rotor according to the single-aerofoil approach instead of a more complex cascade approach.

$$\sigma_S = \frac{C}{t_P} \qquad \textit{Eq. 4-5}$$

$$t_P = \frac{2\pi R}{z} \qquad \textit{Eq. 4-6}$$

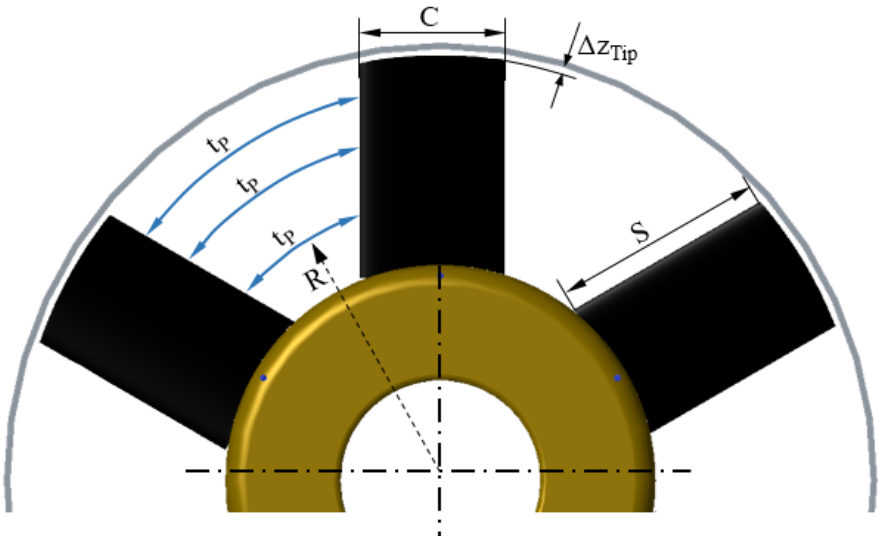

Figure 4-12 Front view of exemplary rotor, including relevant parameters for the rotor solidity.

An optimum of high chord and a high number of blades is obtained for six blades and C = 0.075 m, yielding a minimum solidity for the hub and maximum solidities for the blade tip in a range of $0.36 \leq \sigma_S \leq 0.72$. Thus, the initially analysed aerofoils of C = 0.15 m are downsized by a factor of two. Moreover, only an even number of blades allows for analysing the effects of successively varying the number of fan blades as it is done in Section 5.

The hub radius is determined by the diameter of the PWM-driven electric motor, resulting in R = 0.2 m. Maintaining a tip clearance between the fan blades and the rigid duct itself of Δz_{Tip} = 2 mm yields a span of the fan blades of S = 0.098 m, leading to a total fan diameter of D = 0.396 m. Fan speed was decided to be n = 2000 min^{-1}, being close to the maximum of the electric motor but still allowing for a limited buffer if the axial machine is partially loaded.

Inlet Conditions

The stagger angle γ of a fan represents the absolute angle between the blade chord line and the axial plane of the fan (Figure 4-13). According to *Eq. 4-7*, this angle is composed of the aerodynamic angles of attack AoA and β_0, determining the blade-congruent inflow condition.

$$\gamma = AoA + \beta_0 \qquad \textit{Eq. 4-7}$$

Usually, β_0 is determined by constructing a tangent to the camber line of the aerofoil profile, defining blade-congruent inflow conditions. However, for the NACA65(12)-10 profiles chosen, this is not feasible since the profile line is orientated normal to the camber line for the leading edge and the trailing edge. The reason is that the initial design of the NACA65-series was based on theoretical considerations only, as pointed out by Carolus [66]. The alternative approach is to define an equivalent circular arc, serving as the camber line. Because the rotor is designed according to the single-aerofoil approach, the results obtained for the single aerofoils in the rigid setting (Section 2.2) can be consulted to determine the aerodynamic flow angle AoA.

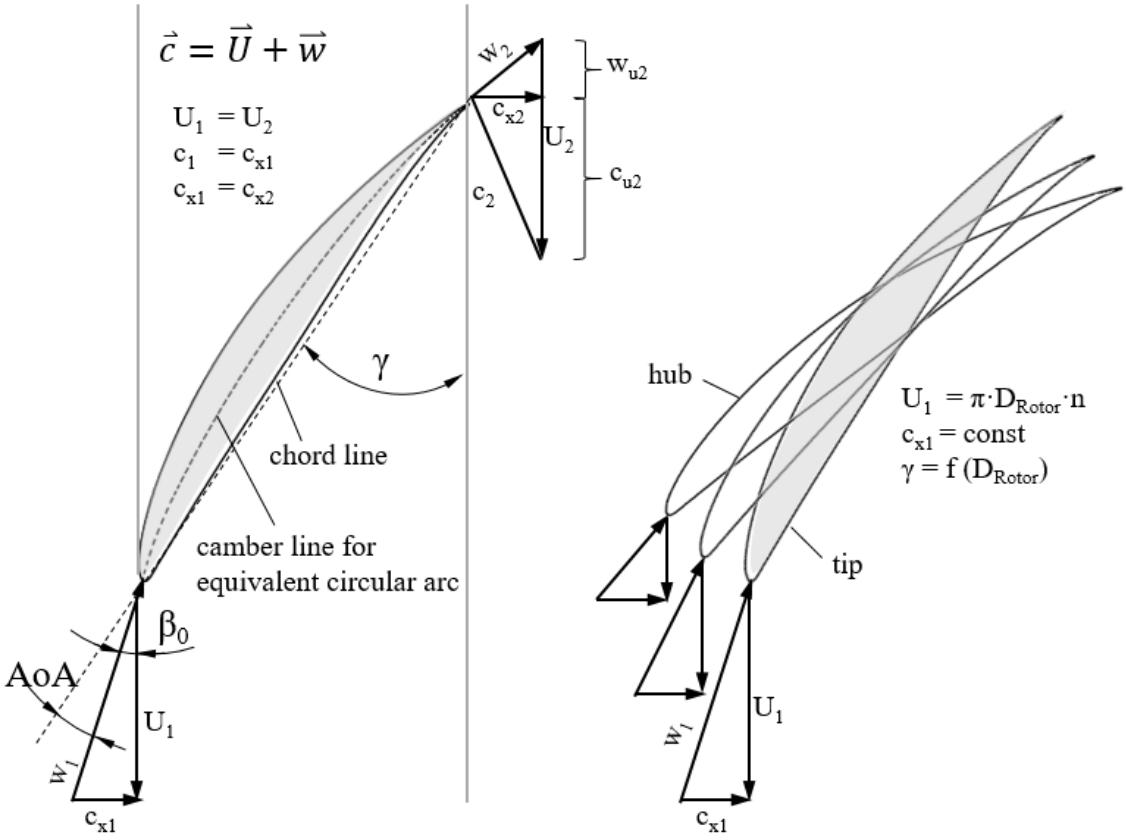

Figure 4-13 Velocity triangles for the rotating NACA65(12)-10 profile at optimum operation conditions (left) and indication of the spanwise change of the stagger angle of the rotor blade due to changes in the circumferential velocity $U_{1,2}$ (right).

Figure 4-14 qualitatively shows the relation between the aerodynamic properties of the single aerofoil (Section 2.2.3) and those of the downscaled six-blade rotor, with the design point of the rotor (position 2 in Figure 4-14) being characterised by a high static pressure rise Δp in combination with maximum efficiency η_{system}. The associated forces on a single aerofoil are the lift coefficient C_L and the lift-to-drag ratio C_L/C_D, characterising the efficiency. Consequently, for the current design of the rotor, the aerodynamic angle AoA = 7 deg was chosen based on the optimum of the C_L/C_D ratio while keeping C_L on a high level as well. For angles AoA < 7 deg (position 1 in Figure 4-14), the absolute lift decreases, and for angles AoA > 7 deg (position 3 in Figure 4-14), the efficiency in terms of the C_L/C_D ratio decreases considerably, since stall phenomena become more apparent.

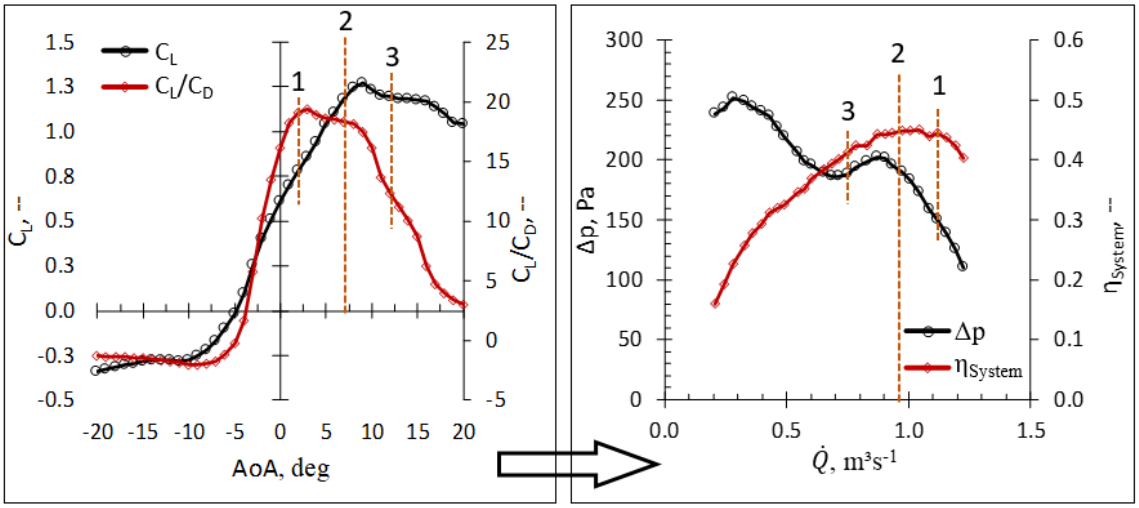

Figure 4-14 Characteristic performance curves for a single NACA65(12)-10 aerofoil at Re = 150,000 (left) vs. the designed 6-blade rotor at n = 2000 min⁻¹ (right).

No inlet guide vanes were used for the current design; therefore, the inlet velocity shows only an axial component (*Eq. 4-8*), without there being a circumferential component of the meridian velocity vector. Moreover, the cross-sectional area on the suction and discharge sides remains constant, which leads to equal axial velocities of the blade's inflow and outflow (*Eq. 4-9*).

$$c_1 = c_{x1} \qquad \textit{Eq. 4-8}$$

$$c_{x1} = c_{x2} \qquad \textit{Eq. 4-9}$$

At a given stagger angle and a given circumferential velocity, the axial component of the meridional velocity can be determined according to *Eq. 4-10*, also specifying the flow rate $\dot{Q}$ (*Eq. 4-11*).

$$c_{x1} = tan(\gamma) \cdot U_1 \qquad \textit{Eq. 4-10}$$

$$\dot{Q} = c_{x1} \cdot A_{Rotor} = c_{x1} \cdot \pi/4 \cdot (D_{Tip}^2 - D_{Hub}^2) \qquad \textit{Eq. 4-11}$$

The meridional velocity is desired to be constant over the blade span ($c_{x1} \neq f(R_{Duct})$). As a consequence, the cross-sectional stagger angle γ differs from hub to tip of the fan. Since the inflow angle at the actual radius of the rotor depends on the resulting vector of circumferential velocity and constant axial velocity, the stagger can be determined according to *Eq. 4-12* and *Eq. 4-13*.

$$\gamma = \tan^{-1}\left(\frac{c_1}{U}\right) \qquad \textit{Eq. 4-12}$$

$$\gamma_{tip} - \gamma_{hub} = \Delta\gamma = \tan^{-1}\left(\frac{c_{x1}}{U_{Tip}}\right) - \tan^{-1}\left(\frac{c_{x1}}{U_{Hub}}\right) \qquad \textit{Eq. 4-13}$$

Outlet Conditions

The specific energy of a turbomachine is defined via Euler's pump and turbine equation. For the fan considered, Euler's pump equation states that the specific energy of a blade Y_E is dependent on the differences between the circumferential components of the meridional velocities for every infinitesimal radial segment (*Eq. 4-14*).

$$Y_E = U_2 \cdot c_{u2} - U_1 \cdot c_{u1} \qquad \textit{Eq. 4-14}$$

As already mentioned, no inlet guide vanes or other elements causing a spin are used; hence *Eq. 4-8* applies, and the circumferential component c_{u1} becomes zero. Consequently, *Eq. 4-14* reduces to *Eq. 4-15*.

$$Y_E = U_2 \cdot c_{u2} \rightarrow \Delta p_{Fan} = Y_E \cdot \rho \qquad \textit{Eq. 4-15}$$

Since the energy of a fan blade strongly depends on the outflow conditions, the design of the fan blade's rear parts requires some further considerations. For the outflow conditions of a fan blade, different loading distributions are possible [66]:

- free vortex design, describing an isoenergetic distribution of the blade loading, meaning that each radial segment possesses the same specific energy (specific blade energy Y_E = constant)
- controlled vortex design, which allows the blade loading distribution to be controlled, for example by moving the main load from the tip closer to the hub or vice versa.

The isoenergetic load distribution requires a radius-dependent scaling of the blade chord since the aerofoil profile is already fixed. This scaling would result in varying solidities σ_s, especially because the hub region would require large chord lengths. Hence, the second approach of a controlled vortex design is chosen. The profile shape is maintained, resulting in a higher loading of the blades close to the tips. On the other hand, this results in stagger angles that are dependent on the radial distribution of the circumferential velocity and in a radius-dependent meridional outflow velocity (*Eq. 4-16*).

$$c_{u2} = U_2 - \tan\gamma \cdot c_{x2} \qquad \textit{Eq. 4-16}$$

According to Euler's equation and the resulting pump equation, the total static pressure rise of an axial fan inside a duct can be determined according to *Eq. 4-17*, yielding the local pressure rise.

$$\Delta p_{stat} = 2\pi \cdot n \cdot r \cdot c_{u2}(r) \cdot \rho \qquad \textit{Eq. 4-17}$$

The flow rate is determined with respect to the local area A_R and the axial velocity distribution c_{x2}.

$$\dot{Q} = \int c_{x2}\, dA_R, \int dA_R = \iint_{0\ 0}^{2\pi\ R} r \cdot dr\, d\phi \qquad \textit{Eq. 4-18}$$

Assuming a constant circumferential distribution of the velocity, the flow rate simplifies to *Eq. 4-19*, practically defining an area-averaged contribution of the meridional velocity to the flow rate.

$$\dot{Q} = 2\pi \int_{R_{Hub}}^{R_{Tip}} c_{x2}(r) \cdot r\, dr \qquad \textit{Eq. 4-19}$$

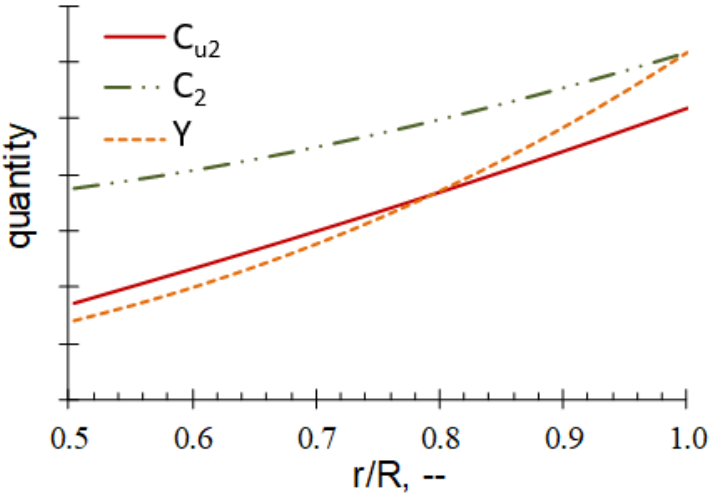

Figure 4-15 Qualitative representation of the fan blade's outflow conditions, scaling from hub to tip of the rotor.

4.5.2 Leading Edge Serration Design

Leading edge serrations are adopted from the rigid domain and are applied to the designed low-pressure axial fan. This already leads to a significantly enhanced complexity of the system to be analysed, including additional noise source mechanisms and influences on the aerodynamic performance. In order to draw conclusions on the efficiency of the previously analysed serrations, a coherent strategy is needed for the transfer. Hence, the initially designed serrations are scaled according to the adopted chord length of the rotor blades, thus maintaining the normalised A/C and λ/C ratios. By use of these non-dimensional serration parameters, an experimental space of the same limits is defined. The Reynolds number, being an integral parameter in the previous analysis, is transformed to the circumferential velocity of the rotor, whereas the turbulence intensity remains grid-generated, albeit, due to the ducted setup, on a higher level.

4.5.3 Structural Analysis

The rotor was manufactured via rapid prototyping, but, as can be seen from Figure 4-16, the rotor is an assembly of four individual parts. The hub is manufactured from acrylnitril-butadien-styrol-copolymer (ABS), the metal core of the blades from DC01 steel, and the blades themselves from a highly resistant photopolymer resin (Figure 4-16). Resin requires a post-cure procedure in order to develop its full mechanical properties but, on the other hand, offers an excellent surface finish without the need for further treatment. In order to assess the ability of this compound to withstand the acting aerodynamic forces while rotating at n = 2000 min^{-1}, a finite element analysis (FEM) of the basic rotor was carried out using *ANSYS Mechanical*.

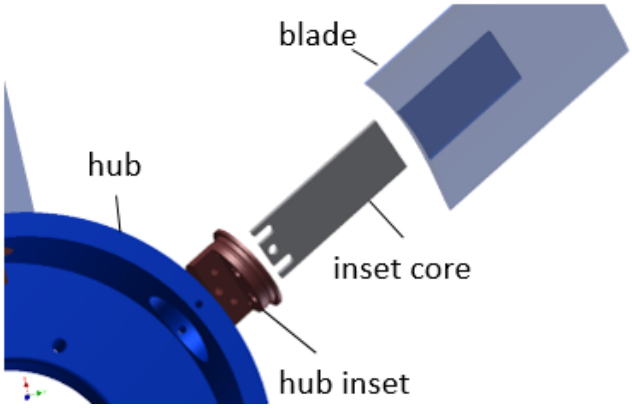

Figure 4-16 Assembly of the designed rotor, showing the hub, the inset cores and the fan blades.

An unstructured mesh was generated with 489,000 elements, with the element size in the range [$1 \cdot 10^{-5}$ m, $1 \cdot 10^{-3}$ m], in which adaptive meshing supported mesh-independent results. Local refinement was applied to the sensitive regions of the hub-blade intersection, to the leading edges, to the trailing edges and to the blade-tip region. The material properties used in this study are listed in Table 4-2. The rotor was modelled without being mounted in the test rig; only the hub was mounted on a rotating support, performing a linear ramp from n = 0 min^{-1} to n = 2400 min^{-1}, as also reported by Biedermann et al. in [164] for a different material. As a consequence, the FEM study focusses on centrifugal forces only and currently disregards aerodynamic forces.

Table 4-2 General material properties of the materials used to perform the FEM analysis and to manufacture the prototypes of the rotor.

Property	Unit	ABS	Resin	Steel
Young's modulus	*GPa*	*2.5*	*2.7*	200
Tensile ultimate strength	*GPa*	*40*	*55.7*	460
Density	*kg/m³*	*1050*	*1100*	7850

As can be seen from Figure 4-17, the total deformation and the von Mises stress were monitored to determine the acting forces. Maximum stresses were found to occur at the crossing between the blade inlet and the blade itself ($7.9 \cdot 10^{7}$ Pa), underpinning the decision to choose steel for the inlay material, which is expected to be well capable of resisting the imposed stresses.

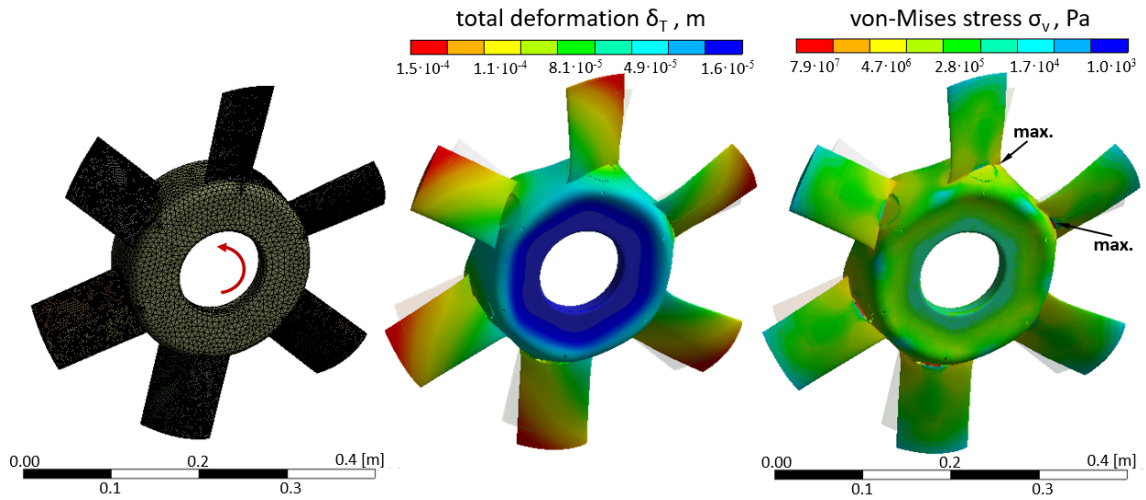

Figure 4-17 Selected FEM results of the baseline rotor at n_{Max} = 2400 min^{-1}.

In the radial direction, a maximum deformation of 0.13 mm takes place, forcing the blades to migrate outwards, while for the axial direction a maximum of 0.019 mm is observed. The resulting maximum total deformation adds up to 0.15 mm and occurs at the trailing-edge region at the blade tips. However, even though the observed deformations are still considered negligible in the given setup, the strong tendency of the blades to migrate outwards requires a reliable mounting procedure. Hence, the blade's inset cores (Figure 4-16) are mounted via highly adhesive glue plus two grub screws per blade to maintain the positive locking of the blades. This also takes into account the additional aerodynamic loading, as a result of which the generated static pressure rise will force the blades in the anti-streamwise direction. These forces are a function of the throttling state or the operating point of the fan.

4.6 Dimensional Analysis

For generalisation purposes, the obtained static pressure rise Δp of the fan and the flow rate $\dot{Q}$ are converted into the non-dimensional pressure coefficient ψ (*Eq. 4-20*) and the flow coefficient φ (*Eq. 4-23*). These coefficients lead to a compensation for varying ambient conditions by taking into account the temperature and the atmospheric pressure by incorporating the fluid density. As has been discussed previously, the chosen design of the serrated leading edges results in different (amplitude-dependent) wetted surfaces of the fan blades since the maximum chord remains constant. This serves mainly three reasons:

1. Keeping the maximum surface constant results in only one baseline reference case for comparison as well as in a constant blade thickness for different serration geometries.
2. A constant maximum chord leads to a constant maximum solidity σ_s and thus prevents an amplitude-dependent interaction effect of successive blades at solidities $\sigma_s \geq 0.7$.
3. It represents a conservative approach that remains close to practical applications, in which serrations might be included as a substituting technology at limited installation space (simply replacing previously-mounted straight blades).

On the other hand, the reduction in wetted surface area of the blades results in penalties for the static pressure rise obtained (*Eq. 4-17*). The flow rate (*Eq. 4-19*) is a function of the meridional velocity component at different spanwise radii and is also directly affected by the loss in area, albeit to a reduced extent. This phenomenon is comparable to a reduction of the blade number (Section 5), resulting in a slight reduction in the flow rates but to more prominent differences in the static pressure rise, continuously increasing with further throttling.

In contrast to the coefficients of lift and drag, for which a normalisation by the wetted surface takes place, the flow and pressure coefficients of a rotating machine have no such compensation. Therefore, preliminary measurements for straight blades of varying chord are needed. Here, three different rotors with straight leading edges are tested. The surface of the three sets of rotor blades equals the wetted surface of the serrated blades with maximum ($C/C_0 = 0.83$), intermediate ($C/C_0 = 0.91$) and no ($C/C_0 = 1$) serration amplitude. Testing these scaled baseline blades, instead of the serrated blades, prevents including possible flow-dependent effects of serrations, which might affect the flow rate or the pressure rise. Two different turbulent cases were tested, showing highly comparable results. For brevity, only the Tu = 2.6 % (G_{01}) turbulent case is shown in Figure 4-18; the results for Tu = 5.3 % (G_{04}) are presented in Appendix D.4. The gathered data show that the (wetted) surface of the blades contribute linearly to the static pressure rise for each semi-infinite radial element. The individual share of each radial element, however, scales with the circumferential velocity as stated in *Eq. 4-17*. Consequently, the circumferential velocity U_{Rot} of the pressure coefficient ψ (*Eq. 4-20*) is defined according to an area-equivalent blade span S_{rep} (*Eq. 4-21*) that is a function of the serration area A_{Serr} (*Eq. 4-22*).

$$\psi = \frac{(\Delta p + \Delta p_{Grid})/\rho}{U_{Rot}^2/2}, U_{Rot} = \pi \cdot n \cdot (D_{Hub} + 2 \cdot S_{rep}) \qquad \textit{Eq. 4-20}$$

$$S_{rep} = \frac{S \cdot C - A_{Serr}}{C} \qquad \textit{Eq. 4-21}$$

$$A_{Serr} = 2C/\lambda \int_0^{\pi} A \cdot sin(\omega x)\, dx \qquad \textit{Eq. 4-22}$$

As *Eq. 4-19* indicates, the flow rate $\dot{Q}$ depends solely on the outflow condition c_{x2} for each radial segment and thus does not scale with the circumferential velocity. The adopted flow value, therefore, considers only the change in aerofoil area $A_{Serr}/2$, caused by the individual serration amplitude (*Eq. 4-23*).

$$\varphi = \frac{\dot{Q}}{U_{rot} \cdot (A - A_{Serr}/2)}, \quad U_{Rot} = \pi \cdot n \cdot (D_{Hub} + 2 \cdot S) \qquad \textit{Eq. 4-23}$$

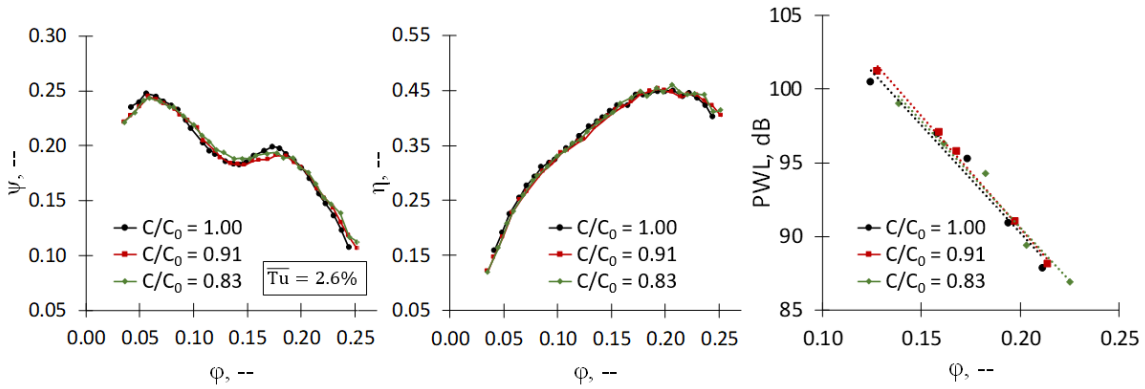

Figure 4-18 Performance results of the baseline rotor with blades of varying chord at Tu = 2.6 %, n = 2000 min⁻¹. Fan characteristic curves of the pressure coefficient (left), the aerodynamic efficiency (centre) and the radiated sound power level (right).

With regard to the additionally monitored sound power levels of the fan (Figure 4-18 right), highly similar results are obtained for the tested blades of varying chord. Therefore, moving from the aerodynamic parameters to the acoustics, the wetted surface of the blades is only of secondary importance, since the level-dominant noise sources of the blades are the blade-tip region, the trailing edges and the leading edges. These are, except for the leading edges, held constant for all the cases to be analysed.

For higher acoustic modes, the local sound pressure is a function of the peripheral duct angle. To take this into account, the spectral information of the three equidistantly distributed microphones on the suction and discharge sides is averaged linearly (*Eq. 4-24*) in order to reduce falsifications caused by non-planar waves.

$$\overline{SPL} = 10lg\left(\frac{1}{n}\sum_{i=1}^{i=n}\bar{p}_{i,RMS}^{2}\Big/ p_0^2\right) \qquad \textit{Eq. 4-24}$$

For the generalizability of the data obtained, the averaged sound pressure level from *Eq. 4-24* is according to ISO 5136 [163], further processed towards the sound power level as stated in *Eq. 3-4*. Analogously, a wall power level (*Eq. 4-25*) is defined for the wall-pressure fluctuations, obtained by use of the pressure tapping points along the fan axis. For comparability reasons, the reference value $p_0 = 2 \cdot 10^{-5}$ Pa is chosen to be the hearing threshold of 1 kHz, as for the SPL (*Eq. 3-5*).

$$WPL = 10lg\left(\frac{\bar{p}_{wall}{}^2}{p_0^2}\right) + \left[10lg\left(\frac{A_E}{A_0}\right) - 10lg\left(\frac{\rho c}{\rho_0 c_0}\right)\right] \qquad \textit{Eq. 4-25}$$

5 Aeroacoustic Study – Successive Blade Variation

This section aims at transferring a serrated design of known performance from the rigid to the rotating domain while varying the number of fan blades from 2 to 6 blades. This approach is expected to allow conclusions on possible interference effects of successive blades and their impact on the noise reduction capability of leading-edge serration. The herewith presented analysis is also published in Biedermann et al. [151].

With regard to the chosen serration, the normalized amplitude (A/C = 0.19) and wavelength (λ/C = 0.17) represent the central point of the previously conducted aeroacoustic study (Section 3.3). The supplementing beamforming results for the same single aerofoil (Section 3.4.2), certifies an overall noise reduction at the leading edge of ΔOASPL = 4.2 dB. This aerofoil is scaled and adapted for the rotor blades, with the design process of the rotor itself taking place according to Section 4.5.

Unlike in the rigid aerofoil, the ratio of integral length scale Λ_L and serration wavelength λ could not be kept constant for the rotating application. As for the open free jet of the tested rigid aerofoils, small values of $\Lambda_L \leq 10$ mm are found, whereas the current test rig provides length scales of significantly higher dimension ($\bar{\Lambda}_L = 69$ mm). Even though the ratios of length scale to serration wavelength do play a role with regard to optimising incoherent excitation of the leading edges [105], the wavelength is considered not to be the key parameter in reducing the radiated noise in rotating applications. In addition, compared to the rigid aerofoils, the scaled chord length of the rotor blades reduces the Reynolds number under investigation by a factor of two to Re = 105,000 for the hub and Re = 210,000 for the blade-tip region. Nevertheless, since no strong dependencies at 250,000 ≤ Re ≤ 600,000 are found for rigid aerofoils [110], the chosen approach allows a qualitative comparison to be made.

5.1 Signal Processing Parameters

Data acquisition took place at a sampling rate of SR = 32,768 Hz and a block size of BS = 65,536, thus yielding a spectral resolution of Δf = 0.5 Hz. Applying an overlapping via Hanning windows of OL = 66.7 % and taking 300 averages result in a total measurement duration of 201 s and provide a reliable data pool with minimised bias.

With the aim of gaining deeper insights into the noise reduction mechanisms, a spectral analysis of the data is required. Based on preliminary analysis of the signals [113], partitioning of the spectral content into its broadband and its discrete contributions proved to be helpful since the underlying noise generation mechanisms are of different physical origin (Section 4.1). In this context, five filters are used, as shown in Figure 5-1. First, the original signal is analysed by use of a bandpass 10 Hz ≤ f ≤ 10 kHz. To cover the low-frequency part, which is of interest especially at higher throttling states, a low-pass with a maximum frequency of 300 Hz is chosen. In order to split the rotor-speed-dependent components from those of broadband character, a customised one-dimensional median filter of the 30th order shows the best performance. In doing so, a frequency band of ± 7.5 Hz around the rotor's fundamental speed, or an integer multiple thereof, is replaced by its median, thus neglecting peaks with high slopes, which, in this case, are representing the tonal components, and resulting in a broadband signal without loss of spectral energy. The tonal filter is specified vice versa, solely showing the chopped-off peaks of the signal. However, when specifying filters for discrete frequency bands, one has to distinguish the tonal filter from the BPF filter, covering only every 6th order of the blade-passing frequency of the rotor (see Figure 5-1). Adding up the tonal and the broadband level yields exactly the level of the original signal.

type	f_{min} [Hz]	f_{max} [Hz]	increment [Hz]
total	*10*	*10,000*	*0.5*
low pass	*10*	*300*	*0.5*
broadband	*10*	*10,000*	*0.5*
tonal	*10*	*10,000*	$33^{1/3} \pm 7.5$
BPF	*10*	*10,000*	200 ± 7.5

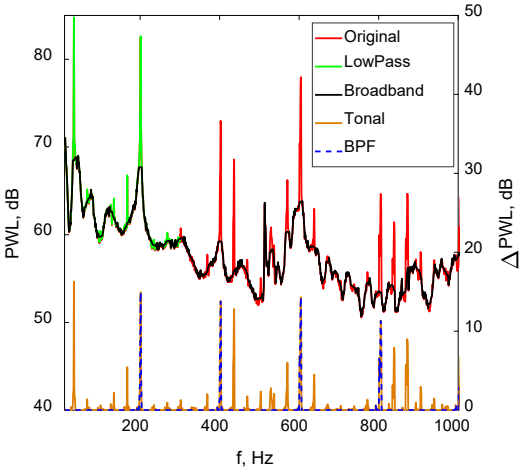

Figure 5-1 Boundary conditions of customised filters (left). An example of a sound power level spectrum for the baseline rotor with applied filters, separating low-frequency, tonal and broadband effects (right) [151].

For analysing purposes of the wall-pressure signals with the aim of identifying possible unsteady flow phenomena, non-synchronized with the rotor speed, the coherence function of the signals obtained from the two pressure tapping points (Figure 4-7) is used. The coherence γ^2 shows the quantitative context of the signals in the frequency range by normalising the cross-spectral density of two signals G_{12} with the spectral densities (G_{11}, G_{22}) of the individual signals according to *Eq. 5-1*. In consequence, the coherence function yields only values $\gamma^2 \in (0..1)$. With adequate averaging of the coherence function in the circumferential direction, the signal parts that are dominant in both signals are highlighted compared to those that exist only in one of the signals [170].

$$\gamma^2(\omega) = \frac{G_{12}(\omega) \cdot G_{12}^*(\omega)}{G_{11}(\omega) \cdot G_{22}(\omega)} \qquad \textit{Eq. 5-1}$$

5.2 Testing Procedure

For a transfer from the rigid to the rotating frame, the blade number of the rotor is increased successively, starting with two blades, increasing to four blades and ending up with the full rotor of six blades, as designed initially (Figure 5-2). As discussed earlier, the baseline rotor is compared to a serrated design of intermediate parameters A14λ13 only, showing a decent aeroacoustic performance (Section 3.3.7). This successive approach is expected to reveal some effects that, at full rotor, are masked or superimposed by other more dominant interaction effects of the blades. The focus does not lie on the aerodynamic meaningfulness of a 2-blade fan but rather on the aeroacoustic development of the final rotor's noise floor, as well as serration effects on the gathered wall-pressure in the blade-tip region.

The inflow conditions are altered according to two approaches. High turbulence is achieved using a coarse biplane square mesh (G_{01}) with a bar-to-bar diameter of 100 mm, generating large-scale vortices 300 mm upstream of the rotor, which impinge on the fan blades and result in significant leading-edge noise. In contrast, the no-grid case (G_{00}) results in low turbulence and can produce dominant rotor trailing-edge noise as well as self-noise. From a more practical point of view, the lower limit is intended to represent common inflow conditions for ducted fans. In contrast, the upper limit is chosen according to the possible inflow conditions of fans and blowers under unfavourable working conditions, such as cooling fans in the immediate vicinity of ventilation grilles or pipe branches and other barriers that obstruct the inflow.

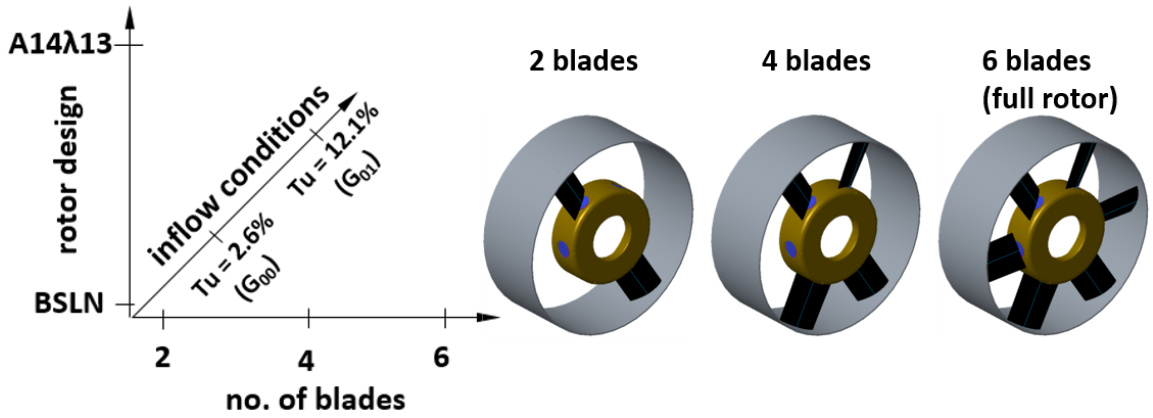

Figure 5-2 Experimental space (left) and models of the investigated rotors (right) [151].

5.3 Aerodynamic Performance

The fan characteristic curves for all the cases tested at high Tu are shown in Figure 5-3. Similar trends were also obtained for the low-turbulent case and are presented in Appendix E.1. The shape of the characteristic curves of the full rotor is typical for axial fans, in which, after an initial increase in the static pressure at high flow coefficients (pre-stall), partial separation at the blade suction sides starts to occur (instability region), characterized by stagnating pressure coefficients. Further throttling again leads to a rise in static pressure, albeit at decreasing aerodynamic efficiency (Figure 5-3). This is the case since the fan is operating post-stall on a secondary characteristic due to the (partially) separated flow. Towards minimum flow coefficients, the separated structures become large-scale and result in minimum aerodynamic efficiencies.

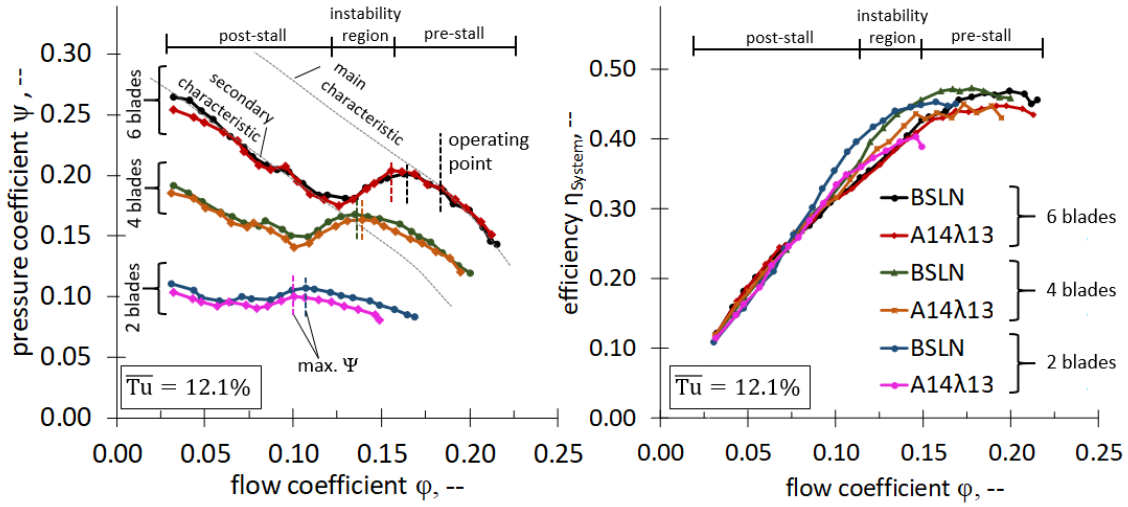

Figure 5-3 Fan characteristic curves (left) and efficiency (right) of the tested baseline (BSLN) and the serrated (A14λ13) rotor for a varying blade number at Tu = 12.1 % [151].

In general, introducing the A14λ13 serration shows a slightly decreased aerodynamic performance for the instability region, especially for the tests at lower blade number. For the optimum operation point, though, quite similar performance is obtained. It is important to note that the maximum chord of the serrated and straight fan blades is kept constant. As a result, the total area of the serrated blades is reduced compared to straight blades, being compensated by the pressure and flow coefficients defined in *Eq. 4-20* and *Eq. 4-23*. Comparing the transition point from pre-stall to the stall region by means of the flow coefficients,

corresponding to the points of maximum pressure at pre-stall, reveals a slight shift towards lower flow coefficients for the serrated cases with 2 and 6 blades (Figure 5-3). This effect can be attributed to the vortex-generating features of the serrations, causing an energisation of the blade boundary layer and delaying the point of separation, as has been described for rigidly mounted aerofoils as well (Section 2.2), even though this effect is expected to be more pronounced for serrations of larger wavelengths and high amplitudes. For the 4-bladed case the uneven distribution of the blades is expected to disrupt and mask the beneficial process of a stall delay, leading to no significant changes, compared to the baseline rotor. However, for all tested cases the stall region of the serrated aerofoils is smaller compared to that of the baseline case. Reducing the number of blades by 1/3rd or 2/3rd generally stresses the aerodynamic differences between the straight leading edges (baseline) and the serrated leading edges. Due to the lower pressure coefficients with lower blade number, the profiles of the fan curves appear to become increasingly flattened on a global scale, even though similar aerodynamic effects to those of the 6-blade case exist.

5.4 Aeroacoustic Results

Like the aerodynamic characteristics in Figure 5-3, the acoustic performance over the fan curve in Figure 5-4 can be subdivided into three regions. First, a region of high flow rates (pre-stall), in which the blade angle corresponds to the flow angle. Here, as can be seen in Figure 5-4 (right), a significant level of turbulence and thus leading-edge noise is generated, giving rise to additional leading-edge broadband noise. The second region is the stall region, in which separation starts to occur. The transition into a (partly) separated flow is delayed for the serration, resulting in potential noise reduction. Third, the region of low flow coefficients (post-stall), in which no high free-stream turbulence is generated but in which significant separation from the blades results in large-scale coherent structures. Here, the acoustic performance with and without turbulence grid appears to be quite similar. Nevertheless, significant noise reduction effects are observed, which are expected to be caused by large-scale structures, separating from the blade suction sides and impinging on the consecutive blades of the rotor.

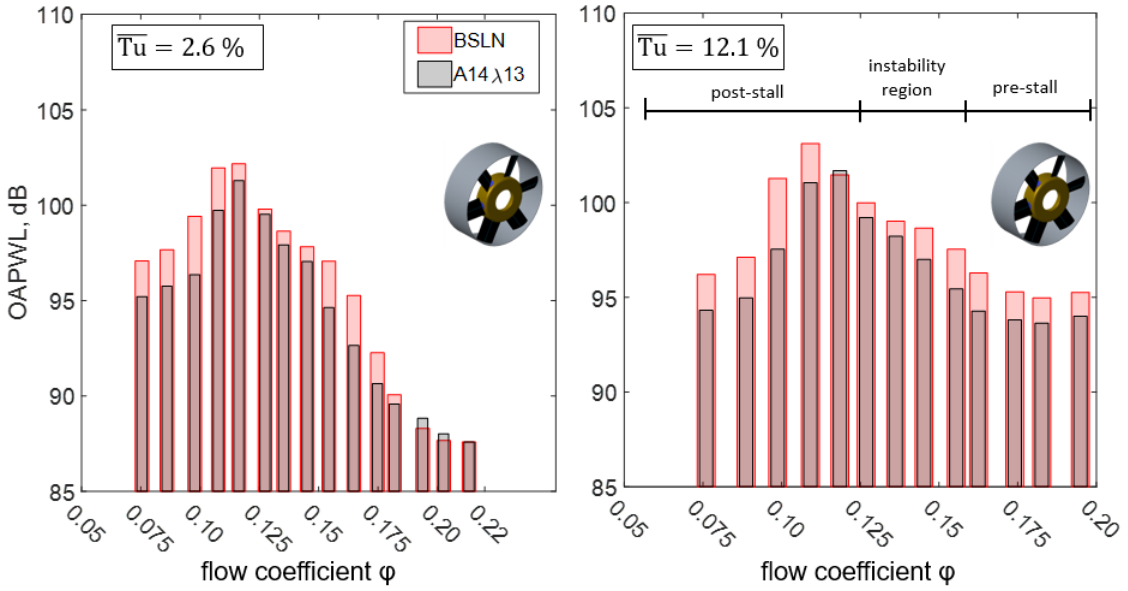

Figure 5-4 Overall sound power level OAPWL of the full rotor (6 blades) at low (left) and high (right) incoming Tu for the fan discharge side [151].

Figure 5-5 shows the changes in overall sound pressure level (ΔOAPWL) at low and high incoming turbulence intensity for the averaged microphone signals from the suction and discharge sides. Note that positive deltas ($\Delta > 0$) indicate noise reduction, whereas negative ones ($\Delta < 0$) result in a noise increase of the serrated rotor compared to the baseline. Qualitatively, the pattern of the noise reduction appears to be highly similar for the low- and the high-turbulent case, except for the pre-stall region, in which efficient noise reduction takes place for the high-turbulent case. Here, at high flow coefficients, the efficient noise reduction indicates the presence of significant leading-edge broadband noise. Comparing the acoustic signature on the suction and the discharge side in Figure 5-5 shows no significant differences, hence justifying the focus on the discharge noise for the upcoming analysis. Reducing the number of blades shows qualitatively the same trend as for the 6-blade case as it is presented in Appendix E.2.

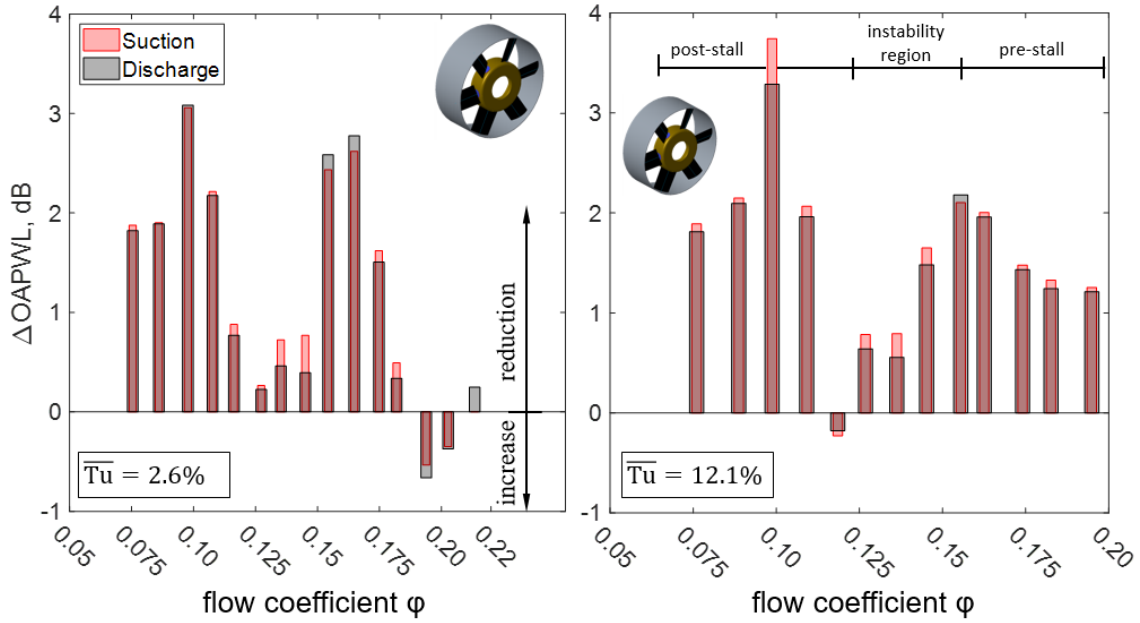

Figure 5-5 Overall sound power level reduction ΔOAPWL of the full rotor (6 blades) at low (left) and high (right) incoming Tu [151].

For more detailed analyses of the noise radiation and noise reduction effects, Figure 5-6 shows the spectral noise radiation of the BSLN rotor at varying flow coefficients and at high incoming turbulence. As can be seen for the pre-stall region at high flow coefficients, the most distinct noise sources can be narrowed down to the fundamental frequency $f = 33^{1/3}$ Hz of the fan and a surrounding broadband hump at $22 \leq f \leq 58$ Hz, as well as the BPF at $f = 200$ Hz. Entering the stall region at $\varphi \leq 0.16$ leads to a significant increase at $f = 300$ Hz, which can be attributed to blade interaction effects. At this particular frequency, partial stall occurs over the blade span, resulting in a constant ratio of the corresponding aerodynamic wavelength (*Eq. 5-2*) to the blade spacing (arc length) of $\lambda_{aero}/b_{arc} = 1.5$, thus indicating an interaction of the separated flow structures with subsequent blades and their harmonics.

$$\lambda_{aero} = \frac{U_{Rot}}{f} \qquad \textit{Eq. 5-2}$$

This is considered meaningful, as during one blade passage of the full rotor, the axial flow covers only a distance of approximately $15 \text{ mm} \leq \Delta x \leq 20$ mm in a range of flow coefficients $0.12 \leq \varphi \leq 0.16$ at nominal speed. At post-stall ($\varphi \leq 0.11$), the overall sound power level is at

its maximum due to a significant increase in broadband noise plus additional low-frequency components that can be observed. This is due to large-scale flow separation (rotating stall), which can be seen at f = ± 14.5 Hz, exciting the fundamental rotor frequency at f = 33.5 Hz and its 4th harmonic at f = 134 Hz. In general, the level-dominating frequency range at low flow coefficients can be stated to be f ≤ 300 Hz.

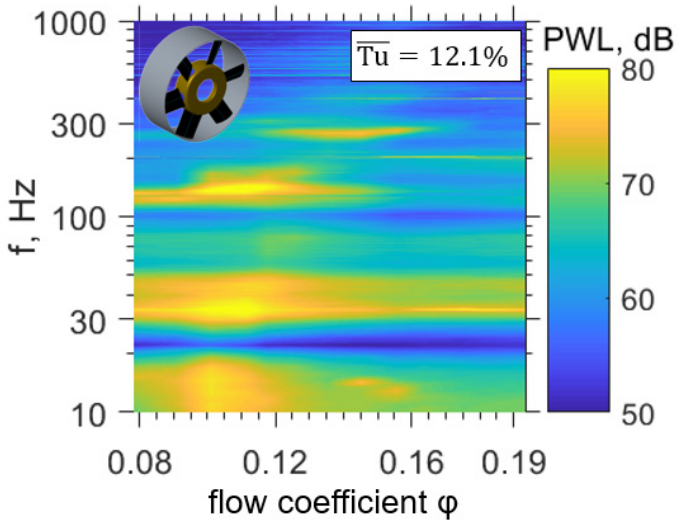

Figure 5-6 Spectrogram of the acoustic signature of the full rotor (BSLN case) for varying flow coefficients at maximum Tu = 12.1 % [151].

Subtracting the spectral noise radiation of the A14λ13 serration from that of the baseline provides the ΔSPL spectrograms in Figure 5-7 for varying number of rotor blades, with positive values indicating a noise reduction and negative values a noise increase. As can be seen, the serration exhibits a lower broadband noise radiation over a large range of flow coefficients, except for the low-frequency part of the stall region at 0.10 ≤ φ ≤ 0.14 for the 6-blade case (Figure 5-7, top). Pre-stall (φ > 0.15), a noise reduction of comprehensive character can be observed, agreeing well with the already described spanwise decorrelation effects of the serrations over the fan blades, leading to destructive interference and reducing vortex-induced leading-edge noise. For the transition area in close vicinity to the stall region, however, these specific effects of the serrations are still in action, but, in addition, the serration's ability to delay the stall by generating counter-rotating vortices come into play. By re-energizing the blade's boundary layer, the flow remains attached, whereas for the baseline reference case, partial separation occurs, leading to a significant increase in the noise level. Consequently, the improved noise reduction capability of the serrated blades close to the unsteady stall-region can be attributed to aerodynamic stall-delaying effects, paired with efficient aeroacoustic reduction of vortex-induced noise due to the sinusoidal contour of the leading edges. At f = 300 Hz, Figure 5-7 (top) shows significant noise reduction for the full-rotor case, indicating the ability of the serrations to reduce the previously described aerofoil interaction noise. The separated structures interact with the fan blades of subsequent blades and can be reduced efficiently by ΔPWL = 3.1 dB in a frequency range of 240 ≤ f ≤ 320 Hz. The blade-passing frequency is also reduced by ΔSPL = 2 dB. These blade-interaction effects can be observed for both the full-rotor and the 4-blade case (Figure 5-7, bottom left), which possess successive blades, spaced only one blade passage apart. For the 2-blade case, however, no such effect is observed since the separated structures are transported away downstream before they can interact with the successive blade's leading edge. Assuming the two single blades to be fully independent of each other without any form of aerodynamic interaction, this observation leads to the statement that leading edge serrations have the potential of affecting blade interaction

noise in a beneficial manner. After entering the stall region, the serrated rotor shows a reduced ability to keep the flow attached, as compared to the corresponding baseline. This reduced ability might be caused by a detrimental interaction of the vortices generated by the serrated leading edges with tip leakage flow structures (crossing of vortices); these effects are found in both the aerodynamic and the aeroacoustic signature.

Moving the focus to the cases tested with a lower number of fan blades (Figure 5-7, bottom) shows similar effects, suggesting a systematic cause, albeit that for lower blade numbers, the region of higher noise radiation extends towards higher frequencies and covers an increased range of flow coefficients. This specific extension of the region, showing a partial noise increase due to the serrations, cannot be attributed to tip leakage effects. In fact, for the 4-blade case, more tonal components, including a slight increase in the surrounding noise floor, are excited due to the uneven distribution of the fan blades. In combination with the lower blade-passing frequency (f_{BPF} = 133 Hz) compared to the full rotor, significant noise sources are shifted towards lower frequencies. For the two-blade case the BPF is once again reduced to f = 66.7 Hz and the global aerodynamics of the rotor is no longer affected significantly, leading to a simultaneous transition into stall for the baseline and the 2-bladed serrated case.

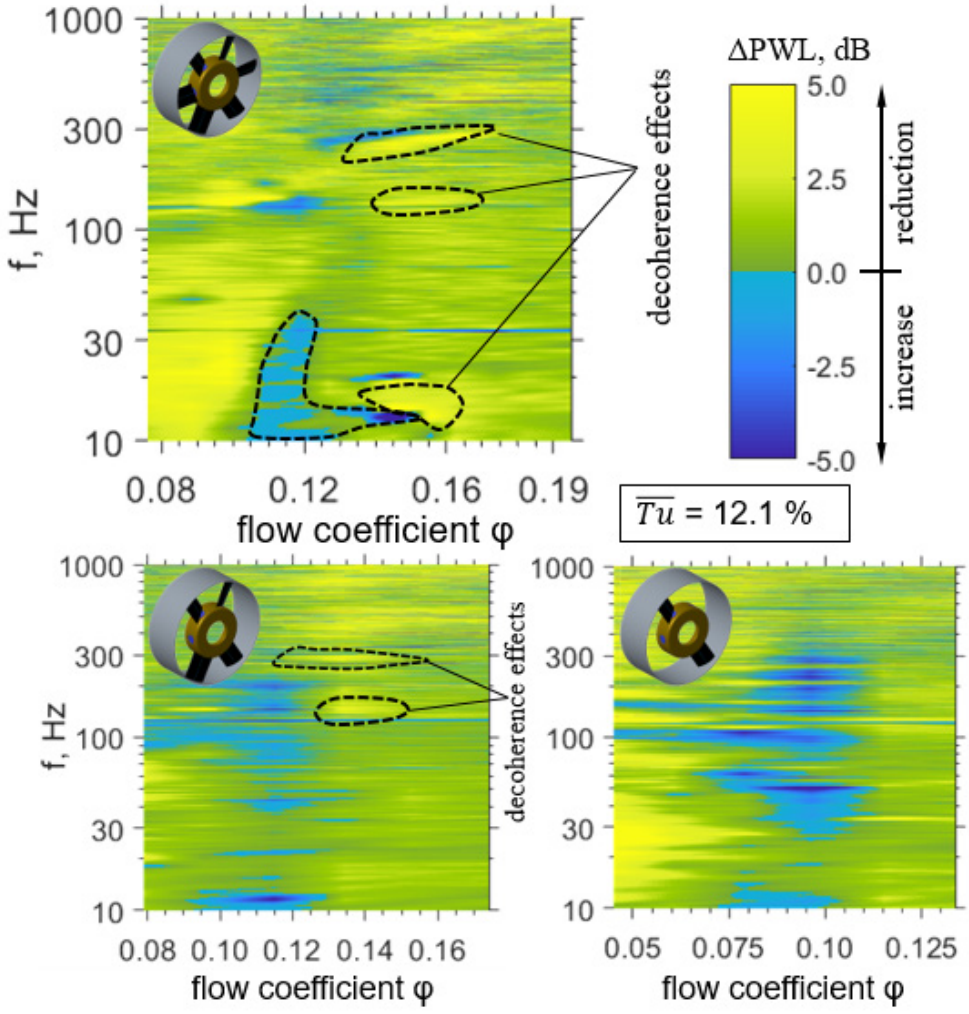

Figure 5-7 Reduction in spectral sound power level (BSLN vs. A14λ13) over varying flow coefficients φ with 6 blades (top), 4 blades (bottom left) and 2 blades (bottom right) at high incoming Tu [151].

Applying the customized filters presented previously in Section 5.1, Figure 5-8 shows the contribution of low-pass (LP), tonal (T) and broadband (BB) components, as well as the reduction in blade-passing frequency (BPF) for the microphone signals on the discharge side of the fan. For the 6-blade case, a clear dependency of the noise reduction capability on the low-

pass and broadband components becomes evident, which shows a highly similar trend when the flow coefficient is varied.
Especially for the highly turbulent inflow conditions, the level-dominant components at pre-stall are the broadband (BB) and the low-frequency (LP) noise, with the broadband part having a slightly higher impact. The noise reduction due to these components increases from high flow coefficients towards the operating point as the serrations efficiently reduce leading edge noise by decorrelation effects along the serrated span of the blades. In the stall region, however, no noise reduction takes place, even though significant broadband and low-frequency noise sources are present. The underlying effect seems to be of aerodynamic nature, where a crossing of the vortices generated by the leading edge serrations and the tip gap reverse flow, affect the aeroacoustic performance in this region.

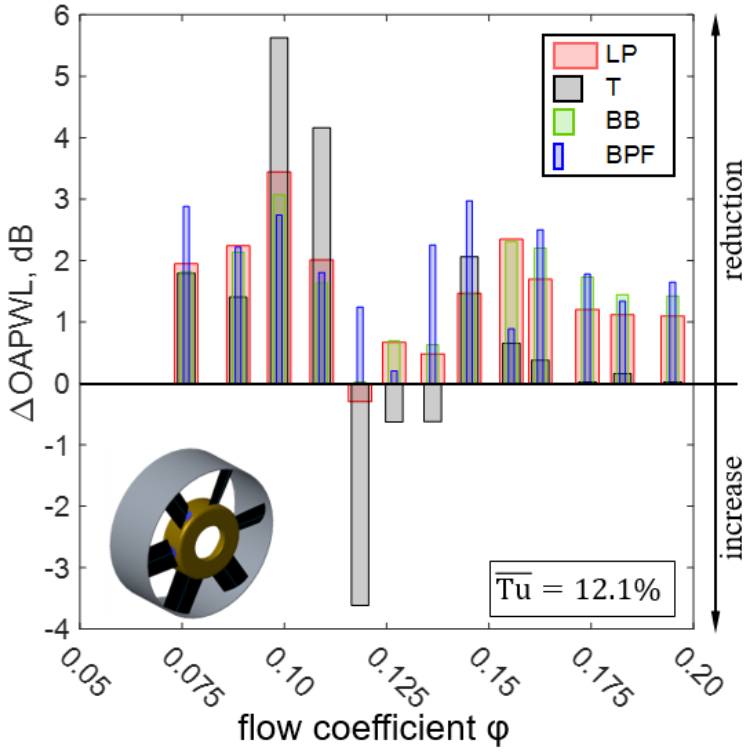

Figure 5-8 Filtered overall sound power level reduction ΔOAPWL for the full rotor (6 blades) at high incoming Tu vs. the flow coefficient φ [151].

At low flow coefficients, the main contribution of the overall noise reduction is once again due to the low-frequency component, which now dominates the broadband part. Here, large-scale structures are separating from the blade suction sides, impinging on the leading edges of subsequent blades. Interestingly, the tonal components for the full rotor show an increase over a large range of flow coefficients. This increase cannot be observed either for the 4-blade or for the 2-blade case (Figure 5-9), which itself shows a more pronounced sensitivity to the LP components. This sensitivity is meaningful as long as the BPFs and their harmonics are shifted towards lower frequencies.

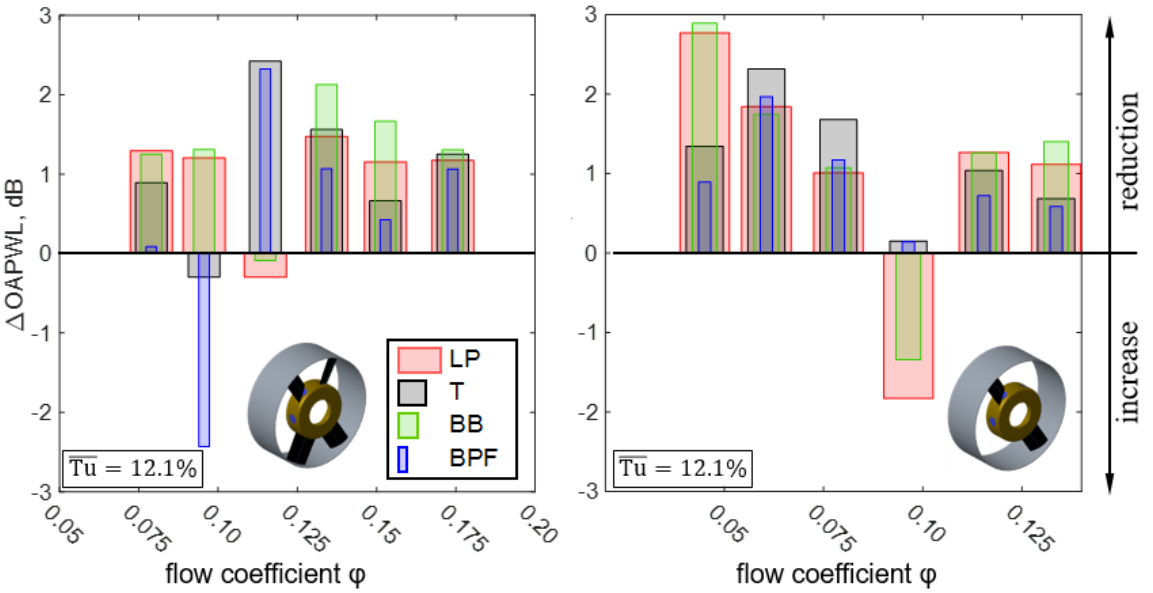

Figure 5-9 Filtered overall sound power level reduction ΔOAPWL for the 4-blade rotor (left) and the 2-blade rotor (right) vs. the flow coefficient φ [151].

5.5 Wall Pressure Analysis

As explained in Section 4.3, wall-pressure measurements are conducted using two pressure-tapping sensors, located at a circumferential distance of one blade passage, corresponding to 60 deg (Figure 4-7). In the axial direction, the sensors are mounted close to the blade-tip leading edge. Figure 5-10 (left) shows the wall-pressure spectra of the full BSLN rotor at high incoming turbulence. The main features that can be observed are strong low-frequency fluctuations at $f \leq 300$ Hz, starting at the beginning of the stall region. These effects can be ascribed to tip-separated flow phenomena, clearly scaling with the flow coefficient and therefore resulting at lower flow coefficients in a shift towards lower frequencies. Interestingly, both the frequency range and the limits of the high-intensity region in Figure 5-10 are comparable to the plot of the spectral airborne-noise radiation in Figure 5-6 for the same case, even though the wall-pressure fluctuations are only partially radiated into noise for higher frequencies. The similar pattern for the low-frequency region, though, suggests a close link between the near-tip region of the rotor and the acoustic noise radiation. Analysing the spectral differences between BSLN and A14λ13 serration in Figure 5-10 (right) shows significant reductions for the serration pre-stall until the stall region is entered. This reduction is clearly of broadband character, once again showing the stall-delaying effect of the serrations. However, the stall region appears to be narrower and also of higher intensity than the stall region of the baseline, leading to an increase in the fluctuations in a limited range of flow coefficients. At high flow coefficients, though, the aeroacoustic effect of the serration comes into play, clearly reducing broadband fluctuations in the near-tip region as indicated in Figure 5-10 (right) for $\varphi \geq 0.15$ as well as in Figure 5-7 (top). Comparing the trend of the wall-pressure fluctuations of the baseline rotor in Figure 5-10 (left) to that of the fan characteristic curves in Figure 5-3 shows high similarities. This indicates that separation effects and reverse flow in the blade-tip region directly affects the near field, although not necessarily leading to noise radiation.

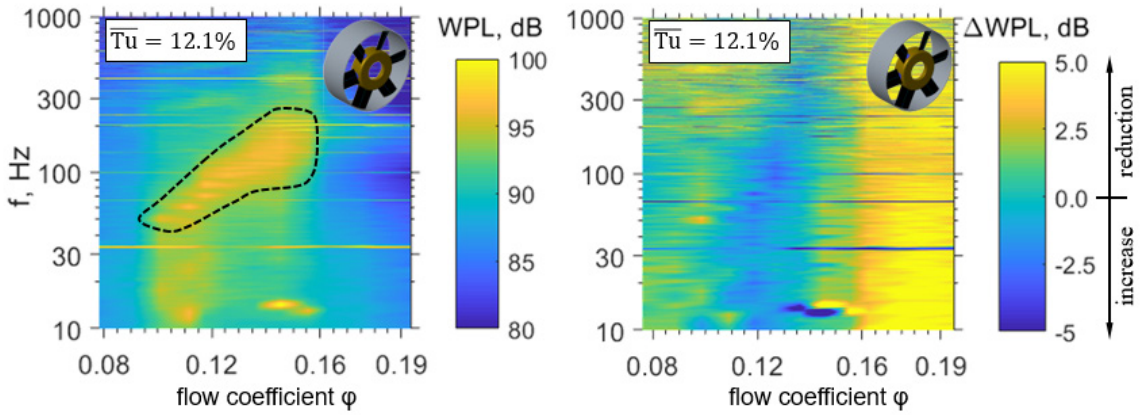

Figure 5-10 Spectral wall-pressure level for the full BSLN rotor (left) and spectral wall-pressure level reduction (right) at the Tu = 12.1 % case over varying flow coefficient φ [151].

As for the acoustic signals, for a specific region at stall, the wall-pressure fluctuations of the serrations, too, are higher than those of the baseline. This region is shifted towards lower frequencies and lower flow coefficients when the number of blades is reduced (Figure 5-11), albeit less intense than for the two-blade case, as lower static pressure differences are achieved. Reducing the number of blades shows an extension of the near-field reduction potential towards lower flow coefficients and higher frequencies, once again due to the shift of significant tonal components to lower frequencies. Moreover, at high flow coefficients φ, the absolute reduction increases continuously from the 2-blade case to the 6-blade case, which might indicate improved blocking effects of the tip gap region due to the vortices generated by the serrations.

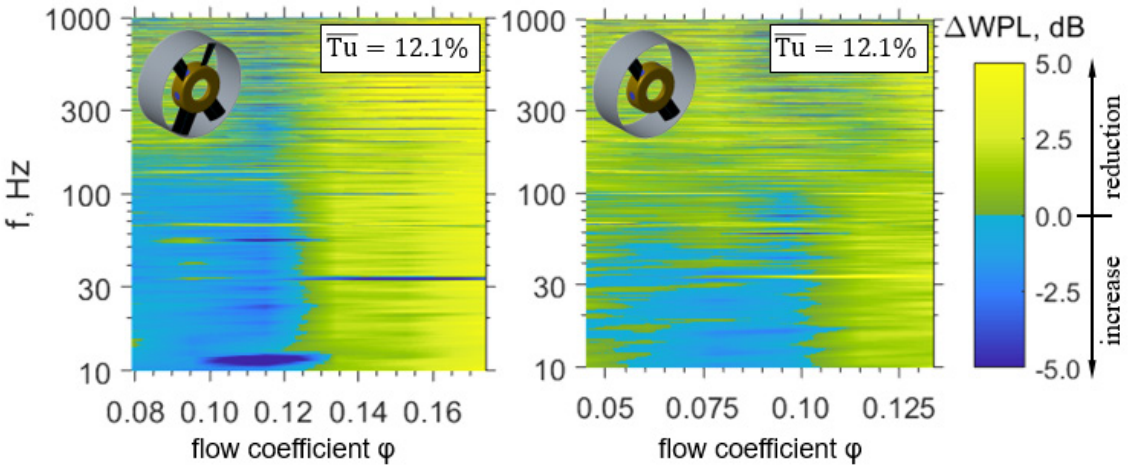

Figure 5-11 Spectral wall power level reduction ΔWPL with 4 blades (left) and 2 blades (right) over varying flow coefficient φ at high incoming Tu = 12.1 % [151].

Wall-pressure fluctuations and near-field information turn out to be of relevance for the noise radiation mainly in the stall region, in which low-frequency phenomena of high intensity are observed. Nevertheless, a significant reduction, especially of broadband character, is observed for the serrations over a large range of flow coefficients, although the reduction is most prominent at pre-stall ($\varphi \geq 0.16$), as can be seen for the filtered wall-pressure signals in Figure 5-12. At $0.09 \leq \varphi \leq 0.12$, the rotating stall affects the wall-pressure reduction capability of the serrations because of low-frequency components (LP filter), but also showing improved performance for lower tonal components (T filter). The broadband components (BB), however, show a higher sensitivity to changing flow conditions and are, therefore, already decreasing when the stall region is entered.

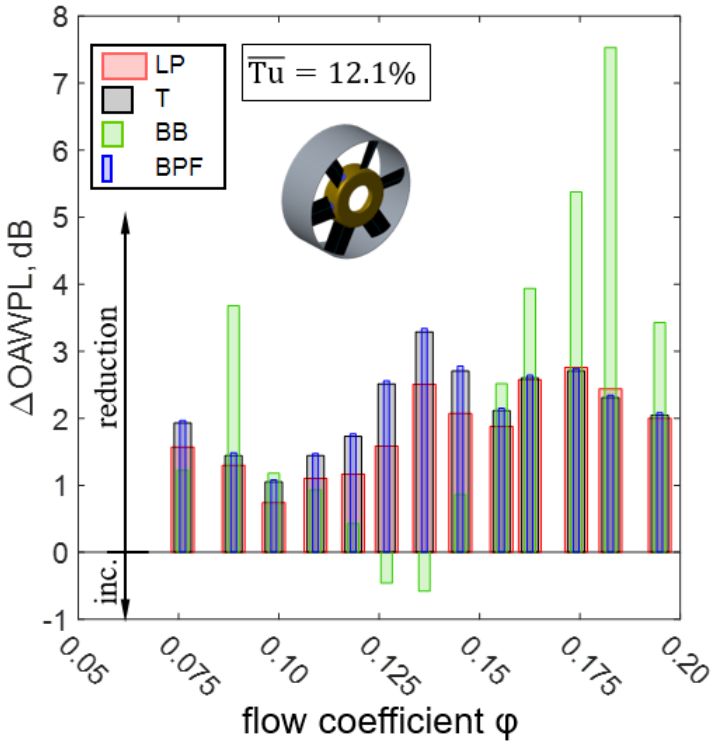

Figure 5-12 Filtered overall wall power level reduction ΔOAWPL with 6 blades over varying flow coefficient φ at high incoming Tu = 12.1 % [151].

Comparing the filtered reduction in wall-pressure level in Figure 5-12 to the filtered noise reduction in Figure 5-8 confirms the general trends at varying flow coefficients but does not provide a direct transferability from the near-field wall pressure fluctuations to the far-field acoustic radiation. Therefore, the cross-power spectrum (CPS) based on the signals from the microphones and near-field wall-pressure tapping points gives further insights into common spectral effects. Figure 5-13 (bottom) shows the CPS, comparing the radiated noise (top) and the wall-pressure signal (centre). In particular, at 100 Hz ≤ f ≤ 200 Hz and 240 Hz ≤ f ≤ 340 Hz, significant broadband peaks are observed that can be traced to the wall-pressure spectrum, indicating that when significant aerodynamic effects such as stall or tip gap flows occur, these aerodynamically generated pressure fluctuations are partially radiated into noise. The same is true for serration effects when an efficient reduction of near-wall structures is achieved. In consequence, the wall-pressure analysis can be used to identify aerodynamic phenomena, which do significantly affect the acoustic performance. In a second step, these phenomena can also be separated from purely aeroacoustic effects of the leading edge serrations.

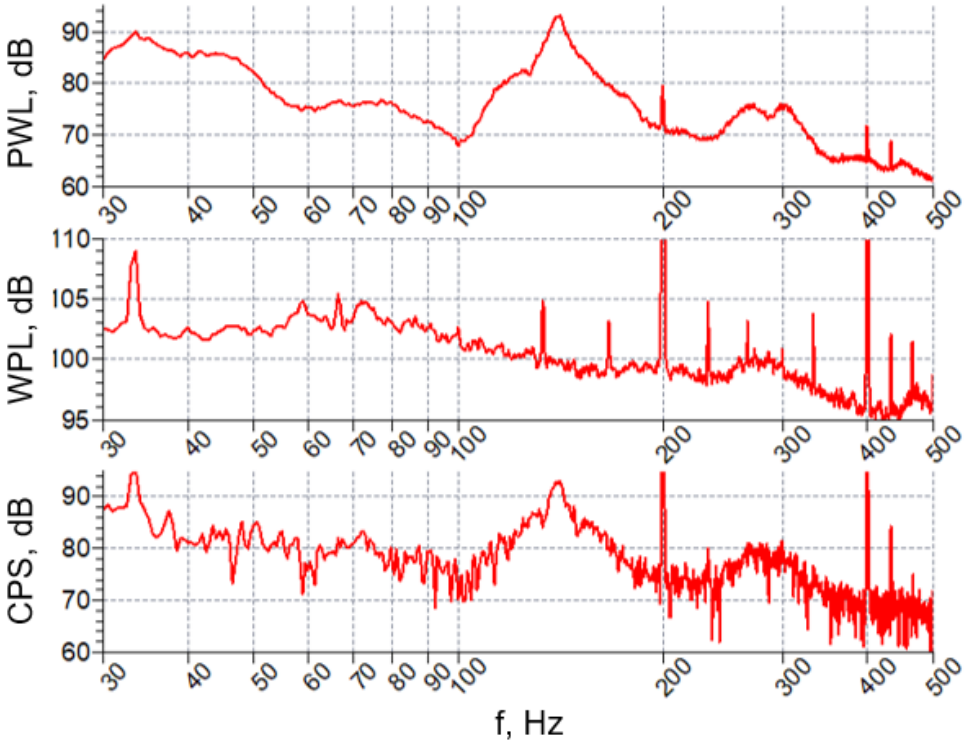

Figure 5-13 Comparison of spectral acoustic radiation (top) and spectral wall-pressure fluctuations (centre) by means of the cross power spectrum (bottom) for the full BSLN rotor at $\varphi = 0.12$, $\psi = 0.19$, $Tu = 12.1$ % [151].

5.6 Coherence Analysis

The significant wall-pressure reduction close to the stall region of the 6-blade case in Figure 5-10 can, among others, be attributed to the stall-delaying effect of the serrations and tends to stagnate at lower flow coefficients. This leads to the question of whether after entering the stall region at $\varphi \leq 0.16$, a second effect comes into play, causing the observed reduction with further throttling. Therefore, the coherence function γ^2 (*Eq. 5-1*), describing the normalized similarity between two signals, is used to analyse the two wall-pressure signals. As can be seen in Figure 5-14, a region of high coherence appears at a low-frequency band of $50\ \text{Hz} \leq f \leq 150\ \text{Hz}$ and its odd integer multiples. The frequency band, at which high coherence occurs, increases with increasing flow coefficients. This becomes meaningful when envisioning the vortex shedding in the blade-tip region in the form of a periodic shedding from an aerofoil's suction side, showing a change in the shedding frequency as a function of the inflow angle. Thus, vortices of lower frequencies but of high aerodynamic wavelength and increased slip to the rotor speed are shed at low flow coefficients in the blade-tip region. The obtained structures of high coherence exist over at least one blade passage and are non-synchronized with the rotor speed, similar to the tip-clearance effects described in [143]. Comparing the coherence spectrum in Figure 5-14 with the wall-pressure fluctuations in Figure 5-10 (dotted region) indicates that only the centre of the high-intensity pressure fluctuations can be ascribed to these rotating structures. However, although these structures are caused by vortex shedding, they are not found in the wall-pressure reduction spectra in Figure 5-10 (right) and Figure 5-11, as they seem to be masked by the global reduction effects in the blade-tip region. Nevertheless, the pressure fluctuations caused by these rotating structures are apparently radiated and reduced by the serrations as they can partly be found in the acoustic spectra in, for example, Figure 5-7 (dotted regions).

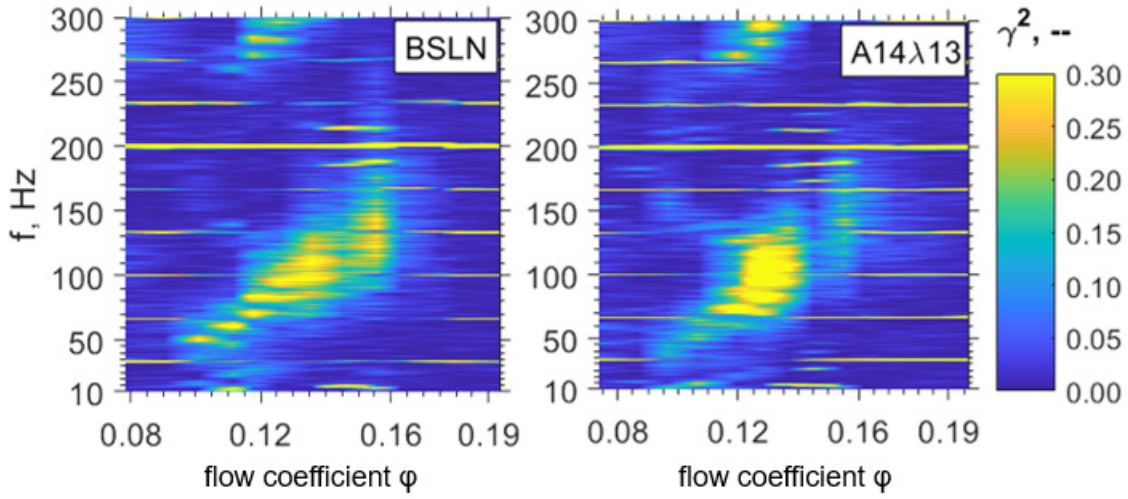

Figure 5-14 Coherence γ^2 for BSLN (left) and A14λ13 (right) over varying flow coefficient φ. Full-rotor case at Tu = 12.1 % [151].

Comparing the coherence of the two individually analysed leading edges, as shown for the 6-blade case in Figure 5-14, reveals a significant reduction when the stall region is approached but an increase in coherence when the stall region is entered. This reduction also affects the acoustic signature (Figure 5-7), including higher harmonics of the coherent regime. This once again indicates a close relationship between the wall-pressure fluctuation and the gathered airborne noise, with the serrations seemingly altering the flow structure of the separated structures.

Only at significant amplitudes of the coherence function γ^2 can the phase spectrum of the complex CPS be analysed as well. Figure 5-15 shows a high coherence and an almost linear trend of the associated phase angle Φ in a frequency band of 60 Hz ≤ f ≤ 140 Hz, indicating a constant propagation speed of a structure within the defined frequency range. At known sensor distance Δx, evaluating the slope of the phase angle $\Delta f/\Delta\varphi$ yields, according to *Eq. 5-3*, the absolute value of the convective propagation speed of the coherent structure.

$$U_{Conv} = \frac{\Delta f \cdot \Delta x \cdot 360}{\Delta \Phi} \qquad \textit{Eq. 5-3}$$

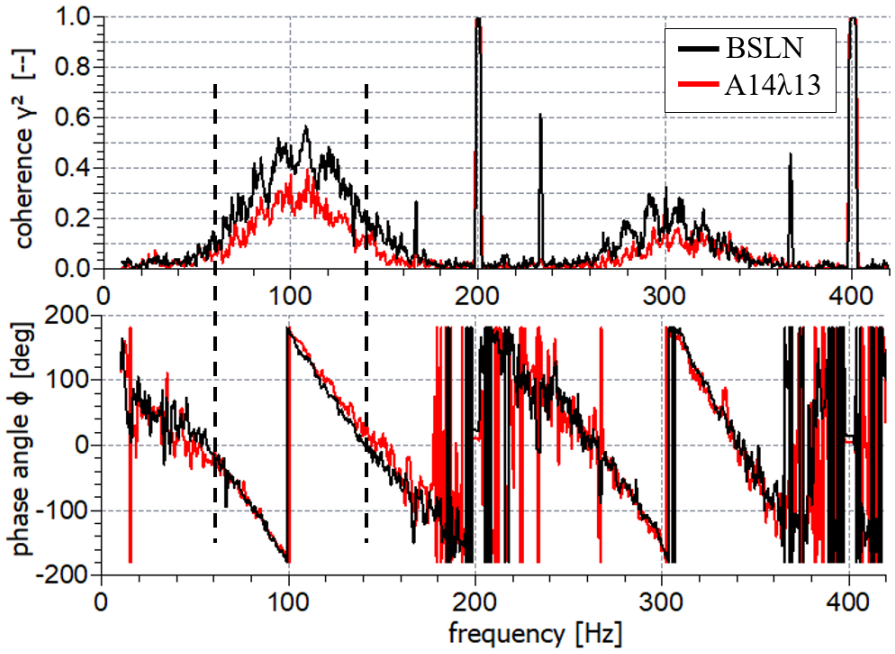

Figure 5-15 Spectral coherence function and phase angle Φ of the two wall-pressure signals at $\varphi = 0.14$, $\psi = 0.18$. Full-rotor case at Tu = 12.1% [151].

Evaluating the extracted convective velocities of the rotating structures (Figure 5-16) at varying flow coefficients shows higher velocities for the baseline case than for the separated structures of the serrated rotor. Hence, for this case, a link between coherence and the corresponding velocity can be established from the phase information. Coherent structures similar to the ones shown in Figure 5-14 are also present for the 4-blade case and, to a lesser extent, also for the 2-blade case. However, the impact of these structures tends to decrease with decreasing blade number. The observed reduction in propagation velocity due to the serrations is expected to be caused by increased mixing when the vortices of the serration and the rotating structure are interacting. In consequence, the scattering of this separated blade-tip structure can be regarded as responsible for the reduction in coherence and, therefore, for a reduction in the radiated noise.

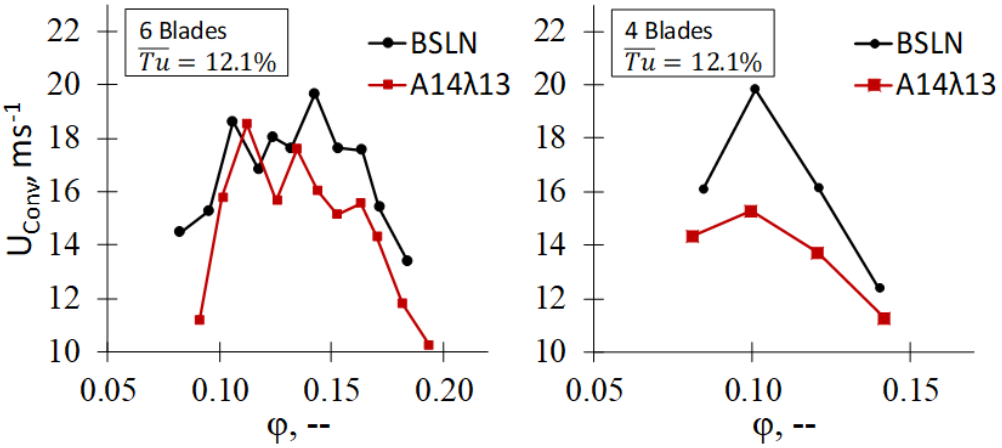

Figure 5-16 Convective velocities U_{Conv} at Tu = 12.1 % between the pressure tapping points for the full rotor (left) and the 4-blade case (right) over varying flow coefficient φ [151].

5.7 Conclusions

An aerofoil with previously well-analysed leading edge serrations is transferred to a rotating frame in the form of a low-pressure axial fan. Comparing a baseline fan with straight leading edges to a serrated fan provides information on the noise reduction capability as well as the aerodynamic performance. However, the focus of the current study is not to maximise the noise reduction but to gain deeper insights into the underlying noise reduction effects over the full-fan characteristic curve. For the identification of transfer effects from the rigid to the rotating frame, a successive approach was chosen, varying the blade number. This approach allows conclusions to be drawn on possible blade interaction, blade-tip influences and reverse flow interactions.

For the serrated rotor, the aerodynamic results show an improved stall range of diminishing global effect with lower blade number. However, this comes with penalties for the aerodynamic pressure coefficient. In the serrated rotor, as compared to the non-serrated rotor, this effect leads to significant noise reduction close to the stall region and is attributed to the vortices generated by the serrated contour, resulting in a delay of stall. For practical applications, the benefits in noise and the drawbacks in terms of the static pressure rise still need to be weighed against each other in the current stage of research.

Aeroacoustically, interaction effects for the full-rotor and, to a lesser extent, for the 4-blade case were identified, with separated structures efficiently being reduced by the serrated leading edges, resulting in noise reduction. In general, the noise reduction capability of the serration increases with increasing blade number. The simultaneously increasing complexity of the flow also leads to more efficient radiation of the potential noise sources, further increasing the range in which leading edge serrations might show beneficial effects. This positive aeroacoustic effect in terms of blade interaction seems promising, especially for applications of low rotor solidity.

The classic high-turbulent inflow conditions, investigated previously for rigidly mounted aerofoils, are dominant only at pre-stall conditions and, though the noise-generating vortices are of large-scale character, at post-stall. Here, the classic decorrelation effects of the serrations show noticeable efficiency. For the remaining parts of the fan curve, the noise reduction capability strongly depends on the underlying phenomena that generate the noise.

Correlating the acoustic signature with the wall-pressure signals, obtained from two circumferentially spaced sensors in the fan axis, revealed a relation between the near-field pressure fluctuations and the radiation into noise. However, this relation was found to be relevant only when strong aerodynamic effects in the blade-tip region exist.

Further processing of the wall-pressure data by means of the coherence and the phase relation between the two sensors revealed the existence of coherent structures, non-synchronized with the rotor speed and of varying slip. These structures appear when the fan instability region is entered and are expected to stem from flow separation close to the blade tip. Introducing serrated rotors leads to a significant shift of these structures towards lower flow coefficients, decreasing the total extent of the coherent vortical structures. This decrease in total extent was found to affect both the near-field wall pressure and the noise radiation. The underlying mechanism is attributed to increased vortex interaction effects, leading to a reduction in the convective vortex velocity and a scattering of the large-scale structures, resulting in a decreased coherence.

6 Parameter Study of a Rotating Application

For a more general analysis of the serration parameters, the five key designs (Figure 6-1), already analysed in the rigid domain by means of aerodynamics (Section 2) and aeroacoustics (Section 3), are scaled according to the adopted chord length of the rotor blades and tested along with a wide operational range of the rotating frame. As discussed previously, it is no longer possible to treat the aerodynamic and the aeroacoustic performance of serrated leading edges separately, as is often done for rigid aerofoils. A simultaneous analysis is thus inevitable, especially since the aeroacoustic efficiency depends on the specific operating point.

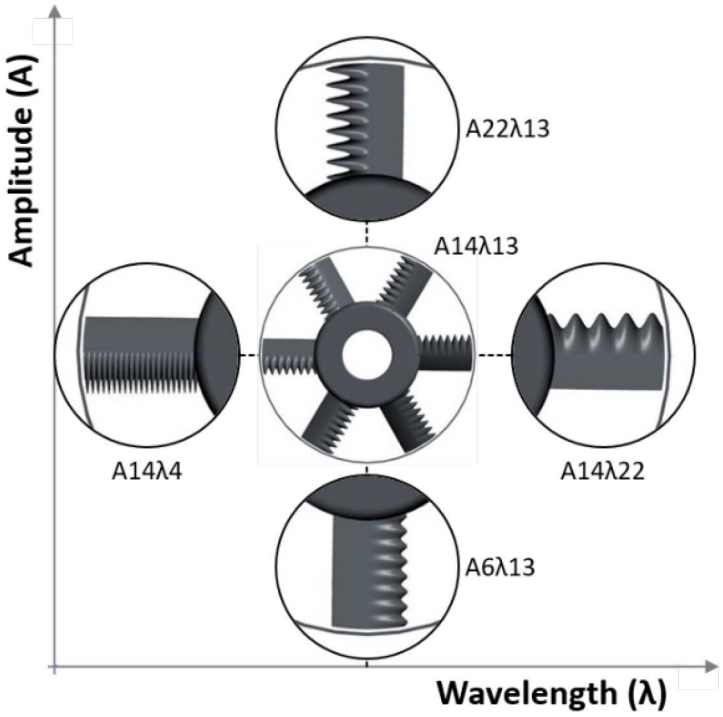

Figure 6-1 Analysed serration designs for the tested rotors. Absolute values for amplitude A and wavelength λ are indicated in mm [167].

The measurement expenditure for obtaining reliable and interpretable results for the aerodynamic characteristics is relatively low, since all measurement quantities are slow and no spectral insights are needed. For the aeroacoustic characteristics and the wall-pressure data, on the other hand, a high-frequency resolution and a sufficient number of block averages are needed in order to provide smooth spectra of low stochastic noise; otherwise the measurement results become polluted. This results in significant experimental efforts and long measurement times. As a consequence, the aerodynamic performance was monitored in high detail with small increments in the flow coefficients, as can be seen in Section 6.1, whereas for the aeroacoustic measurements, the increment in flow coefficient was increased (Section 6.2). For completeness, the aerodynamic performance was monitored during the aeroacoustic measurements as well, serving for validation.

6.1 Aerodynamics

Similar aerodynamic trends are observed for all the turbulent cases tested. For brevity, the fan characteristic curves of the serration configurations tested, as well as the baseline case, are presented in Figure 6-2 at low turbulence intensity, whereas the aerodynamic performance for higher Tu can be found in Appendix F.1. Generally, the results obtained are highly comparable to those in the rigid domain (Section 2.2.3), showing maximum performance for small

amplitudes and high wavelengths. Pre-stall at $\varphi > 0.17$, no significant differences between the tested models are visible except for the A14λ4 case of minimum wavelength. The aerodynamic efficiency, though, shows significant differences for the same range of flow coefficients, which can be attributed to the previously described vertical and diagonal shift of the C_L/C_D coefficients of rigid aerofoils equipped with leading edge serrations (Section 2.2.3). Because of the continuous increase in drag due to the vortex-generating and crossflow effects, serrations of low serration wavelength and high serration amplitudes tend to show poorer performance. The differences in the serrated rotors become more prominent when the operation range is further extended to lower flow coefficients. In this parameter region, as soon as the fan operates on a secondary characteristic, less pressure rise at a significantly reduced performance is achieved, clearly scaling with the serrated design parameters.

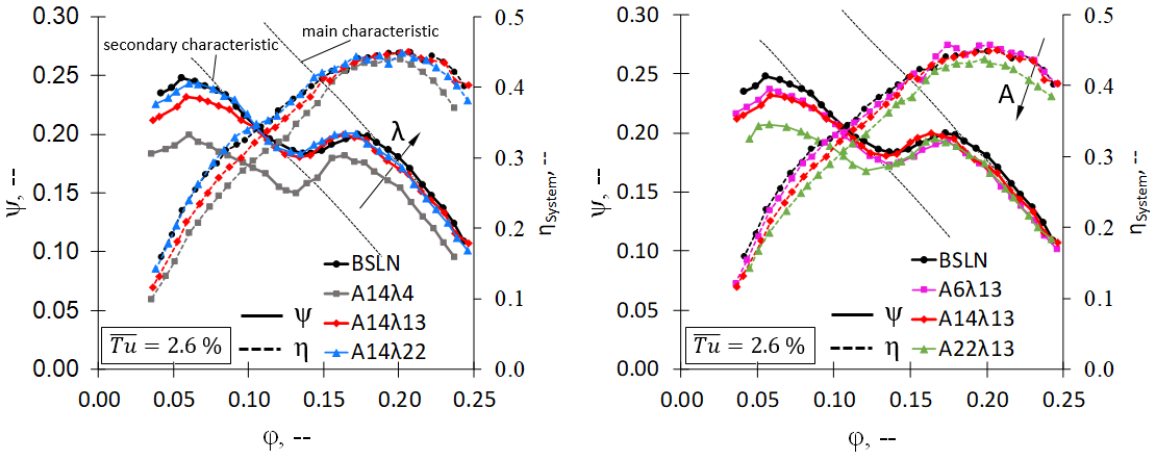

Figure 6-2 Characteristic curves of pressure vs. flow coefficient for the tested rotor configurations at varying serration wavelength λ (left) and serration amplitude A (right). Tu = 2.6 %.

As already indicated in Section 5.3, a slight increase in the onset of stall in the form of a shifting pressure maximum is observed with increasing serration amplitude and decreasing serration wavelength. More globally, this shift tends to increase with increasing A/λ from A6λ13 (A/λ = 0.46) to A14λ13 (A/λ = 1.08) to A14λ4 (A/λ = 3.5).

6.2 Aeroacoustics

6.2.1 Turbulence Sensitivity

For the aeroacoustic response of the tested rotor, Figure 6-3 (left) shows the sensitivity of the baseline rotor to varying grid-generated levels of turbulence for seven discrete points along the fan characteristic curve, together with the aerodynamic properties (Figure 6-3, right). It is clear that particularly for high flow coefficients $\varphi > 0.17$ or in the pre-stall regime, the rotor blades are prone to turbulence-ingested noise radiation. For lower flow coefficients $\varphi < 0.17$, initial instability effects, such as local and partial separation from the blade suction sides and tip leakage flow, occur, followed by large-scale separation with further throttling of the system. These separation and crossflow effects tend to dominate the aeroacoustic response of the rotor, making it insensitive to the comparatively small disturbances in the generated turbulence, as can be derived from the collapsing curves in Figure 6-3 (left). This observed impact of the turbulence on the sound power level (PWL) shows close qualitative agreement with the experimental results of Carolus and Stremel [148], who also tested a ducted low-pressure axial fan, showing PWL increases of up to 20 dB due to stall. Similar results were also found by Krömer et al. [171], who tested the effect of inflow disturbances for axial fans with a short ducted casing. Moreover, Carolus and Stremel [148] observed a turbulence-induced increase in

the stall margin (in which the noise starts to increase) due to delayed flow separation. This delayed flow separation is also seen in the present results in the form of the acoustic and the aerodynamic response (Figure 6-3), even though a clear confirmation is not possible because of the limited resolution of the measurements.

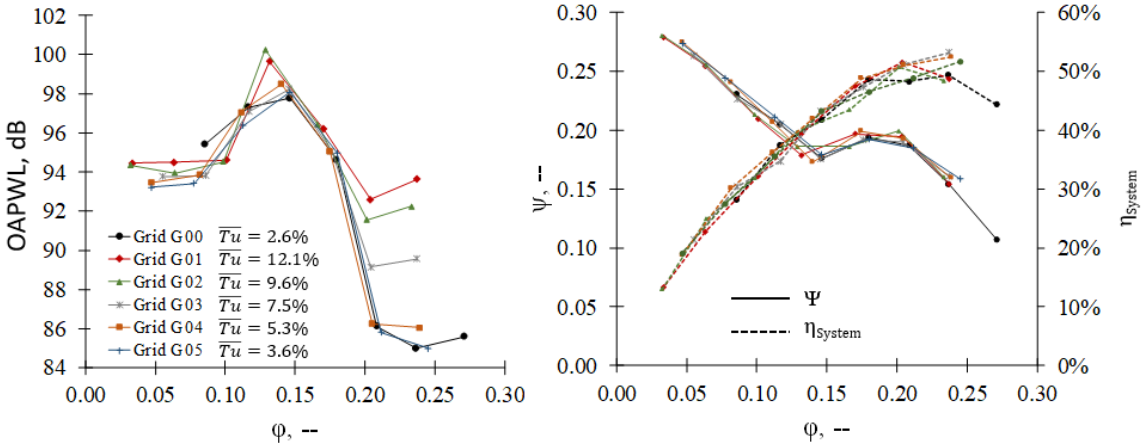

Figure 6-3 Effect of inlet turbulence Tu on the radiated overall sound power level OAPWL of the baseline rotor (left) vs. the flow coefficient φ. Associated aerodynamic performance (right).

As a consequence of the observed distribution of the turbulence sensitivity, the serrated leading edges are expected to work aeroacoustically only for high flow coefficients according to the well-investigated principles described for rigidly mounted aerofoils (Section 3.2.1). For low flow coefficients ($\varphi \leq 0.17$), additional mechanisms of the serrations as described in Section 5 are present, leading to a significant noise reduction, even though on the basis of aerodynamic flow phenomena.

6.2.2 General Noise Reduction Trends

The overall effect of the tested rotors is presented in Figure 6-4 for all the turbulence grids investigated, showing that the baseline rotor radiates higher noise at all operating points. As discussed in Section 6.2.1, grid-generated turbulence-rotor interaction noise, in particular, is reduced. For maximum flow coefficients, this overall reduction is in the region of $\Delta PWL \leq 2.5$ dB, showing only little influence of the underlying turbulence level, even though the absolute level of the radiated noise increases most significantly with increasing Tu.

The most distinct differences to the baseline rotor occur in the transition region from pre-stall towards instability. The acoustic effect of the onsetting stall in this region is most efficiently shifted towards lower flow coefficients, even though the aerodynamic performance does not indicate a comparable shift in the fan characteristic curves. In terms of serration parameters, this shift tends to scale with the serration amplitude, but also the A/λ ratio seems to play a minor role, tending to increase the shift for higher ratios.

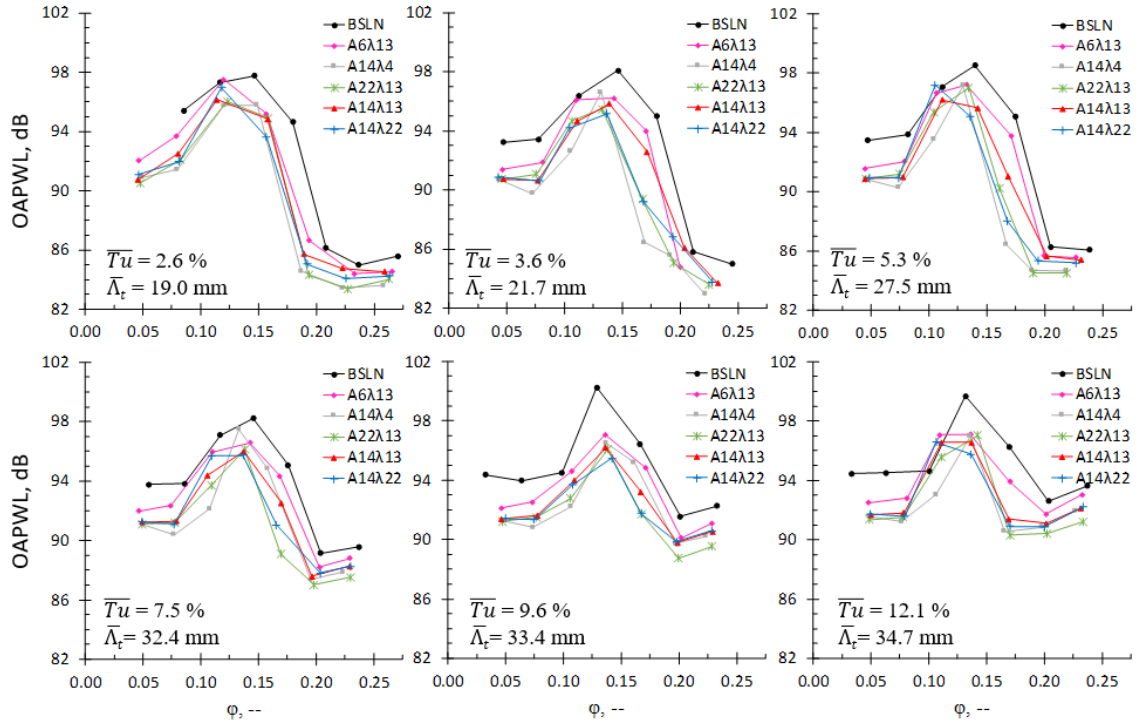

Figure 6-4 Overall sound power level OAPWL for five serrated rotors and a baseline case. The level of incoming Tu increases from top left to bottom right.

The most dominating parameter in terms of the noise reduction, though, is the turbulence intensity, showing a continuous widening of the observed increase in the 'acoustic stall margin', which leads to differences of up to ΔPWL = 6 dB for Tu = 12.1 % and ΔPWL = 8 dB for Tu = 5.3 %. The underlying effect is suspected to be an efficient reduction in small-scale separation due to the known decorrelation effects along the aerofoil span, as well as an efficient shift in coherent structures towards lower flow coefficients, as described in Section 5. This underlying effect, however, requires further validation by taking into account the spectral composition; see Section 6.2.3 and Section 7.

6.2.3 Spectral Broadband Noise Reduction

With the purpose of directly comparing the broadband noise reduction between rigidly mounted aerofoils and the rotating application, the gathered signals are filtered in the frequency domain, as shown in Section 5.1. Here, the fan-speed-dependent tonal components are replaced by a one-dimensional 20th-order median filter of the original signal. The spectral differences between the serrated and the baseline cases yield the noise reduction, which is scaled via the Strouhal number (*Eq. 3-3*), based on the serration amplitude A. However, instead of taking the mean axial velocity U_0 as the normalisation parameter, the mean velocity at the rotor blades $\bar{c}_{x1}$ (Figure 4-13) is chosen.

Figure 6-5 shows the spectral noise reduction at varying turbulence intensity for the serrated rotors tested. As discussed in Section 3.4.1, Chaitanya et al. [103] stated that the spectral noise reduction scales according to *Eq. 3-2* for the rigidly mounted aerofoils with $a_S = 10$ and $b_S = 10$ for an optimum serration design. However, the beamforming study in Section 3.4.2 identified that this optimum increases to $a_S = 15$ and $b_S = 10$ if only the leading-edge section is used. The results presented in Figure 6-5 once again reveal a logarithmic scaling, with the noise reduction capability scaling with the turbulence intensity, predominantly affecting the prefactor, and changing it from $a_S = 10$ for the lowest Tu to $a_S = 22$ for the

highest Tu. Maximum amplitudes show the highest potential for reducing RTI noise. A small wavelength, too, turns out to be beneficial but has less impact.

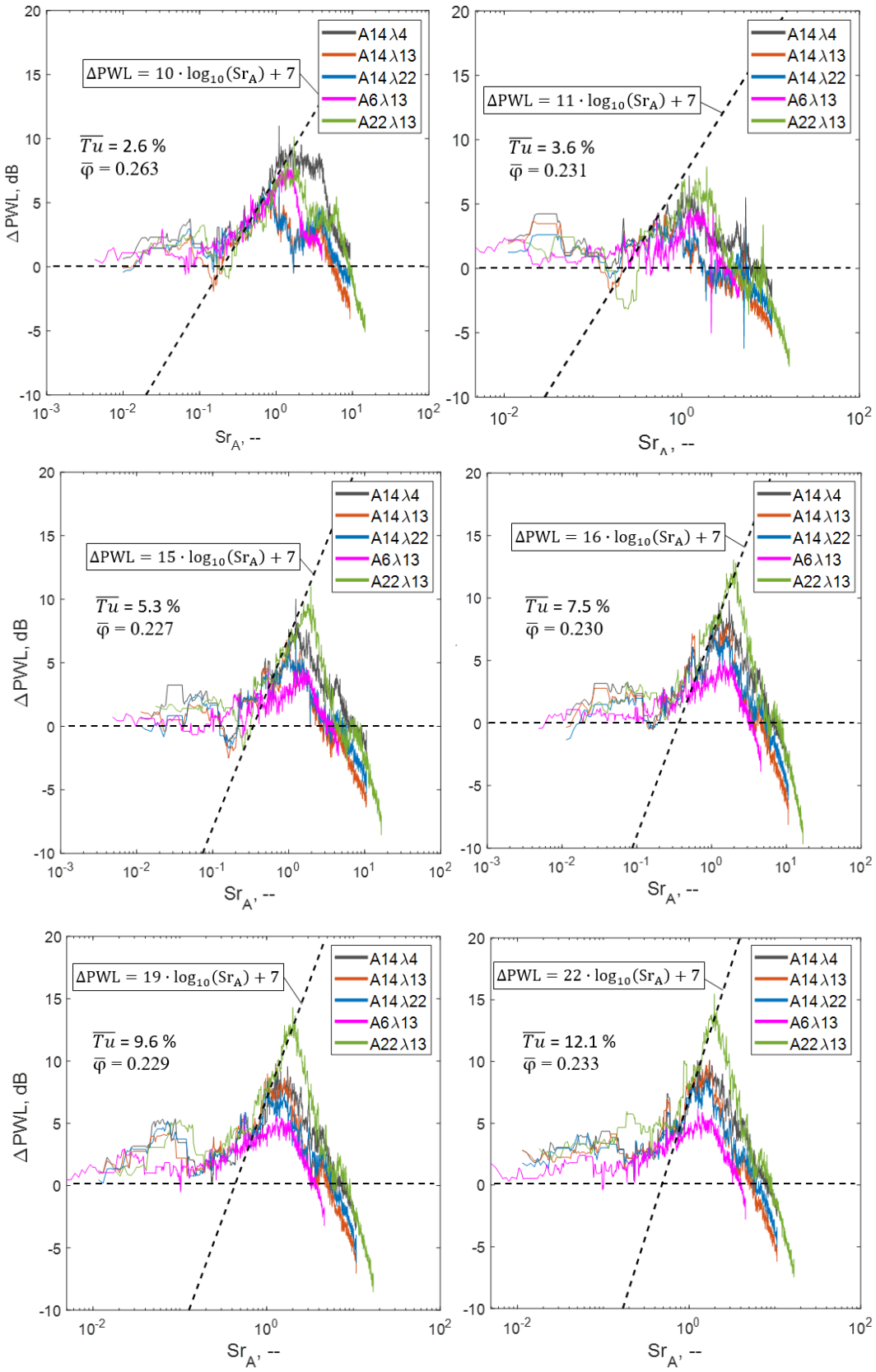

Figure 6-5 Spectral sound power level reduction ΔPWL of the tested rotors at maximum flow coefficient φ and varying Tu. 20th-order median-filtered signals of broadband components only.

As it is mentioned previously, a spectral scaling of the noise reduction according to *Eq. 3-2* indicates a reduction of leading edge broadband noise in accordance with the well-known aeroacoustic noise reduction mechanisms of serrated leading edges in rigidly mounted applications (Section 3.2.1). Altering the flow coefficients of the tested rotors (Figure 6-6), however, reveals a spectral scaling law that is highly dependent on the operating point. At flow coefficients $\varphi > 0.19$, the grid-generated broadband noise is clearly reduced, whereas significantly stronger low-frequency components are induced and also reduced at partial loading of the fan at $\varphi \approx 0.17$ (Figure 6-6 left). Minimum flow coefficients again show a log-dependent scaling of the noise reduction, albeit at a considerably lower level.

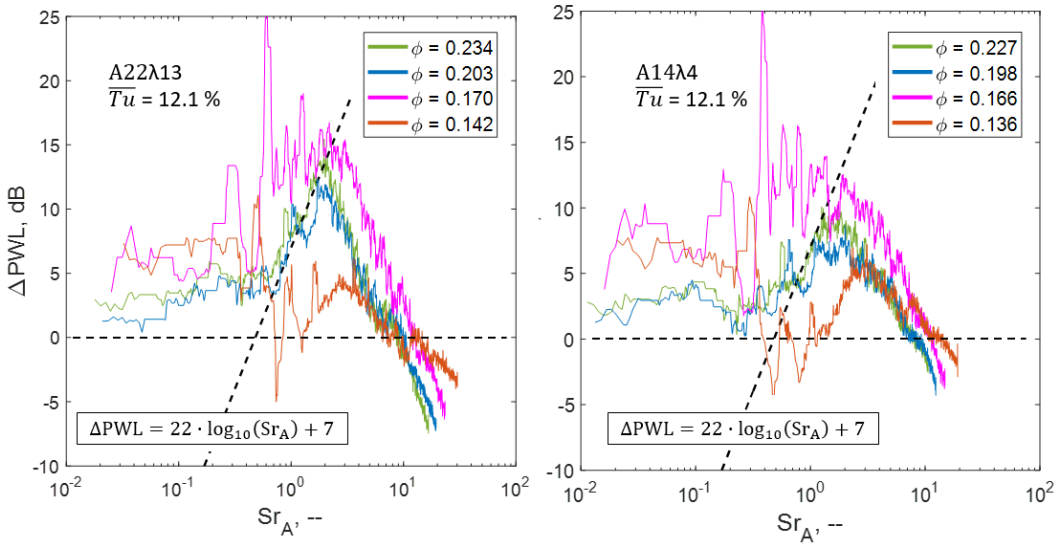

Figure 6-6 Spectral sound power level reduction ΔPWL at varying flow rate for two different serration wavelengths A22λ13 (left) and A22 λ4 (right). Tu = 12.1 %

As can be derived from Figure 6-4, at low Tu ($\leq$ 5.3 %), small wavelengths outperform the larger ones and result in a shift of low-noise towards smaller flow coefficients. For high Tu, however, large wavelengths show the superior pattern, which can also be linked to the Λ/λ-ratio. The spectral analysis in Figure 6-7 shows that the broadband noise reduction continuously improves with decreasing wavelength, following the Sr scaling law. However, for the low-frequency domain Sr $\leq$ 0.7, intermediate to large wavelengths clearly outperform the small wavelengths by efficiently reducing the local separation RTI noise of the upstream blades. This holds true for all turbulence level tested but shows an enhanced effect for cases with lower Tu.

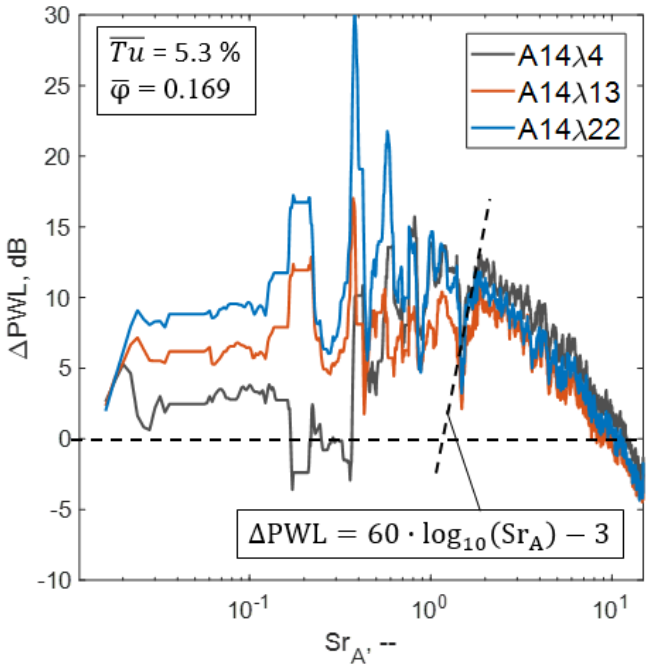

Figure 6-7 Spectral sound power level reduction ΔPWL at the instability region $\varphi = 0.169$ and $Tu = 5.3$ % at varying serration wavelength.

6.3 Conclusions

The parameter study provides detailed insights into the aerodynamic performance as a function of the serration parameters. For the most relevant operation range $\varphi \leq 0.13$, a similar aerodynamic performance of the serrated and the non-serrated rotors was observed with the exception of minimum wavelengths. The aerodynamic efficiency, on the other hand, is reduced due to the increased drag induced by the serrations. Generally, maximum static pressure rise is obtained for low to intermediate amplitudes and large wavelengths. The same is true for the aerodynamic efficiency, comparing well to the previously analysed rigidly mounted aerofoils.

By means of aeroacoustic noise radiation and reduction, small wavelengths and high amplitudes are found to be most efficient, although a differentiation between the specific points of operation is inevitable. The classic broadband noise reduction due to spanwise decorrelation is observed only for intermediate to high flow coefficients. For the instability region at partial load conditions, the previously observed aerodynamic increase in the stall margin (Section 5.3) also results in an increase in the 'acoustic stall margin', which is even more pronounced. Note that the noise reduction mechanism in this region is mainly of aerodynamic origin.

Spectral analysis of the median-filtered narrow-band spectra allowed a direct comparison between the broadband noise reduction and the rigidly mounted aerofoils, showing high similarities in the underlying scaling law but higher prefactors, which control the slope of the noise reduction.

In summary, a meaningful link between the rigid and the rotating domain could be established, providing the first evidence of aeroacoustic efficiency without severe aerodynamic penalties. On the other hand, the study was limited in its resolution along the characteristic curve, indicating the need for further and more comprehensive analysis.

7 Aeroacoustic Modelling of Serrated Rotors

In order to obtain more general statements on the effect of serrated rotors, the aim of this section is an adequate modelling of the investigated systems. The serrated as well as non-serrated rotor designs are complex systems with aerodynamic and aeroacoustic target values. In the case of rigidly mounted aerofoils under high-turbulent inflow conditions, the radiated noise is clearly dominated by the broadband components, resulting from the interaction of turbulent structures and the rigid leading edge. The same applies to the effect of serrated leading edges. In contrast, transferring the aerofoils to a rotating system clearly increases the system's complexity because of the underlying noise sources. This increase in complexity gives rise to additional influences on rotor-speed-dependent tonal components, as well as tip-gap effects, interaction effects between adjacent blades, and interaction with downstream structures, such as, for example, struts or stators. In consequence, a successful modelling of the resulting overall level requires a minimum knowledge on the spectral composition of the multiple noise sources, which is dependent on the operation point of the rotor. Moreover, both aerodynamic and aeroacoustic target values are highly interrelated and need to be taken into account in an equitable manner. Common statistical-empirical modelling approaches, such as the design of experiments (DoE) methodology [112, 172], are limited to second-order models. Even though the global aerodynamic trends of a fan should be properly describable by a quadratic model, these quadratic regression functions are expected to be inadequate when it comes to the modelling of more detailed (spectral) dependencies. Aiming at identifying alternative modelling approaches for the rotating system, preliminary investigations are reported in Section 7.1, comparing the DoE approach to more advanced artificial neural networks (ANNs), which are unlimited in terms of functional complexity. Section 7.2 outlines the chosen modelling approach for the rotating system, and the results obtained are presented in Section 7.3.

7.1 Preliminary Investigations

As it is stated in Section 3.3.1, numerous experimental designs are available to sample the space of interest, which is defined by the maximum and minimum values of the parameters. For this preliminary analysis, three different experimental designs are used and compared in terms of the number of necessary experiments and the resulting accuracy on evenly distributed test data. The presented preliminary results are based on a fundamental study of the baseline rotor and are described in more detail by Biedermann et al. [113].

The first experimental design is the circumscribed central composite design (C-CCD), already described in Section 3.3.1, and consists of a two-level factorial design as well as the star points at the borders of the design space. Consequently, the C-CCD has five different settings for each factor, as can be seen in Figure 7-1 (top left), in which the green rectangles represent the factorial design and the orange rectangles represent the star points. The second experimental design is the Box-Behnken design (BBD) [173], which is a fractional three-level design, exhibiting orthogonal statistical properties (Figure 7-1, top right). The BBD uses factor-level combinations at the surfaces of the design space. Both the C-CCD and the BBD are used to model a quadratic response surface regression [113].

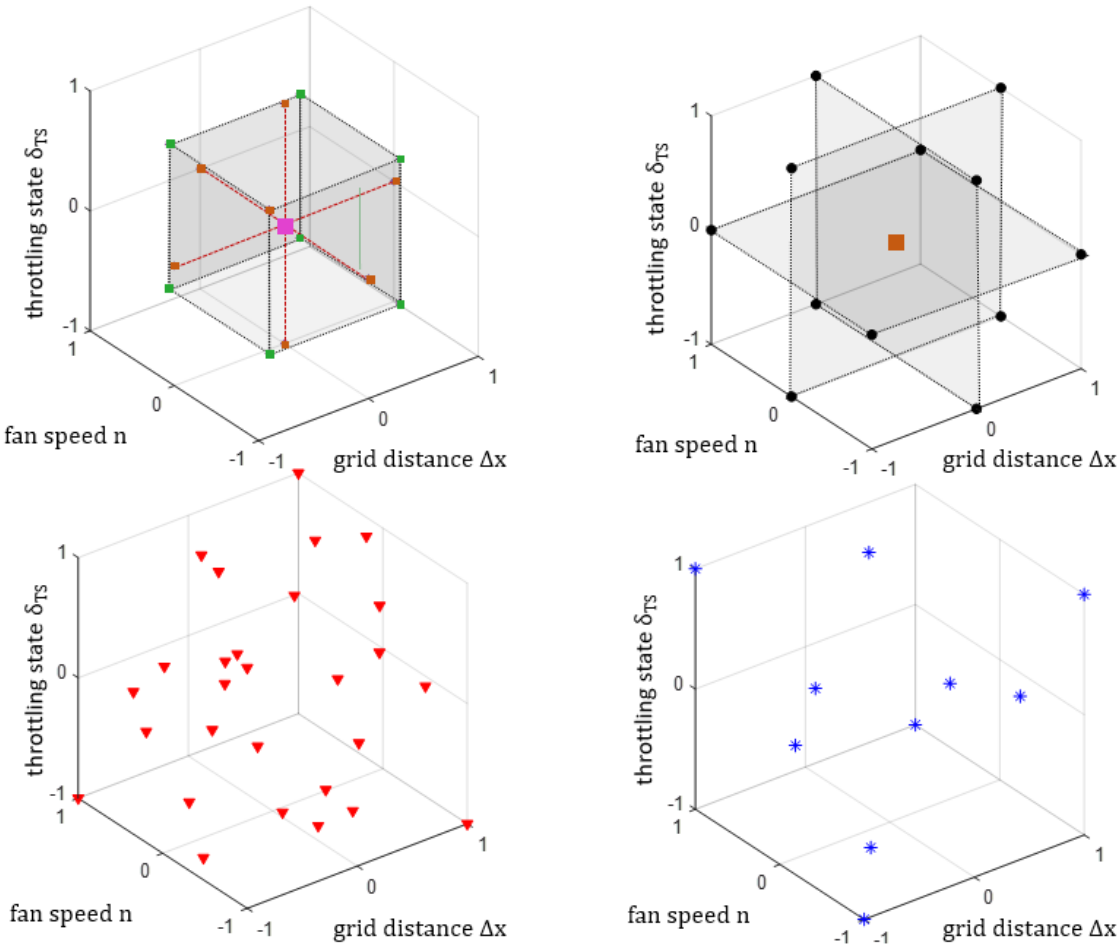

Figure 7-1 Tested experimental designs: central composite design (top left), Box-Behnken design (top right) and Latin hypercube sampling (bottom left). Additional spatial distribution of test data (bottom right) [113].

In recent research, experimental designs are increasingly adapted for numerical approaches [174], such as the design of experiments methodology. In contrast to these designs, Latin hypercube sampling (LHS) was originally developed for computer-aided experiments [175, 176] but is now applied to a complex problem of experimental character. One of the LHS attributes is that the number of levels for every factor (recall: three for BBD and five for C-CCD) equals the total number of factor-level combinations (Figure 7-1, bottom left). Consequently, every factor-level combination is a unique setting. As a result, the LHS allows extracting more diverse information from the design space compared to the C-CCD and the BBD but leads to more cumbersome experiments, especially if a factor requires manufacturing effort. The creation of an LHS is of stochastic nature, which is the reason that designs of more advantageous or disadvantageous nature can be created. To assess different designs, one or more criteria need to be used. For this case study, the maximin criterion [177, 178], evaluating the maximum-to-minimum Euclidean distance between the factor-level combinations, and the pairwise correlation criterion, evaluating the order of commingled factors effects, are used to rate 15,000 randomly created designs [113]. For further reading on LHS and possible optimisation criteria, see for example [179, 177]. To obtain additional information in the corners of the design space, a fractional two-level design is added to the LHS. The design so created can be seen in Appendix G.1. Instead of modelling a quadratic response surface regression, as for the C-CCD and the BBD, the information sampled with the LHS is used to train an artificial neural network (ANN; for further details on ANNs, see [180]). To prevent the ANN from overfitting the data, it is usually split into samples for training (i.e. adapting the parameters of the ANN) and validation (i.e. assessing predictive capabilities on unused or independent data).

For the preliminary investigations in this section, however, a training algorithm according to Bayesian learning [181] is used, which does not require splitting the data into these two subsets, which allows a maximum of samples that can be used for the training of the ANN. On the other hand, the Bayesian learning algorithm tends to produce smooth response functions and is limited in terms of modelling systems of high complexity with high approximation quality.

To test the three generated models against independent data, ten additional measurements are performed (Figure 7-1, bottom right) of which six are spread uniformly across the design space. The remaining four measurements, however, are located at the outer corners of the experimental space, which are traditionally hard to approximate by any model. All three approaches are used to model both the aerodynamic and the aeroacoustic performance of the baseline fan by varying three continuous parameters, namely the rotational fan speed ($1000\ \text{min}^{-1} \leq n \leq 2000\ \text{min}^{-1}$), the level of incoming turbulence ($Tu = f(\Delta x/D)$) and the throttling state δ_{TS} according to *Eq. 7-1* in a range of $0 \leq \delta_{TS} \leq 1$ [113]. The last definition was chosen to generate a parameter that is independent of the fan speed. A continuously adjustable turbulence level was obtained by using a single turbulence grid while varying the distance $\Delta x/D$ to the rotor, resulting in $5.0\ \% \leq Tu \leq 10.4\ \%$.

$$\delta_{TS} = 1 - \frac{\dot{Q}}{\dot{Q}_{Max.}} \qquad \textit{Eq. 7-1}$$

As for developing the statistical-empirical aeroacoustic model in Section 3.3, the DoE models (BB and C-CCD design) in the current section were also generated by using the data analysis software *Statistica®*. The artificial neural networks, based on the Latin hypercube sampling, on the other hand, were trained by use of the *MATLAB Deep Learning Toolbox™*. Detailed information on the training algorithm as well as the chosen data sets for training, testing and validation are provided in Section 7.2.

7.1.1 General Performance

All generated models are rated by the coefficient of determination R^2, which is determined according to *Eq. 7-2*, where y_i is the observed response of the i-th sample, $\hat{y}_i$ is the predicted response of the i-th sample, $\bar{y}$ is the mean of the observed responses and n_{R^2} is the number of samples. The coefficient of determination allows assessing how well the observed values of a system's response can be approximated by the output of a model. A value of R^2 close to one means that the unexplained variance of the model is relatively small compared to the total variance of the data, thus representing a good approximation [113].

$$R^2 = 1 - \frac{\sum_i (y_i - \hat{y}_i)^2}{\sum_i (y_i - \bar{y})^2}, i = 1..n_{R^2} \qquad \textit{Eq. 7-2}$$

Table 7-1 shows the obtained fit of the target values considered. It is seen that the fit of the model mainly shows high values ($R^2 \geq 0.95$) for all chosen approaches, albeit that the Box-Behnken design's response surface regression shows the highest values for the systems' efficiency and the artificial neural network, based on Latin hypercube sampling, fits best for the acoustic target values [113]. Analysing the fit of the independent test data, however, shows a dramatic decrease in the performance of the quadratic models ($R^2 \leq 0.9$) but high performance for the artificial neural network, even though there is still room for further improvement. The aerodynamic trends of Δp_{Fan} and $\dot{Q}$ are properly describable by a quadratic model, in accordance

with the theory of fluid mechanics. The mapping of the systems' efficiency, on the contrary, tends to be more challenging and even collapses ($R^2 \leq 0.7$) when it comes to aeroacoustics, requiring a more complex modelling approach. The experimental effort of the LHS increases by 17 % (24 → 28 runs) compared to the C-CCD and by 87 % compared to the BBD (15 → 28 runs). However, the performance measured by the coefficient of determination R^2 with regard to the test data for $p_{Suction}$ increases by 65 % (79 % $p_{Discharge}$) compared to the C-CCD approach and by 59 % (75 % $p_{Discharge}$) compared to the BBD approach [113].

Table 7-1 Coefficients of determination R^2 for model data and independent test data, comparing different sampling designs and modelling approaches [113].

			No. of Samples	aerodynamic			aeroacoustic	
				Δp_{Fan}	$\dot{Q}$	η_{System}	$p_{Suction}$	$p_{Discharge}$
DoE	BBD	Model Data	15	0.999	0.995	0.998	0.887	0.889
		Test Data	10	0.993	0.991	0.831	0.614	0.555
	CCD	Model Data	24	0.973	0.957	0.727	0.934	0.918
		Test Data	10	0.969	0.937	0.696	0.593	0.543
ANN	LHS	Model Data	28	0.997	0.997	0.951	0.986	0.972
		Test Data	10	0.995	0.994	0.966	0.978	0.973

7.1.2 Spectral Application

As shown in the previous section, the use of artificial neural networks (combined with LHS) allows a precise and accurate prediction of all the target values as well as for a good approximation of the investigated experimental space. However, especially in aeroacoustics and vibroacoustics, information on the spectral shape is essential for providing additional information on the underlying noise generation mechanisms of, for example, fans. Moreover, accounting for the human perception of noise by means of the relative loudness (e.g. A-weighting) requires a frequency analysis as well, since it takes place solely in the frequency domain. Therefore, the conclusions drawn on the superiority of the ANNs vs. the classic statistical-empirical modelling approaches are directly adopted for the purpose of processing the available experimental data towards a spectral model. Because only ANNs are considered for the spectral application and all information gained (Section 7.1.1) shall be used, the full experimental database, including data points from the LHS, the C-CCD, the BBD and the test design (excluding one for actual testing), can be used for a proof-of-concept with regard to spectral approximation. The resulting ANNs do not directly provide information on the systematic relation and influence of the parameters on the target values. However, performing parameter studies based on the ANNs by varying single influencing parameters solves this dilemma and offers the same benefits as the statistical-empirical models based on the design of experiments methodology [113] as for example in Section 3.3.

In order to maximise the spectral information while keeping the amount of data on a reasonable level, 1/3rd-octave bands in a mid-frequency range of 16 Hz $\leq$ f $\leq$ 10 kHz are analysed. This results, in addition to the already described target values, in 58 extra target values, each one representing a fully independent ANN, describing the sound pressure of just one 1/3rd-octave band. The training of the ANNs is performed by using the complete measurement data pool but for one data point, which is used for independent testing. During the training with the above-mentioned algorithm, the maximum relative deviation from the full data set is used to evaluate different networks. The performance is measured by using the training data and

calculating the relative deviation in comparison to the observation of every approximated 1/3rd-octave band for every data point. Table 7-2 shows the maximum, the mean and the median of the deviations, in both the decibel scale and the (linear) Pascal scale, separate for the suction side and the discharge side. Especially in the field of aeroacoustics, it is important to note that only the uncertainty related to the Pascal scale shows a physically interpretable fit of the model, whereas the dB scale is more related to the human perception of sound [113]. Thus, the deviation in the dB scale strongly depends on the referenced underlying mean level since it scales logarithmically.

Table 7-2 Averaged fit of 29 1/3rd-octave band target values at mid frequencies 16 Hz ≤ f ≤ 10 kHz [113].

	Suction Side		Discharge Side	
	dB–scale	Pa–scale	dB–scale	Pa–scale
Median Deviation in %	0.30	2.70	0.26	2.25
Mean Deviation in %	0.53	4.93	0.46	4.15
Maximum Deviation in %	4.58	46.12	6.21	65.01

For the analysed data, the median and the mean deviation show a reasonably good fit of the model with deviations smaller than 5 % in the Pascal scale, for which the discharge side outperforms the suction side. This can be attributed to a slightly better aeroacoustic treatment of the discharge side by the anechoic termination, showing an improved ability to suppress back reflections at the duct exit due to impedance differences. The maximum deviation, though, is significantly higher and indicates the need for further validation and, possibly, a bigger data pool to decrease the experimental noise. For gaining some insight into the ability to generalise, one data point that is not part of the training data is used for a prediction of the spectral information. The comparison between the prediction and the experimental data is presented in Figure 7-2. Qualitatively, the trend of the SPL with the frequency is considered to be well approximated. The same applies to the quantitative nature of the prediction, even though single frequencies exhibit a lack of fit, affecting the total accuracy of the modelled experimental space.

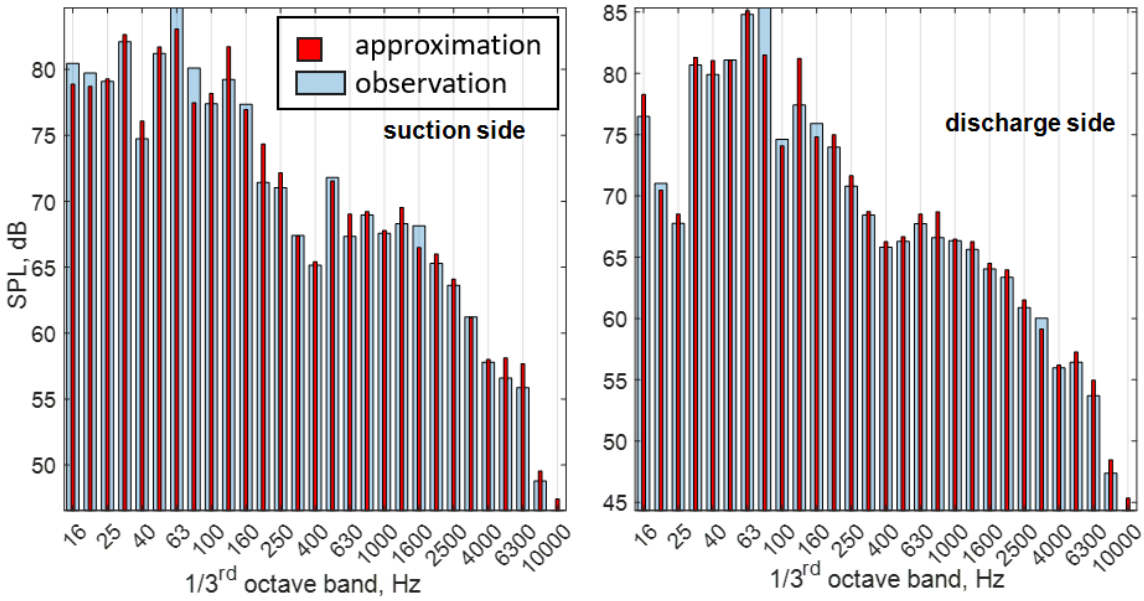

Figure 7-2 Spectral content of the suction side (left) and the discharge side (right) by means of 1/3rd-octave bands. Test of full baseline rotor and comparison to independent test data at Tu = 5.5 %, n = 1061 min^{-1}, δ_{TS} = 63.4 % [113].

The reason for this inaccuracy is suspected to be the independent nature of the ANNs for each 1/3rd-octave band, which hinders a cross-transfer of spectral information. Thus, slight variations such as, for example, those in the rotational speed might lead to a shift of the tonal components or the BPF from one 1/3rd-octave band into the neighbouring one, leading to a strong increase in the complexity of the experimental space and/or the requirements for the modelling approach [113]. This effect needs to be accounted for in the final modelling approach.

7.2 Final Modelling Approach

The results of the preliminary study in Section 7.1 show that the artificial neural networks (ANNs) based on the LHS outperform the more established design of experiments methods, particularly when it comes to the highly non-linear aeroacoustic and vibroacoustic target values. Consequently, the artificial neural networks based on Latin hypercube sampling are considered to be suitable for modelling a rotating system, comprising varying inflow parameters but also varying fan-blade geometries in the form of leading edge serrations. However, the preliminary study also uncovered the need for slight improvements in the modelling strategy and a re-adjustment of the influencing factors as well as the target values.

7.2.1 Influencing Factors and Experimental Design

As an extension of the preliminary study in Section 7.1, focussing on the general modelling of an axial baseline rotor, rotors equipped with leading edge serrations are implemented for the final modelling approach. Therefore, the chosen experimental space has four dimensions. The two geometrical factors are the serration amplitude and the serration wavelength. Disregarding effects of the previously modelled fan speed enables a conversion of the initially chosen throttling state δ_{TS} into the flow coefficient φ. This factor, however, is limited to the region of technical importance ($0.13 \leq \varphi \leq 0.21$), reducing avoidable complications. The fourth factor is the turbulence intensity, defined by the different turbulence grids as described in Section 4.4, at a fixed distance ($\Delta x/D = 0.75$) to the rotor plane. In consequence, the Tu represents a categorical parameter since the Tu cannot be adjusted continuously. Nevertheless, interpolation between the different turbulent states is considered meaningful since the level of the turbulence scales almost linearly (Figure 7-3) with the chosen grid size, as is also proposed by Laws and Livesey [2]. Similar considerations apply to the transversal integral length scale Λ_t, even though the uncertainty is of higher magnitude. The variation in these parameters is expected to provide sufficient information on the system's performance, which can be described by target values still to be defined.

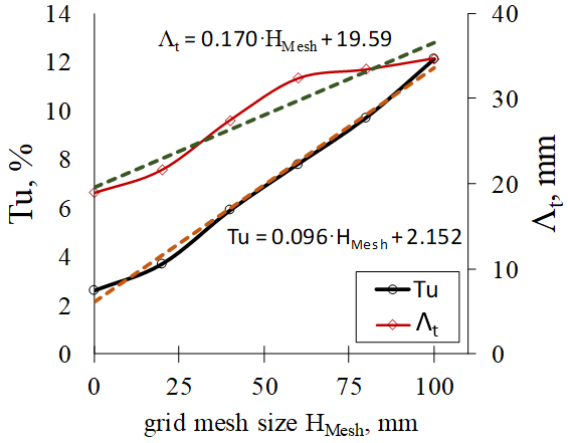

parameter	unit	f_{min}	f_{max}
A	*mm*	*6*	*22*
λ	*mm*	*4*	*22*
φ	--	*0.13*	*0.21*
Tu	*%*	*2.6*	*12.1*

Figure 7-3 Grid-dependency of turbulence intensity Tu and transversal integral length scale Λ_t (left) and investigated range of influencing parameters (right).

For the Latin hypercube sampling, which is used for the artificial neural networks, a number of variations in accordance with the amount of model data is needed. The outer limits of each factor are fixed, as Figure 7-3 (right) indicates. For the training of the modelling approaches, however, the factor levels are all normalised in a range of (-1..1). Once again a Latin hypercube design based on the maximin criterion is chosen out of 15.000 randomly created designs. To keep the manufacturing effort of the fan blades on a manageable level, the number of samples has been kept to a minimum of 78 samples. The LHS so generated is supplemented with a factorial design in order to incorporate the outer corners of the spanned experimental space, resulting in another 54 samples. Finally, for validation purposes, three randomly chosen samples are taken from the LHS data base and are excluded from the training of the ANNs. Hence, these samples feature unique serration parameters, unknown to the later-generated neural networks and can be used for testing the ability of the artificial neural networks to generalise. The non-dimensional test matrix with detailed information on the run conditions for each sample is also presented in Appendix G.2.

From a practical point of view, the test matrix requires manufacturing of 1 BSLN blade set, 7 sets for the CCD, 8 for the LHS and 3 sets for the validation. This adds up to 114 fan blades (19 sets · 6 blades/set), which were all manufactured via rapid prototyping. For conducting the single measurements, defined by the test matrix, a randomised strategy is chosen in order to minimise systematic influences due to differences in the mounting (tolerances, etc.) or trends of ambient parameters such as the atmospheric pressure or the temperature.

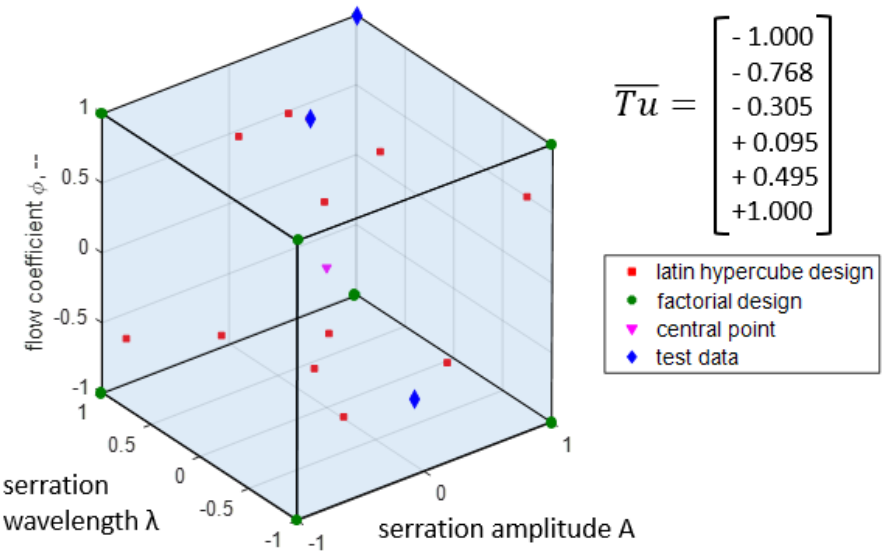

Figure 7-4 Sampling of the continuous experimental space for each turbulence level. Indicated test samples are used for one predefined turbulence level only.

7.2.2 Target Values

The definition of appropriate target values turns out to be the crucial part of evaluating a given system as these variables are required to describe the system's characteristic performance with the necessary accuracy. Moreover, they need to be describable in terms of the chosen influencing parameters [113]. As already mentioned in Section 7.1, the target values are of aerodynamic and aeroacoustic nature and are listed in Table 7-4.

Aerodynamic parameters are the pressure rise between the suction side and the discharge side of the fan, defined by the pressure coefficient ψ. The system's efficiency η_{System} defines the second target value. The acoustic target values are more complex. First, the signals gathered from the wall-mounted microphone arrays on the suction and discharge sides of the fan are individually averaged linearly in order to compensate for radial differences. The same is true for the wall-pressure fluctuations measured at the two pressure tapping points in the rotor

plane. Afterwards, the sound pressure (wall pressure) is processed to produce sound power levels PWL (wall pressure levels WPL) according to *Eq. 3-4* and *Eq. 4-25*, taking into account the ambient conditions by means of the density and the speed of sound.

As concluded from the preliminary spectral analysis in Section 7.1.2, a more coherent modelling of the aeroacoustic fan characteristics is required, taking into account the different noise source origins of tonal and broadband components. Hence, the chosen approach is to incorporate a separation of the tonal and broadband components of the underlying spectra. In this sense, the preconditioned sound power spectra are processed by use of the customised filtering algorithm (Table 7-3) described in Section 5.1. In the algorithm used here, as opposed to the filtering method described in Section 5.1, no low-pass filtering is applied since for modelling, the full broadband and tonal spectra are subdivided into their 1/3rd-octave band equivalents. In consequence, all the signals are separated into their broadband (BB), tonal (T) and BPF components using median filtering. It is important to note that the tonal components at frequencies corresponding to the first six blade-passing frequencies are removed from the filtered tonal spectra and subsequently used for the definition of separate BPF spectra.

Table 7-3 Settings of customised filters used for post-processing the gathered data to generate the data basis for training the ANN.

type	f_{min} [Hz]	f_{max} [Hz]	increment [Hz]
total	*10*	*10,000*	*0.5*
broadband	*10*	*10,000*	*0.5*
tonal	*10*	*10,000*	$33^{1/3} \pm 7.5$
BPF	*10*	*10,000*	200 ± 7.5

For comparison purposes, the first aeroacoustic target values are the overall sound power levels as well as the summed levels of the individual filtered components (the broadband signal, the tonal components and the first six BPF). The same applies to the wall power level, albeit that no BPF spectra are generated. Subsequently, the obtained sound (wall) power spectra of tonal and broadband components are subdivided into their 1/3rd-octave band equivalents, with each 1/3rd-octave band representing one individual target value. Adding up the defined target values results in 116 individual, fully independent neural networks for the serrations and the baseline each.

*Table 7-4 Target values in the time and the frequency domain as well as of aerodynamic and aeroacoustic character. An individual, fully independent ANN is generated for each target value. * indicates 1/3rd-octave band mid-frequencies.*

Aerodynamic			Acoustic			Wall Pressure		
Abbrev.	No. RV	--	Abbrev.	f-Range	No. RV	Abbrev.	f-Range	No. RV
ψ	*1*	Sum Level	$OAPWL_{Total}$	*10-10,000*	*1*	$OAWPL_{Total}$	*10-5,000*	*1*
η	*1*		$OAPWL_{BB}$	*10-10,000*	*1*	$OAWPL_{BB}$	*10-5,000*	*1*
			$OAPWL_{T}$	*10-10,000*	*1*	$OAWPL_{T}$	*10-5,000*	*1*
			$OAPWL_{BPF}$	*200-1,200*	*1*	--	--	--
		Spectral	PWL_{BB}	*12.5-7,943**	*29*	WPL_{BB}	*12.5-3,981**	*26*
			PWL_{T}	*25-7,943**	*24*	WPL_{T}	*25-3,981**	*22*
			PWL_{BPF}	*200-1,200*	*6*	--	--	--
Sum	2				63			51

In this regard, the broadband components of each frequency band can still be modelled independently, thereby avoiding the disturbing effects of shifting significant tonal components between the single-octave bands or the influence of possibly occurring duct modes [113]. The separately modelled speed-dependent tonal fraction is added at a later stage.

7.2.3 Training, Fit and Validation

As for Section 7.1, the artificial neural networks were trained by use of the *MATLAB Deep Learning Toolbox™*. In contrast to the used Bayesian learning algorithm in Section 7.1, the Levenberg-Marquardt [182] algorithm was used for training the data for the final modelling since it is a very fast algorithm and also allows a quite autonomous training without the need to specify the hyper parameters for the training. This is considered meaningful, since the preliminary investigations in Section 7.1 emphasised the high complexity and strong non-linearity of the considered aeroacoustic system, hence demanding for a training algorithm with a higher degree of freedom. However, minimising the deviations takes place by use of the standard back-propagation approach. In contrast to the Bayesian learning algorithm, the data pool now needs to be subdivided into training and validation data. The training data is used for training the neural networks, whereas the validation data serves a monitoring of the training process in order to prevent overfitting, which in turn will lead to a low generalization ability. In order to obtain the optimum distribution of training and validation data, an iterative process is applied while monitoring the training performance. The criterion for aborting the training requires 40 successive networks, which perform worse than the hitherto existing network. The training of this optimum network is repeated since the performance also depends on the values of the initial weights. As a result, for the current networks, 88 % of the data pool is used for training, while 10 % is used as validation data. Overfitting is prevented by evaluating the prediction error on the validation data. If the error rises for six consecutive times, the training is aborted. Moreover, also for the purpose of preventing overfitting the data, the number of weights w and bias b values (the hyperparameters of the ANN) is set to be lower than the number of input data sets. According to *Eq. 7-3*, the number of hyperparameters N_{HP} is determined by taking into account the number of inputs i and the number of neurons in the hidden layer plus one output neuron. Whereas the number of inputs is fixed, the number of neurons is varied according to the set criterion, although a low number is favoured.

$$N_{HP} = i \cdot N_{Neurons} + 2 \cdot N_{Neurons} + 1 \qquad \textit{Eq. 7-3}$$

The remaining 2 % of the data pool represents arbitrarily chosen test points that have no share in training or monitoring but are used as fully independent test data. The performance of the neural networks with regard to these test points describes the ability of the model to generalise.

The number of hidden layers of a network is another parameter that can be varied. However, one hidden layer is considered sufficient [183] for describing a technical process, also keeping the current training of the system at a lower complexity. Figure 7-5 shows the network structure for the overall sound power level, with the network consisting of four inputs and one hidden layer with 12 neurons. After deciding on the algorithm, the structure and the hyperparameters of the ANN, the computational cost is relatively low. Using a standard desktop computer, it takes less than 24 hours to train all the 116 individual ANNs with the current settings, which is negligible compared to the experimental effort to generate the underlying data basis.

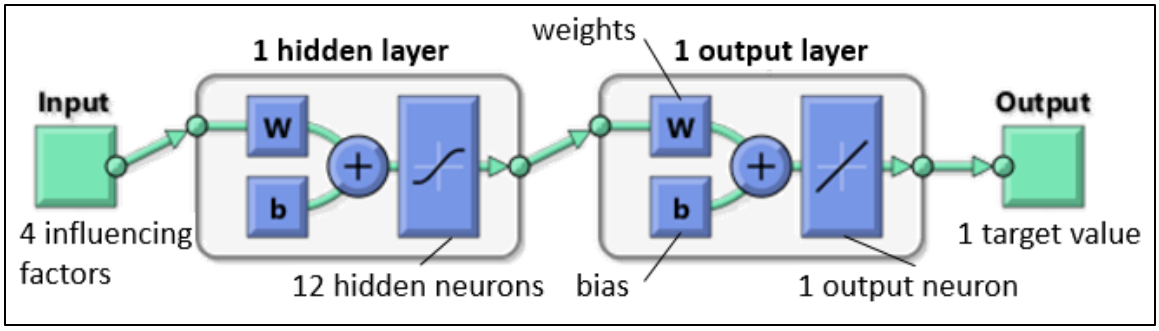

Figure 7-5 Exemplarily extracted network structure for the OAPWL. Structure remains constant for all generated ANNs except for the number of hidden neurons.

The general fit of the model is listed in Table 7-5, in which the coefficients of determination R^2 (*Eq. 7-2*) are defined based on 98 % of the data pool. Both aerodynamic and acoustic performance reach an acceptable fit, with especially the latter consistently performing at values $R^2 > 96$ %. For the wall-pressure data, but particularly for the modelling of the discrete frequencies, a significantly lower performance is obtained. This lower performance also affects the values that monitor the total performance (WPL_{Total}), whereas the broadband components might allow a certain degree of validity. However, due to the complexity of the modelled system, the focus of the current analysis is restricted to the aerodynamic and acoustic target values only. Taking into account the ability of the networks to model the spectral composition of the acoustic signals, Table 7-5 once again shows high R^2 with an average performance of $94\ \% \leq R^2 \leq 99\ \%$. For comparison purposes, Figure 7-6 shows the distribution of the measured (observed) values and the model predictions for the aerodynamic target values as well as the overall sound power level. The diagonal line represents a perfect fit of model and input data.

Table 7-5 Coefficient of determination R^2 for the target values based on both training data and validation data (129 data points) of the data input for the ANN.

	Aerodynamic		Acoustic			Wall Pressure		
	Abbrev.	R^2	Abbrev.		R^2	Abbrev.		R^2
Sum Level	ψ	0.935	$OAPWL_{BB}$	--	0.993	$OAWPL_{BB}$	--	0.863
	η	0.941	$OAPWL_{T}$	--	0.995	$OAWPL_{T}$	--	0.367
	--	--	$OAPWL_{BPF}$	--	0.962	--	--	--
	--	--	$OAPWL_{Total}$	--	0.997	$OAWPL_{Total}$	--	0.719
Spectral	--	--		Min	0.972		Min	0.354
	--	--	PWL_{BB}	Max	0.999	WPL_{BB}	Max	97.6
	--	--		AV	0.993		AV	79.8
	--	--		Min	0.791		Min	0.353
	--	--	PWL_{T}	Max	0.998	WPL_{T}	Max	0.985
	--	--		AV	0.978		AV	0.689
	--	--		Min	0.917		--	--
	--	--	PWL_{BPF}	Max	0.988	--	--	--
	--	--		AV	0.944		--	--

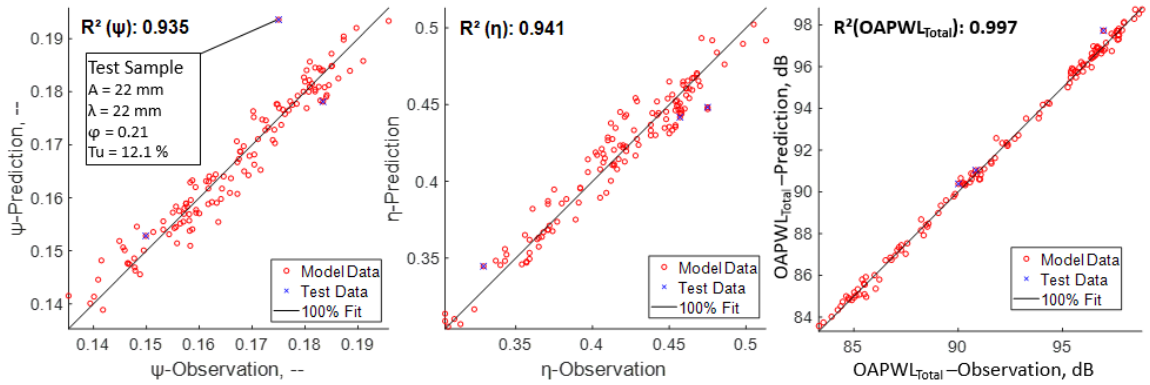

Figure 7-6 Prediction and observation plots of overall performance for three selected target values.

As mentioned previously, the ability of the system to generalise is tested by validating against three fully independent test points. The performance is measured by using the training data and calculating the relative deviation in comparison to every approximated target value for every data point. Table 7-6 shows the maximum, the mean and the median of the deviations for the aerodynamic, aeroacoustic and wall-pressure near-field target values of overall character. As can be seen, a remarkable fit is obtained for the acoustic prediction, showing mean and median deviations of $< 1\ \%_{\mathrm{dB}}$ for all target values, but also the flow coefficients and the system's efficiency are predicted at considerably high accuracy, taking into account all the possible influencing factors of the experimental measurements. However, as can be seen from Figure 7-6 (left), one of the validation data points equals one of the outliers, when predicting the flow coefficient Ψ, indicating a poor aerodynamic prediction performance. This can be explained by the fact, that this very data point possesses parameter levels, which are all at maximum, hence being one of the corner points of the experimental space. These corner points are naturally hard to predict, even though acoustically a much improved prediction accuracy is obtained (Figure 7-6 right).

Table 7-6 Absolute error for validation against three independent test data points.

	Aerodyn.		Acoustic		Wall Pressure	
	Abbrev.	Dev.%	Abbrev.	Dev.%$_{\mathrm{dB}}$	Abbrev.	Dev.%$_{\mathrm{dB}}$
Mean Deviation		*3.09*		*0.72*		*3.69*
Median Deviation	ψ	*2.12*	*OAPWL$_{BB}$*	*0.97*	*OAWPL$_{BB}$*	*3.59*
Max. Deviation		*5.41*		*1.07*		*6.19*
Mean Deviation		*1.67*		*0.68*		*1.86*
Median Deviation	η	*1.56*	*OAPWL$_{T}$*	*0.92*	*OAWPL$_{T}$*	*2.34*
Max. Deviation		*2.87*		*1.01*		*2.54*
Mean Deviation		--		*0.63*		--
Median Deviation	--	--	*OAPWL$_{BPF}$*	*0.42*	--	--
Max. Deviation		--		*1.29*		--
Mean Deviation				*0.47*		*2.35*
Median Deviation	--		*OAPWL$_{Tota}$*	*0.42*	*OAWPL$_{Tota}$*	*2.45*
Max. Deviation				*0.79*		*3.63*

Apart from monitoring the overall prediction accuracy of the chosen validation samples, a spectral comparison, too, is possible by evaluating all the individual 1/3rd-octave bands for the broadband and the discrete noise components of the gathered signals. This spectral comparison allows more precise insights into the ability to model the spectral composition of the acoustic signals. A contrasting juxtaposition of observed vs. approximated target values is shown in Figure 7-7 and Figure 7-8 for the first six blade-passing frequencies. Generally, a remarkable prediction accuracy is obtained. Even for the previously discussed test point at extreme parameter settings (corner point), which shows a relatively poor test performance in terms of

aerodynamics, the approximated spectral values in Figure 7-7 (left) show a close fit to the observed (measured) data. This holds true for all the modelled components of the signal, namely the broadband component and the discrete components, including the level of the blade-passing frequencies (Figure 7-8).

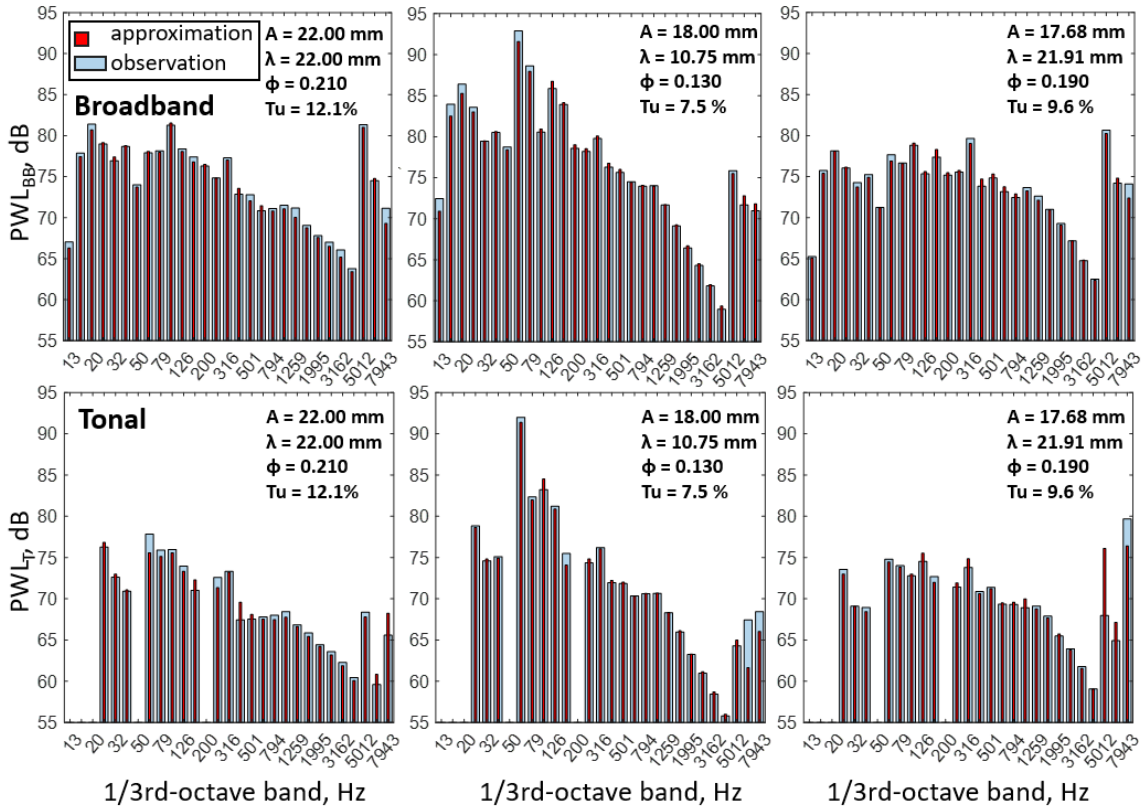

Figure 7-7 Spectral sound power level PWL comparison of the 1/3rd-octave bands, separated in broadband (top) and tonal (bottom) fractions for three independent test points. Blue bars indicate measurement results (observation), red bars the model prediction (approximation).

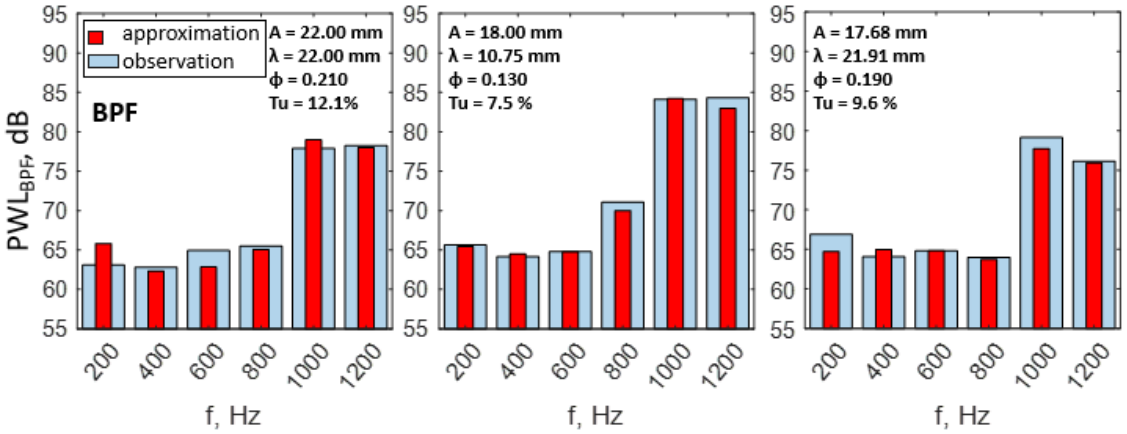

Figure 7-8 Spectral sound power level PWL comparison for the blade-passing frequencies (1st – 6th harmonic) for three independent test points. Blue bars indicate measurement results (observation), red bars the model prediction (approximation).

7.3 Aeroacoustic Results

As outlined in Section 7.2.3, a reasonable fit and quality of the approximation is obtained for the aerodynamic and aeroacoustic target values in both the overall and the spectral domain. This is confirmed for the model fit itself, as well as in terms of more general performance by testing against independent test data. The highest performance is obtained for the aeroacoustic response values, an observation that is in agreement with the need to systematically describe the acoustic effect of the serrations in rotating applications. The aerodynamic trends and tendencies are already outlined in Section 6.1 in high detail and match the predictions of the generated model. As a consequence, this section concentrates mainly on the aeroacoustic dependencies. Aerodynamic target values are implemented at a later stage in Section 7.3.3, with the multi-objective optimisation enabling a combined analysis of aeroacoustic and aerodynamic requirements.

7.3.1 Effect of Parameters

Turbulence Intensity

The turbulence intensity is the key inflow parameter for regulating the level of inflow distortion, associated with leading-edge broadband noise effects. The acoustic signature of the tested fan with and without serrated leading edge shows a clear dominance of turbulence-generated noise for high flow coefficients, whereas throttling of the system clearly attenuates this effect (Figure 7-9, left). This matches previously observed trends [171, 148] since the fan approaches the instability region in which partial stall occurs on the fan blade suction sides. In addition, aeroacoustic tip leakage effects tend to increase in relevance with rising pressure gradient between the suction and the discharge side of the fan. By means of the noise reduction capability of serrated rotors, Figure 7-9 (right) shows the effect at intermediate serration parameters while the turbulence intensity is varied. It becomes apparent that the level of inflow distortion has different effects along a fan characteristic curve. First, at high flow coefficients $\varphi \geq 0.185$, a high level of turbulence results in maximum noise reduction effects. This is meaningful since broadband leading-edge noise is the dominant noise source in this region and is reduced efficiently by decoherence effects and (partly) destructive interference effects. For lower flow coefficients, however, a low level of turbulence clearly leads to maximum noise reduction. Here, the dependency of the dominant noise sources relative to the level of inflow distortion needs to be taken into consideration.

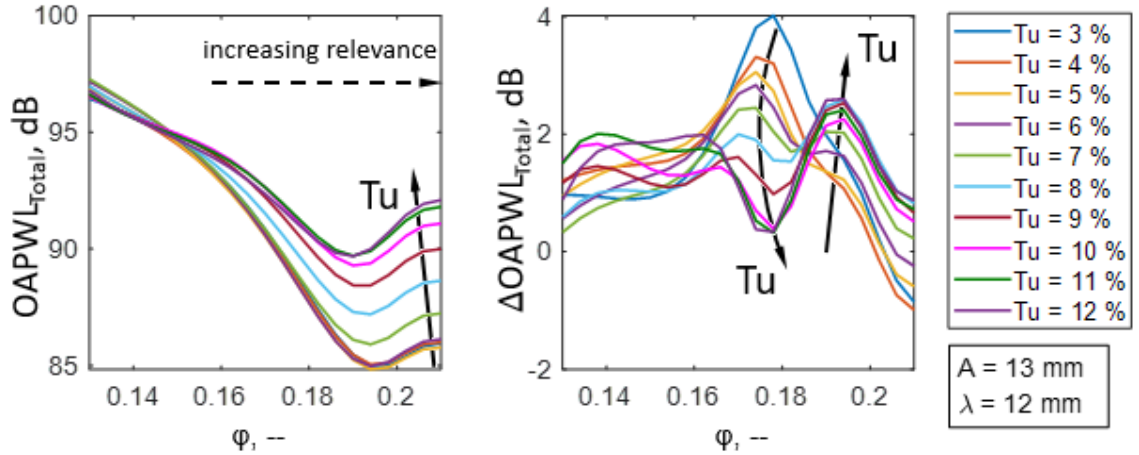

Figure 7-9 Effect of turbulence intensity on overall sound power level (left) and overall sound power level reduction (right) of serrated rotor at intermediate parameter setting A13λ12. Predicted trends, generated via the ANNs.

When the fan instability region is approached, the reduction of stall-initiated broadband noise is shifted towards lower flow coefficients, as shown in Figure 7-10 (left). This is due to an increased sensitivity of the serration to the turbulent structures under partial load and leads to less efficient noise reduction in this region. T,his pattern directly affects the overall noise reduction. The increase in the level of inlet distortion also amplifies the excitation of the discrete components (Figure 7-10 right), including the BPF and their harmonics. However, the serration appears to be less efficient in reducing these discrete components at high turbulent conditions, hence showing the best performance for low Tu. This trend adds to the shifted broadband noise reduction and results in the opposing trend for the Tu, as shown in Figure 7-9 (right).

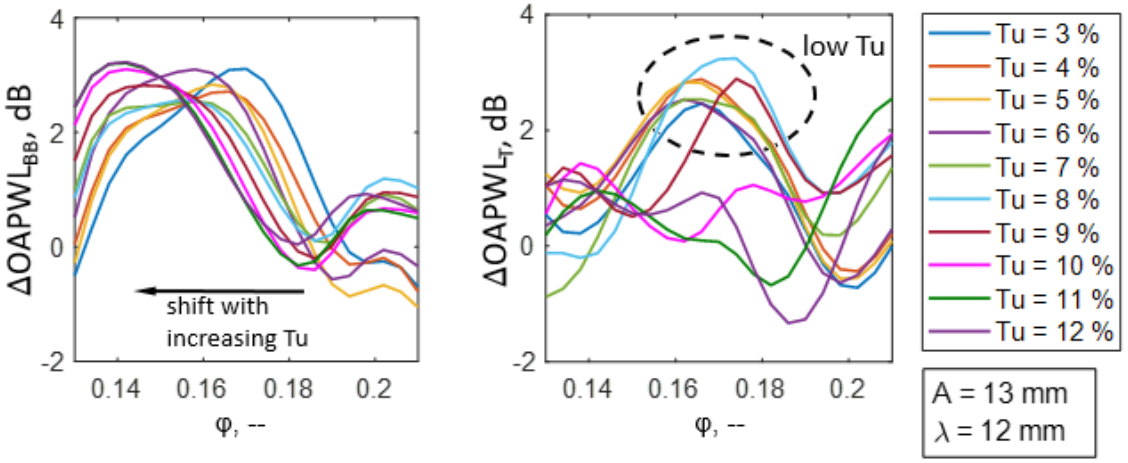

Figure 7-10 Effect of Tu on broadband (left) and tonal (right) components of the overall sound power level reduction at intermediate levels of serration amplitude and serration wavelength. Predicted trends, generated via the ANNs.

Serration Amplitude

As reported previously, both noise radiation and noise reduction show a clear dependency on the serration amplitude. Reducing the flow coefficients for the fan leads to the onset of (partial) stall (Figure 7-11 left), resulting in a sharp increase in the noise level for the baseline reference case in the instability region at $\varphi \leq 0.18$. This aeroacoustic onset is significantly delayed and reduced with implementing leading edge serrations, as is indicated by the shift in the acoustic throttling curves in Figure 7-11 (left). Maximum noise reduction effects are obtained for the highest serration amplitudes. The vortex generating features of the serrations are held responsible for the delay effect and the smooth transition from pre-stall to stall due to early partial separation at the serration roots [38, 39, 23, 25, 18, 28]. Another mechanism affecting the noise reduction is observed for high flow coefficients $\varphi \approx 0.195$ (Figure 7-11 right). Here, significant grid-generated leading-edge broadband noise is present, dominating the acoustic noise radiation. As for rigidly mounted aerofoils, high serration amplitudes cause increased spanwise decorrelation effects [67, 84, 86] as well as significant destructive interference effects [1], leading to a noise reduction in this region. This is confirmed by the typical spectral scaling of the noise reduction [1], as further outlined in Section 7.3.2. As can be seen in Figure 7-11 (right), the above-mentioned two mechanisms combine to a distinct pattern of noise reduction, in which the delay in the acoustic onset of stall is the dominant effect and shows a maximum reduction in the sound power level of $\Delta PWL = 6$ dB for the highest serration amplitude.

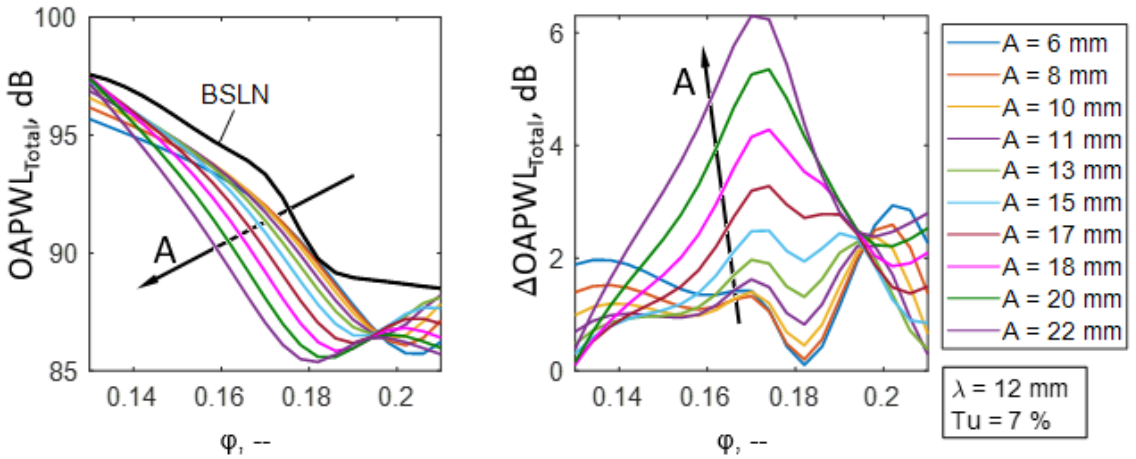

Figure 7-11 Overall sound power level (left) and sound power level reduction (right) at varying flow coefficients φ. Mean effect of serration amplitude at intermediate levels of free-stream turbulence and serration wavelength. Predicted trends, generated via the ANNs.

In Figure 7-12 the noise reduction pattern described before is fragmented into its broadband (left) and tonal (right) as well as into its BPF components in Figure 7-13. This helps to assess their individual contributions to the overall noise reduction. The effect of broadband noise reduction appears to be at a relatively similar level for high to intermediate flow coefficients, although the effect decreases considerably for lower values (Figure 7-12, left). However, for the broadband noise reduction, the well-known aeroacoustic mechanisms of serrated leading edges (Section 3.2.1) are responsible, although the origin of the vortices, interacting with the rotor blades, switch from grid-generated at high flow values to stall-initiated for intermediate flow coefficients. The reduction in discrete components by means of tonal effects (Figure 7-12, right) appears to be responsible for the extension of the overall noise reduction (Figure 7-11, right) towards higher flow coefficients with increasing serration amplitudes. At flow coefficients $\varphi \leq 0.155$, however, the individual noise reduction curves are collapsing, showing a strong negative gradient and ending up in slight noise amplification for minimum flow coefficients.

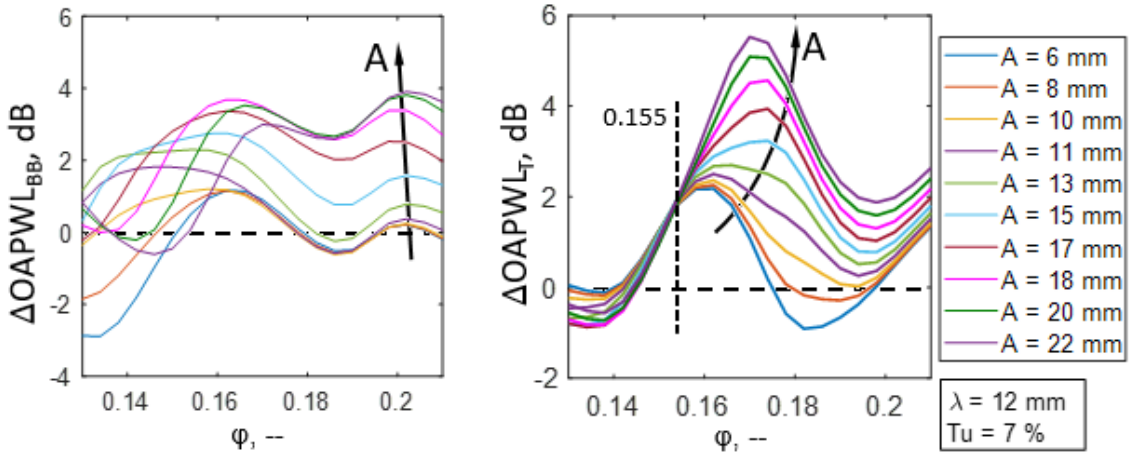

Figure 7-12 Overall sound power level reduction of broadband (left) and tonal components (right) at varying flow coefficients φ. Mean effect of the serration amplitude at intermediate levels of free-stream turbulence and serration wavelength. Predicted trends, generated via the ANNs.

Analysing the generation and reduction of the blade-passing frequency and its harmonics gives another pattern than for the discrete frequencies in general. The reference baseline case indicates strongly excited BPF for three regions within the fan characteristic curve (Figure 7-13, left). Applying serrations once again leads to a shift of these excited regions towards higher flow coefficients but also shows a clear attenuation for the radiated noise.

A possible cause could be the tip leakage effects of the serrations, as described in Section 5. In these effects, coherent structures, interacting with the rotor blades, are reduced in intensity as well as shifted significantly towards low flow coefficients. Further trends for a varying serration wavelength are presented in Appendix G.3.

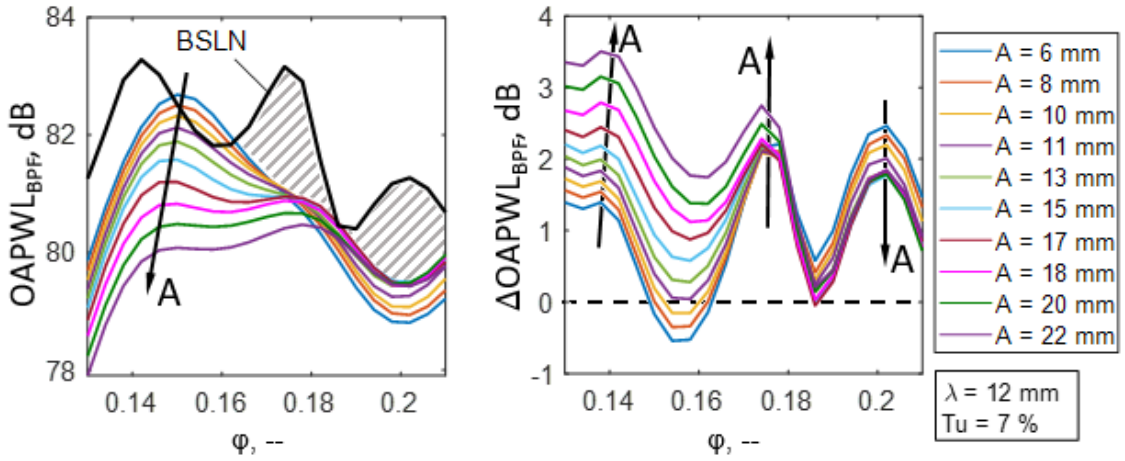

Figure 7-13 Overall sound power level (left) and sound power level reduction (right) of the first six blade-passing frequencies at varying flow coefficients φ. Mean effect of the serration amplitude at intermediate levels of free-stream turbulence and serration wavelength. Predicted trends, generated via the ANNs.

Serration Wavelength

Though significant, the effect of the serration wavelength (Figure 7-14) appears to be less dominant than the effect of the serration amplitude. This observation is in agreement with the reported trends of the serration wavelengths for rigidly mounted aerofoils (Section 3.3.7). Varying the serration wavelength by keeping the serration amplitude constant at an intermediate level results in a maximum overall sound power reduction of up to $\Delta OAPWL = 5.5$ dB. Generally, the effect of the serration wavelength shows a high similarity to the effect of the serration amplitude, with small wavelengths being most beneficial for maximum noise reduction. This is especially true for the dominant noise reduction effect in the instability region $0.14 \leq \varphi \leq 0.18$ (Figure 7-14, top left). However, contrary to the trends of the serration amplitude, the influence of the wavelength diminishes for higher flow coefficients. This becomes apparent in the form of collapsing curves, with only maximum wavelengths showing an effect on the noise reduction capability. This collapse can be attributed mainly to the broadband noise reduction in Figure 7-14 (bottom left), showing no shift with varying serration wavelength as is the case for a variation in the serration amplitude at high flow coefficients (Figure 7-12, left). Further trends for a varying serration wavelength are presented in Appendix G.4.

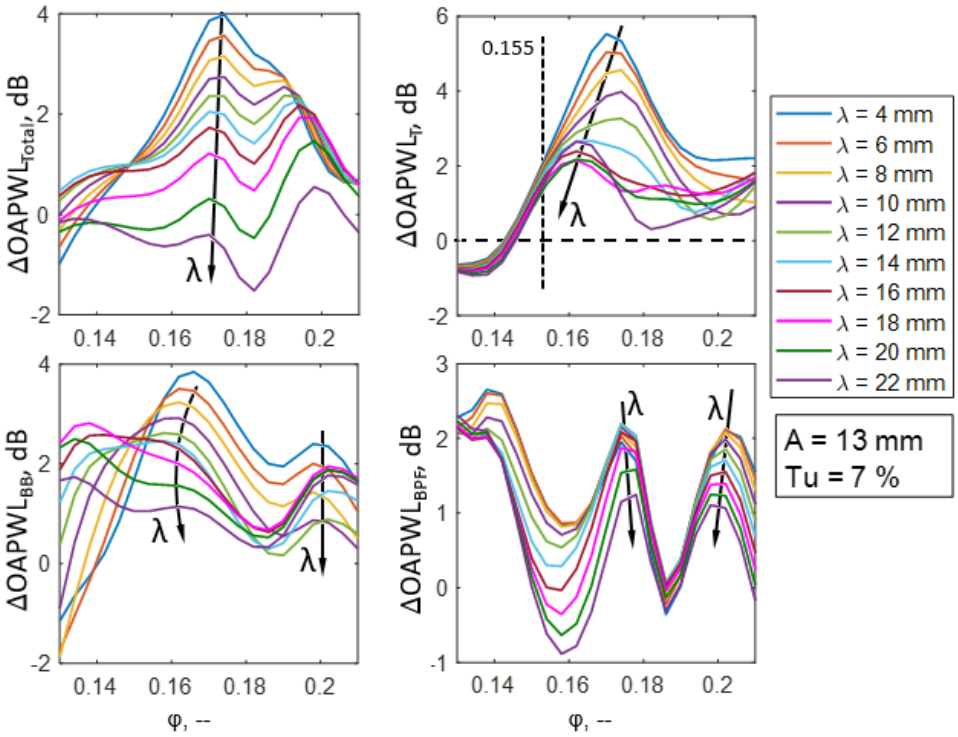

Figure 7-14 Mean effect of the serration wavelength on the overall sound power level reduction ΔOAPWL for the total noise (top left), tonal noise (top right), broadband noise (bottom left) and BPF noise (bottom right). Values of free-stream turbulence and serration amplitude remain on intermediate levels. Predicted trends, generated via the ANNs.

7.3.2 Spectral Application

One of the main benefits of having developed a spectral model is the possibility of obtaining structured information on the effect of single influencing parameters with regard to the noise radiation at the different 1/3rd-octave bands analysed. Figure 7-15 shows a continuous variation in the turbulence intensity for three different flow coefficients. Note that each 1/3rd-octave band shown in Figure 7-15 is determined based on an individually trained ANN, neglecting possible dependencies between adjacent frequency bands. The spectral composition of the broadband component of the sound power level reveals the dominance of broadband leading-edge noise for intermediate to high flow coefficients, whereas further throttling of the fan results in highly similar spectral trends for all the turbulent states. Here, large-scale separation effects dominate the acoustic signature at low frequencies, and the low axial velocity produces only little high-frequency turbulence. Moreover, the relevant range of potential broadband noise reduction can be defined as 20 Hz ≤ f ≤ 3 kHz.

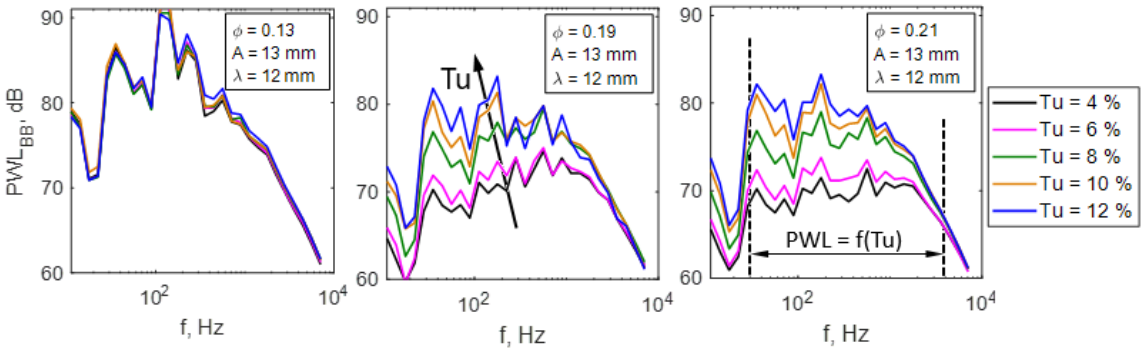

Figure 7-15 Spectral effect of Tu on the sound power level at low (left), intermediate (centre) and high (right) flow coefficient φ. Predicted trends, composed of 29 individual ANNs for the 1/3rd-octave bands for each Tu.

As a consequence, the spectral broadband noise reduction as a function of the serration parameters (Figure 7-16) shows a noise reduction for 200 Hz ≤ f ≤ 3 kHz at high flow coefficients. Even though based on 1/3rd-octave bands, with each band being represented by an individual artificial neural network, the observed spectral pattern is highly similar to the experimentally obtained ones as reported in Sections 3.4.1 and 6.2.3. The noise reduction increases logarithmically from the low to the mid-frequency range. The peak value is obtained at f ≈ 1 kHz. At higher frequencies, aerofoil self-noise becomes increasingly dominant, resulting in an attenuating effect of the noise reduction. As reported in Section 7.3.1, the effect of the serration wavelength (Figure 7-16, left) is only of minor character except for the region of the main reduction, in which a scaling towards low wavelengths becomes apparent. For the serration amplitude (Figure 7-16, right), on the contrary, an improved noise reduction of broadband character is clearly visible for maximum amplitudes.

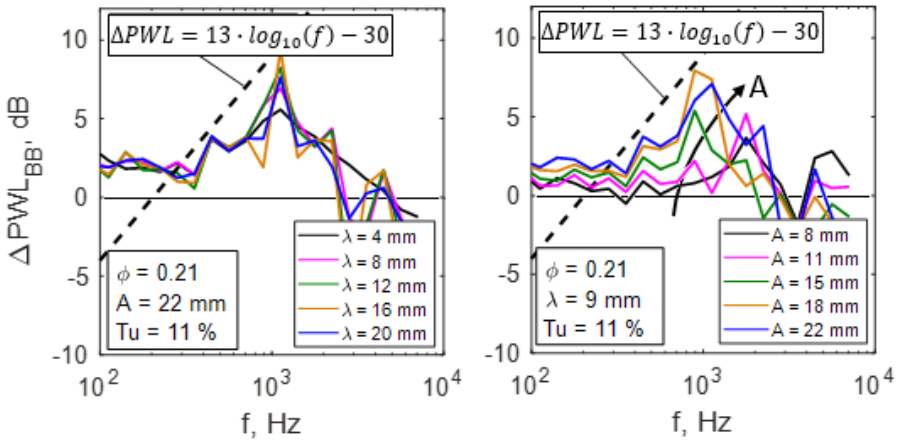

Figure 7-16 Spectral broadband sound power level reduction in 1/3rd-octave bands. Variation in serration amplitude (left) and wavelength (right). Predicted trends, composed of 29 individual ANNs for the 1/3rd-octave bands for each λ or A.

Going one step further allows generating three-dimensional spectrograms, providing information on the acoustic signature for the full-fan characteristic curve for the reference rotor and an example serration (Figure 7-17, left and centre). Both figures clearly show the increase in noise due to the onset of stall when the flow coefficients are reduced. This takes initially part in the mid-frequency range but tends to migrate towards lower frequencies as the separated structures at the fan blades grow larger. This qualitatively matches the patterns observed for previous measurements as presented in Figure 5-6 in both magnitudes and spectral composition. The resulting noise reduction (Figure 7-17, right) indicates a varying lower frequency limit beyond which significant noise reduction is achieved. Starting at f = 200 Hz for maximum flow values, the noise reduction decreases with further throttling to f = 100 Hz since dominant flow separation starts to occur in the stall region. Moreover, strong noise attenuation is observed at f = 1 kHz for the full range of operation, showing only a slight shift towards lower frequencies. This once again indicates the global significance of the serration when it comes to broadband noise reduction. Additional plots for rotors with varying serration parameters are presented in Appendix G.5.

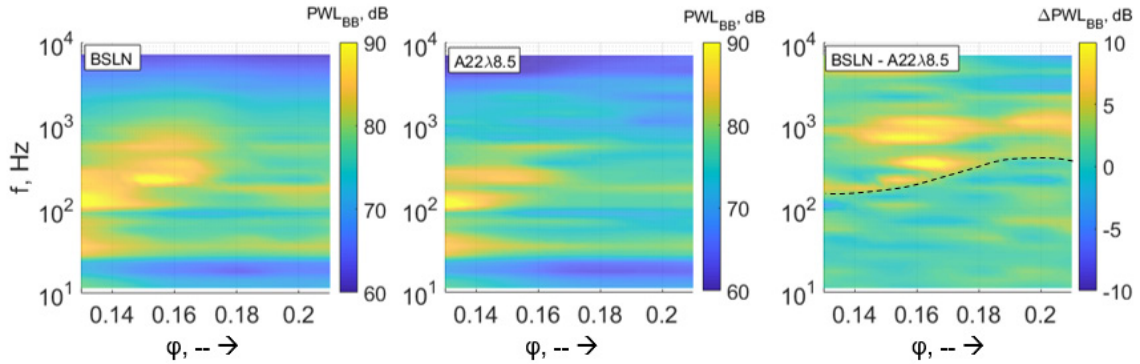

Figure 7-17 Spectrograms for the BSLN rotor and a selected serration configuration at Tu = 11 %. Predicted trends, composed of 29 individual ANNs for the 1/3rd-octave bands for each φ.

7.3.3 Multi-Objective Optimisation

As already outlined in Section 3.3.8, multi-objective optimisation of target values by means of a Pareto front can help to indicate solutions that may be more beneficial than others. The generated model is already highly complex with four input variables and 116 output variables (target values). Especially for practical applications and the design of customised serrations, only the optimum based on a limited number of target values is desired. Hence, using ANNs with good accuracy to approximate the Pareto front is a powerful and fast tool for optimising the underlying system [113]. The multi-objective particle swarm optimisation (MOPSO) method is again used to vary the parameter setting of each input variable within the non-dimensional boundaries of the defined experimental space IP ∈ [-1, 1]. This method is implemented in *MATLAB*, where the computational expenditure is in the range of minutes to generate a multi-objective Pareto front. For the current system, ten desired optima are defined, as listed in Table 7-7, where the differences in flow coefficient $\Delta\Psi$ and aerodynamic efficiency $\Delta\eta$ are defined according to *Eq. 7-4* and *Eq. 7-5*. For the particle swarm optimisation, a population size of 150, as well as a number of 200 iterations, proved sufficient to obtain stable solutions for the two-dimensional Pareto optima.

$$\Delta\Psi = \Psi_{Serr} - \Psi_{BSLN} \qquad \textit{Eq. 7-4}$$

$$\Delta\eta = \eta_{Serr} - \eta_{BSLN} \qquad \textit{Eq. 7-5}$$

Table 7-7 Defined pairs of target values for the localisation of the Pareto fronts as well as the desired optimisation towards a minimum or a maximum of the target values (TV).

No.	TV I	TV II	Desired		No.	TV I	TV II	Desired
1	$OAPWL_{Total,\,Serr}$	ψ_{Serr}	Min/Max		*6*	$\Delta OAPWL_{Total}$	$\Delta\eta$	Max/Max
2	$\Delta OAPWL_{Total}$	ψ_{Serr}	Max/Max		*7*	$\Delta OAPWL_{BB}$	$\Delta\eta$	Max/Max
3	$\Delta OAPWL_{Total}$	$\Delta\psi$	Max/Max		*8*	$\Delta OAPWL_{Total}$	$\Delta OAPWL_{BB}$	Max/Max
4	$\Delta OAPWL_{BB}$	$\Delta\psi$	Max/Max		*9*	$\Delta OAPWL_{T}$	$\Delta OAPWL_{BB}$	Max/Max
5	$\Delta OAPWL_{Total}$	η_{Serr}	Max/Max		*10*	ΔPWL_{BPF600}	ΔPWL_{BPF200}	Max/Max

However, for the generated Pareto optima it is important to note that a comparative discussion such as for continuous parameter variations in the previous sections is highly restricted. The influencing parameters represent four degrees of freedom from which both of the target values to be optimised can freely chose in order to generate the desired global

maximum/ minimum. Therefore, the Pareto fronts show no coherent optimum trend but rather single individual optima, all representing independent solutions for the assigned task.

Figure 7-18 shows the Pareto front for the overall noise radiation and the associated pressure coefficient for the serrated rotors (left), as well as the noise reduction capability as a function of the pressure coefficient (right). If the focus is on the maximum pressure coefficients, minimum noise radiation (Figure 7-18 left) is obtained for a low turbulence intensity of Tu = 3.76 %, intermediate flow coefficient in the pre-stall regime ($\varphi = 0.186$) and at maximum serration amplitude (A = 22 mm) and wavelength (λ = 22 mm). This matches the previously observed trends, in which high wavelengths are observed to be crucial for high aerodynamic performance. The low Tu prevents the generation of significant broadband noise at the associated flow coefficients. Changing the focus to minimum noise radiation, however, essentially results in a reduction of both serration design parameters (A = 6 mm, λ = 4 mm) what is in line with the maximum noise reduction while maintaining high pressure coefficients (Figure 7-18 right).

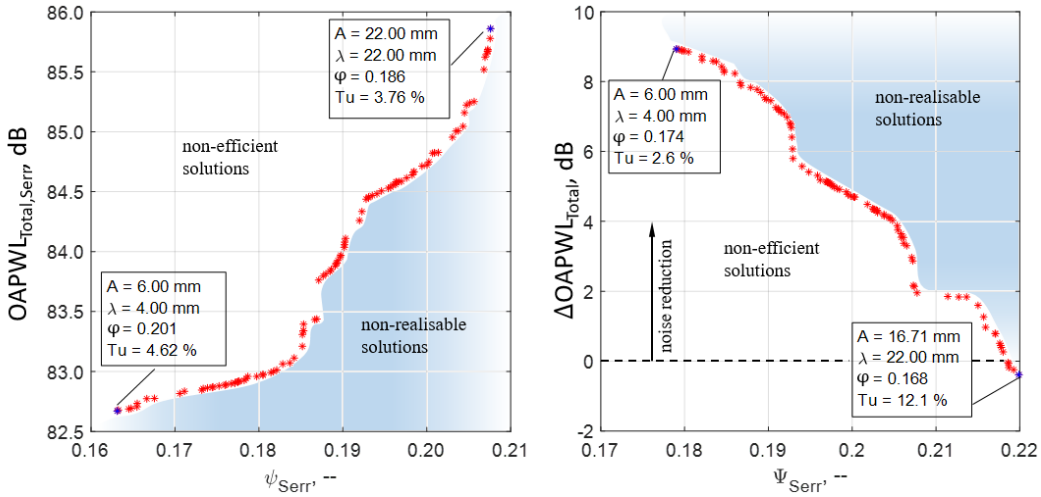

Figure 7-18 Minmax optimum of sound power level $OAPWL_{Serr}$ vs. pressure coefficients ψ_{Serr} (left). Maxmax optimum of sound power level reduction $\Delta OAPWL$ vs. pressure coefficients ψ_{Serr} (right).

Switching to the differences in the pressure coefficients, Figure 7-19 indicates that an improved aerodynamic performance ($\Delta\Psi > 0$) is always accompanied by an increase in turbulence intensity at lower flow coefficients, with the serrations appearing to be less prone to disturbances of the flow field.

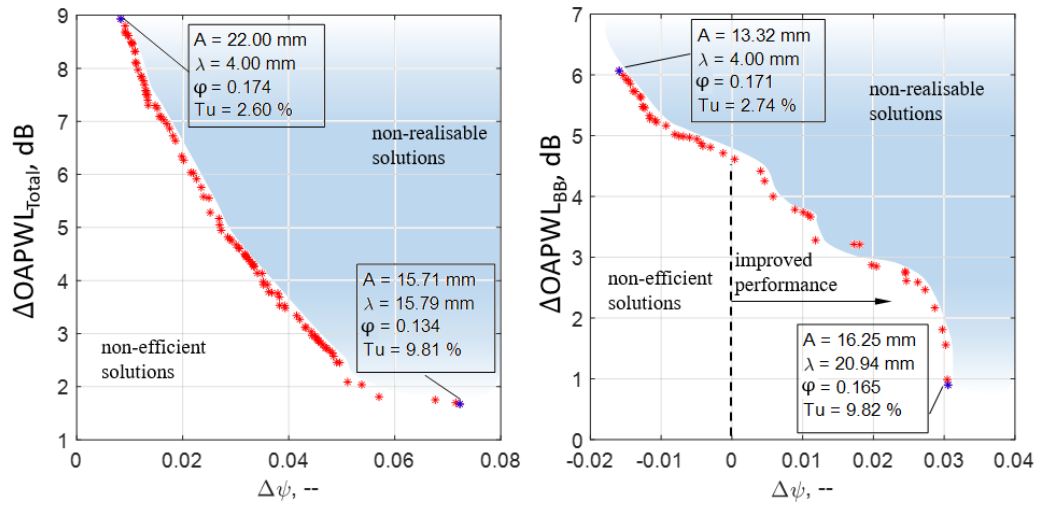

Figure 7-19 Maxmax optima of the overall sound power level reduction $\Delta OAPWL$ (left) and broadband sound power reduction $\Delta OAPWL_{BB}$ (right) vs. differences in the pressure coefficients $\Delta\psi$.

Incorporating the aerodynamic efficiency as a design parameter (Figure 7-20, left) shows remarkably high efficiencies at only a marginal noise reduction of 0.5 dB. However, reducing the flow coefficient to $\varphi = 0.178$ leads to a noise reduction with relatively high gradient, resulting in $\Delta PWL = 6.6$ dB at $\eta_{Serr} = 48$ %. Further reduction of the serration wavelength optimises the noise reduction but also attenuates the aerodynamic efficiency due to drag penalties of small-wavelength serrations. A Pareto front of high informative value is presented in Figure 7-20 (right), showing the overall sound power level reduction $\Delta OAPWL$ as a function of differences in aerodynamic efficiency $\Delta\eta$ (see also *Eq. 7-5*). As observed in the previous aerodynamic studies (Section 6.1), high serration wavelengths lead to maximum efficiency, even outperforming the baseline reference case at maximum flow coefficients (positions 1 and 2 in Figure 7-20 right). However, only little noise reduction is obtained for this region, which can be drastically increased to $\Delta PWL = 6.8$ dB by reducing the serration wavelength (position 3 in Figure 7-20 right). Further reduction enables optimising the noise reduction up to $\Delta PWL = 8.9$ dB, but this comes at the cost of a significant decrease in aerodynamic efficiency, though still higher ($\Delta\eta > 0$) than for the baseline case (position 4 in Figure 7-20 right).

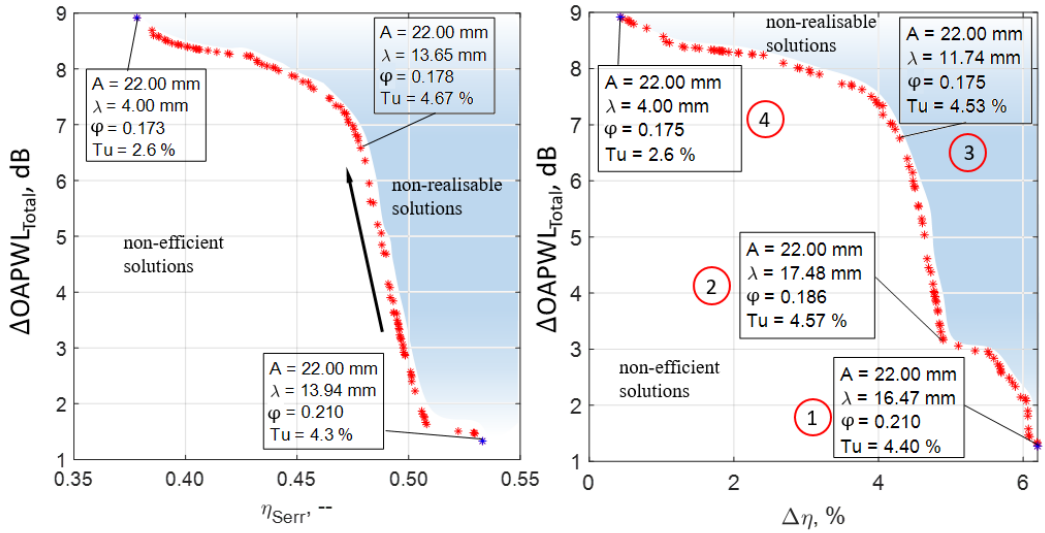

Figure 7-20 Maxmax optimum of sound power level reduction ΔOAPWL vs. aerodynamic efficiency η_{Serr} (left). Maxmax optimum of sound power level reduction ΔOAPWL vs. differences in aerodynamic efficiency Δη (right).

Similar to the overall reduction in Figure 7-20 (right), the trend of the broadband reduction also appears to be highly influenced by the serration wavelength (Figure 7-21 left). At the same system's efficiency, a maximum reduction of broadband noise of up to $\Delta PWL_{BB} = 5$ dB is possible, which can be further improved to $\Delta PWL_{BB} = 6$ dB by taking into account significant penalties in efficiency ($\Delta\eta = -6$ %). A common feature for significant noise reduction is the low wavelength, whereas large ones are required for high aerodynamic efficiency.

Aiming at an optimum between the overall sound power reduction and the broadband component (Figure 7-21, right) shows a contribution of the broadband attenuation of $\Delta PWL_{BB} = 3.7$ dB, while the overall reduction of $\Delta PWL = 8.9$ dB appears to be dominated by the discrete and the BPF components. This is also confirmed by the relation between the discrete and broadband noise reduction in Figure 7-22 (left). However, maximum broadband noise reduction while keeping the overall reduction on a high level is obtained for low Tu and intermediate amplitudes.

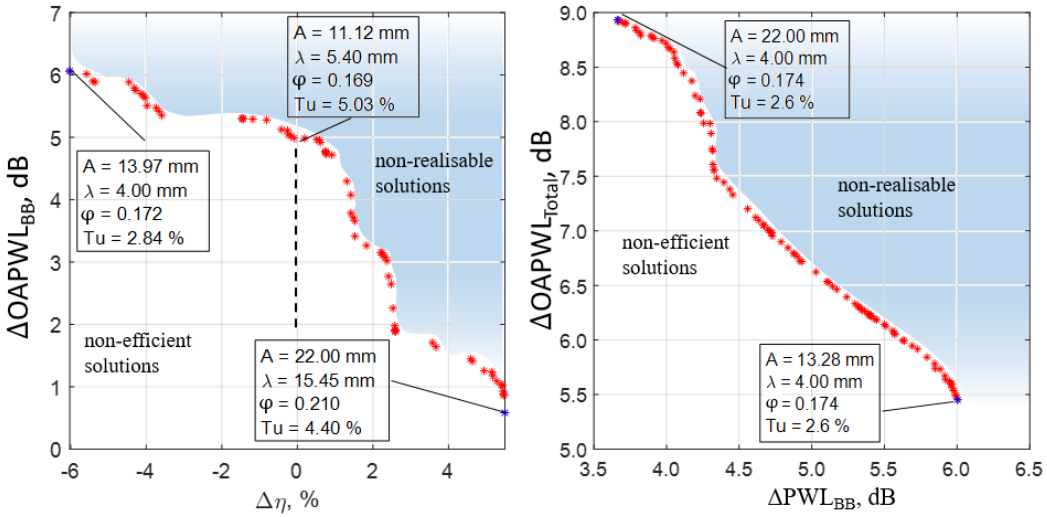

Figure 7-21 Maxmax optimum of broadband sound power level reduction $\Delta OAPWL_{BB}$ vs. differences in aerodynamic efficiency $\Delta\eta$ (left). Maxmax optimum of overall sound power level reduction $\Delta OAPWL$ vs. the broadband sound power level reduction ΔPWL_{BB} (right).

Figure 7-22 (left) shows the optimum of the single components with regard to the overall sound power reduction. Both turbulence intensity and serration amplitude can be identified as driving parameters for this functional relationship. High Tu in combination with high amplitudes leads to a maximum reduction in discrete noise components, whereas the reverse patterns are observed for the reduction in broadband noise.

Also for the spectral target values, a customised optimisation is possible, as shown in Figure 7-22 (right) for two distinct BPF frequencies. An optimum between both target values is reached for minimum wavelengths and intermediate amplitudes (position 3 in Figure 7-22 right), in which the BPF at 200 Hz is reduced by $\Delta PWL_{BPF} = 8$ dB and the BPF_{600Hz} by almost $\Delta PWL_{BPF} = 6$ dB. Increasing the wavelength (position 4 in Figure 7-22 right) seems to drastically decrease the noise reduction potential for the 200 Hz components, but an additional increase in amplitude (positions 5 and 6 in Figure 7-22 right) leads to the maximum performance in reducing the 600 Hz component. For the 200 Hz component, however, a clear decrease towards low turbulence (Tu = 2.5 %) and lower flow coefficients provides the maximum reduction (position 1 in Figure 7-22 right).

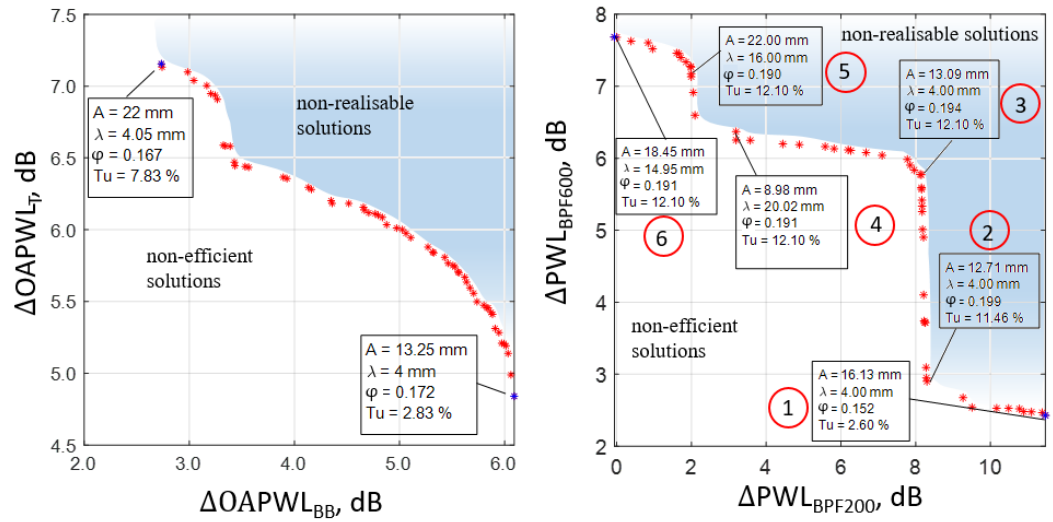

Figure 7-22 Maxmax optimum of the sound power level reduction for the discrete $\Delta OAPWL_{Discrete}$ and the broadband $\Delta OAPWL_{BB}$ components (left). Maxmax optimum of the spectral BPF noise reduction Δ_{BPF} for the 1st and 3rd harmonic (right).

7.3.4 Conclusions

A sampling of the experimental space by use of the Latin hypercube design plus a factorial design allowed developing a model, in which target values in the time and frequency domains and of both aerodynamic and acoustic character can be approximated with high accuracy. A total of 116 target values was defined, which can be described by individual artificial neural networks. A reasonable fit was observed for the aerodynamic performance, clearly outperformed by the aeroacoustic parameters in the time and frequency domains, showing an average fit of $R^2 = 94\ \% - 99\ \%$. Only target values referring to wall-pressure fluctuation show, especially for the discrete components, a significantly reduced performance, which can be attributed to the relatively low number of sample points as well as the highly sensitive behaviour of the measured quantities in the blade-tip region of the tested fan.

Testing the model against three fully independent test points within the experimental space yields a remarkable fit, even for the spectral distribution in 1/3rd-octave bands. This proves the ability of the model to generalise, consequently leading to an analysis of the system's performance by continuously varying selected parameters. The general aerodynamic and aeroacoustic trends were found to be in line with the results of the foregoing measurement campaigns and also indicated crucial parameters for the reduction of the single signal components by means of broadband and discrete noise. Moreover, a careful analysis of the fan characteristic curves also allows extracting the different noise sources and their sensitivity to the tested serration parameters.

Finally, a heuristic multi-objective optimisation leads to the definition of two-dimensional Pareto optimal solutions for selected pairs of target values, allowing specific insights into optimal serration design. This is crucial especially for reconciling opposing trends, such as the noise reduction capability and the aerodynamic performance. The chosen optimisation strategy, moreover, enables a customised design of serrated leading edges, tailored for specific operation conditions of the axial fan. Because of the ability to approximate in the spectral domain, even filtering becomes possible and allows considering, for example, A-weighting effects.

Nonetheless, the model requires further refinement, especially with regard to the wall-pressure signals, still showing a poor performance. Observed and proposed mechanisms need to be confirmed by more substantial inflow measurements or by numerical approaches. Moreover, implementation of the blade design parameters such as, for example, the sweep and the lean angles of the blades might lead to more general conclusions on the ability of the serrations to reduce noise and, hence, to broad application possibilities in industry.

8 Summary

An extensively analysed NACA65(12)-10 aerofoil was transferred to the rotating system by defining a 6-blade axial low-pressure fan according to the single-aerofoil approach. This took place concerning the aerodynamic and aeroacoustic data obtained from rigidly tested single aerofoils. Moreover, the design parameters of the leading edge serrations, too, were successively scaled and transferred to the prototype rotors. These rotor configurations were tested according to the in-duct method described in ISO 5136, allowing simultaneous analysis of the aerodynamic and the aeroacoustic performance as well as of the wall-pressure fluctuations in the tip region of the fan blades. The emphasis of the extensively analysed rigidly mounted single aerofoils and the low-pressure axial fans were different but facilitated maximum information to be obtained on the transferability of serrated leading edges. On the one hand, this was achieved by focussing on an identification of the fundamental noise reduction mechanisms and the aerodynamic flow patterns for the single, less complex aerofoils to better understand the effects of leading edge serrations. For the rotating system, on the other hand, the focus was on assessing the overall aerodynamic and aeroacoustic potential of serrated leading edges and identifying commonalities with the previously analysed single aerofoils.

Single Aerofoils

The overall performance of a NACA65(12)-10 aerofoil, equipped with serrated leading edges, was described by developing a comprehensive and highly accurate statistical-empirical model, which is able to describe the effects of the five main influencing parameters (Re, Tu, A/C, λ/C, AoA) on the aeroacoustic and the aerodynamic performance. For the first time, combined information on the aerodynamic and aeroacoustic performance for all relevant parameters is available. This allows multi-objective optimisation algorithms to define leading edge serration designs and testing conditions, in which both the aerodynamic and the aeroacoustic performance are at their optimum.

More detailed information on the location of the noise sources and the pure noise reduction capability of serrated leading edges was obtained from an experimental study by use of the array beamforming technique. A general trend of shifting noise sources with the serration roots was observed and attributed to hitherto only numerically obtained noise reduction effects, supplementing the validity of the proposed mechanisms. The same is true for an optimum ratio of the serration wavelength to the integral length scale, where an analysis of the spectral composition of the noise reduction allowed to define spectral scaling laws.

In addition to the reduction of the turbulence-induced broadband leading edge noise, a separate analysis of the trailing edge noise also revealed a significant potential of the serrations to reduce the trailing edge noise. The underlying mechanisms were found to be destructive interference effects of the wakes from the suction side and the pressure side of the serrated aerofoil, which are out of phase.

Aerodynamically, vortices generated by the leading edge serrations were found to be responsible for a complex three-dimensional separation pattern, clearly scaling with the serration amplitude and the serration wavelength. The observed separation process was identified as responsible for delayed onset of stall, though at a lower aerodynamic efficiency, also resulting in a smooth stall characteristic.

Transfer Findings for the Low-Pressure Axial Fans

The aerodynamic trends for the single aerofoils can be confirmed in terms of the overall fan performance, where small serration amplitudes and maximum serration wavelengths lead to maximum pressure coefficients as well as maximum efficiencies. Also, a small increase of the rotors' stall margin can be confirmed when applying serrations.

In terms of aeroacoustics, the effect of the leading edge serration parameters is more diverse. Pre-stall, the low-pressure fan shows a comparable sensitivity of the noise reduction towards high serration amplitudes and small serration wavelengths. Here, the spectral scaling of the broadband noise reduction also appears to be highly similar to the scaling laws proposed for the rigidly mounted aerofoils. The scaling coefficients, however, were found to be dominated by the serration amplitude and the turbulence intensity. This strongly suggests that the spanwise decorrelation of the noise sources and the destructive interference between the serration peak and the serration root are the driving effects for the pre-stall noise reduction.

Decreasing the flow coefficients leads to strong attenuation of these effects and emphasises that an aerodynamic mechanism dominates a further noise reduction with a focus on the blade-tip region. For the serrated rotors, a clear shift in the onset of the tip leakage flow towards lower flow coefficients was observed. This leads to significant noise reduction in the transition region from pre-stall to stall of the investigated rotors. This shift is presumably caused by the vortex generation effect of the serrations in the blade-tip region, resulting in re-energising effects for the boundary layer and thus delaying partial stall. Moreover, the generated vortices are considered capable of blocking the tip gap region, impeding the ability of the blade-tip reverse flows to interact with the blade tips. As a consequence, the underlying noise reduction mechanisms in this region are predominantly aerodynamic effects.

Moreover, a study that successively varied the number of fan blades identified that leading edge serrations beneficially influence blade interaction effects by dissolving turbulent structures, occurring from separation effects at preceding blades.

Aeroacoustic and Aerodynamic Model for Low-Pressure Axial Fans

After a detailed analysis of the overall performance of serrated rotors, the fans' aerodynamic and aeroacoustic performance was modelled by sampling the experimental space to train artificial neural networks. These artificial neural networks were found to be of high accuracy, where not only the overall noise radiation was modelled but also the spectral composition. Here, dividing the spectral content into its more physical components, namely the broadband components, on the one hand, and the fan-speed-dependent discrete (tonal) components, on the other hand, allowed a precise and independent modelling of the acoustic radiation. By now, the current model is capable of predicting the influence of four influencing parameters on the aerodynamic and acoustic performance. These parameters are the serration parameters (the serration amplitude and the serration wavelength) and the parameters characterising the flow properties (the flow coefficient and the turbulence intensity). Also for the defined artificial neural networks, multiple target values can be optimised simultaneously by using a multi-objective optimisation approach. The defined Pareto optima provided non-weighted solutions for tailoring the rotor design and the flow conditions according to defined target values, be it in terms of the spectral composition or in terms of the aerodynamic performance.

The ability of the model for the rotor to generalise the results in terms of predicting absolute values is at the current stage expected to be limited to similar test settings as well as highly similar aerofoil types. Nevertheless, the general trends are considered to be of high value also for axial rotors of different geometry.

9 Outlook

In the presented thesis, first attempts were made to transfer the knowledge of rigidly mounted leading edge serrations to the rotating domain. The main noise reduction potential and common scaling laws were identified. However, even though the effects of several influencing parameters on the noise generation and the aerodynamic performance were analysed, some questions remain to be answered and some other aspects came into focus due to the analysis conducted.

First of all, counter-rotating vortices were found to be generated at the serration shoulders, leading to upwash and downwash effects of the fluid. In consequence, the effective angle of attack varies along any spanwise serration contour, being higher than the geometrical AoA for the root regions and promoting delayed flow separation at peak locations [29, 38]. This effective angle of attack is a function of the chosen aerofoil type and the vorticity, which itself depends on the serration parameters. On the other hand, for generating the sinusoidal leading edge contour, the current serration design is based on straining the leading-edge profile from the tips towards the roots. As depicted in Figure 9-1 (left), relative to the peak location, this procedure leads to lower geometrical AoA for the root region. This can be compensated for by, for example, introducing serration mid-peaks of upward-twisted orientation (Figure 9-1, right). Future research needs to outbalance these two effects of vorticity-induced upwash and design-caused reduction in the angle of attack in order to optimise the serration contour and to develop serrated aerofoil designs of higher consistency with regard to the spanwise effective angle of attack.

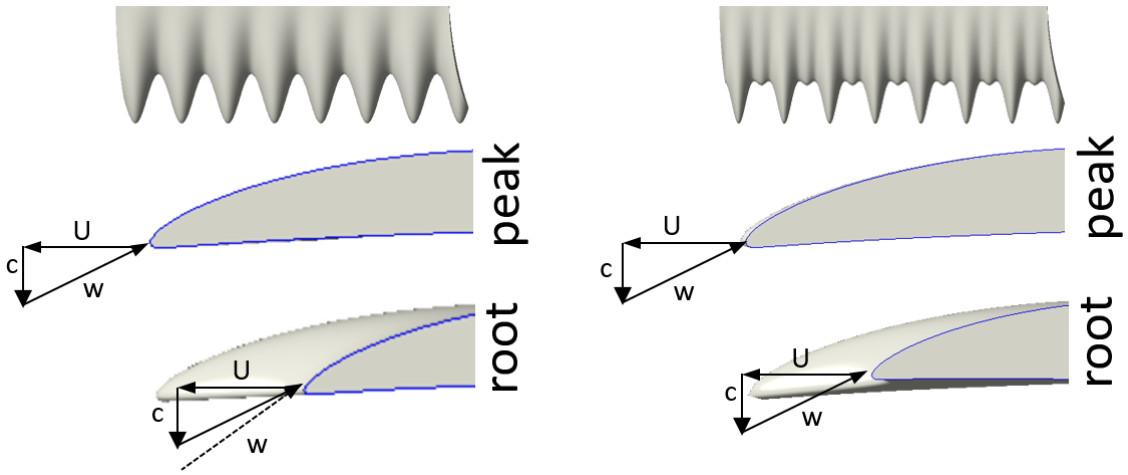

Figure 9-1 Standard serration with inlet velocity triangle (left) and serration with modified mid-peak to match the velocity triangles of the peak (right).

Another aspect, not yet transferred from the rigid domain, is the aeroacoustic and aerodynamic efficiency of serration designs optimised by means of double-wavelength, slitted or slitted-root serrations, showing promising results for single aerofoils [108, 106, 103]. These optimised designs are based on maximum spanwise decorrelation concepts as well as destructive interference effects. However, for the rotating application, superior performance of these designs is put into question since the analyses carried out showed the classical serration effects to be mainly present only at relatively high flow coefficients. Considered more meaningful are novel serration designs that focus on an increased vortex generation close to the tip region as well as minimum drag generation and low lift penalties. This leads to considerations of the speed-dependent characteristics of the serrated blades. The circumferential velocity increases linearly from hub to tip of the blades. Moreover, due to the controlled vortex design, the blade loading is known to be at its maximum close to the blade tips. This predestines the outer one-third of the blades for aerodynamic optimisation and the outermost region of the blades for vortical

optimisation to alter unsteady flow phenomena due to tip gap reverse flows from the pressure to the suction side of the blades. A target-oriented approach could be a spanwise variable ratio of amplitude to wavelength, as shown in Figure 9-2 (left).

An upcoming task for the marketability of serrated rotors is an extension of the analyses carried out to more complex fan design parameters, such as blade dihedral or forward- and backward-skewed blades (Figure 9-2 right). The aeroacoustic signature of forward-skewed rotors, in particular, was found to be highly receptive to the inflow conditions, showing remarkable broadband noise under high turbulence [150]. In consequence, this provides a clear potential of reducing ATI noise by implementing serrations. It needs to be shown whether the extracted noise reduction capability of the tested serrated rotors holds true for these changed fan design parameters. Moreover, different loading designs, too, need to be incorporated into future studies, preferably in order to provide information on the degree to which hitherto obtained results can be generalised.

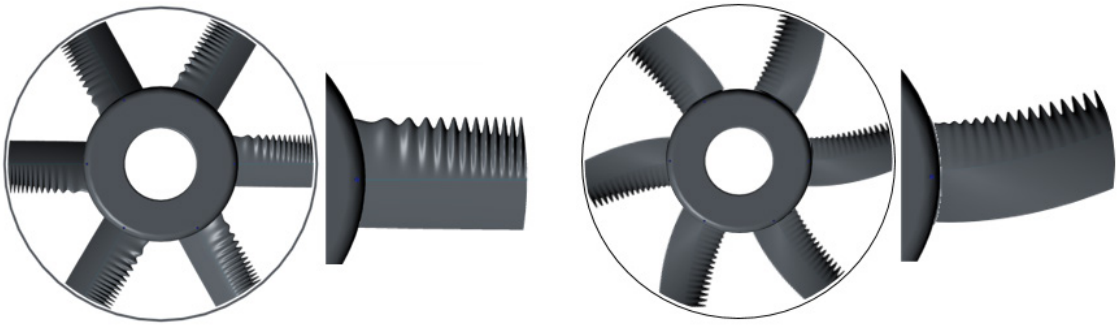

Figure 9-2 Rotors with spanwise variations in A/λ serration ratio (left) and with forward-skewed serrated blades (right).

The proposed studies into the effect of leading edge serrations on additional blade design parameters should be followed by an adaption of the generated artificial neural networks. In ideal circumstances, test data of uniformly distributed samples within the extended experimental space can be incorporated into the existing model. This is expected to lead to a more generalised approximation of the global aeroacoustic and aerodynamic performance as well as to spectral prediction of the radiated noise. This is particularly important for the modelled unsteady wall-pressure fluctuations, which still show comparably low performance. Ultimately, the model can be used to derive a sophisticated design tool for serrated rotors, providing tailored solutions at given operating conditions. The extension of the current artificial neural networks by taking into account additional parameters is considered the more intelligent way to provide a reliable model for industrial applications. The alternatively required experimental expenditure of deriving independent models for any specific practical application task usually outbalances the benefits to be gained. A turning point, however, would be the transition from experimental to numerical investigations, but especially for aeroacoustics, this is not considered feasible at the current stage of acoustic research.

References

[1] Chaitanya, P., Joseph, P., Narayanan, S., Vanderwel, C., Turner, J., Kim, J. W., and Ganapathisubramani, B., "Performance and mechanism of sinusoidal leading edge serrations for the reduction of turbulence–aerofoil interaction noise," *Journal of Fluid Mechanics*; Vol. 818, 2017, pp. 435–464. doi: 10.1017/jfm.2017.141.

[2] Laws, E. M., and Livesey, J. L., "Flow Through Screens," *Annual Review of Fluid Mechanics*; Vol. 10, No. 1, 1978, pp. 247–266. doi: 10.1146/annurev.fl.10.010178.001335.

[3] Peake, N., and Parry, A. B., "Modern Challenges Facing Turbomachinery Aeroacoustics," *Annual Review of Fluid Mechanics*; Vol. 44, No. 1, 2012, pp. 227–248. doi: 10.1146/annurev-fluid-120710-101231.

[4] European Commission, "Flightpath 2050. Europe's vision for aviation ; maintaining global leadership and serving society's needs," *report of the High-Level Group on Aviation Research*, Publ. Off. of the Europ. Union, Luxembourg, 2011.

[5] Buck, S., Oerlemans, S., and Palo, S., "Experimental validation of a wind turbine turbulent inflow noise prediction code," *22nd AIAA/CEAS Aeroacoustics Conference*, 2016. doi: 10.2514/6.2016-2953.

[6] Locke, C., "Humpback Whales Solve a Big Problem for Wind Turbines," http://www.wired.com/2015/11/whales-wind-turbines/, [retrieved 26 January 2016].

[7] Fish, F. E., and Battle, J. M., "Hydrodynamic design of the humpback whale flipper," *Journal of Morphology*; Vol. 225, No. 1, 1995, pp. 51–60. doi: 10.1002/jmor.1052250105.

[8] Graham, R. R., "The Silent Flight of Owls," *Journal of the Royal Aeronautical Society*; Vol. 38, No. 286, 1934, pp. 837–843. doi: 10.1017/s0368393100109915.

[9] Anderson, G. W., "An Experimental Investigation of a High Lift Device on the Owl Wing," Air Force Institute of Technology, 1973.

[10] Lilley, G., "A study of the silent flight of the owl," *4th AIAA/CEAS Aeroacoustics Conference*, 1998. doi: 10.2514/6.1998-2340.

[11] Ito, S., "Aerodynamic Influence of Leading-Edge Serrations on an Airfoil in a Low Reynolds Number," *Journal of Biomechanical Science and Engineering*; Vol. 4, No. 1, 2009, pp. 117–123. doi: 10.1299/jbse.4.117.

[12] Sarradj, E., Fritzsche, C., and Geyer, T., "Silent Owl Flight: Bird Flyover Noise Measurements," *AIAA Journal*; Vol. 49, No. 4, 2011, pp. 769–779. doi: 10.2514/1.J050703.

[13] Glegg, S. A., and Devenport, W. J., "Leading Edge Noise from Very Thick Airfoils with Vertical Fences," *23rd AIAA/CEAS Aeroacoustics Conference*, Virginia, 2017. doi: 10.2514/6.2017-3495.

[14] Geyer, T. F., Wasala, S. H., Cater, J. E., Norris, S. E., and Sarradj, E., "Experimental Investigation of Leading Edge Hook Structures for Wind Turbine Noise Reduction," *22nd AIAA/CEAS Aeroacoustics Conference*, 2016. doi: 10.2514/6.2016-2954.

[15] Wood, D., "Envira-North Systems Ltd," http://www.enviranorth.com/index.html, [retrieved 26 January 2016].

[16] Dewar, S. W., Watts, P., and Fish, F. E., US patent, *US 8,535,008 B2*, 2008.

[17] Soderman, P. T., "Aerodynamic Effects of Leading-Edge Serrations on a Two-Dimensional Airfoil," Ames Research Center and U.S. Army Air Mobility R&D Laboratory, NASA TM X-2643, 1972.

[18] Miklosovic, D. S., Murray, M. M., Howle, L. E., and Fish, F. E., "Leading-edge tubercles delay stall on humpback whale (Megaptera novaeangliae) flippers," *Physics of Fluids*; Vol. 16, No. 5, 2004, pp. L39. doi: 10.1063/1.1688341.

[19] Miklosovic, D. S., Murray, M. M., and Howle, L. E., "Experimental Evaluation of Sinusoidal Leading Edges," *Journal of Aircraft*; Vol. 44, No. 4, 2007, pp. 1404–1408. doi: 10.2514/1.30303.

[20] Johari, H., Henoch, C. W., Custodio, D., and Levshin, A., "Effects of Leading-Edge Protuberances on Airfoil Performance," *AIAA Journal*; Vol. 45, No. 11, 2007, pp. 2634–2642. doi: 10.2514/1.28497.

[21] Yoon, H. S., Hung, P. A., Jung, J. H., and Kim, M. C., "Effect of the wavy leading edge on hydrodynamic characteristics for flow around low aspect ratio wing," *Computers & Fluids*; Vol. 49, No. 1, 2011, pp. 276–289. doi: 10.1016/j.compfluid.2011.06.010.

[22] Rostamzadeh, N., Hansen, K. L., Kelso, R. M., and Dally, B. B., "The formation mechanism and impact of streamwise vortices on NACA 0021 airfoil's performance with undulating leading edge modification," *Physics of Fluids*; Vol. 26, No. 10, 2014, p. 107101. doi: 10.1063/1.4896748.

[23] Hansen, K. L., Kelso, R. M., and Dally, B. B., "The Effect of Leading Edge Tubercle Geometry on the Performance of Different Airfoils," *7th World Conference on Experimental Heat Transfer, Fluid Mechanics and Thermodynamics*, 2009.

[24] Hansen, K., Kelso, R., and Doolan, C., "Reduction of Flow Induced Tonal Noise Through Leading Edge Tubercle Modifications," *16th AIAA/CEAS Aeroacoustics Conference*, 2010. doi: 10.2514/6.2010-3700.

[25] Hansen, K. L., Kelso, R. M., and Dally, B. B., "Performance Variations of Leading-Edge Tubercles for Distinct Airfoil Profiles," *AIAA Journal*; Vol. 49, No. 1, 2011, pp. 185–194. doi: 10.2514/1.J050631.

[26] Borg, J., *The effect of leading edge serrations on dynamic stall*, Master thesis, University of Southampton, 2012.

[27] Chong, T. P., Vathylakis, A., McEwen, A., Kemsley, F., Muhammad, C., and Siddiqi, S., "Aeroacoustic and Aerodynamic Performances of an Aerofoil Subjected to Sinusoidal Leading Edges," *21st AIAA/CEAS Aeroacoustics Conference*, 2015. doi: 10.2514/6.2015-2200.

[28] Zhang, M. M., Wang, G. F., and Xu, J. Z., "Experimental study of flow separation control on a low-Re airfoil using leading-edge protuberance method," *Experiments in Fluids*; Vol. 55, No. 4, 2014, p. 321. doi: 10.1007/s00348-014-1710-z.

[29] van Nierop, E. A., Alben, S., and Brenner, M. P., "How bumps on whale flippers delay stall: An aerodynamic model," *Physical review letters*; Vol. 100, No. 5, 2008, p. 54502. doi: 10.1103/PhysRevLett.100.054502.

[30] Hansen, K. L., Rostamzadeh, N., Kelso, R. M., and Dally, B. B., "Evolution of the streamwise vortices generated between leading edge tubercles," *Journal of Fluid Mechanics*; Vol. 788, 2016, pp. 730–766. doi: 10.1017/jfm.2015.611.

[31] Al-Okbi, Y., Chong, T. P., and Stalnov, O., "Mimicking the serration effects on aerofoil by leading edge blowing," *24th AIAA/CEAS Aeroacoustics Conference*, 2018. doi: 10.2514/6.2018-3287.

[32] Skillen, A., Revell, A., Pinelli, A., Piomelli, U., and Favier, J., "Flow over a Wing with Leading-Edge Undulations," *AIAA Journal*; Vol. 53, No. 2, 2015, pp. 464–472. doi: 10.2514/1.J053142.

[33] Cai, C., Zuo, Z., Liu, S., and Wu, Y., "Effect of a single leading-edge protuberance on NACA 634-021 airfoil performance," *ISROMAC*, 2016.

[34] Custodio, D., *The Effect of Humpback Whale-like Leading Edge Protuberances on Hydrofoil Performance*, Master thesis, Worcester Polytechnic Institute, Worcester, USA, 2007.

[35] E. Guerreiro, J. L., and M. Sousa, J. M., "Low-Reynolds-Number Effects in Passive Stall Control Using Sinusoidal Leading Edges," *AIAA Journal*; Vol. 50, No. 2, 2012, pp. 461–469. doi: 10.2514/1.J051235.

[36] Zhang, M. M., Wang, G. F., and Xu, J. Z., "Aerodynamic Control of Low-Reynolds-Number Airfoil with Leading-Edge Protuberances," *AIAA Journal*; Vol. 51, No. 8, 2013, pp. 1960–1971. doi: 10.2514/1.J052319.

[37] Melo De Sousa, J., and Camara, J., "Numerical Study on the Use of a Sinusoidal Leading Edge for Passive Stall Control at Low Reynolds Number," *51st AIAA Aerospace Sciences Meeting*, 2013. doi: 10.2514/6.2013-62.

[38] Cai, C., Zuo, Z., Maeda, T., Kamada, Y., Li, Q.'a., Shimamoto, K., and Liu, S., "Periodic and aperiodic flow patterns around an airfoil with leading-edge protuberances," *Physics of Fluids*; Vol. 29, No. 11, 2017, p. 115110. doi: 10.1063/1.4991596.

[39] Pedro, H. T., and Kobayashi, M. H., "Numerical Study of stall delay on humpback whale flippers," *46th AIAA Aerospace Sciences Meeting and Exhibit*, 2008.

[40] Rostamzadeh, N., Kelso, R. M., and Dally, B., "A numerical investigation into the effects of Reynolds number on the flow mechanism induced by a tubercled leading edge," *Theoretical and Computational Fluid Dynamics*; Vol. 31, No. 1, 2017, pp. 1–32. doi: 10.1007/s00162-016-0393-x.

[41] Chen, J.-H., Li, S.-S., Nguyen, V.T., J.-H Chen, S.-S Li, and V T Nguyen, "The Effect of Leading Edge Protuberances on the Performance of Small Aspect Ratio Foils," *15th International Symposium on Flow Visualisation*, 2012. doi: 10.13140/RG.2.1.3716.7841.

[42] Timmer, W. A., "An Overview of NACA 6-Digit Airfoil Series Characteristics with Reference to Airfoils for Large Wind Turbine Blades," *47th AIAA Aerospace Science Meeting*, 2009. doi: 10.2514/6.2009-268.

[43] Kim, M. J., Yoon, H. S., Jung, J. H., Chun, H. H., and Park, D. W., "Hydrodynamic characteristics for flow around wavy wings with different wave lengths," *International Journal of Naval Architecture and Ocean Engineering*; Vol. 4, No. 4, 2012. doi: 10.2478/IJNAOE-2013-0110.

[44] Zhang, L. Y., He, L., and Stüer, H., "A Numerical Investigation of Rotating Instability in Steam Turbine Last Stage," *Journal of Turbomachinery*; Vol. 135, No. 1, 2013, p. 11009. doi: 10.1115/1.4006330.

[45] Custodio, D., Henoch, C. W., and Johari, H., "Aerodynamic Characteristics of Finite Span Wings with Leading-Edge Protuberances," *AIAA Journal*; Vol. 53, No. 7, 2015, pp. 1878–1893. doi: 10.2514/1.J053568.

[46] Gross, A., and Fasel, H. F., "Numerical Investigation of Passive Separation Control for an Airfoil at Low-Reynolds-Number Conditions," *AIAA Journal*; Vol. 51, No. 7, 2013, pp. 1553–1565. doi: 10.2514/1.J051553.

[47] Chaitanya, P., Narayanan, S., Joseph, P., Vanderwel, C., Kim, J. W., and Ganapathisubramani, B., "Broadband noise reduction through leading edge serrations on realistic aerofoils," *21st AIAA/CEAS Aeroacoustics Conference*, 2015. doi: 10.2514/6.2015-2202.

[48] Biedermann, T., Kameier, F., Koster, O., Schreiber, D., Chong, T. P., and Paschereit, C.O., "Polyoptimisation of the Aerodynamic and Aeroacoustic Performance of Aerofoils with Serrated Leading Edges," *23rd AIAA/CEAS Aeroacoustics Conference*, 2017. doi: 10.2514/6.2017-3493.

[49] Gawad, A. F., "Utilization of Whale-Inspired Tubercles as a Control Technique to Improve Airfoil Performance," *Transaction on Control and Mech. Systems*; Vol. 2, No. 5, 2013, pp. 212–218.

[50] Gawad, A. F. A., "Numerical Simulation of the Effect of Leading-Edge Tubercles on the Flow Characteristics around an Airfoil," *Proceedings of the ASME 2012 International Mechanical Engineering Congress & Exposition*, 2012.

[51] European Commission, "FLOCON (Adaptive and Passive Flow Control for Fan Broadband Noise Reduction): CORDIS : Projects & Results Periodic Report Summary 3 -," 213411, 2015.

[52] Abbott, I. H., Doenhoff, A. E., and Stivers, L. S., "Summary of Airfoil Data," NACA National Advisory Committee for for Aeronautics, 1945.

[53] Gruber, M., *Airfoil noise reduction by edge treatments*, Ph.D. thesis, University of Southampton, UK, 2012.

[54] Koster, O., *Investigation on the Aeroacoustics and Flow Pattern of a NACA65(12)-10 Aerofoil with Serrated Leading Edges*, Master thesis, University of Applied Sciences Duesseldorf, Dueesseldorf, Germany, 2017.

[55] Schreiber, D., *Aerodynamische Untersuchung eines NACA 65-(12)10 mit Leading Edge Serrations unter Verwendung numerischer Methoden*, Master thesis, University of Applied Sciences Duesseldorf, Duesseldorf, Germany, 2017.

[56] Barlow, J. B., Rae, W. H., and Pope, A., *Low-speed wind tunnel testing,* 3rd edn., Wiley, New York, 1999. ISBN: 978-0471557746.

[57] Bogdonoff, S. M., and Bogdonoff, H. E., "Blade Design Data for Axial-Flow Fans and Compressors," NACA National Advisory Committee for for Aeronautics, Wartime Report, 1945.

[58] Shelton, A., Abras, J., Jurenko, R., and Smith, M. J., "Improving the CFD Predictions of Airfoils and Wings in Stall," *43rd AIAA Aerospace Sciences Meeting and Exhibit*, 2005. doi: 10.2514/6.2005-1227.

[59] Drela, M., and Youngren, H., "Xfoil 6.94 User Guide," *xfoil*, MIT, USA, 2013.

[60] Hunt, J.C.R., Wray, A.A., and Moin, P., "Eddies, Streams, and Convergence Zones in Turbulent Flows," Center for Turbulence Research, 1988, https://ntrs.nasa.gov/archive/nasa/casi.ntrs.nasa.gov/19890015184.pdf, [retrieved 2019].

[61] Blake, W. K., *Mechanics of Flow-Induced Sound and Vibration, Volume 2. Complex Flow-Structure Interactions,* 2nd edn., Elsevier Science, San Diego, 2017.

[62] Paterson, R. W., and Amiet, R. K., "Acoustic Radiation and Surface Pressure Characteristics of an Airfoil due to Incident Turbulence," United Technologies Research Center for Langley Research Center, NASA CR-2733, 1976.

[63] Oerlemans, S., and Migliore, P., "Aeroacoustic Wind Tunnel Tests of Wind Turbine Airfoils," *10th AIAA/CEAS Aeroacoustics Conference*, 2004. doi: 10.2514/6.2004-3042.

[64] Staubs, J. K., *Real Airfoil Effects on Leading Edge Noise*, Ph.D. thesis, Virginia State University, Blacksburg, USA, 2008.

[65] Amiet, R. K., "Acoustic Radiation from an Airfoil in a Turbulent Stream," *Journal of Sound and Vibration,* No. 41(4), 1975, 407-420. doi: 10.1016/S0022-460X(75)80105-2.

[66] Carolus, T., *Ventilatoren*, Vieweg+Teubner Verlag, Wiesbaden, 2013. doi: 10.1007/978-3-8348-2472-1.

[67] Narayanan, S., Chaitanya, P., Haeri, S., Joseph, P., Kim, J. W., and Polacsek, C., "Airfoil noise reductions through leading edge serrations," *Physics of Fluids*; Vol. 27, No. 2, 2015, p. 25109. doi: 10.1063/1.4907798.

[68] Ayton, L. J., and Chaitanya, P., "Analytical and experimental investigation into the effects of leading-edge radius on gust–aerofoil interaction noise," *Journal of Fluid Mechanics*; Vol. 829, 2017, pp. 780–808. doi: 10.1017/jfm.2017.594.

[69] Gill, J., Zhang, X., and Joseph, P., "Symmetric airfoil geometry effects on leading edge noise," *The Journal of the Acoustical Society of America*; Vol. 134, No. 4, 2013, pp. 2669–2680. doi: 10.1121/1.4818769.

[70] Evers, I., and Peake, N., "On sound generation by the interaction between turbulence and a cascade of airfoils with non-uniform mean flow," *Journal of Fluid Mechanics*; Vol. 463, 2002. doi: 10.1017/S0022112002008698.

[71] Gershfeld, J., "Leading edge noise from thick foils in turbulent flows," *The Journal of the Acoustical Society of America*; Vol. 116, No. 3, 2004, pp. 1416–1426. doi: 10.1121/1.1780575.

[72] Moriarty, P., Guidati, G., and Migliore, P., "Prediction of Turbulent Inflow and Trailing-Edge Noise for Wind Turbines," *11th AIAA/CEAS Aeroacoustics Conference*, 2005. doi: 10.2514/6.2005-2881.

[73] Lysak, P. D., Capone, D. E., and Jonson, M. L., "Prediction of high frequency gust response with airfoil thickness effects," *Journal of Fluids and Structures*; Vol. 39, 2013, pp. 258–274. doi: 10.1016/j.jfluidstructs.2013.02.006.

[74] Kim, J. W., Haeri, S., and Joseph, P. F., "On the reduction of aerofoil–turbulence interaction noise associated with wavy leading edges," *Journal of Fluid Mechanics*; Vol. 792, 2016, pp. 526–552. doi: 10.1017/jfm.2016.95.

[75] Paruchuri, C., *Aerofoil geometry effects on turbulence interaction noise*, Ph.D. thesis, University of Southampton, Southampton, UK, 2017.

[76] Desquesnes, G., Terracol, M., and Saugat, P., "Numerical investigation of the tone noise mechanism over laminar airfoils," *Journal of Fluid Mechanics*; Vol. 591, 2007. doi: 10.1017/S0022112007007896.

[77] Geyer, T., Sarradj, E., and Giesler, J., "Application of a Beamforming Technique to the Measurement of Airfoil Leading Edge Noise," *Advances in Acoustics and Vibration*; Vol. 2012, No. 3, 2012, pp. 1–16. doi: 10.1155/2012/905461.

[78] Arbey, H., and Bataille, J., "Noise generated by airfoil profiles placed in a uniform laminar flow," *J . Fluid Mech.*; Vol. 1983, No. 134, 1983, pp. 33–47.

[79] Fink, M. R., "Prediction of airfoil tone frequencies," *Journal of Aircraft*; Vol. 12, No. 2, 1975, pp. 118–120. doi: 10.2514/3.44421.

[80] Hersh, A. S., and Hayden, R. E., "Aerodynamic Sound Radiation from Lifting Surfaces with and without Leading-Edge Serrations," NASA AMES Research Center, NASA-5974, 1971.

[81] McAlpine, A., Nash, E. C., and Lowson, M. V., "On the Generation of Discrete Frequency Tones by the Flow around an Aerofoil," *Journal of Sound and Vibration*; Vol. 222, No. 5, 1999, pp. 753–779. doi: 10.1006/jsvi.1998.2085.

[82] Turner, J., and Kim, J. W., "Towards Understanding Aerofoils with Wavy Leading Edges Interacting with Vortical Disturbances," *22st AIAA/CEAS Aeroacoustics Conference*, 2016. doi: 10.2514/6.2016-2952.

[83] Turner, J. M., and Kim, J. W., "Aeroacoustic source mechanisms of a wavy leading edge undergoing vortical disturbances," *Journal of Fluid Mechanics*; Vol. 811, 2017, pp. 582–611. doi: 10.1017/jfm.2016.785.

[84] Haeri, S., Kim, J. W., Narayanan, S., and Joseph, P., "3D calculations of aerofoil-turbulence interaction noise and the effect of wavy leading edges," *20th AIAA/CEAS Aeroacoustics Conference*, 2014. doi: 10.2514/6.2014-2325.

[85] Chen, W., Qiao, W., Wang, L., Tong, F., and Wang, X., "Rod-Airfoil Interaction Noise Reduction Using Leading Edge Serrations," *21st AIAA/CEAS Aeroacoustics Conference*, 2015. doi: 10.2514/6.2015-3264.

[86] Lau, A. S. H., Haeri, S., and Kim, J. W., "The effect of wavy leading edges on aerofoil–gust interaction noise," *Journal of Sound and Vibration*; Vol. 332, No. 24, 2013, pp. 6234–6253. doi: 10.1016/j.jsv.2013.06.031.

[87] Lyu, B., and Azarpeyvand, M., "On the noise prediction for serrated leading edges," *Journal of Fluid Mechanics*; Vol. 826, 2017, pp. 205–234. doi: 10.1017/jfm.2017.429.

[88] Clair, V., Polacsek, C., Le Garrec, T., Reboul, G., Gruber, M., and Joseph, P., "Experimental and Numerical Investigation of Turbulence-Airfoil Noise Reduction Using Wavy Edges," *AIAA Journal*; Vol. 51, No. 11, 2013, pp. 2695–2713. doi: 10.2514/1.J052394.

[89] Ayton, L. J., and Kim, J. W., "An analytic solution for the noise generated by gust-aerofoil interaction for plates with serrated leading edges," *Journal of Fluid Mechanics*; Vol. 2018, No. 853, 2018, pp. 515–536. doi: 10.1017/jfm.2018.583.

[90] Roger, M., and Carazo, A., "Blade-Geometry Considerations in Analytical Gust-Airfoil Interaction Noise Models," *16th AIAA/CEAS Aeroacoustics Conference*, 2010. doi: 10.2514/6.2010-3799.

[91] Narayanan, S., Joseph, P., Haeri, S., and Kim, J. W., "Noise Reduction Studies from the Leading Edge of Serrated Flat Plates," *20th AIAA/CEAS Aeroacoustics Conference*, 2014. doi: 10.2514/6.2014-2320.

[92] Polacsek, C., Reboul, G., Clair, V., Le Garrec, T., and Deniau, H., "Turbulence-airfoil interaction noise reduction using wavy leading edge: An experimental and numerical study," *Inter Noise 2011*, 2011.

[93] Chong, T. P., Vathylakis, A., Joseph, P. F., and Gruber, M., "Self-Noise Produced by an Airfoil with Nonflat Plate Trailing-Edge Serrations," *AIAA Journal*; Vol. 51, No. 11, 2013, pp. 2665–2677. doi: 10.2514/1.J052344.

[94] Roger, M., Schram, C., and De Santana, L., "Reduction of Airfoil Turbulence-Impingement Noise by Means of Leading-Edge Serrations and/or Porous Material," *19th AIAA/CEAS Aeroacoustics Conference*, 2013. doi: 10.2514/6.2013-2108.

[95] Gruber, M., Joseph, P., Polacsek, C., and Chong, T. P., "Noise reduction using combined trailing edge and leading edge serrations in a tandem airfoil experiment," *33rd AIAA Aeroacoustics Conference*, 2012. doi: 10.2514/6.2012-2134.

[96] Chen, W., Qiao, W., Wang, X., Wang, L., and Tong, F., "An Experimental and Numerical Investigation of Airfoil Instability Noise with Leading Edge Serrations," *22nd AIAA/CEAS Aeroacoustics Conference*, 2016. doi: 10.2514/6.2016-2956.

[97] Brooks, T. F., Marcolini, M. A., and Pope, D. S., "Airfoil trailing-edge flow measurements," *AIAA Journal*; Vol. 24, No. 8, 1986, pp. 1245–1251. doi: 10.2514/3.9426.

[98] Myers, M. R., and Kerschen, E. J., "Influence of incidence angle on sound generation by airfoils interacting with high-frequency gusts," *Journal of Fluid Mechanics*; Vol. 292, No. -1, 1995, p. 271. doi: 10.1017/S0022112095001522.

[99] Lacagnina, G., Chaitanya, P., Berk, T., and Joseph, P., "Effect of Leading Edge serrations in reducing aerofoil noise near stall conditions," *24th AIAA/CEAS Aeroacoustics Conference*, 2018. doi: 10.2514/6.2018-3285.

[100] Hersh, A. S., Soderman, P. T., and Hayden, R. E., "Investigation of Acoustic Effects of Leading-Edge Serrations on Airfoils," *Journal of Aircraft*; Vol. 11, No. 4, 1974, pp. 197–202. doi: 10.2514/3.59219.

[101] Turner, J., and Kim, J. W., "Aeroacoustic effects of the trailing edge of an undulated aerofoil subjected to impinging disturbances," *23rd AIAA/CEAS Aeroacoustics Conference*, 2017. doi: 10.2514/6.2017-3494.

[102] Lacagnina, G., Hasheminejad, S. M., Paruchuri, C. C., Joseph, P., Chong, T. P., and Stalnov, O., "Leading edge serrations for the reduction of aerofoil separation self-noise," *23rd AIAA/CEAS Aeroacoustics Conference*, 2017. doi: 10.2514/6.2017-4169.

[103] Chaitanya, P., Joseph, P., Narayanan, S., and Kim, J. W., "Aerofoil broadband noise reductions through double-wavelength leading-edge serrations: A new control concept," *Journal of Fluid Mechanics*; Vol. 855, 2018, pp. 131–151. doi: 10.1017/jfm.2018.620.

[104] Turner, J., Kim, J. W., Paruchuri, C. C., and Joseph, P., "Towards Understanding Aerofoils with Dual-Frequency Wavy Leading Edges Interacting with Vortical Disturbances," *22nd AIAA/CEAS Aeroacoustics Conference*, 2016.
doi: 10.2514/6.2016-2951.

[105] Chaitanya, P., Narayanan, S., Joseph, P., and Kim, J. W., "Leading edge serration geometries for significantly enhanced leading edge noise reductions," *22nd AIAA/CEAS Aeroacoustics Conference*, 2016. doi: 10.2514/6.2016-2736.

[106] Chaitanya, P., Joseph, P., and Ayton, L., "On the superior performance of leading edge slits over serrations for the reduction of aerofoil interaction noise," *24th AIAA/CEAS Aeroacoustics Conference*, 2018. doi: 10.2514/6.2018-3121.c1.

[107] Ayton, L. J., and Chaitanya, P., "Analytic solutions for reduced leading-edge noise aerofoils," *24th AIAA/CEAS Aeroacoustics Conference*, 2018. doi: 10.2514/6.2018-3284.

[108] Chaitanya, P., and Joseph, P., "Slitted leading edge profiles for the reduction of turbulence-aerofoil interaction noise," *The Journal of the Acoustical Society of America*; Vol. 143, No. 6, 2018, p. 3494. doi: 10.1121/1.5040972.

[109] Juknevicius, A., Chong, T. P., and Woodhead, P. C., "Leading Edge Noise Reduction of Thin Aerofoil by the Straight and Curved Serrations of the Add-on Type," *23rd AIAA/CEAS Aeroacoustics Conference*, 2017. doi: 10.2514/6.2017-3491.

[110] Biedermann, T. M., Chong, T. P., Kameier, F., and Paschereit, C. O., "Statistical-Empirical Modelling of Airfoil Noise Subjected to Leading Edge Serrations," *AIAA Journal*; Volume 55, issue 9, 2017, pp. 3128–3142. doi: 10.2514/1.J055633.

[111] NIST/SEMATECH, "e-Handbook of Statistical Methods," https://www.itl.nist.gov/div898/handbook/, [retrieved 22 April 2019].

[112] Siebertz, K., van Bebber, D., and Hochkirchen, T., *Statistische Versuchsplanung*, Springer Verlag, Berlin, 2010. doi: 10.1007/978-3-642-05493-8.

[113] Biedermann, T. M., Reich, M., Kameier, F., Adam, M., and Paschereit, C.O., "Assessment of Statistical Sampling Methods and Approximation Models Applied to Aeroacoustic and Vibroacoustic Problems," *Advances in Aircraft and Spacecraft Science AASS*, accepted manuscript, scheduled November 2019.

[114] Vathylakis, A., Chong, T. P., and Kim, J. H., "Design of a low-noise aeroacoustic wind tunnel facility at Brunel University," *20th AIAA/CEAS Aeroacoustics Conference*, 2016. doi: 10.2514/6.2014-3288.

[115] Brooks, T., Marcolini, M., and Pope, D., "Airfoil trailing edge flow measurements and comparison with theory, incorporating open wind tunnel corrections,". doi: 10.2514/6.1984-2266.

[116] Aufderheide, T., Bode, C., Friedrichs, J., and Kozulovic, D., "The Generation of Higher Levels of Turbulence in in a Low-Speed Cascade Windtunnel by Pressurized Tubes," *11th World Congress on Computational Mechanics*; Vol. 2014, 2014.

[117] Rozenberg, Y., *Modélisation analytique du bruit aérodynamique à large bande des machines tournantes : utilisation de calculs moyennés de mécanique des fluides*, Ph.D. thesis, École Centrale de Lyon, Lyon, France, 2007.

[118] Schade, H., and Kameier, F., *Strömungslehre,* 4th edn., de Gruyter, Berlin, 2013. doi: 10.1515/9783110292237

[119] Coello, C.A.C., Pulido, G. T., and Lechuga, M. S., "Handling multiple objectives with particle swarm optimization," *IEEE Transactions on Evolutionary Computation*; Vol. 8, No. 3, 2004, pp. 256–279. doi: 10.1109/TEVC.2004.826067.

[120] Biedermann, T. M., Czeckay, P., Geyer, T. F., Kameier, F., and Paschereit, C. O., "Effect of Inflow Conditions on the Noise Reduction Through Leading Edge Serrations," *AIAA Journal*; Vol. 2, 2019, pp. 1–6. doi: 10.2514/1.J057831.

[121] Biedermann, T.M., Czeckay, P., Geyer, T., Kameier, F., and Paschereit, C.O., "Noise Source Identification of Aerofoils Subjected to Leading Edge Serrations using Phased Array Beamforming," *24th AIAA/CEAS Aeroacoustics Conference*, 2018. doi: 10.2514/6.2018-3794.

[122] Sarradj, E., Fritzsche, C., Geyer, T., and Giesler, J., "Acoustic and aerodynamic design and characterization of a small-scale aeroacoustic wind tunnel," *Applied Acoustics*; Vol. 70, No. 8, 2009, pp. 1073–1080. doi: 10.1016/j.apacoust.2009.02.009.

[123] Sijtsma, P., "CLEAN Based on Spatial Source Coherence," *13th AIAA/CEAS Aeroacoustics Conference (28th AIAA Aeroacoustics Conference)*; AIAA 2007-3436, 2007. doi: 10.2514/6.2007-3436.

[124] Herold, G., and Sarradj, E., "Performance analysis of microphone array methods," *Journal of Sound and Vibration*; Vol. 401, 2017, pp. 152–168. doi: 10.1016/j.jsv.2017.04.030.

[125] Sarradj, E., Herold, G., Sijtsma, P., Merino Martinez, R., Geyer, T. F., Bahr, C. J., Porteous, R., Moreau, D., and Doolan, C. J., "A Microphone Array Method Benchmarking Exercise using Synthesized Input Data," *23rd AIAA/CEAS Aeroacoustics Conference*, 2017. doi: 10.2514/6.2017-3719.

[126] Bahr, C. J., Humphreys, W. M., Ernst, D., Ahlefeldt, T., Spehr, C., Pereira, A., Leclère, Q., Picard, C., Porteous, R., Moreau, D., Fischer, J. R., and Doolan, C. J., "A Comparison of Microphone Phased Array Methods Applied to the Study of Airframe Noise in Wind Tunnel Testing," *23rd AIAA/CEAS Aeroacoustics Conference*, 2017. doi: 10.2514/6.2017-3718.

[127] Hinze, J. O., *Turbulence,* 2nd edn., McGraw-Hill, New York, 1987. ISBN: 0070290377.

[128] Roach, P. E., "The generation of nearly isotropic turbulence by means of grids," *International Journal of Heat and Fluid Flow*; Vol. 8, No. 2, 1987, pp. 82–92. doi: 10.1016/0142-727X(87)90001-4.

[129] Schulz-Hausmann, F. K. v., "Wechselwirkung ebener Freistrahlen mit der Umgebung," *VDI Fortschrittsberichte Strömungstechnik 1985*, Vol. 7.

[130] Brooks, T. F., Pope, D. S., and Marcolini, M. A., "Airfoil Self-Noise and Prediction," NASA AMES Research Center, NASA Reference Publication 1218, 1989.

[131] Chong, T. P., Biedermann, T., Koster, O., and Hasheminejad, S. M., "On the Effect of Leading Edge Serrations on Aerofoil Noise Production," *24th AIAA/CEAS Aeroacoustics Conference*, 2018. doi: 10.2514/6.2018-3289.

[132] Neise, W., "Lärm und Lärmbekämpfung bei Ventilatoren - Eine Bestandsaufnahme," DFVLR Forschungsbericht 80-161980, Berlin, 1980.

[133] Wright, S. E., "The acoustic spectrum of axial flow machines," *Journal of Sound and Vibration*; Vol. 45, No. 2, 1976, pp. 165–223. doi: 10.1016/0022-460X(76)90596-4.

[134] Lowson, M.V., "Theoretical Studies of Compressor Noise," NASA Langley Research Center, NASA CR-1287, Washington D.C., 1969.

[135] Morfey, C. L., "Tone Radiation from an Isolated Subsonic Rotor," *The Journal of the Acoustical Society of America*; Vol. 49, 5B, 1971, pp. 1690–1692. doi: 10.1121/1.1912561.

[136] Goldstein, M. E., Rosenbaum, B. M., and Albers, L. U., "Sound Radiation from a High-Speed Axial-Flow Fan due to the Inlet Turbulence Quadrupole Interaction," NASA Langley Research Center, 1974.

[137] Kameier, F., *Experimentelle Untersuchung zur Entstehung und Minderung desBlattspitzen-Wirbellärms axialer Strömungsmaschinen*, Ph.D. thesis, TU Berlin, Berlin, 1993.

[138] Neifach, I., *Aeroakustische Optimierung einer druckseitig angeordneten Strebenkonfiguration bei axialen Niederdruckventilatoren in PKW-Kühlerlüftermodulen*, Master thesis, University of Applied Sciences Duesseldorf, Duesseldorf, 2017.

[139] Gutin, L., "On the Sound Field of a Rotating Propeller," Translation of ‚Über das Schallfeld einer rotierenden Luftschraube', Physikalische Zeitschrift der Sowietunion, 1936.

[140] Reese, H., *Anwendung von instationären numerischen Simulationsmethoden zur Berechnung aeroakustischer Schallquellen bei Axialventilatoren*, Fortschritt-Berichte VDI Reihe 7, Strömungstechnik, VDI-Verlag, Duesseldorf, 2007.

[141] Bommes, L., ed., *Ventilatoren,* 2nd edn., Vulkan-Verl., Essen, 2003. ISBN: 3802732006.

[142] Sharland, I. J., "Sources of noise in axial flow fans," *Journal of Sound and Vibration*; Vol. 1, No. 3, 1964, pp. 302–322. doi: 10.1016/0022-460X(64)90068-9.

[143] Kameier, F., and Neise, W., "Rotating Blade Flow Instability as a Source of Noise in Axial Turbomachines," *Journal of Sound and Vibration*; Vol. 203, No. 5, 1997, pp. 833–853. doi: 10.1006/jsvi.1997.0902.

[144] Na, G.-D., Kameier, F., Springer, N., Mauß, M., and Paschereit, C. O., "URANS Simulations and Experimental Investigations on Unsteady Aerodynamic Effects in the Blade Tip Region of a Shrouded Fan Configuration," *ASME. Turbo Expo: Volume 1: Aircraft Engine; Fans and Blowers; Marine; Honors and Awards* ():V001T09A003*,* ASME, 2017. doi: 10.1115/GT2017-63680.

[145] Reese, H., Carolus, T., and Kato, C., "Numerical Prediction of the Aeroacoustic Sound Sources in a Low Pressure Axial Fan with Inflow Distortion," *Fan Noise 2007*, 2007.

[146] Amiet, R. K., "Noise Produced by Turbulent Flow into a Propeller or Helicopter Rotor," *AIAA Journal*; Vol. 15, No. 3, 1977, pp. 307–308. doi: 10.2514/3.63237.

[147] Schneider, M., *Der Einfluss der Zuströmbedingungen auf das breitbandige Geräusch eines Axialventilators*, Siegen, Ph.D. thesis, University of Siegen, Siegen, 2005.

[148] Carolus, T., and Stremel, M., "Blade Surface Pressure Fluctuations and Acoustic Radiation from an Axial Fan Rotor Due to Turbulent Inflow," *Acta Acustica united with Acustica*, Vol. 88, pp. 472–482, https://www.ingentaconnect.com/contentone/dav/aaua/2002/00000088/00000004/art00002 [retrieved 2019].

[149] Daroukh, M., Moreau, S., Gourdain, N., Boussuge, J., and Sensiau, C., "Influence of Distortion on Fan Tonal Noise," *22nd AIAA/CEAS Aeroacoustics Conference*, 2016. doi: 10.2514/6.2016-2818.

[150] Zenger, F., Herold, G., and Becker, S., "Acoustic Characterization of Forward- and Backward-Skewed Axial Fans under Increased Inflow Turbulence," *22nd AIAA/CEAS Aeroacoustics Conference*, 2016. doi: 10.2514/6.2016-2943.

[151] Biedermann, T. M., Kameier, F., and Paschereit, C. O., "Successive Aeroacoustic Transfer of Leading Edge Serrations from Single Airfoil to Low-Pressure Fan Application," *ASME Journal of Engineering for Gas Turbines and Power*; Vol. 2019, 2019. doi: 10.1115/1.4044362.

[152] Asghar, A., Perez, R. E., and Allan, W. D.E., "Application of Leading Edge Tubercles to Enhance Propeller Performance," *24th AIAA/CEAS Aeroacoustics Conference*, 2018. doi: 10.2514/6.2018-3647.

[153] Ibrahim, I. H., and New, T. H., "A Numerical Study on the Effect of Leading-Edge Modifications Upon Propeller Flow Characteristics," *International Symposium On Turbulence and Shear Flow Phenomena*, 2015.

[154] Corsini, A., Delibra, G., and Sheard, A. G., "The application of sinusoidal blade-leading edges in a fan-design methodology to improve stall resistance," *Proceedings of the Institution of Mechanical Engineers, Part A: Journal of Power and Energy*; Vol. 228, No. 3, 2013, pp. 255–271. doi: 10.1177/0957650913514229.

[155] Lieblein, S., Schwenk, F. C., and Broderick, R. L., "Diffusion Factor for Estimating Losses and Limiting Blade Loadings in Axial-Flow-Compressor Blade Elements," NACA National Advisory Committee for for Aeronautics, 1953.

[156] Corsini, A., Delibra, G., and Sheard, A. G., "On the Role of Leading-Edge Bumps in the Control of Stall Onset in Axial Fan Blades," *Journal of Fluids Engineering*; Vol. 135, No. 8, 2013. doi: 10.1115/1.4024115.

[157] Arndt, R. E. A., and Nagel, R. T., "Effect of leading edge serrations on noise radiation from a model rotor," *AIAA 5th Fluid and Plasma Dynamics Conference*; Vol. 1972, 1972. doi: 10.2514/6.1972-655. Withdrawn.

[158] Corsini, A., Delibra, G., Rispoli, F., and Sheard, A. G., "Aeroacoustic Assessment of Leading Edge Bumps in Industrial Fans," *Fan 2015*, 2015.

[159] Zenger, F., Müller, J., and Becker, S., "Investigation of Aeroacoustic Properties of Low-Pressure Axial Fans with Different Blade Stacking," *23rd AIAA/CEAS Aeroacoustics Conference*, 2017. doi: 10.2514/6.2017-3389.

[160] ISO, "Industrial fans – Performance testing using standardized airways (ISO 5801:2007)," 2008.

[161] Krömer, F., and Becker, S., "Experimental investigation of the sound reduction by leading edge serrations on a at-plate axial fan," *24th AIAA/CEAS Aeroacoustics Conference*, 2018. doi: 10.2514/6.2018-2955.

[162] Devenport, W. J., Staubs, J. K., and Glegg, S. A. L., "Sound radiation from real airfoils in turbulence," *Journal of Sound and Vibration*; Vol. 329, No. 17, 2010, pp. 3470–3483. doi: 10.1016/j.jsv.2010.02.022.

[163] ISO, "Acoustics – Determination of sound power radiated into a duct by fans and other air-moving devices – In-duct method (ISO 5136:2003)," 2009.

[164] Biedermann, T., Kameier, F., and Paschereit, O., "Optimised Test Rig for Measurement of Aerodynamic and Aeroacoustic Performance of Leading Edge Serrations in Low-Speed Fan Application," *Proceedings of ASME Turbo Expo 2018*, 2018. doi: 10.1115/GT2018-75369.

[165] Shin, H.-C., Graham, W., Sijtsma, P., Andreou, C., and Faszer, A. C., "Implementation of a Phased Microphone Array in a Closed-Section Wind Tunnel," *AIAA Journal*; Vol. 45, No. 12, 2007, pp. 2897–2909. doi: 10.2514/1.30378.

[166] Allen, C. S., Blake, W. K., Dougherty, R. P., Lynch, D., Soderman, P. T., Underbrink, J. R., and Mueller, T. J., eds., *Aeroacoustic Measurements*, Springer Verlag, Berlin, 2002. doi: 10.1007/978-3-662-05058-3.

[167] Biedermann, T.M., Chong, T.P., Kameier, F., and Paschereit, C.O., "On the Transfer of Leading Edge Serrations from Isolated Aerofoil to Ducted Low-Pressure Fan Application," *24th AIAA/CEAS Aeroacoustics Conference*, 2018. doi: 10.2514/6.2018-2956.

[168] Möser, M., *Messtechnik der Akustik*, Springer Verlag, Berlin, 2010. doi: 10.1007/978-3-540-68087-1.

[169] Wojno, J. P., Mueller, T. J., and Blake, W. K., "Turbulence Ingestion Noise, Part 2: Rotor Aeroacoustic Response to Grid-Generated Turbulence," *AIAA Journal*; Vol. 40, No. 1, 2002, pp. 26–32. doi: 10.2514/2.1637.

[170] Kameier, F., *Computer-Based Measurement Technologies. Data Acquisition and Data Processing*, lecture notes, University of Applied Sciences Duesseldorf, Duesseldorf, 2017.

[171] Krömer, F. J., *Sound emission of low-pressure axial fans under distorted inflow conditions*, Ph.D. thesis, Friedrich-Alexander-University Erlangen-Nuremberg, FAU University Press, Erlangen, Germany, 2018. doi: 10.25593/978-3-96147-089-1.

[172] Adam, M., *Statistische Versuchsplanung und Auswertung (DoE Design of Experiments)*, lecture notes, University of Applied Sciences Duesseldorf, Dusseldorf, 2012.

[173] Box, G. E. P., and Behnken, D. W., "Some New Three Level Designs for the Study of Quantitative Variables," *Technometrics*; Vol. 2, No. 4, 1960, p. 455. doi: 10.2307/1266454.

[174] Alam, F. M., McNaught, K. R., and Ringrose, T. J., "A comparison of experimental designs in the development of a neural network simulation metamodel," *Simulation Modelling Practice and Theory*; Vol. 12, 7-8, 2004, pp. 559–578. doi: 10.1016/j.simpat.2003.10.006.

[175] Mckay, M. D., Beckman, R. J., and Conover, W. J., "A Comparison of Three Methods for Selecting Values of Input Variables in the Analysis of Output from a Computer Code," *Technometrics*; Vol. 42, No. 1, 2000, p. 55. doi: 10.2307/1271432.

[176] Reich, M., Adam, M., and Lambach, S., "Comparison of different Methods for Approximating Models of Energy Supply Systems and Polyoptimising the Systems-Structure and Components-Dimension," *ECOS 2017 - The 30th International Conference on Efficiency, Cost, Optimization and Environmental Impact of Energy Systems*, 2017.

[177] Joseph, V. R., and Hung, Y., "Orthogonal-MaxiMin Latin Hypercube Designs," *Statistica Sinica* [online], Vol. 2008, Vol. 18, no. 1, 2008, pp. 171–186, www.jstor.org/stable/24308251, [retrieved 2019].

[178] Chongjie Zhang, Julie A. Shah, "Definitions of Fairness in Decision-Making under Uncertainty," *Proceedings of the Twenty-Ninth AAAI Conference on Artificial Intelligence* [online], 2015, https://aaai.org/ocs/index.php/AAAI/AAAI15/paper/view/9943/9806, [retrieved 2019].

[179] Viana, F. A. C., "Things you wanted to know about the Latin hypercube design and were afraid to ask," *10th World Congress on Structural and Multidisciplinary Optimization*, 2013.

[180] Samarasinghe, S., *Neural networks for applied sciences and engineering. From fundamentals to complex pattern recognition*, Auerbach Verlag, Boca Raton, 2007. doi: 9780849333750.

[181] Dan Foresee, F., and Hagan, M. T., "Gauss-Newton approximation to Bayesian learning," *Proceedings of International Conference on Neural Networks (ICNN'97),* IEEE, 1997, pp. 1930–1935. doi: 10.1109/ICNN.1997.614194.

[182] Hagan, M. T., and Menhaj, M. B., "Training feedforward networks with the Marquardt algorithm," *IEEE transactions on neural networks*; Vol. 5, No. 6, 1994, pp. 989–993.
doi: 10.1109/72.329697.

[183] Hecht-Nielsen, R., "Kolmogorov's Mapping Neural Network Existence Theorem," *IEEE First Annual International Conference on Neural Networks, No.* 3, 1987, pp. 11–13.

[184] Allen, H. J., and Vincenti, W. G., "Wall Interference in a Two-Dimensional-Flow Wind Tunnel, with Consideration of the Effect of Compressibility," *National Advisory Committee for Aeronautics Collection*, Report No. 782, pp. 155–183, 1944.

IV. Appendices

Appendix A Aerodynamics: Single Aerofoil

A.1 Data Correction for Experimental Force Measurements

Three force components were measured, namely the lift forces at the aft F_A and the fore F_F load cell as well as a drag force F_D^*, still to be corrected since being contaminated by parasitic and lift-induced drag. The resulting lift and drag forces are obtained via *Eq. A.1-1*, where a_0, b_0 and c_0 are the zero readings of the load cells when no flow is present. The accuracy of the readings is found to be ± 0.05 N.

$$F_L = (F_A - a_0) + (F_F - b_0) \qquad \textit{Eq. A.1-1}$$

$$F_D = (F_D^* - c_0) \qquad \textit{Eq. A.1-2}$$

Prior measurements, zero reading adjustments of the balance were performed followed by a calibration, using dead weights to provide information on lift and drag forces of known dimension. The calibration was repeated for three times to account for possible uncertainties, where the resulting calibration curve turned out to show an excellent agreement for a linear dependency of resulting forces and applied load (coefficient of determination $R^2 = 1$).

However, these quantities do not take into account effects of blocking through the wind tunnel walls nor of the wake blockage, estimating the effect of the induced pressure gradient in vicinity of the aerofoils wake on the lift and drag forces. In summary, the presence of the side walls as well as floor and ceiling of the wind tunnel would result in higher lift and drag compared to an aerofoil in an unbounded stream. According to Barlow et al. [56], the corrected coefficients of lift and drag are defined as per *Eq. A.1-3* and *Eq. A.1-4*.

$$C_D = C_{D,u} \cdot (1 - 3\varepsilon_{sb} - 2\varepsilon_{wb}) \qquad \textit{Eq. A.1-3}$$

$$C_L = C_{L,u} \cdot [1 - \sigma - 2(\varepsilon_{sb} + \varepsilon_{wb})\,] \qquad \textit{Eq. A.1-4}$$

$$\sigma = \pi^2/48 \cdot (C/H)^2 \qquad \textit{Eq. A.1-5}$$

The factor σ describes the aerofoil size relative to the wind tunnel [184]. The solid-blockage correction ε_{sb} is necessary to compensate for the tunnel walls and is estimated according to Barlow et al. [56] in *Eq. A.1-6,* where t is the maximum aerofoil thickness, H the wind tunnel test section height and λ_2 the body shape factor. This shape factor is a function of the aerofoil thickness ratio t/C and is determined with $\Lambda_{TR} = 0.165$ being an empirical value for the NACA65 series.

$$\varepsilon_{sb} = \frac{\pi^2}{3} \cdot \frac{\lambda_2}{4} \cdot \frac{t^2}{H^2} \; with \; \lambda_2 = \frac{\Lambda_{TR} \cdot C^2}{4 \cdot t^2} \qquad \textit{Eq. A.1-6}$$

The wake of an aerofoil in a closed test section is attenuated relative to the mean flow velocity and, since continuity laws are valid, on the other hand, the fluid further away from the wake is accelerated. This leads to a pressure gradient normal to the flow, resulting in a velocity increment at the model that needs to be compensated for, leading to the wake-blockage ε_{wb} correction in *Eq. A.1-7*. The effect of the wake blockage is particularly true when experiencing stall effects, hence showing large-scale separated flow.

$$\varepsilon_{wb} = C_{D,u} \cdot \frac{C}{2H} \qquad \textit{Eq. A.1-7}$$

A.2 Uncertainty Analysis of BSLN Aerofoil Data

An uncertainty analysis is carried out exemplarily for the BSLN case at $U_0 = 15$ ms^{-1}. It is based on the Student's distribution and a confidence interval of 95 %. Additional reference data by Bogdonoff et al. [57] at $U_0 = 67$ ms^{-1}, Re $\approx 5 \cdot 10^5$.

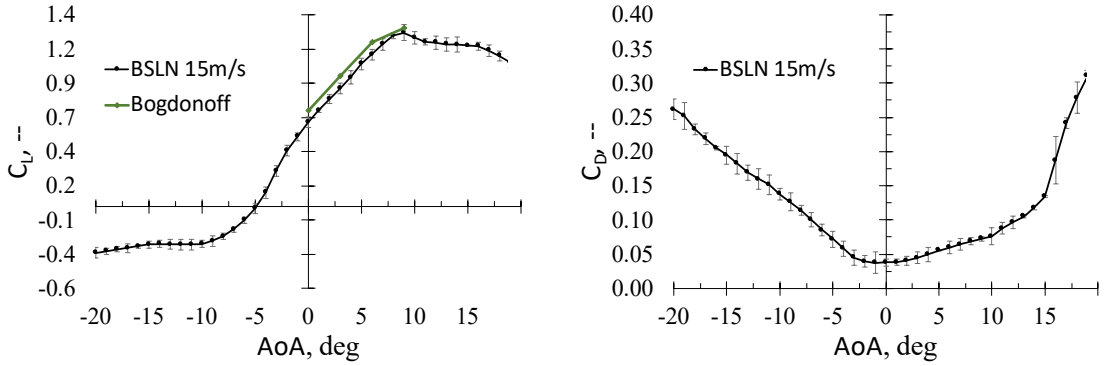

Figure 0-1 Overall aerodynamic performance by means of coefficient of lift (left) and drag (right). Indicated error bars based on uncertainty analysis and additional plot of reference pre-stall data by Bogdonoff et al. [57]. $U_0 = 15$ ms^{-1}.

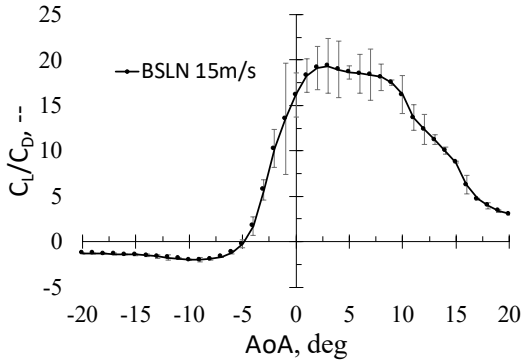

Figure 0-2 Overall aerodynamic lift-to-drag performance of BSLN aerofoil at $U_0 = 15$ ms^{-1}, including error bars.

A.3 Supplementary Aerodynamic Force Measurements at $U_0 = 25$ ms^{-1}

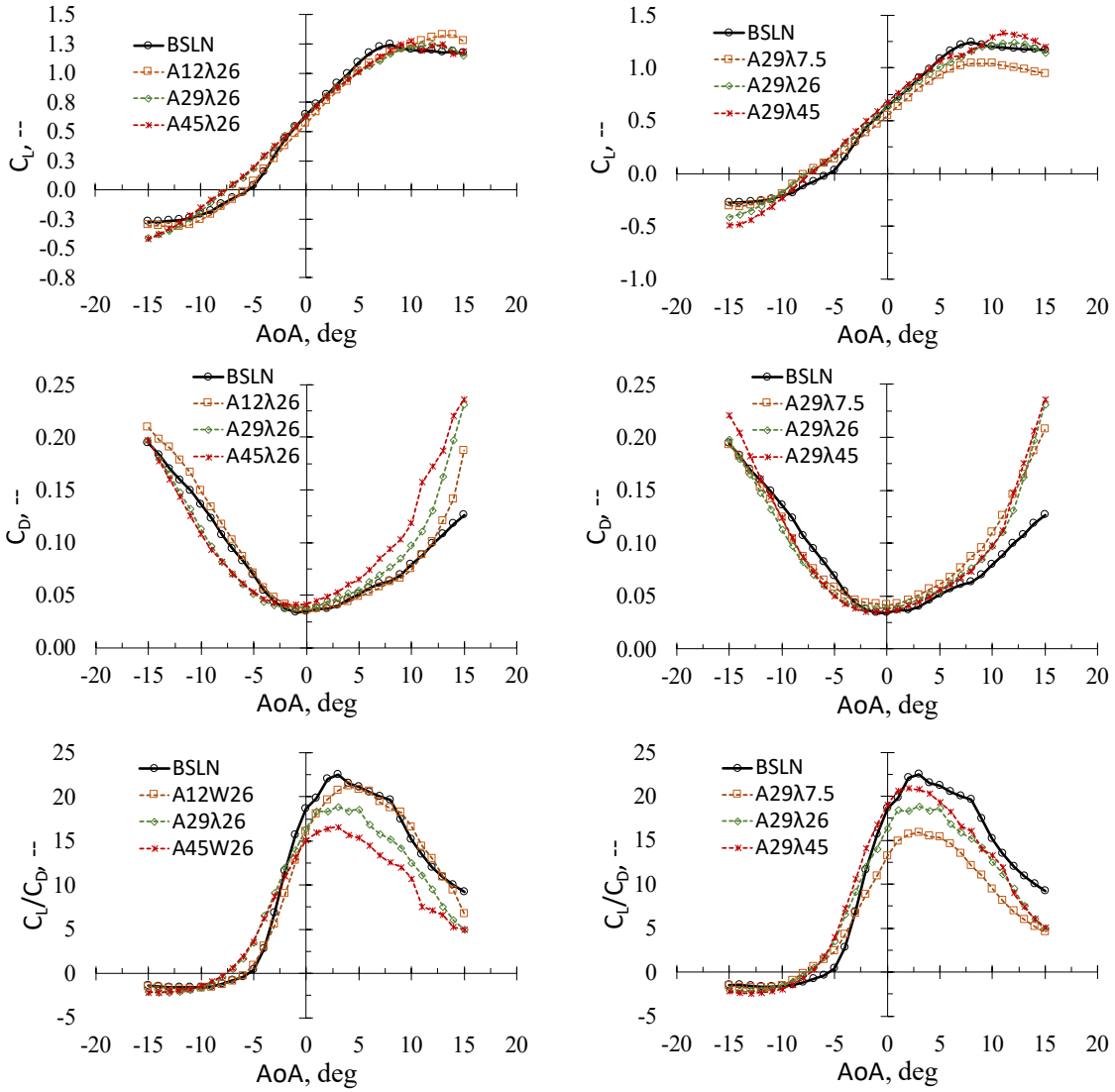

Figure 0-3 Experimental results of all tested serration configurations at $U_0 = 25$ ms^{-1} for varying serration amplitude (left) and serration wavelength (right). Coefficients of lift (top), drag (centre) and lift-to-drag (bottom).

Table A-1 Summary of lift and drag performance for 10 tested aerofoils subjected to leading edge serrations at $U_0 = 25$ ms^{-1} and -20 deg ≤ AoA ≤ +20 deg.

ID	A [mm]	λ [mm]	$C_{L\,zero\,AoA}$ [-]	$AoA_{zero\,CL}$ [deg]	$C_{L\,max}$ [-]	AoA_{cri} [ft]	$(C_L/C_D)_{max}$ [-]	A_{WS} [m²]
A12λ26	12	26	0.57	-5.7	1.32	14.0	21.26	0.0702
A22λ18	22	18	0.60	-7.0	1.23	11.0	19.31	0.0668
A22λ34	22	34	0.58	-6.2	1.30	14.0	20.55	0.0668
A29λ26	29	26	0.63	-7.5	1.24	12.0	18.85	0.0645
A29λ45	29	45	0.68	-7.3	1.33	11.0	20.87	0.0645
A29λ7.5	29	7.5	0.55	-7.7	1.04	8.0	15.88	0.0645
A35λ18	35	18	0.67	-8.3	1.29	11.0	17.26	0.0624
A35λ34	35	34	0.64	-7.7	1.31	12.0	18.01	0.0624
A4λ26	45	26	0.63	-7.6	1.27	10.0	16.56	0.0591
BSLN	**-**	**-**	**0.64**	**-5.5**	**1.24**	**8.0**	**22.51**	**0.0743**

Appendix B Aerodynamics: Numerical Investigations

B.1 Single Wavelength Results vs. Double Wavelength Results

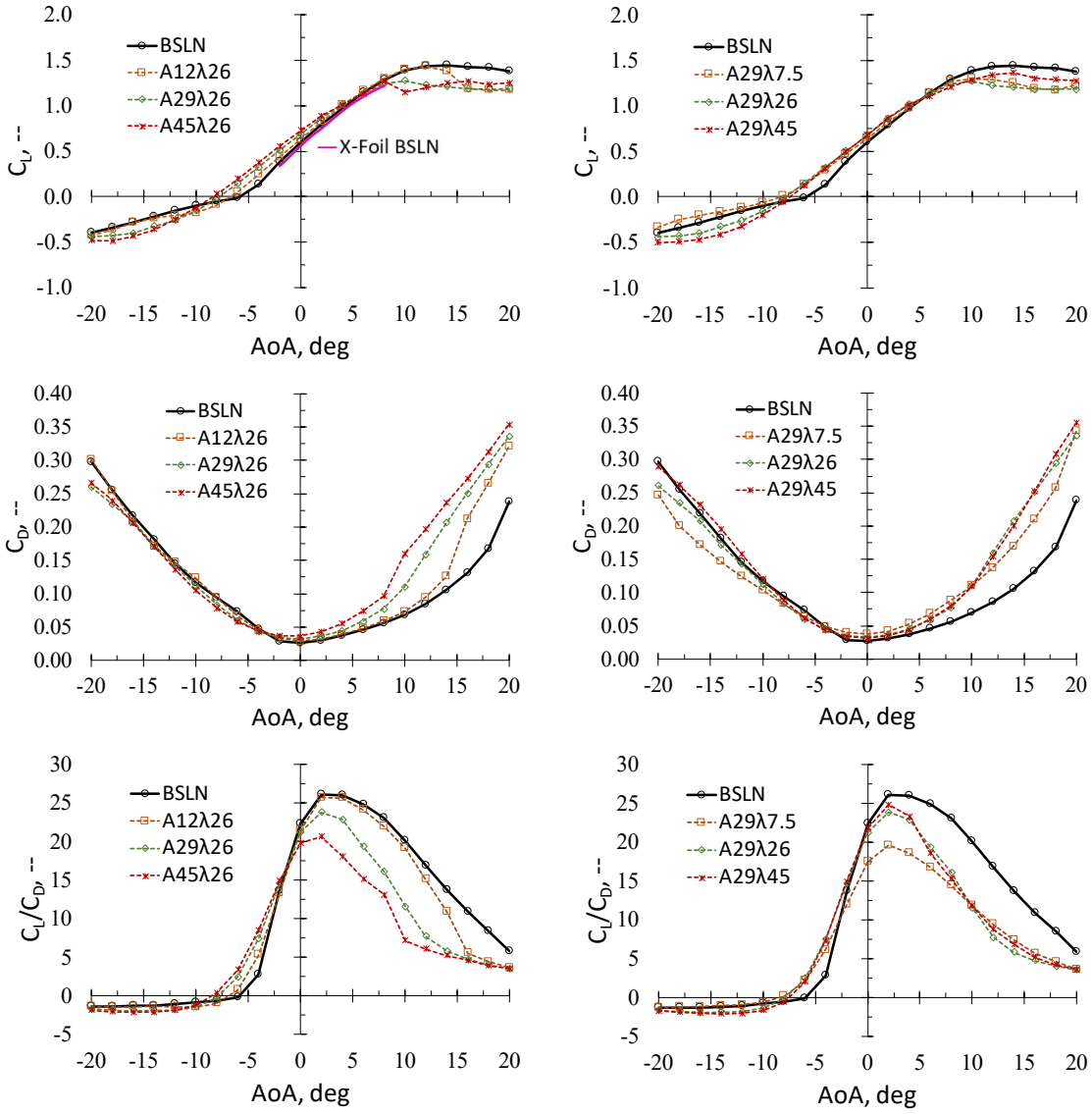

Figure B-1 Numerical trends of aerodynamic performance for all simulated serration configurations at $U_0 = 15\ ms^{-1}$ for varying serration amplitude (left) and serration wavelength (right). Spanwise extension of numerical domain by one serration wavelength λ. Coefficients of lift (top), drag (centre) and lift-to-drag (bottom).

B.2 Direct Comparison of Experimental/ Numerical Results

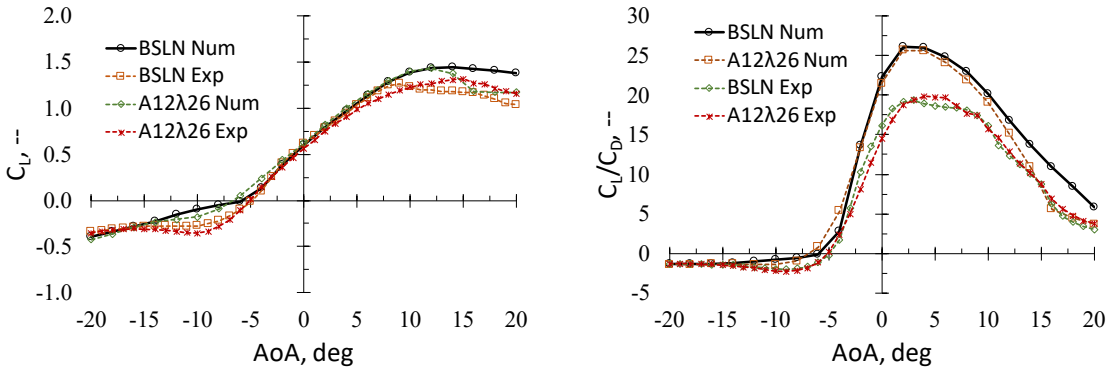

Figure B-2 Coefficients of lift (left) and lift-to-drag ratio (right). Direct comparison of aerodynamic forces based on experimental and numerical results. Extension of computational domain = 2λ.

B.3 Skin Friction Coefficients

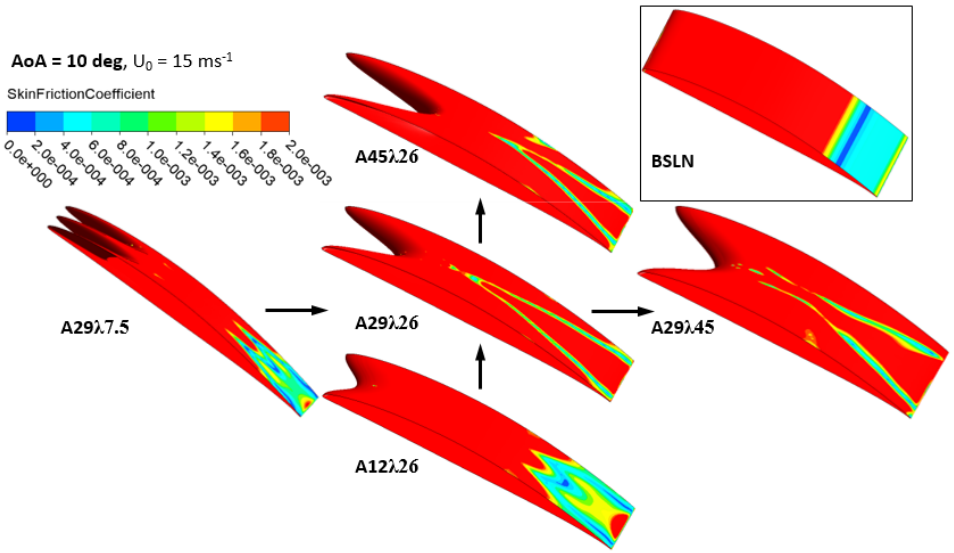

Figure B-3 Skin friction coefficient for monitoring separation over the aerofoil contour. U_0 = 15 ms^{-1}, AoA = 10 deg.

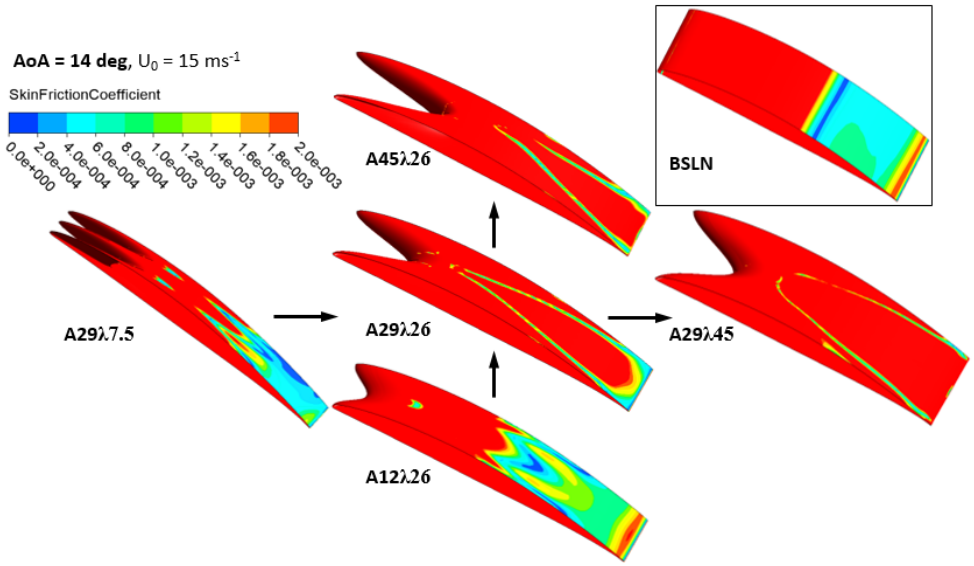

Figure 0-4 Skin friction coefficient for monitoring separation over the aerofoil contour. U_0 = 15 ms^{-1}, AoA = 14 deg.

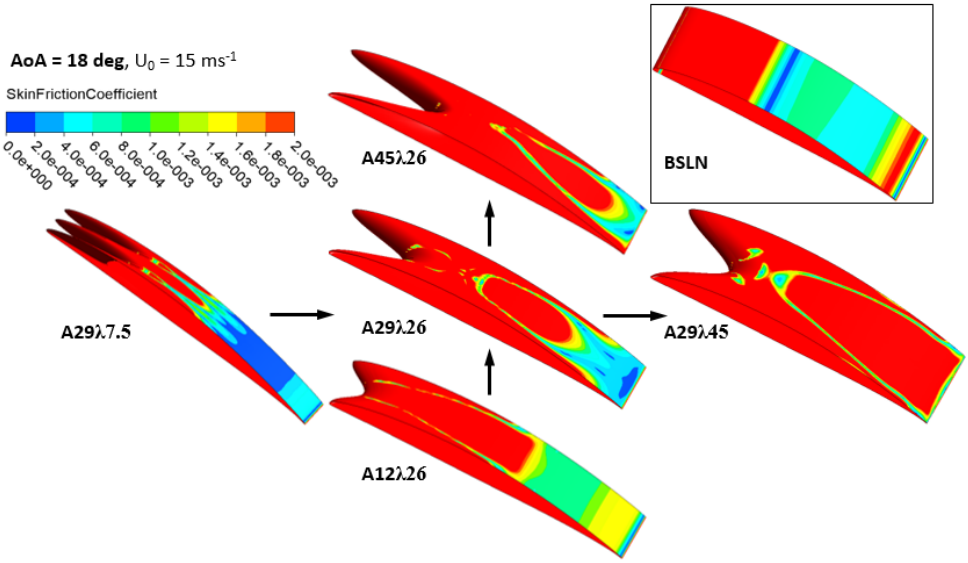

Figure 0-5 Skin friction coefficient for monitoring separation over the aerofoil contour. U_0 = 15 ms^{-1}, AoA = 18 deg.

Appendix C Aerofoil-Turbulence-Interaction Noise

C.1 Test Matrix DoE

Table C-1 Non-dimensional DoE test matrix.

Run	Re	Tu	A/C	λ/C	AoA
1	-1,000	-1,000	-1,000	-1,000	-1,000
2	-1,000	-1,000	-1,000	-1,000	1,000
3	-1,000	-1,000	-1,000	1,000	-1,000
4	-1,000	-1,000	-1,000	1,000	1,000
5	-1,000	-1,000	1,000	-1,000	-1,000
6	-1,000	-1,000	1,000	-1,000	1,000
7	-1,000	-1,000	1,000	1,000	-1,000
8	-1,000	-1,000	1,000	1,000	1,000
9	-1,000	1,000	-1,000	-1,000	-1,000
10	-1,000	1,000	-1,000	-1,000	1,000
11	-1,000	1,000	-1,000	1,000	-1,000
12	-1,000	1,000	-1,000	1,000	1,000
13	-1,000	1,000	1,000	-1,000	-1,000
14	-1,000	1,000	1,000	-1,000	1,000
15	-1,000	1,000	1,000	1,000	-1,000
16	-1,000	1,000	1,000	1,000	1,000
17	1,000	-1,000	-1,000	-1,000	-1,000
18	1,000	-1,000	-1,000	-1,000	1,000
19	1,000	-1,000	-1,000	1,000	-1,000
20	1,000	-1,000	-1,000	1,000	1,000
21	1,000	-1,000	1,000	-1,000	-1,000
22	1,000	-1,000	1,000	-1,000	1,000
23	1,000	-1,000	1,000	1,000	-1,000
24	1,000	-1,000	1,000	1,000	1,000
25	1,000	1,000	-1,000	-1,000	-1,000
26	1,000	1,000	-1,000	-1,000	1,000
27	1,000	1,000	-1,000	1,000	-1,000
28	1,000	1,000	-1,000	1,000	1,000
29	1,000	1,000	1,000	-1,000	-1,000
30	1,000	1,000	1,000	-1,000	1,000
31	1,000	1,000	1,000	1,000	-1,000
32	1,000	1,000	1,000	1,000	1,000
33	-2,378	0,000	0,000	0,000	0,000
34	2,378	0,000	0,000	0,000	0,000
35	0,000	-2,378	0,000	0,000	0,000
36	0,000	2,378	0,000	0,000	0,000
37	0,000	0,000	-2,378	0,000	0,000
38	0,000	0,000	2,378	0,000	0,000
39	0,000	0,000	0,000	-2,378	0,000
40	0,000	0,000	0,000	2,378	0,000
41	0,000	0,000	0,000	0,000	-2,378
42	0,000	0,000	0,000	0,000	2,378
43 (C)	0,000	0,000	0,000	0,000	0,000
44 (C)	0,000	0,000	0,000	0,000	0,000
45 (C)	0,000	0,000	0,000	0,000	0,000
46 (C)	0,000	0,000	0,000	0,000	0,000
47 (C)	0,000	0,000	0,000	0,000	0,000
48 (C)	0,000	0,000	0,000	0,000	0,000
49 (C)	0,000	0,000	0,000	0,000	0,000
50 (C)	0,000	0,000	0,000	0,000	0,000
51 (C)	0,000	0,000	0,000	0,000	0,000
52 (C)	0,000	0,000	0,000	0,000	0,000
53 (C)	0,000	0,000	0,000	0,000	0,000
54 (C)	0,000	0,000	0,000	0,000	0,000
55 (C)	0,000	0,000	0,000	0,000	0,000
56 (C)	0,000	0,000	0,000	0,000	0,000
57 (C)	0,000	0,000	0,000	0,000	0,000
58 (C)	0,000	0,000	0,000	0,000	0,000
59 (C)	0,000	0,000	0,000	0,000	0,000

Table C-2 DoE test matrix with absolute dimensions of the influencing parameters.

Run	Re	Tu	A/C	λ/C	AoA
1	351422	3,07	0,144	0,122	-1,7
2	351422	3,07	0,144	0,122	1,7
3	351422	3,07	0,144	0,228	-1,7
4	351422	3,07	0,144	0,228	1,7
5	351422	3,07	0,236	0,122	-1,7
6	351422	3,07	0,236	0,122	1,7
7	351422	3,07	0,236	0,228	-1,7
8	351422	3,07	0,236	0,228	1,7
9	351422	4,51	0,144	0,122	-1,7
10	351422	4,51	0,144	0,122	1,7
11	351422	4,51	0,144	0,228	-1,7
12	351422	4,51	0,144	0,228	1,7
13	351422	4,51	0,236	0,122	-1,7
14	351422	4,51	0,236	0,122	1,7
15	351422	4,51	0,236	0,228	-1,7
16	351422	4,51	0,236	0,228	1,7
17	498578	3,07	0,144	0,122	-1,7
18	498578	3,07	0,144	0,122	1,7
19	498578	3,07	0,144	0,228	-1,7
20	498578	3,07	0,144	0,228	1,7
21	498578	3,07	0,236	0,122	-1,7
22	498578	3,07	0,236	0,122	1,7
23	498578	3,07	0,236	0,228	-1,7
24	498578	3,07	0,236	0,228	1,7
25	498578	4,51	0,144	0,122	-1,7
26	498578	4,51	0,144	0,122	1,7
27	498578	4,51	0,144	0,228	-1,7
28	498578	4,51	0,144	0,228	1,7
29	498578	4,51	0,236	0,122	-1,7
30	498578	4,51	0,236	0,122	1,7
31	498578	4,51	0,236	0,228	-1,7
32	498578	4,51	0,236	0,228	1,7
33	250001	3,79	0,190	0,175	0,0
34	599999	3,79	0,190	0,175	0,0
35	425000	2,08	0,190	0,175	0,0
36	425000	5,50	0,190	0,175	0,0
37	425000	3,79	0,081	0,175	0,0
38	425000	3,79	0,299	0,175	0,0
39	425000	3,79	0,190	0,049	0,0
40	425000	3,79	0,190	0,301	0,0
41	425000	3,79	0,190	0,175	-4,0
42	425000	3,79	0,190	0,175	4,0
43 (C)	425000	3,79	0,190	0,175	0,0
44 (C)	425000	3,79	0,190	0,175	0,0
45 (C)	425000	3,79	0,190	0,175	0,0
46 (C)	425000	3,79	0,190	0,175	0,0
47 (C)	425000	3,79	0,190	0,175	0,0
48 (C)	425000	3,79	0,190	0,175	0,0
49 (C)	425000	3,79	0,190	0,175	0,0
50 (C)	425000	3,79	0,190	0,175	0,0
51 (C)	425000	3,79	0,190	0,175	0,0
52 (C)	425000	3,79	0,190	0,175	0,0
53 (C)	425000	3,79	0,190	0,175	0,0
54 (C)	425000	3,79	0,190	0,175	0,0
55 (C)	425000	3,79	0,190	0,175	0,0
56 (C)	425000	3,79	0,190	0,175	0,0
57 (C)	425000	3,79	0,190	0,175	0,0
58 (C)	425000	3,79	0,190	0,175	0,0
59 (C)	425000	3,79	0,190	0,175	0,0

C.2 Aeroacoustics - Surface Regression Functions (DoE Analysis)

Table C-3 Model coefficients for the individual aeroacoustic influencing parameters (IP) to predict the acoustic target values.

IP	$OASPL_{Serr}$, dB	$OASPL_{BSLN}$, dB	ΔOASPL, dB
Prefactor	80.5686041	84.3925890	3.9206740
Re	4.8407794	4.4867297	-0.3540497
Re^2	-0.5040150	-0.5680398	-0.0636089
Tu	1.8918868	2.0869653	0.1950785
Tu^2	-0.7632403	-0.6640181	0.0996380
A/C	-0.9494303	0.0000000	0.9249610
$(A/C)^2$	0.0687524	0.0000000	-0.1383372
λ/C	0.2442662	0.0000000	-0.2669226
$(λ/C)^2$	0.0991875	0.0000000	-0.1625558
AoA	-0.3328381	-17.5763860	0.1570742
AoA^2	-0.0164398	-0.1502285	-0.1333728
Re·Tu	0.0090862	0.0334969	0.0244107
Re·(A/C)	0.0787650	0.0000000	-0.0634829
Re·(λ/C)	-0.0866182	0.0000000	0.0666362
Re·AoA	0.0625244	-0.0323810	-0.0949054
Tu·(A/C)	-0.0776263	0.0000000	0.0646254
Tu·(λ/C)	-0.1628793	0.0000000	0.1467954
Tu·AoA	0.0822120	0.1193257	0.0371137
(A/C) ·(λ/C)	0.0558373	0.0000000	-0.0614529
(A/C) ·AoA	0.0173559	0.0000000	-0.0409523
(λ/C)·AoA	-0.1409842	0.0000000	0.1294765

C.3 Aerodynamics - Surface Regression Functions (DoE Analysis)

Table C-4 Model coefficients for the individual aerodynamic influencing parameters (IP) to predict the coefficients of lift.

IP	$C_{L\ Serr}$, --	$C_{L\ BSLN}$, --	ΔC_L, --
Prefactor	0.6413642	0.6308728	-0.0123273
Re	0.0000000	0.0000000	0.0000000
Re^2	-0.0008443	0.0012701	0.0021065
Tu	0.0000000	0.0000000	0.0000000
Tu^2	-0.0008443	0.0012701	0.0021065
A/C	0.0283686	0.0000000	-0.0283686
$(A/C)^2$	-0.0070809	0.0000000	0.0083432
λ/C	0.0008236	0.0000000	-0.0008236
$(λ/C)^2$	-0.0043969	0.0000000	0.0056591
AoA	0.1428302	0.1645440	0.0217139
AoA^2	-0.0034859	-0.0105739	-0.0070959
Re·Tu	0.0000000	0.0000000	0.0000000
Re·(A/C)	0.0000000	0.0000000	0.0000000
Re·(λ/C)	0.0000000	0.0000000	0.0000000
Re·AoA	0.0000000	0.0000000	0.0000000
Tu·(A/C)	0.0000000	0.0000000	0.0000000
Tu·(λ/C)	0.0000000	0.0000000	0.0000000
Tu·AoA	0.0000000	0.0000000	0.0000000
(A/C) ·(λ/C)	-0.0079171	0.0000000	0.0079171
(A/C) ·AoA	-0.0052574	0.0000000	0.0052574
(λ/C)·AoA	-0.0013690	0.0000000	0.0013690

Table C-5 Model coefficients for the individual influencing parameters (IP) to predict the coefficients of drag.

IP	$C_{D\ Serr}$, --	$C_{D\ BSLN}$, --	ΔC_D, --
Prefactor	0.0396757	0.0330924	-0.0068547
Re	0.0000000	0.0000000	0.0000000
Re^2	-0.0001510	0.0001877	0.0003375
Tu	0.0000000	0.0000000	0.0000000
Tu^2	-0.0001510	0.0001877	0.0003375
A/C	0.0016899	0.0000000	-0.0016899
$(A/C)^2$	-0.0001814	0.0000000	0.0003680
λ/C	-0.0010597	0.0000000	0.0010597
$(λ/C)^2$	-0.0001444	0.0000000	0.0003309
AoA	0.0018574	-0.0002981	-0.0021554
AoA^2	0.0014770	0.0029958	0.0015176
Re·Tu	0.0000000	0.0000000	0.0000000
Re·(A/C)	0.0000000	0.0000000	0.0000000
Re·(λ/C)	0.0000000	0.0000000	0.0000000
Re·AoA	0.0000000	0.0000000	0.0000000
Tu·(A/C)	0.0000000	0.0000000	0.0000000
Tu·(λ/C)	0.0000000	0.0000000	0.0000000
Tu·AoA	0.0000000	0.0000000	0.0000000
(A/C) ·(λ/C)	-0.0006585	0.0000000	0.0006585
(A/C) ·AoA	0.0012456	0.0000000	-0.0012456
(λ/C)·AoA	-0.0003554	0.0000000	0.0003554

Appendix D Transfer Analysis – From Aerofoil to Rotor

D.1 Phase Spectrum of Employed Sound Intensity Capsules

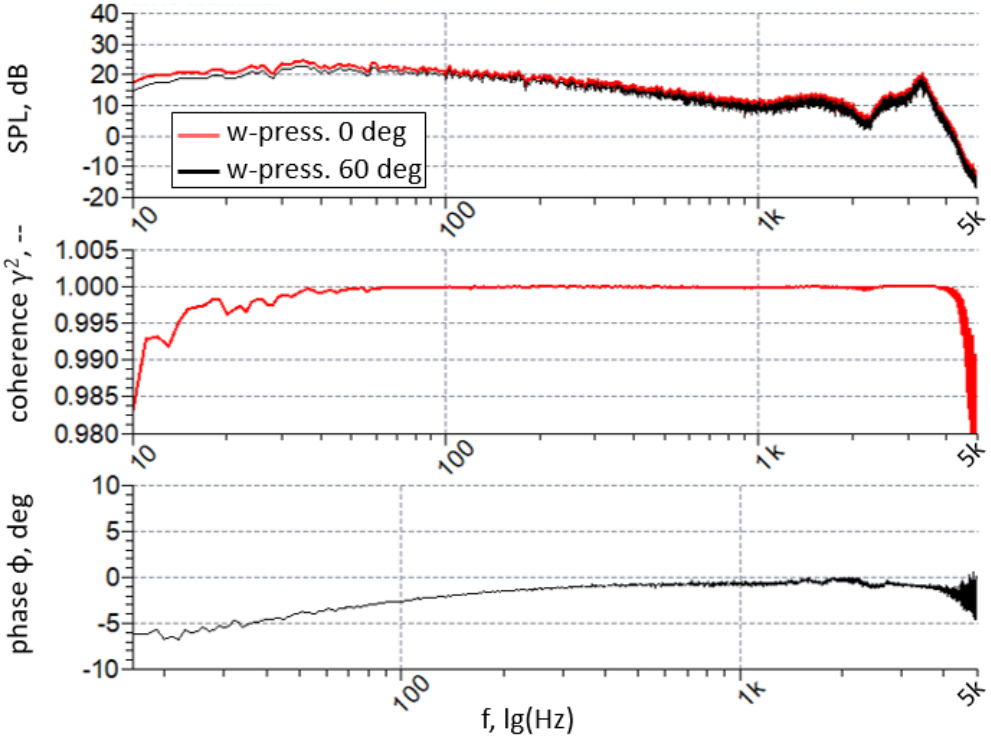

Figure D-1 Contrasting juxtaposition of signals from the sound intensity probe-capsules, used for analysis of the wall-pressure fluctuations. Spectra for the sound pressure level (top), the resulting coherence (centre) and the phase difference between the two probes (bottom).

D.2 Inflow Patterns with Different Turbulence Grids

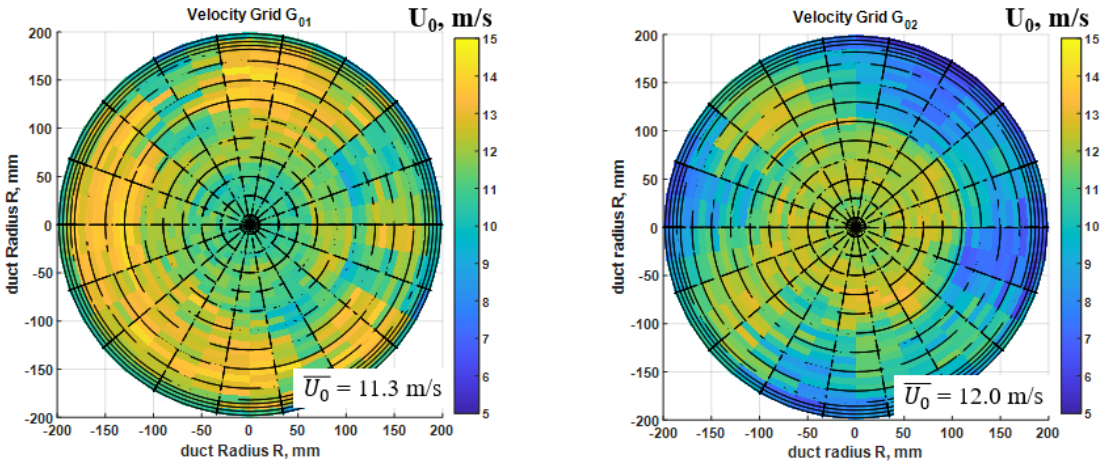

Figure D-2 Local distribution of longitudinal velocity for grid G_{01} (left) and G_{02} (right) at $n = 2000\ min^{-1}$, distance grid-to-probe $\Delta x = 0.3\ m$.

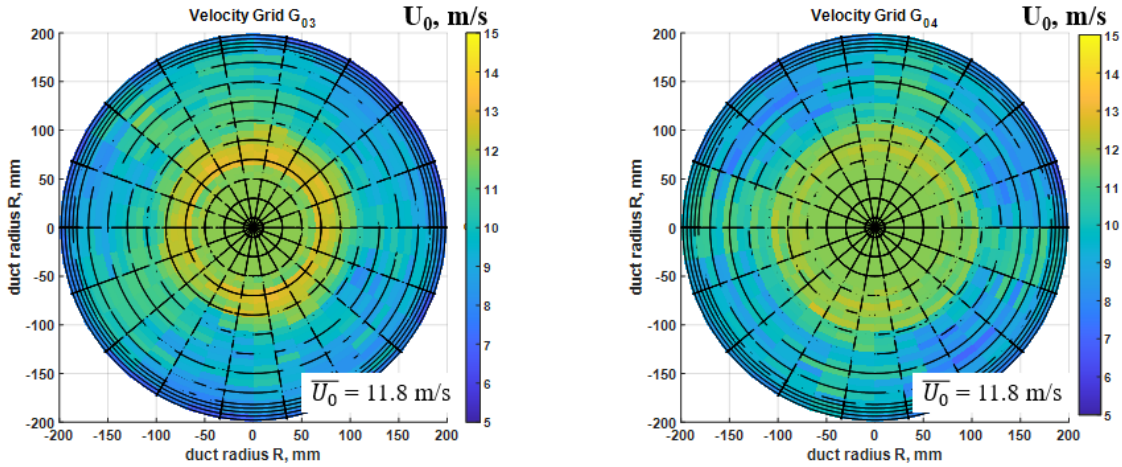

Figure D-3 Local distribution of longitudinal velocity for grid G_{03} (left) and G_{04} (right) at $n = 2000\ min^{-1}$, distance grid-to-probe $\Delta x = 0.3\ m$.

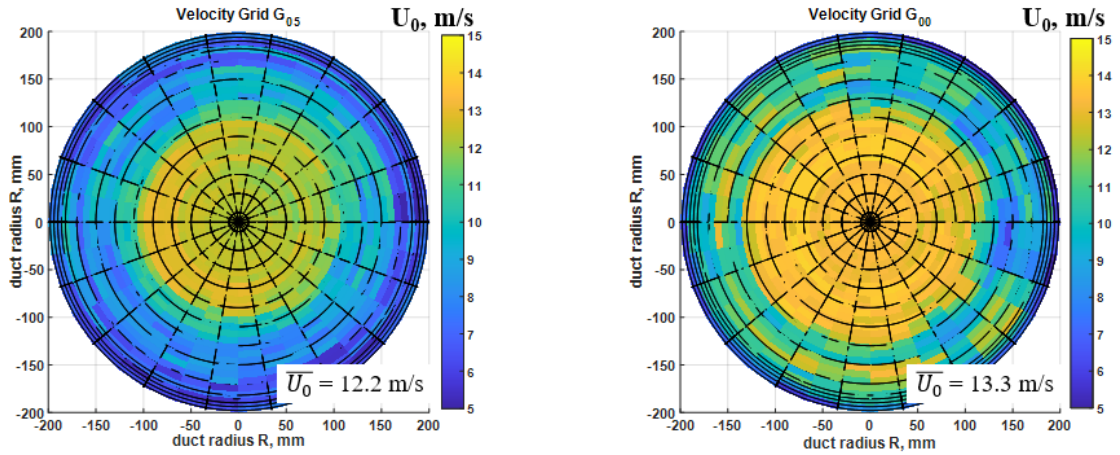

Figure D-4 Local distribution of longitudinal velocity for grid G_{05} (left) and the no-grid case G_{00} (right) at $n = 2000\ min^{-1}$, distance grid-to-probe $\Delta x = 0.3\ m$.

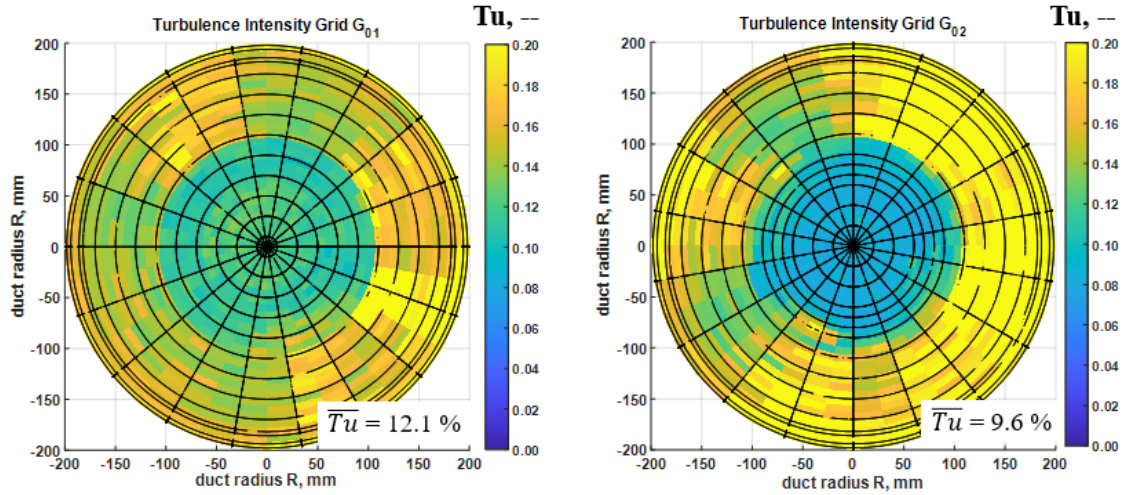

Figure D-5 Local distribution of longitudinal turbulence intensity for grid G_{01} (left) and G_{02} (right) at $n = 2000\ min^{-1}$, distance grid-to-probe $\Delta x = 0.3$ m.

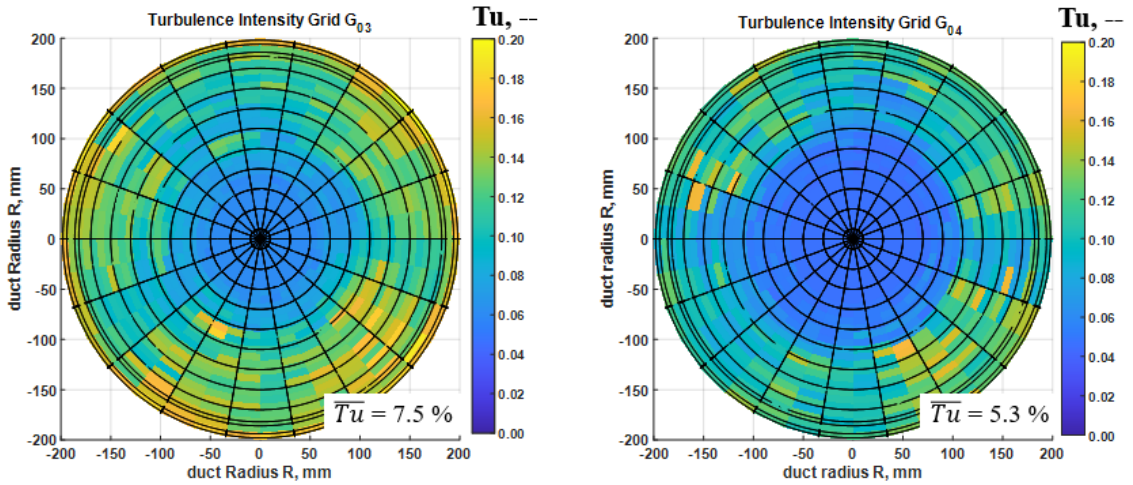

Figure D-6 Local distribution of longitudinal turbulence intensity for grid G_{03} (left) and G_{04} (right) at $n = 2000\ min^{-1}$, distance grid-to-probe $\Delta x = 0.3$ m.

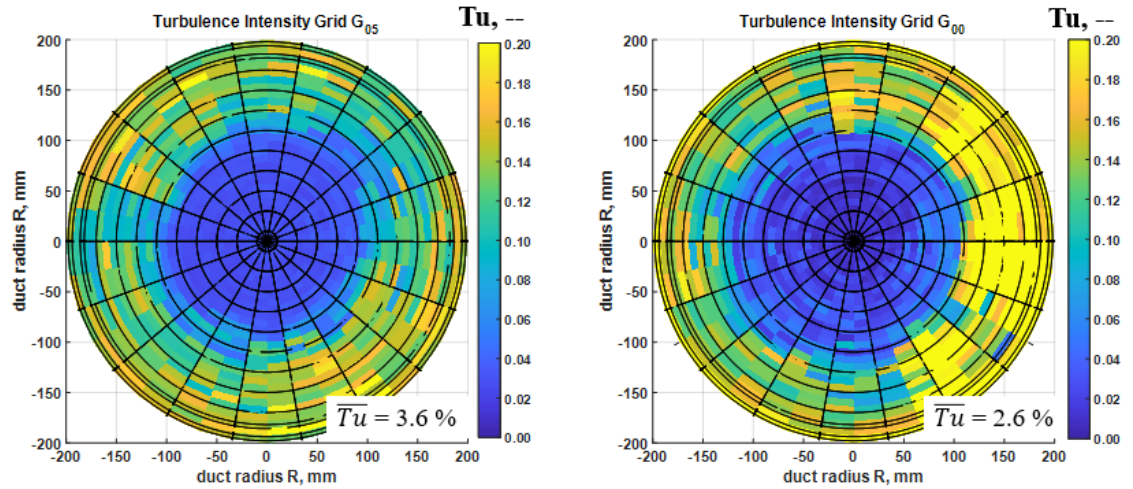

Figure D-7 Local distribution of longitudinal turbulence intensity for grid G_{05} (left) and the no-grid case G_{00} (right) at $n = 2000\ min^{-1}$, distance grid-to-probe $\Delta x = 0.3$ m.

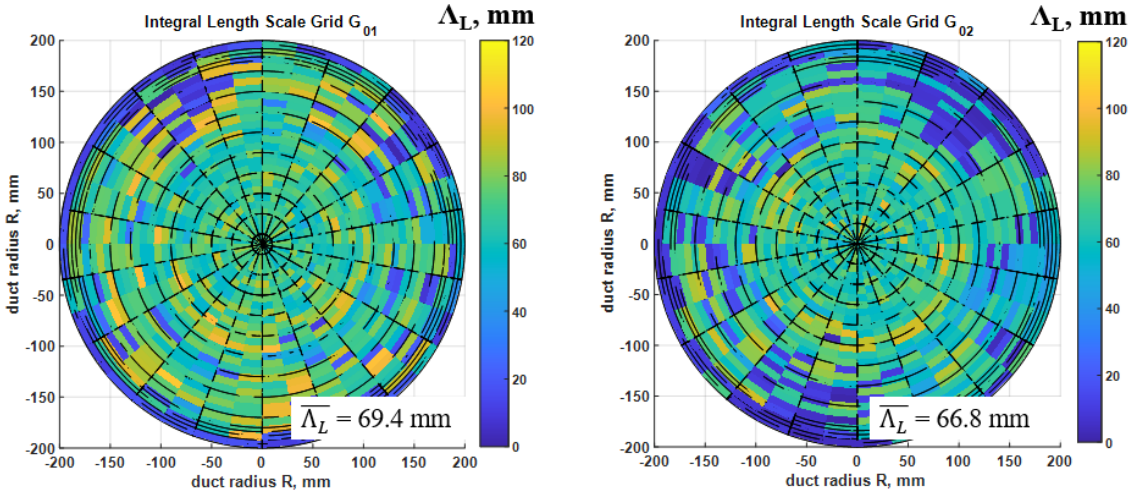

Figure D-8 Local distribution of longitudinal integral length scale for grid G_{01} (left) and G_{02} (right) at $n = 2000\ min^{-1}$, distance grid-to-probe $\Delta x = 0.3$ m.

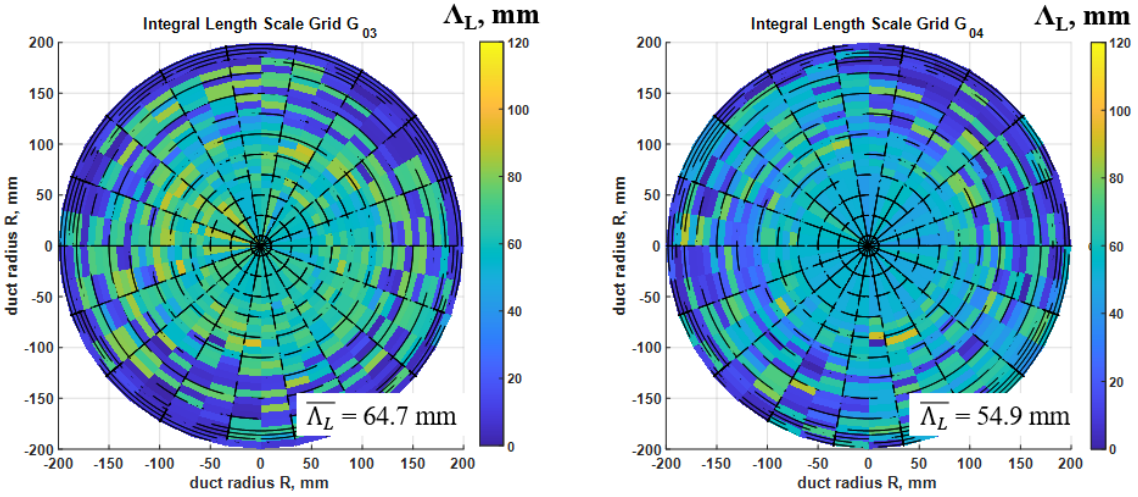

Figure D-9 Local distribution of longitudinal integral length scale for grid G_{03} (left) and G_{04} (right) at $n = 2000\ min^{-1}$, distance grid-to-probe $\Delta x = 0.3$ m.

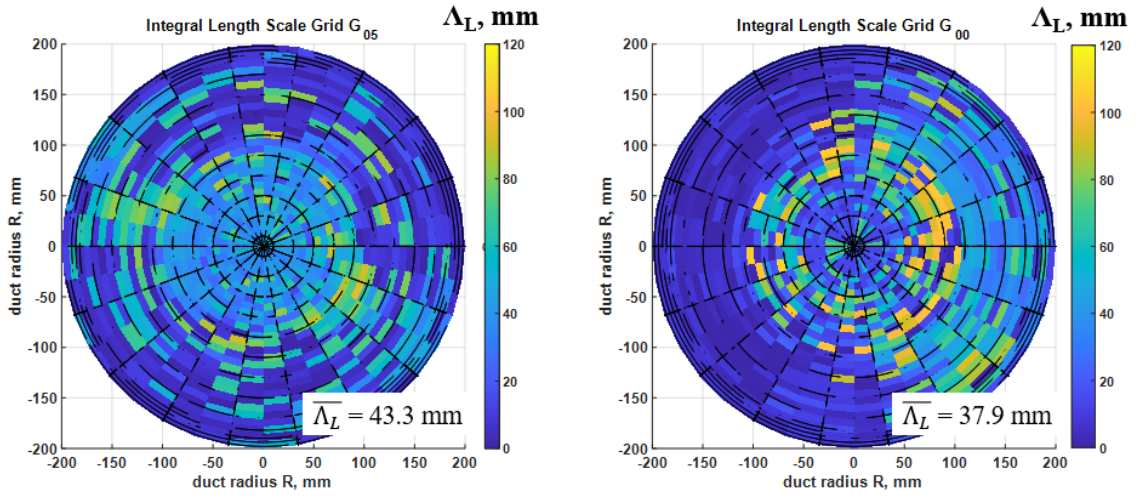

Figure D-10 Local distribution of longitudinal integral length scale for grid G_{05} (left) and the no-grid case G_{00} (right) at $n = 2000\ min^{-1}$, distance grid-to-probe $\Delta x = 0.3$ m.

D.3 Circumferentially Averaged Inflow Profiles with Different Turbulence Grids

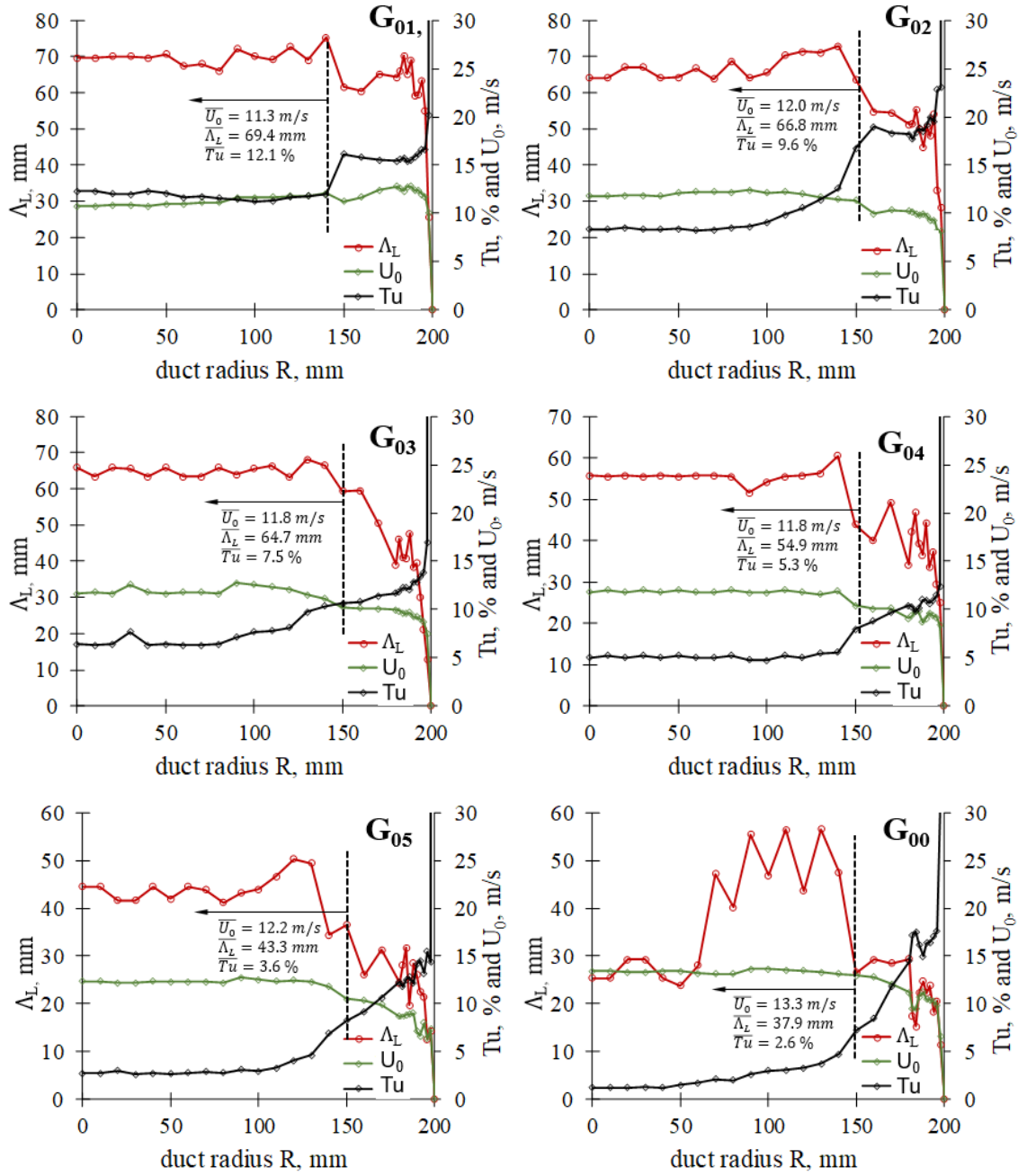

Figure D-11 Circumferentially averaged turbulent properties vs. the radial duct position for the tested turbulence grids at n = 2000 min^{-1}.

D.4 Dimensional Analysis – Scaling with the Aerofoil Chord

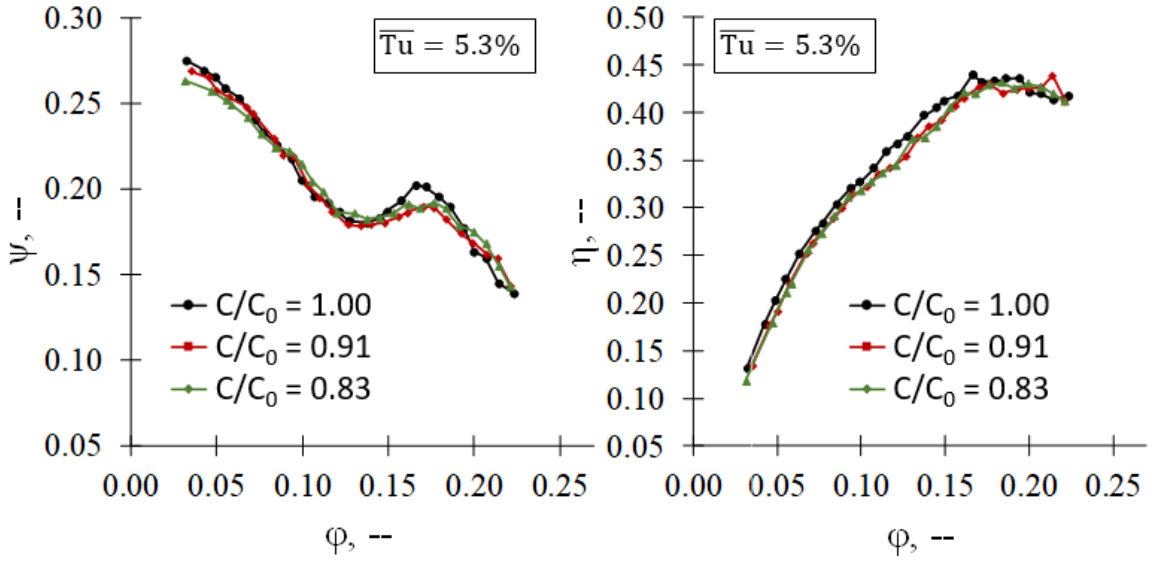

Figure D-12 Aerodynamic scaling with grid G_{04} installed while difference in surface is compensated according to the presented approach.

Appendix E Successive Blade Variation

E.1 Fan Characteristic Curves at low Tu – No Grid Case G_{00}

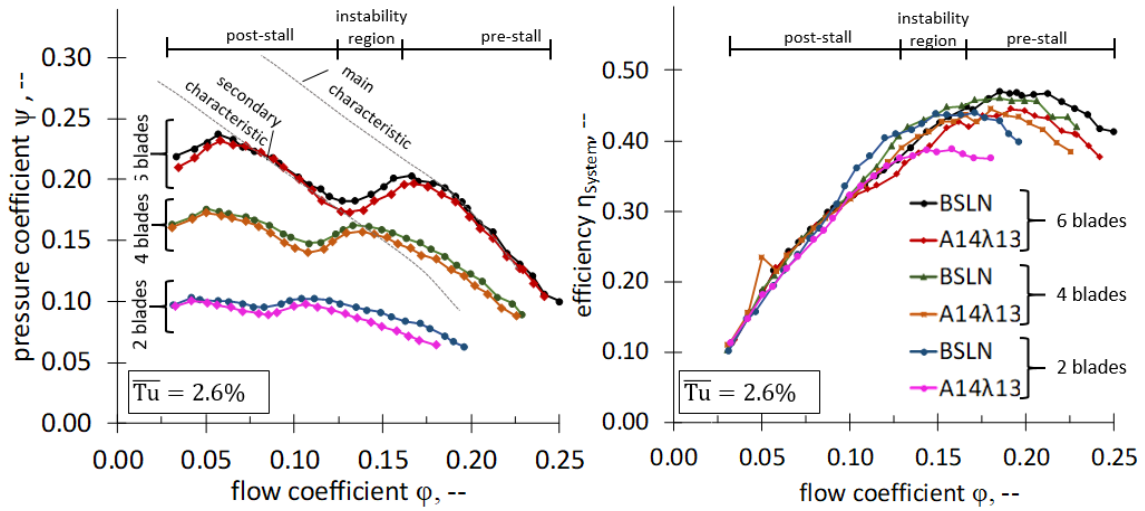

Figure E-1 Fan characteristic curves (left) and efficiency (right) of the tested baseline (BSLN) and the serrated (A14λ13) rotor for a varying blade number at Tu = 2.6 %.

E.2 ΔOAPWL for 4-bladed and 2-bladed Rotor Designs

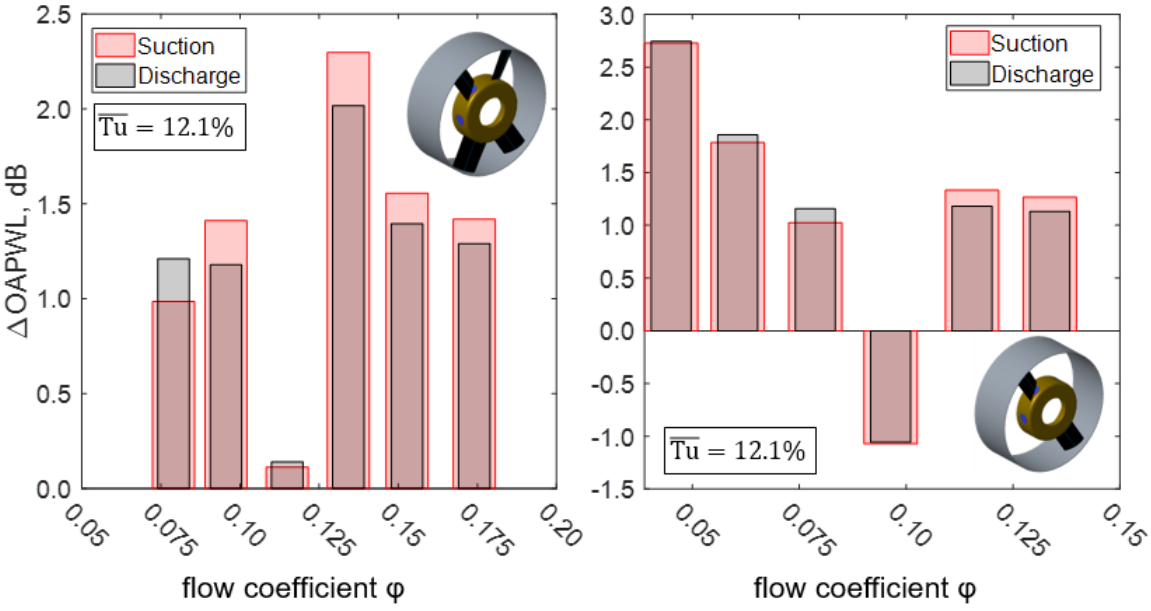

Figure E-2 Overall sound power level reduction ΔOAPWL of the 4-bladed rotor (left) and the 2-bladed rotor (right) at high incoming Tu.

Appendix F Parametric Study of Rotating Application

F.1 Aerodynamic Performance Parameter Variation for Tu = 5.3 %.

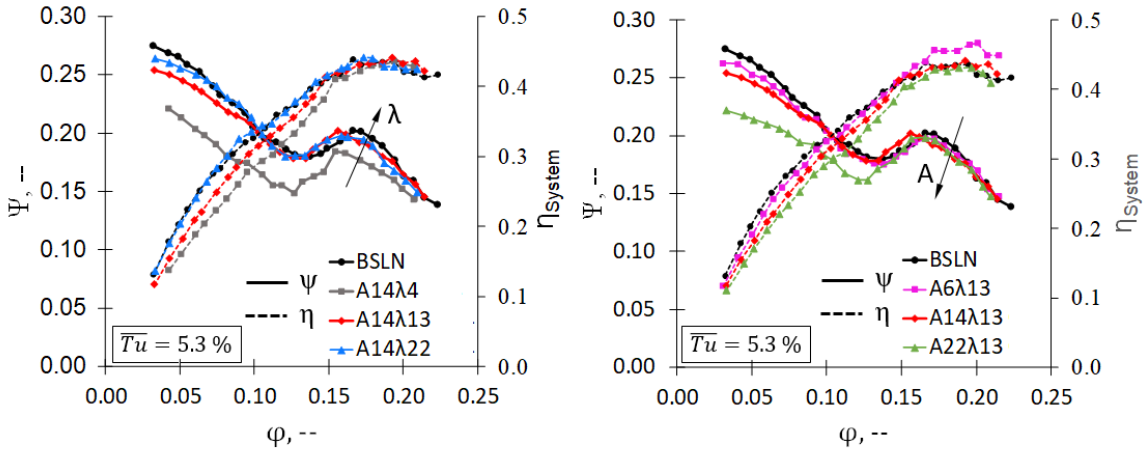

Figure F-1 Characteristic curves of pressure vs. flow coefficient for the tested rotor configurations at varying serration wavelength λ (left) and serration amplitude A (right). Tu = 5.3 % (Grid G_{04}).

Appendix G Aeroacoustic Modelling of Serrated Rotor

G.1 Test Matrix for Preliminary Investigations

Table G-1 Test matrix for the Latin hypercube sampling (left) and the circumscribed central composite design (C-CCD).

	non-dimensional			absolute		
	Δz	n	δ_{TS}	Δz	n	δ_{TS}
	--	--	--	mm	min^{-1}	%
LHS	1.000	-1.000	-1.000	500	1000	0
	-1.000	1.000	-1.000	100	2000	0
	-1.000	-1.000	1.000	100	1000	100
	1.000	1.000	1.000	500	2000	100
	0.473	-0.654	0.446	395	1173	72
	0.320	-0.213	-0.838	364	1393	8
	-0.298	0.254	0.982	240	1627	99
	-0.608	-0.911	-0.381	178	1044	31
	0.807	0.797	0.136	461	1898	57
	-0.850	0.391	-0.224	130	1695	39
	0.360	-0.546	-0.312	372	1227	34
	0.954	0.134	0.887	491	1567	94
	-0.168	-0.991	0.613	266	1005	81
	0.272	0.920	-0.458	354	1960	27
	-0.858	-0.304	-0.951	128	1348	2
	-0.641	0.450	0.220	172	1725	61
	-0.674	-0.312	0.616	165	1344	81
	-0.662	0.785	-0.136	168	1893	43
	0.300	0.567	-0.833	360	1783	8
	-0.236	-0.850	-0.655	253	1075	17
	0.605	0.281	0.907	421	1641	95
	0.877	-0.661	0.027	475	1169	51
	0.838	-0.167	0.486	468	1417	74
	0.358	0.890	-0.230	372	1945	39
	-0.558	0.263	-0.850	188	1632	7
	-0.180	0.609	0.908	264	1804	95
	-0.880	-0.426	0.184	124	1287	59
	0.088	-0.833	-0.648	318	1083	18

	non-dimensional			absolute		
	Δz	n	δ_{TS}	Δz	n	δ_{TS}
	--	--	--	mm	min^{-1}	%
C-CCD	-1.000	-1.000	-1.000	181	1203	20
	-1.000	-1.000	1.000	181	1203	80
	-1.000	1.000	-1.000	181	1797	20
	-1.000	1.000	1.000	181	1797	80
	1.000	-1.000	-1.000	419	1203	20
	1.000	-1.000	1.000	419	1203	80
	1.000	1.000	-1.000	419	1797	20
	1.000	1.000	1.000	419	1797	80
	-1.681	0.000	0.000	100	1500	50
	1.681	0.000	0.000	500	1500	50
	0.000	-1.684	0.000	300	1000	50
	0.000	1.684	0.000	300	2000	50
	0.000	0.000	-1.667	300	1500	0
	0.000	0.000	1.667	300	1500	100
	0.000	0.000	0.000	300	1500	50
	0.000	0.000	0.000	300	1500	50
	0.000	0.000	0.000	300	1500	50
	0.000	0.000	0.000	300	1500	50
	0.000	0.000	0.000	300	1500	50
	0.000	0.000	0.000	300	1500	50
	0.000	0.000	0.000	300	1500	50
	0.000	0.000	0.000	300	1500	50
	0.000	0.000	0.000	300	1500	50
	0.000	0.000	0.000	300	1500	50

Table G-2 Test matrix for the Box-Behnken design and for the independent test data for validating the different sampling approaches.

	non-dimensional			absolute		
	Δz	n	δ_{TS}	Δz	n	δ_{TS}
	--	--	--	mm	min^{-1}	%
Box-Behnken	-1.000	-1.000	0.000	100	1000	50
	-1.000	1.000	0.000	100	2000	50
	1.000	-1.000	0.000	500	1000	50
	1.000	1.000	0.000	500	2000	50
	-1.000	0.000	-1.000	100	1500	0
	-1.000	0.000	1.000	100	1500	100
	1.000	0.000	-1.000	500	1500	0
	1.000	0.000	1.000	500	1500	100
	0.000	-1.000	-1.000	300	1000	0
	0.000	-1.000	1.000	300	1000	100
	0.000	1.000	-1.000	300	2000	0
	0.000	1.000	1.000	300	2000	100
	0.000	0.000	0.000	300	1500	50
	0.000	0.000	0.000	300	1500	50
	0.000	0.000	0.000	300	1500	50

	non-dimensional			absolute		
	Δz	n	δ_{TS}	Δz	n	δ_{TS}
	--	--	--	mm	min^{-1}	%
Test	-1.000	-1.000	-1.000	100	1000	0
	1.000	1.000	-1.000	500	2000	0
	1.000	-1.000	1.000	500	1000	100
	-1.000	1.000	1.000	100	2000	100
	-0.484	-0.395	-0.856	203	1302	7
	0.773	0.295	-0.253	455	1647	37
	0.209	0.519	0.935	342	1760	97
	-0.290	0.741	-0.598	242	1870	20
	-0.735	-0.068	0.403	153	1466	70
	0.508	-0.878	0.269	402	1061	63

G.2 Test Matrix LHS + Factorial Core

Table G-3 Test matrix for the final ANN modelling approach, where the sampling of the experimental space is composed of a Latin hypercube design plus the factorial core to include the corners of the experimental space. The baseline rotor is samples with five samples per turbulence level and three test samples are defined for validation.

final sampling design		non-dimensional				absolute			
		A	λ	φ	Tu	A	λ	ϕ	Tu
		--	--	--	--	mm	mm	--	%
	LHS	1.00	-0.75	0.50	[-1, -0.77, -0.31, 0.09, 0.49, 1]	22.00	6.25	0.19	[2.6, 3.6, 5.3, 7.5, 9.6, 12.1]
		-0.75	-1.00	0.25	[-1, -0.77, -0.31, 0.09, 0.49, 1]	8.00	4.00	0.18	[2.6, 3.6, 5.3, 7.5, 9.6, 12.1]
		0.75	1.00	-0.25	[-1, -0.77, -0.31, 0.09, 0.49, 1]	20.00	22.00	0.16	[2.6, 3.6, 5.3, 7.5, 9.6, 12.1]
		-0.25	-0.50	-0.75	[-1, -0.77, -0.31, 0.09, 0.49, 1]	12.00	8.50	0.14	[2.6, 3.6, 5.3, 7.5, 9.6, 12.1]
		0.25	0.50	0.75	[-1, -0.77, -0.31, 0.09, 0.49, 1]	16.00	17.50	0.2	[2.6, 3.6, 5.3, 7.5, 9.6, 12.1]
		-1.00	0.75	-0.50	[-1, -0.77, -0.31, 0.09, 0.49, 1]	6.00	19.75	0.15	[2.6, 3.6, 5.3, 7.5, 9.6, 12.1]
		-0.50	0.25	1.00	[-1, -0.77, -0.31, 0.09, 0.49, 1]	10.00	15.25	0.21	[2.6, 3.6, 5.3, 7.5, 9.6, 12.1]
		0.50	-0.25	-1.00	[-1, -0.77, -0.31, 0.09, 0.49, 1]	18.00	10.75	0.13	[2.6, 3.6, 5.3, 7.5, 9.6, 12.1]
		0.46	0.99	0.49	[-1, -0.77, -0.31, 0.09, 0.49, 1]	17.68	21.91	0.1896	[2.6, 3.6, 5.3, 7.5, 9.6, 12.1]
		-0.81	-0.93	-0.01	[-1, -0.77, -0.31, 0.09, 0.49, 1]	7.52	4.63	0.1696	[2.6, 3.6, 5.3, 7.5, 9.6, 12.1]
		0.84	-0.14	-0.91	[-1, -0.77, -0.31, 0.09, 0.49, 1]	20.72	11.74	0.1336	[2.6, 3.6, 5.3, 7.5, 9.6, 12.1]
		-0.42	0.53	-0.58	[-1, -0.77, -0.31, 0.09, 0.49, 1]	10.64	17.77	0.1468	[2.6, 3.6, 5.3, 7.5, 9.6, 12.1]
		0.16	-0.34	0.93	[-1, -0.77, -0.31, 0.09, 0.49, 1]	15.28	9.94	0.2072	[2.6, 3.6, 5.3, 7.5, 9.6, 12.1]
	factorial core	1.00	1.00	-1.00	[-1, -0.77, -0.31, 0.09, 0.49, 1]	22.00	22.00	0.13	[2.6, 3.6, 5.3, 7.5, 9.6, 12.1]
		1.00	-1.00	-1.00	[-1, -0.77, -0.31, 0.09, 0.49, 1]	22.00	4.00	0.13	[2.6, 3.6, 5.3, 7.5, 9.6, 12.1]
		-1.00	1.00	-1.00	[-1, -0.77, -0.31, 0.09, 0.49, 1]	6.00	22.00	0.13	[2.6, 3.6, 5.3, 7.5, 9.6, 12.1]
		-1.00	-1.00	-1.00	[-1, -0.77, -0.31, 0.09, 0.49, 1]	6.00	4.00	0.13	[2.6, 3.6, 5.3, 7.5, 9.6, 12.1]
		1.00	-1.00	1.00	[-1, -0.77, -0.31, 0.09, 0.49, 1]	22.00	4.00	0.21	[2.6, 3.6, 5.3, 7.5, 9.6, 12.1]
		1.00	1.00	1.00	[-1, -0.77, -0.31, 0.09, 0.49, 1]	22.00	22.00	0.21	[2.6, 3.6, 5.3, 7.5, 9.6, 12.1]
		-1.00	1.00	1.00	[-1, -0.77, -0.31, 0.09, 0.49, 1]	6.00	22.00	0.21	[2.6, 3.6, 5.3, 7.5, 9.6, 12.1]
		0.00	0.00	0.00	[-1, -0.77, -0.31, 0.09, 0.49, 1]	14.00	13.00	0.17	[2.6, 3.6, 5.3, 7.5, 9.6, 12.1]
		-1.00	-1.00	1.00	[-1, -0.77, -0.31, 0.09, 0.49, 1]	6.00	4.00	0.21	[2.6, 3.6, 5.3, 7.5, 9.6, 12.1]
	BSLN	0.00	0.00	0.13	[-1, -0.77, -0.31, 0.09, 0.49, 1]	0.00	0.00	0.13	[2.6, 3.6, 5.3, 7.5, 9.6, 12.1]
		0.00	0.00	0.15	[-1, -0.77, -0.31, 0.09, 0.49, 1]	0.00	0.00	0.15	[2.6, 3.6, 5.3, 7.5, 9.6, 12.1]
		0.00	0.00	0.17	[-1, -0.77, -0.31, 0.09, 0.49, 1]	0.00	0.00	0.17	[2.6, 3.6, 5.3, 7.5, 9.6, 12.1]
		0.00	0.00	0.19	[-1, -0.77, -0.31, 0.09, 0.49, 1]	0.00	0.00	0.19	[2.6, 3.6, 5.3, 7.5, 9.6, 12.1]
		0.00	0.00	0.21	[-1, -0.77, -0.31, 0.09, 0.49, 1]	0.00	0.00	0.21	[2.6, 3.6, 5.3, 7.5, 9.6, 12.1]
	Test	1.0	1.0	1.00	1	22.00	22.00	0.21	12.1
		0.5	-0.25	-1	0.09	18.00	10.75	0.13	7.5
		0.46	0.99	0.49	0.49	17.68	21.91	0.19	9.6

G.3 ANN Predictions: Varying the Serration Amplitude

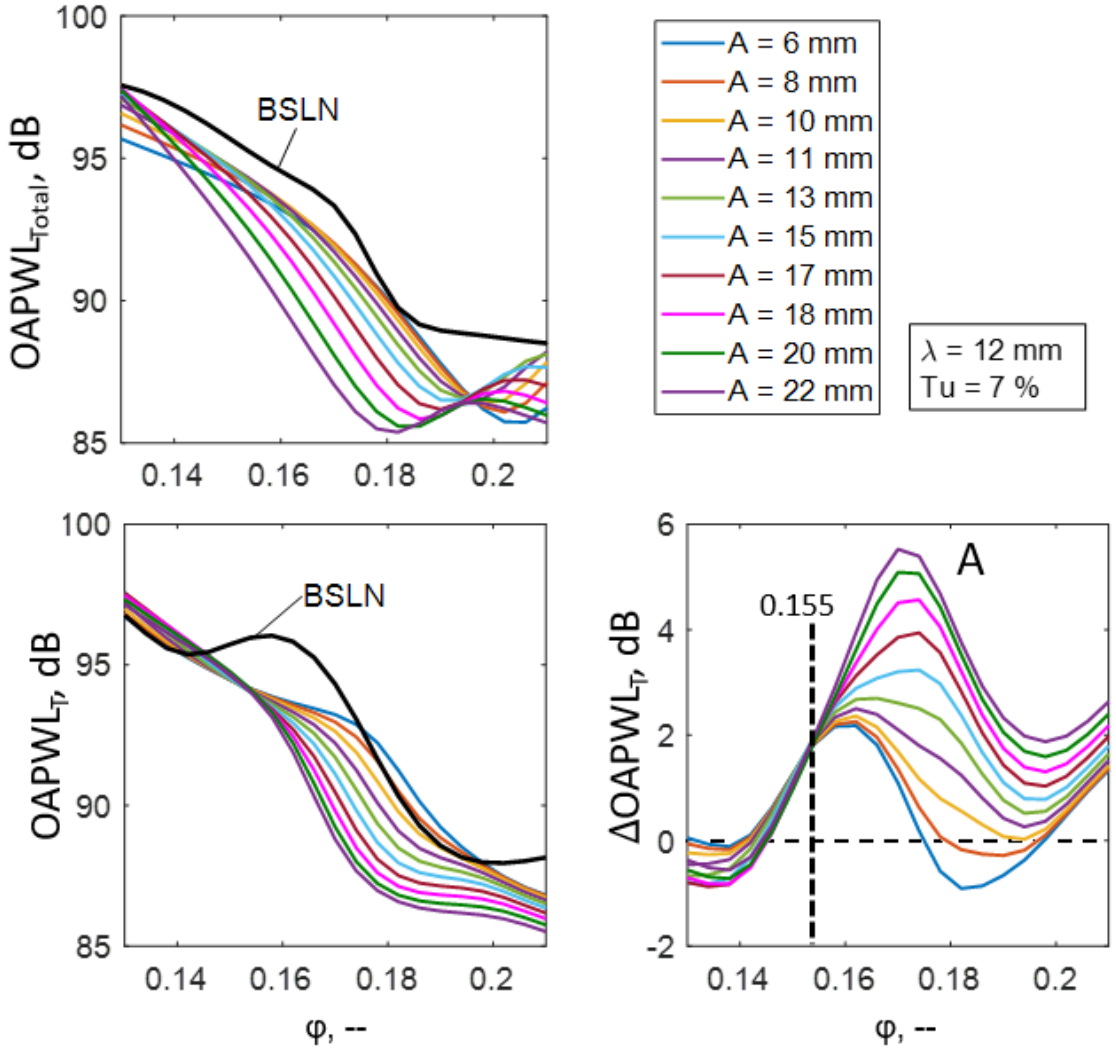

Figure G-1 Mean effect of the serration amplitude on the overall sound power level OAPWL for the total (top left) and tonal (bottom left) components as well as sound power level reduction ΔOAPWL for tonal components (bottom right). Values of free-stream turbulence and serration wavelength remain on intermediate levels. Predicted trends, generated via the ANNs.

G.4 ANN Predictions: Varying the Serration Wavelength

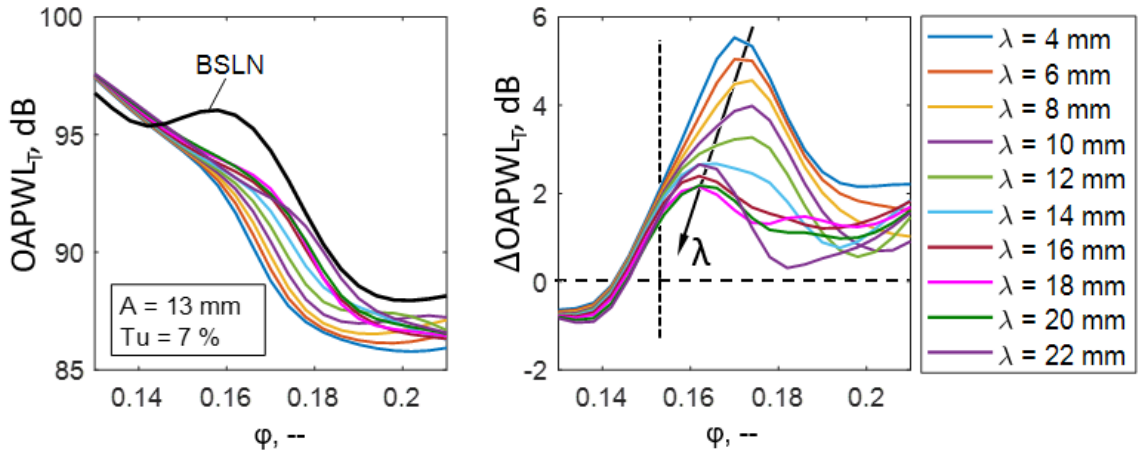

Figure G-2 Mean effect of the serration wavelength on the tonal overall sound power level (left) and noise reduction (right). Values of free-stream turbulence and serration amplitude remain on intermediate levels. Predicted trends, generated via the ANNs.

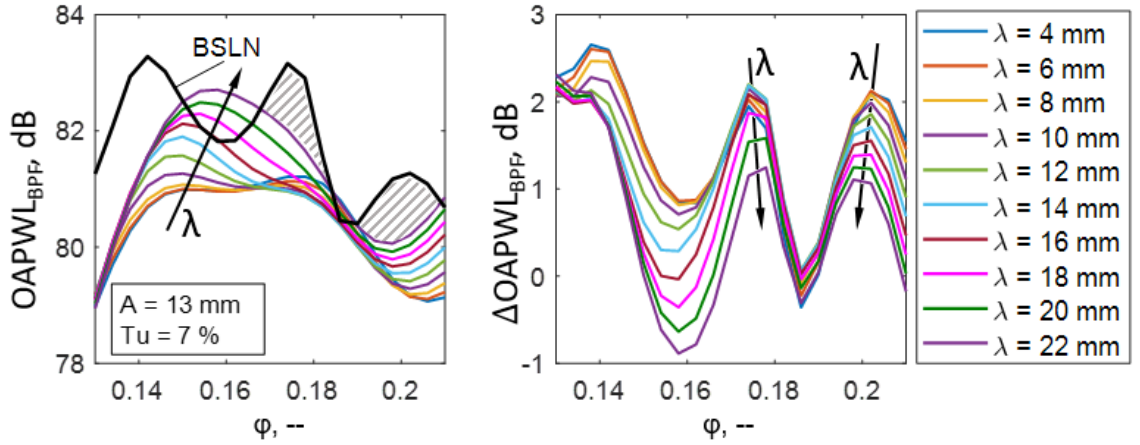

Figure G-3 Mean effect of the serration wavelength on the BPF overall sound power level (left) and noise reduction (right). Values of free-stream turbulence and serration amplitude remain on intermediate levels. Predicted trends, generated via the ANNs.

G.5 ANN Predictions: Spectral Applications

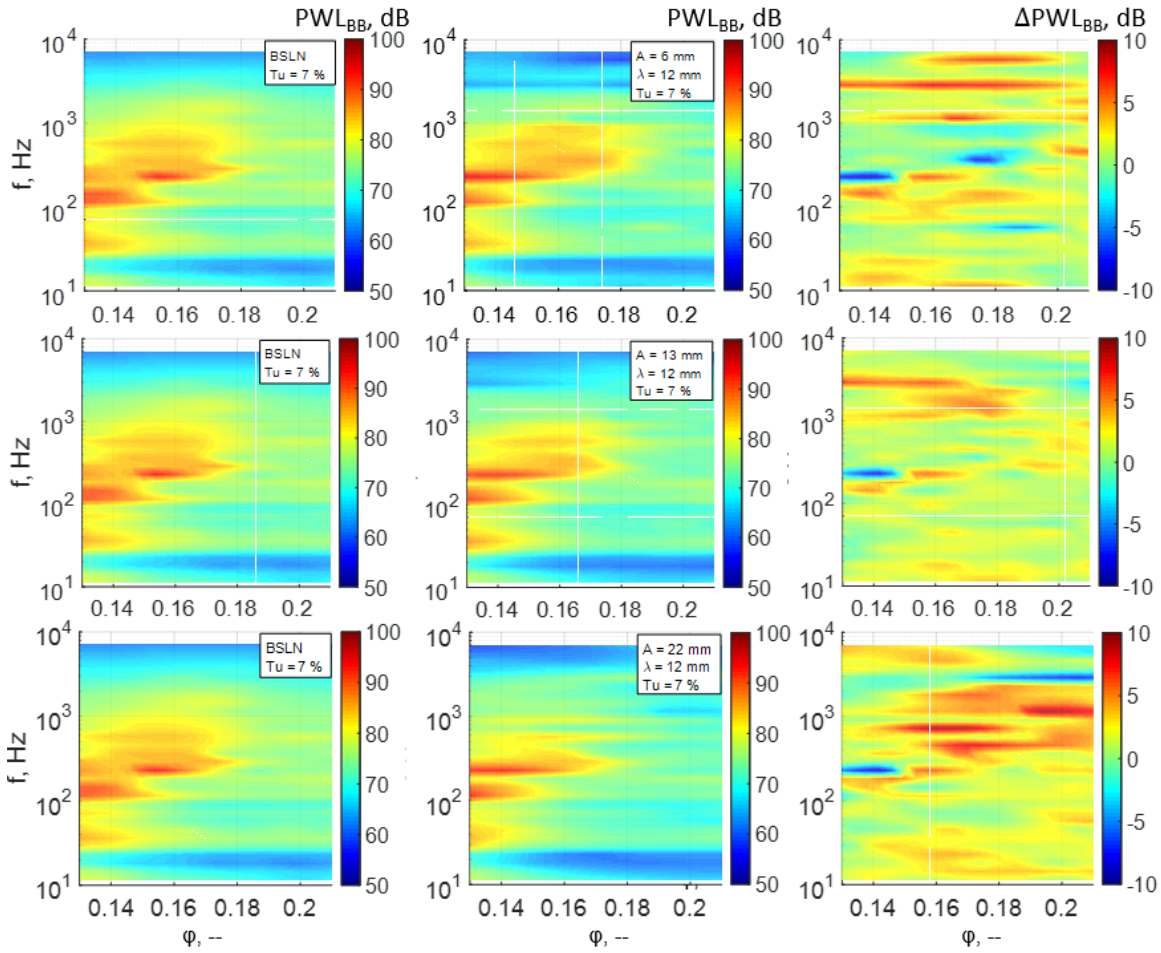

Figure G-4 Spectrograms for the broadband sound power level of the BSLN rotor (left) and a selected serration configuration (centre) as well as the resulting noise reduction (right). Variation of serration amplitude from minimum (top) to intermediate (centre) and maximum (bottom). Serration wavelength (λ = 12 mm) and turbulence intensity (Tu = 7 %) remain on intermediate levels. Predicted trends, composed of 29 individual ANNs for the 1/3rd-octave bands for each φ.

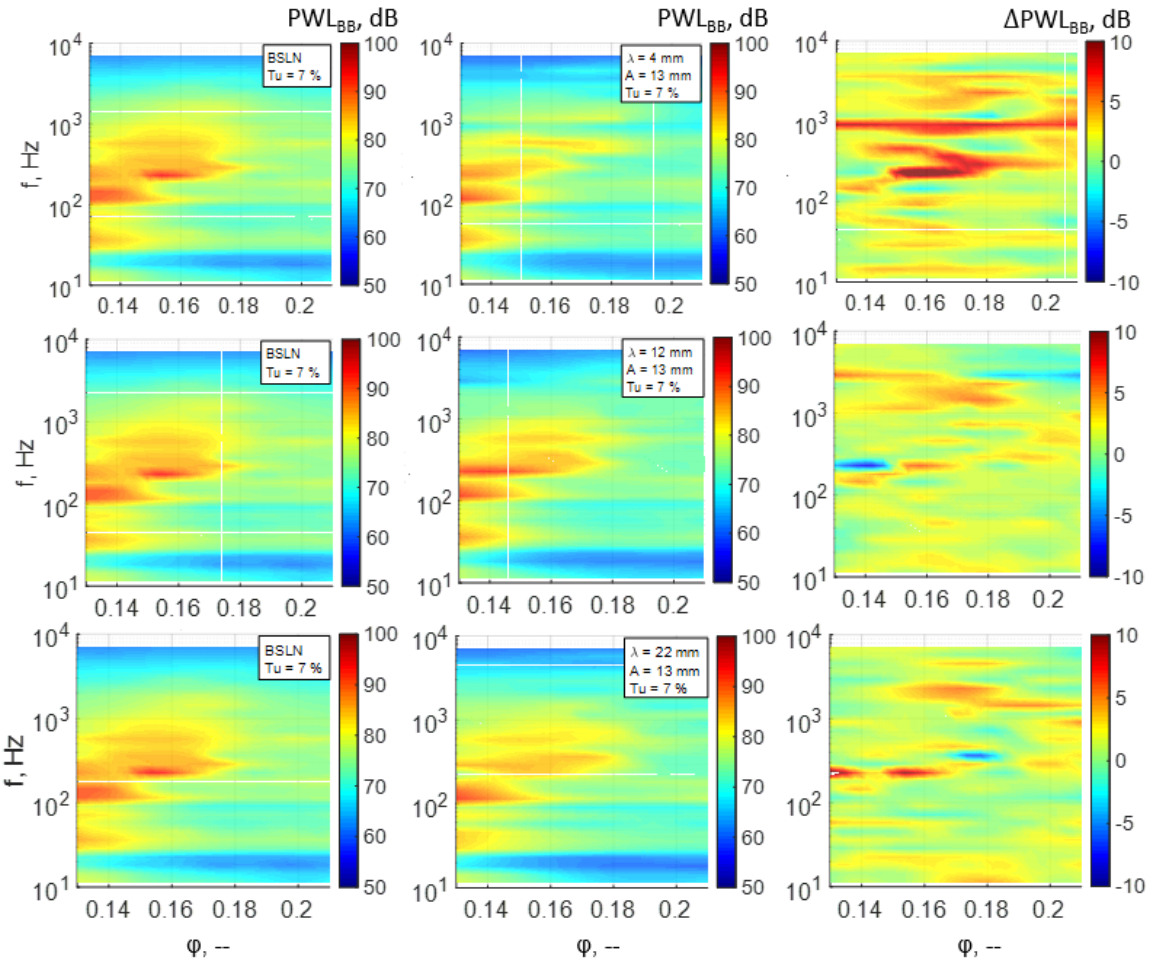

Figure G-5 Spectrograms for the broadband sound power level of the BSLN rotor (left) and a selected serration configuration (centre) as well as the resulting noise reduction (right). Variation of serration wavelength from minimum (top) to intermediate (centre) and maximum (bottom). Serration amplitude (A = 13 mm) and turbulence intensity (Tu = 7 %) remain on intermediate levels. Predicted trends, composed of 29 individual ANNs for the 1/3rd-octave bands for each φ.

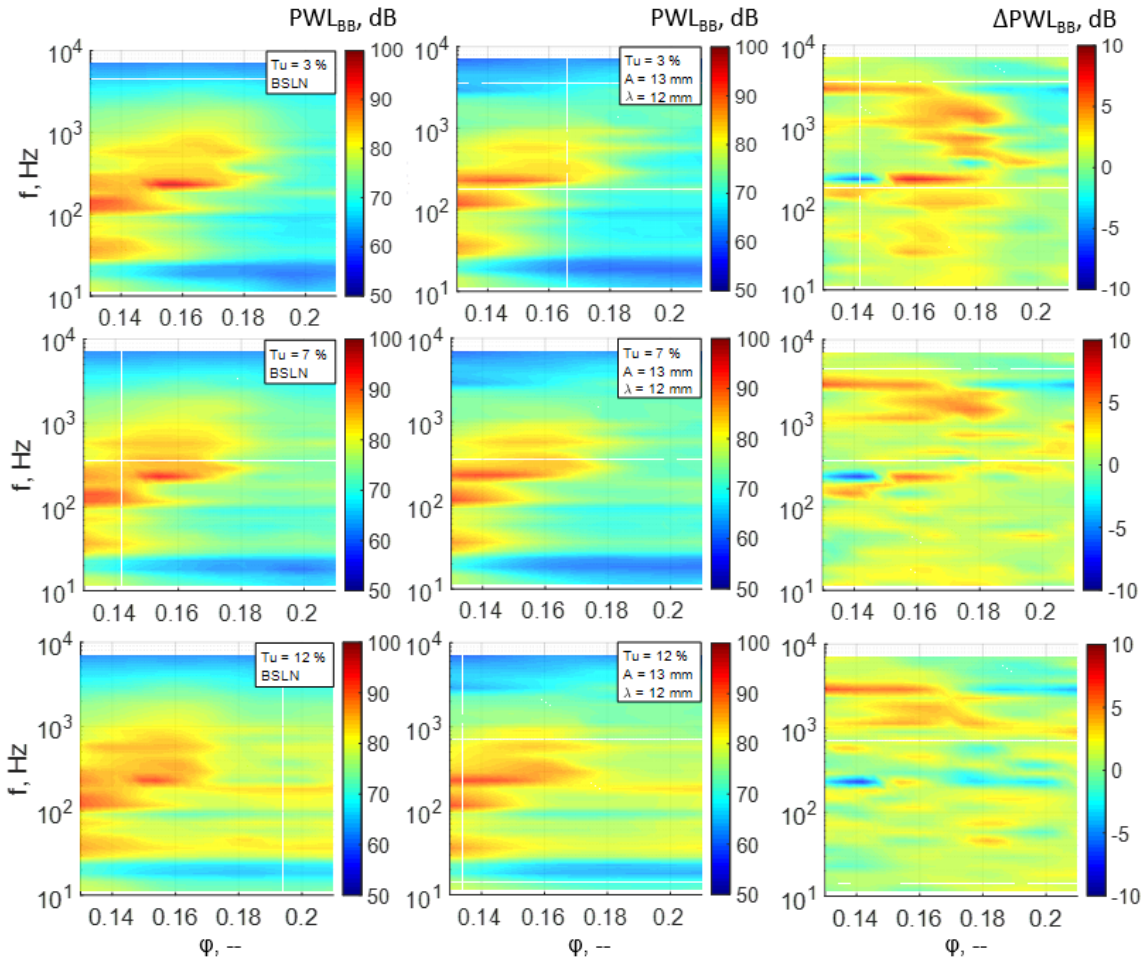

Figure G-6 Spectrograms for the broadband sound power level of the BSLN rotor (left) and a selected serration configuration (centre) as well as the resulting noise reduction (right). Variation of turbulence intensity from minimum (top) to intermediate (centre) and maximum (bottom). Serration amplitude (A = 13 mm) and serration wavelength (λ = 12 mm) remain on intermediate levels. Predicted trends, composed of 29 individual ANNs for the 1/3rd-octave bands for each φ.